Semi-Dilute Polymer Solutions in Strong Flows. Part I: Birefringence and Flow Modification in Extensional Flows. Part II: Chaotic Mixing in Time-Periodic Flows.

Thesis by

Ricky Chiu-Yin Ng

In Partial Fulfillment of the Requirements
for the Degree of
Doctor of Philosophy

California Institute of Technology
Pasadena, California

1990

(Submitted October 31, 1989)

哲理明言：

学海无涯，

回头是岸。

伍超贤

一九八九年十月

Dedicated:

To my parents,

and to my late grandmother.

Acknowledgements

I would like to thank my research advisor, Professor L. G. Leal, for his guidance and his support throughout the course of this work. His enthusiasm and insight in fundamental research have always been my guiding light. I have benefited a great deal through interactions with him and his research group. In particular, I am indebted to Dr. Paul Dunlap and Dr. Enrique Geffroy-Aguilar who have assisted me in many ways, especially in the experimental works that were foreign to me in the beginning of this research program. Professor D. F. James of the University of Toronto, Canada, has participated in the second part of this research program during his sabatical leave at Caltech, and I thank him for his intellectual stimulation that has enlightened my research interests. I am also grateful to Professor J. M. Ottino (from the University of Massachussetts, Amherst), Professor S. Wiggins, Professor J. F. Brady, Professor N. W. Tschoel, and Tasso Kaper for their interest in this work and for many valuable discussions.

I am thankful for the financial support provided by the Department of Chemical Engineering through the Union Oil Fellowship for my first year graduate study. This research has been supported by the Office of Naval Research, for which I am grateful.

The Caltech community has offered me a resourceful environment for improving my academic and research skills. I thank each and every one of those who have taught and/or assisted me in every aspect of my graduate study at Caltech. In particular, Chic Nakawatase's fine craftsmanship was invaluable in the design and construction of the experimental apparatus. Experimental data for the shear viscosity measurements are provided by Dr. William Milliken, and I thank him for his effort. I am indebted to Dave Loren for his assistance in the searching of the digital imaging system for the mixing studies. Also, assistance in many computer-related matters given by Alex Ho, Rick Koshi, John Bauer, Dr. Moshe Shapiro,

and Evangelos Petroutsos is greatly appreciated. I must also thank George Griffin, John Yehle, Floyd Litreal, Helen Dewitt, and Kathy Lewis for their help in the department.

In my years at Caltech, it has been both a rewarding and an enjoyable experience for me to know a great number of friends. In particular, I would like to thank the following list of friends for their support and friendship: Alex, Atta, Chuan, Lai, Chi-Fai, Ken, Fai-Mok, Suk-Man, Wilman, Paul Chan, Kwok-Wai, In-Seok, Boon-Khim, Chi Fong (#1 and #2), Chris, Judy, Thu, Chak, Pete, Kiat, Richard, Renita, Greg, Sing-Ung, Ming, and Terence.

Most of all, I wish to express sincere gratitude to my family for their support, love, and encouragement. In particular, my parents have been understanding, loving, and supportive throughout my years at Caltech. Their sacrifice and love for me have been the sole inspiration in my graduate student life.

Abstract

The non-Newtonian effects of semi-dilute polymer solutions in laminar two-dimensional steady and time-periodic *strong* flows are examined separately in two parts of this thesis. Strong flows are flows that can induce large deformation of the polymer molecules. The first part of this thesis is the study of flow-induced stretching of macromolecules in semi-dilute solutions and the subsequent modification to *extensional* flows in a two-roll and a four-roll mill. Experimental results are presented for flow birefringence, which provides a measure of the degree of polymer extension. In addition, we report on velocity gradient measurements via the technique of homodyne light scattering for solutions of various polymer concentrations in the dilute to semi-dilute regime. Model predictions are also discussed using an interacting dumbbell model. In the second part of the thesis, we examine fluid mixing and transport in two-dimensional time-periodic Stokes flows produced in a *blinking two-roll mill* (BTRM) for both Newtonian and polymer solutions. Here, we report experimental data obtained by the technique of flow visualization using dye tracer, as well as quantitative measurements using a digital imaging technique.

The flow birefringence results for 100, 1500, and 4500 ppm polystyrene in viscous solvents indicate that increasing concentration will inhibit stretching of polymer molecules due to strong intermolecular interactions. The birefringence data for all three solutions correlate with the eigenvalue of the velocity gradient tensor for different extensional flows in the 2-roll and the 4-roll mill. Inception and cessation of steady extensional flows show distinctive overshoots in birefringence for the semi-dilute (1500 and 4500 ppm) solutions. Complementary velocity gradient measurements show a significant inhibition of large strain rates when a sufficient amount of *extended* polymer is present (the dilute 100 ppm solution shows no flow effect). The onset of polymer-induced changes in the flow (flow modification) occurs at a *critical* effective volume concentration, $\phi_c \sim 175$, based upon the volume of spheres that circumscribe the extended polymer chain, for

both semi-dilute solutions. The magnitude of flow modification is larger in the less concentrated 1500 ppm solution due to the competing effects of increasing concentration and the inhibition of polymer extension which tends to lower the effective volume concentration, ϕ_{eff}. The correlation of the magnitude of flow modification with ϕ_{eff} is revealed by the local (pointwise) velocity gradient measurements for different concentration polymer solutions.

Various molecular models for non-dilute polymer solutions are discussed. The best comparison with the present flow birefringence data is obtained from the predictions of an interacting nonlinear elastic dumbbell (FENE-IDB) model. The FENE-IDB model predictions show a smooth transition of dilute solution behavior to semi-dilute solution behavior. In dilute solutions, the birefringence normalized with polymer concentration (or specific birefringence) is independent of concentration, c. However, the specific birefringence is proportional to c^{-1} when plotted versus the dimensionless eigenvalue of the velocity gradient tensor, $\tau\gamma\sqrt{\lambda}$, for semi-dilute solutions. We also noted that the relaxation time of polymer, τ, is dependent on c for semi-dilute solutions.

Studies of mixing and fluid transport properties in time-periodic laminar BTRM flows are first performed for Newtonian solutions. Fluid mixing is shown to be either *regular* or *chaotic* depending on the characteristic period of oscillation, μ. Chaotic (efficient) mixing is achieved *globally* in the flow device when $\mu \geq 0.5$. The results in the mixing study can be compared qualitatively with dynamical systems theory predictions of chaos in time-periodic vortex-pair flows. The effect of polymer (a 1500 ppm solution of polystyrene in viscous solvent) on chaotic mixing and fluid transport in the BTRM flows is an O(1) decrease in both the area of mixing and the rate of fluid transport between different regions of the flow when compared with the corresponding Newtonian data. The onset of the polymer effect on the flow occurs at a critical Deborah number of $(De)_c \sim 2$. This high De effect may be related to polymer-induced changes to both the weak and strong

flow regions in the BTRM since the time-periodic flow is alternatively *strong* and mostly *weak* in the Lagrangian frame of reference.

Table of Contents

INTRODUCTION

Dilute polymer solutions in *strong* flows have been shown to exhibit dramatic non-Newtonian effects. Strong flows correspond to flows that are capable of inducing large deformation of the polymer molecules. Specifically, a linear polymer chain in a strong flow can be extended exponentially in time. The dilute solutions exhibit no measurable non-Newtonian flow effects in simple shear flow, which is classified as a *weak* flow. The well-known *Toms* phenomenon [1] of turbulent drag reduction in pipe flows due to the presence of a minute amount of polymer additive in a solution is the classical, and the ealiest (discovered in 1948) example of a strong flow effect for dilute polymer solutions. Although turbulent flows cannot be characterized in detail to determine the existence of critical strong flow conditions for polymer stretching, the local flow structure of turbulent pipe flow near the wall is likely to provide an extensional component (time-dependent) in the flow. Indeed, Batchelor [2] has shown using a simple model for particle motion in homogeneous turbulence that exponential stretching of material line can occur in these turbulent flows. In addition, experimental observations of a sharp pressure increase in laminar flow through porous media [3] and in sink flow [4], and inhibition of large strain rates in two-dimensional extensional flows [5], have also suggested that the polymer-induced flow effect in dilute solutions is the result of large deformation of polymers that are oriented and stretched by a strong flow.

In order to understand the strong flow effects, it is important to study both the effects of the flow on polymer conformation *and* the effect of the polymer on the flow. A two-roll and a four-roll mill can provide an approximation of two-dimensional linear extensional (strong) flows that are well-characterized by previous investigators from this laboratory [5,6]. In Chapter I, the technique of flow birefringence, which provides a measure of polymer extension, and velocity gradient measurements using homodyne light scattering, are performed on polymer solutions with concentrations in the dilute to semi-dilute regime in steady

extensional flows generated by the two-roll and the four-roll mill. Transient flow birefringence experiments are also performed for inception and cessation of steady extensional flows. We are interested in the effect of increasing concentrations on flow-induced stretching of polymer and subsequent flow modification. The onset and magnitude of flow modifications are found to be dependent on an *effective* volume concentration based upon the volume of spheres which circumscribe the extended polymer molecules. The degree of flow modification also shows a correlation with the effective volume concentration using different concentration polymer solutions. The results may provide an explanation for the observation of maximum drag reduction with increasing polymer concentrations.

The flow birefringence data are useful for testing dumbbell models for non-dilute polymer solutions. In Chapter II, an interacting FENE dumbbell (FENE-IDB) model is developed for semi-dilute polymer solutions in two-dimensional extensional flows. The theory is based on a Hookean dumbbell model for interacting dumbbells proposed by Hess [7]. The effect of a nonlinear spring (Warner spring) is examined. The predicted dynamic behavior of the polymer in extensional flow is distinctively different from dilute solution behavior. A polymer molecule in dilute solution can be extended to its full contour length by the extensional flow, whereas a significant decrease in the degree of extension of polymer is predicted for semi-dilute solutions. Model predictions agree well with steady birefringence data that show *inhibition* of stretching as the polymer concentration is increased, presumably due to an increased level of intermolecular interactions.

The studies above are for steady flows and show *localized* interaction between the polymer and the flow. However, polymer molecules in turbulent flow would experience a complicated time-dependent flow history. The blinking two-roll mill (BTRM) is built to provide a time-periodic laminar flow that shows chaotic particle motion when the *strength* of the flow is sufficiently large. The dynamics of dilute polymer solutions in the BTRM flow is more directly relevant to the polymer

behavior in the context of turbulent drag reduction, than studies in steady flows. First, from the Lagrangian frame of reference seen by a polymer molecule, the BTRM flow is alternatively strong and (mostly) weak and this is similar to the environment seen by a polymer in a turbulent flow. Second, the region of the flow domain where the flow is strong on average, in the sense that there is an exponential separation of material points, is substantial – in fact the region covers the whole of the two-roll mill for a high enough roller speed or a long enough period for blinking.

Before the study of the effect of polymer in time-periodic flows, the characteristics of the BTRM flow is first investigated using Newtonian fluids. The results are presented in Chapter III. The essential proofs, such as the existence of Smale horseshoe structure or a positive Liapunov exponent, for chaos in the context of dynamical systems theory, are revealed by performing mixing experiments using the techniques of flow visualization with dye tracer and quantitative measurements using digital imaging analysis for Newtonian solutions in the BTRM flows. The rate of interfacial area generation, the area and regions of chaotic mixing, and the rate of fluid transport (redistribution of fluid elements) between various regions of the flow are obtained from the quantitative measurements. The results can be compared qualitatively with theoretical studies of time-periodic vortex-pair flows by Aref [8] and Rom-Kedar *et al.* [9].

The mixing results for Newtonian fluids indicate the potential for a strong flow effect with polymer solutions in the BTRM flow. In Chapter IV, experimental evidence of non-Newtonian effects for a dilute polymer solution in the BTRM flow is reported. The area of chaotic mixing and the rate of fluid transport show an O(1) decrease when compared with the corresponding Newtonian results. The onset of polymer effect on the flow occurs at a critical Deborah number of $(De)_c \sim 2$. This high De effect for dilute polymer solution may be related to the polymer-induced changes in both the weak and strong flow regions of the BTRM flow.

References

[1] Toms, B. A., *Proc. 1st Int. Congr. Rheol.*, **2**, 135 (1948).

[2] Batchelor, G. K., *Proc. Roy. Soc. Lond. A*, **213**, 349 (1952).

[3] Durst, F., Haas, R., Interlhal, W., *Rheol. Acta*, **21**, 572 (1982).

[4] James, D. F., Saringer, J. H., *J. Fluid Mech.*, **97**, 655 (1980).

[5] Dunlap, P. N., Leal, L. G., *J. Non-Newt. Fluid Mech.* **23**, 5 (1987).

[6] Fuller, G. G., Leal, L. G., *Rheol. Acta*, **19**, 580 (1980).

[7] Hess, W., *Rheol. Acta*, **23**, 477 (1984).

[8] Aref, H., *J. Fluid Mech.*, **143**, 1 (1984).

[9] Rom-Kedar, V., Leonard, A., Wiggins, S., "*An Analytical Study of Transport, Mixing and Chaos in an Unsteady Vortical Flow*," *J. Fluid Mech.*, to appear (1989).

Part I: Birefringence and Flow Modification in Extensional Flows

Chapter I

Concentration Effects on Birefringence and Flow Modification of Semi-Dilute Polymer Solutions in Extensional Flows

Concentration Effects on Birefringence and Flow Modification of Semi-Dilute Polymer Solutions in Extensional Flows

R. C.-Y. Ng*

Department of Chemical Engineering
California Institute of Technology
Pasadena, California 91125

and L. G. Leal†

Department of Chemical & Nuclear Engineering
University of California
Santa Barbara, California 93106

* Present address: Mobil Research and Development Corp., Dallas Research Laboratory, Dallas, TX 75244-4312, U.S.A.

† To whom all correspondence should be addressed

Abstract

The effect of polymer concentration on flow birefringence and flow modification (polymer-induced changes on the flow field) in two-dimensional extensional flows for polystyrene solutions with concentration from dilute to semi-dilute regime in a two-roll and a four-roll mill are examined. The experiments are performed using the techniques of flow birefringence which provides a measure of macromolecular extension, and homodyne light scattering which directly measures the velocity gradient in the flow field. The concentration of the polymer solutions are 1500 and 4500 ppm that correspond to ~ 0.33 and $1.0 \times c^{\star}$, the critical concentration for domain overlap of the coiled polymer molecule at equilibrium, respectively. Results from a dilute 100 ppm solution of the same polymer sample by previous investigators [8] are also presented for comparison. From the steady flow birefringence results, high concentration appears to inhibit extension of the polymer chains due to intermolecular interactions. In addition, inception and cessation of steady flow experiments show distinctive overshoots in birefringence. Various molecular models for non-dilute polymer solutions are discussed and compared with flow birefringence data. The main result in this study is that the semi-dilute polymer solutions (1500 and 4500 ppm) show significant inhibition of high strain rates as is evident from the velocity gradient measurements. The decrease in velocity gradient from the Newtonian value is up to 28% in the 4-roll mill and 20% in the 2-roll mill. The onset of flow modification corresponds to a critical effective volume concentration of spheres circumscribing the extended polymer chain to be $\phi_c \sim 175$ for *both* semi-dilute solutions. The degree of flow modification also shows correlation with ϕ using different concentration polymer solutions.

1. Introduction

The interesting *Toms* phenomenon [1] of drag reduction, where the presence of a minute amount of polymer additive in a solution causes a great reduction in drag in turbulent pipe flow, provides one strong motivation for studying the dynamic behavior of dilute solutions of macromolecules in flow. These long chain molecules respond to straining forces in a flow by deforming and reorienting from their initial or equilibrium configuration. This macromolecular motion can give rise to non-Newtonian fluid behavior, even in solutions of only a few parts per million by weight (ppm) of the polymer. The deformation (conformation change) of a flexible polymer induced by a *strong* flow [2,3] corresponds to the so-called coil-stretch (C-S) transition, in which the equilibrium coiled configuration of the polymer chain extends abruptly to a near fully stretched state. Important indications of the C-S transition in dilute polymer solutions include a sharp pressure drop increase in flow through porous media [4] and in sink flow [5]; the abrupt onset of flow birefringence in stagnation flows of various geometry [6-8]; and drag reduction in turbulent pipe flows [9,10].

In order to understand the effect of flow induced stretching of dilute polymer solutions on a flow field, previous investigators from this laboratory [7,8] have applied flow birefringence and homodyne light scattering techniques to provide, respectively, a direct indication of the C-S transition and the detection of a significant decrease in the velocity gradient relative to that for a Newtonian fluid. Dunlap and Leal [8] correlated the onset of a polymer-induced decrease in the velocity gradient (we will refer to this polymer-induced effect as *flow modification* throughout this paper) to strong interactions between the stretched polymer chains aligned locally along the outflow axis near the stagnation region of a four-roll mill. Their measurements suggested that the necessary condition for flow modification was that an effective volume concentration based on spheres circumscribing the elongated polymer chains must exceed $\sim 4000 - 6000$. They also estimated that

the corresponding increase in elongational viscosity (or equivalently extra stress) due to the stretched polymer was around ~ 500 times that of the solvent. Therefore, the dilute polymer solution appeared to inhibit development of high strain rates due to this apparent increase in elongational viscosity. However, Dunlap and Leal only found an O(1) change in the velocity gradient even though the estimated extra stress due to polymer stretching is of $O(10^2)$. Since one would expect to see an influence on the flow for even an O(1) increase in polymer stress, Dunlap and Leal suggested that the polymer effect may be so localized in their flow device that changes in the flow are difficult to detect with a scattering volume that is $\sim 150\mu m$ in diameter ($1/40^{th}$ and $1/200^{th}$ of the gap between the opposing rollers in the 2-roll and 4-roll mills, respectively). Thus, it was hypothesized that actual onset of flow modification did not show up until the polymer effect had spread over a region of size comparable to the scattering volume. With higher concentrations, the birefringence is initially spread out over a larger region of the flow field and this question is not so significant.

Delocalization of birefringence for moderately concentrated polymer solutions has, in fact, been demonstrated by earlier investigators [11-14]. In addition, Gardner *et al.* [11] have measured flow modifications for polymer solutions in a cross-slot device using laser-doppler velocimetry. However, these investigators could detect an effect of the polymer only when the polymer concentration was above the critical value $c^\star$, corresponding to the existence of polymer-polymer interactions in the equilibrium state. In the present study, we compare rheological properties of polymer solutions with concentrations well below and near the critical concentration $c^\star$, using both birefringence and pointwise velocity gradient measurements by homodyne light scattering to provide a correlation between polymer conformation and flow modification. The application of the homodyne light scattering technique to study the flow has a definite advantage over conventional laser velocimetry studies. In particular, Dunlap and Leal [8] have already pointed

out the better sensitivity of homodyne light scattering (which directly provides velocity gradient data) relative to the LDV technique used by Gardner *et al.* [11].

In the present work, we considered concentrations in the transition regime between dilute and semi-dilute in order to achieve a qualitative understanding of the role of intermolecular interactions and high effective volume concentration on the onset of stretching, the transition from coil to stretch (C-S) state, and flow modifications. Our studies include both steady state and transient data, for flows generated in a four-roll and two-roll mill where the velocity $\mathbf{v}$ is given approximately by

$$\mathbf{v} = \gamma \quad (\mathbf{\Gamma} \cdot \mathbf{r}) \tag{1}$$

where

$$\mathbf{\Gamma} = \begin{pmatrix} 0 & 1 & 0 \\ \lambda & 0 & 0 \\ 0 & 0 & 0 \end{pmatrix} \quad , \quad -1 \leq \lambda \leq 1$$

The range of flow types in this study is for $\lambda > 0$ which is in the strong flow regime necessary for high chain extension [3,15]. The transient birefringence data is particularly interesting because birefringence overshoot has been observed by Fuller and Leal [16] for start-up of a pure straining flow in the 4-roll mill for moderately concentrated polymer solutions. Fuller and Leal related the overshoot phenomenon to predictions of a temporary entanglement network theory [17]. However, no overshoot was observed either experimentally and theoretically for dilute solutions in these strong flows. It is therefore interesting to study transient behavior of polymer solutions in the intermediate concentration regime. Time-dependent birefringence results are presented here for both the inception and cessation of steady extensional flows in the two-roll and four-roll mills. Pronounced overshoots in birefringence were detected when the shear rate exceeds a critical value in these semi-dilute solutions.

The relevance of studying different polymer concentrations in the drag reduction context is due to the fact that the degree of drag reduction reaches an asymptote with increasing concentration, even though it is found to increase proportionally to concentration for extremely dilute solutions. The polymer concentration which exhibits maximum drag reduction is of the order of one tenth of the critical (entanglement) concentration c^* [18]. Therefore, the response of polymer molecules to straining flow in the concentration regime between dilute and concentrated solutions should provide a better understanding of the inhibition of drag reduction by too large quantities of polymer in a solvent. Berman [9] was able to correlate drag reduction in turbulent pipe flow for dilute and semi-dilute solutions of flexible polymer with concentration to the one-half power and interpreted this as a result of high effective volume concentration and molecular interactions. We will show that the changes of flow measured in this concentration regime also exhibit a similar inhibition with increasing concentration in the ability of the polymer to produce a decrease in the strain rate.

We will briefly discuss experimental details. Then, results for flow birefringence (in steady and transient flows) and homodyne light scattering (in steady flows) for polystyrene solutions with concentration in the dilute to semi-dilute regime will be presented in the following sections. The onset and degree of flow modification show a correlation with both the polymer extension and polymer concentration. Since the birefringence data can provide a measure of polymer extension, predictions from non-dilute molecular models can be tested with the data. This may explain certain features that are observed experimentally. In particular, in the present study, the birefringence data are compared with predictions from an *interacting FENE dumbbell model* which combines a polymer-polymer interaction (force) term introduced by Hess [19] with the dilute FENE dumbbell model in an attempt to account for non-dilute concentration effects.

2. Experimental Details

Experimental investigations of the dynamics of semi-dilute polystyrene solutions were conducted in both a four-roll mill and a two-roll mill using a flow birefringence technique to provide a measure of macromolecular extension, and homodyne light scattering to study flow modifications (velocity gradient changes) in the polymer solutions. The characteristics of the polymer solutions, the homodyne light scattering technique, the flow devices, and experimental techniques for steady and transient flow birefringence are discussed next.

2.1 Materials

The polymer used is a polystyrene sample (PS2) of $M_w \sim 1.86 \times 10^6$ and polydispersity index $M_w/M_n = 1.06$, manufactured by Pressure Chemical Co. The solvent (TCP6) is a low $M_w \sim 6000$ polystyrene from Polysciences dissolved in tricresylphosphate(TCP). In order to achieve high viscosity and thus keep all experimental runs at a low Re number (< 5) even at the highest strain rates, 10% by weight of the low M_w sample is needed as a thickener. The low M_w sample was first dissolved in TCP with gentle heating and stirring. Dissolution took about a week. Then, the solvent TCP6 was filtered through a $0.22\mu m$ Duropore filter by Millipore. This step is essential for the dynamic light scattering experiments discussed below. High molecular weight PS2 is then added to TCP6 with heating at $\sim 45°C$ and slow stirring. Two concentrations of 1500 and 4500 ppm PS2 were prepared independently in solvent TCP6. These polymer solutions appeared to be optically clear after about a week of heating and stirring.

Another batch of polystyrene (PS2) from Pressure Chemical was also used in a preliminary experiment. This sample had a polydispersity index of 1.30 and a slightly higher M_w of 2×10^6. This fairly monodisperse polymer was dissolved in a high viscosity mixed solvent (CW) which is a mixture of 40% by weight TCP

and 60% Chlorowax 40 (CW40), a chlorinated paraffin product from Diamond Shamrock. Chlorowax is a rather poor solvent for polystyrene but its high viscosity ($\sim$ 50 poise) and compatibility with TCP and polystyrene are desirable for increasing the solution viscosity. The polymer was first dissolved in the better solvent TCP with warming at $\sim 35°$C. Then, CW40 was added to the mixture to increase the solution viscosity. Gentle heating and stirring were necessary to speed up the dissolution process. This solution took more time (about three weeks) to become optically clear because of the slow dispersion of large clumps that existed even in the mixed solvent. The polystyrene concentration used in this mixed solvent is about 1500 ppm.

Table 1. Solvent Properties at $20°C$

Solvent	η_s (poise)	ρ (gm/cc)	n	$C = \frac{\Delta n_s}{\gamma(1+\lambda)\eta_s}$ $\times 10^9 (gm/cc)$
TCP6	11.3	1.160	1.562	0.57
CW	9.29	1.174	1.526	0.18
LV	11.2	1.120	1.520	0.12
TCP	0.87	1.166	1.550	0.36*

* measured at 7.5°C, $\eta_s = 2.75$ poise

The solvents were characterized by independent measurements of density, viscosity, and refractive index. Density of the solvent was measured by a pycnometer. Cannon-Fenske and Ubbelohde viscometers were used to measure viscosity with temperature control at $20° \pm 0.01°$C. An ABBE-56 refractometer was used to measure refractive indices for the solutions at 20°C. Solvent properties for the polymer solutions are presented in Table 1 together with values for the LV solvent for comparison.

The concentrations of the polymer solutions are 1500 and 4500 ppm which corresponds to about 0.33 and 1.0 $\times c^\star$. Here, $c^\star$ is the so-called critical concentration above which molecular entanglements begin to dominate the macroscopic equilibrium (or near equilibrium) behavior of the polymer solution, such as the relaxation spectrum in shear flow. For a closed packed sphere configuration with the macromolecules in their equilibrium coil state, $c^\star$ may be written as

$$c^\star = \frac{M_w \phi^\star}{N_A \frac{4}{3}\pi r_G^3 \rho} \tag{2}$$

where $\phi^\star$ is the volume fraction above which polymer-polymer interaction becomes important in the equilibrium state, and r_G is the equilibrium radius of gyration. The value for r_G can be estimated from quasi-elastic light scattering. Earlier data from this laboratory [20] determined r_G to be $\sim$ 560 Å for the $2\times10^6 M_w$ sample in a different solvent, and thus $c^\star \sim$ 4500 ppm for our case neglecting any differences in the solvent. Since we are interested in concentrations near or below the critical concentration $c^\star$, the two concentrations 1500 and 4500 ppm were used. Results from a 100 ppm PS2 sample in Chlorowax LV(LV) by Dunlap and Leal [8] are also presented here for comparison.

In order to characterize the polymer solutions, zero shear viscosity measurements were performed using Ubbelohde capillary viscometers to give an estimate of the polymer relaxation time. The characteristic relaxation time τ for the polymer can be obtained from the measured viscosity via the relationship [61]

$$\tau = \frac{(\eta - \eta_s) M_w}{c \rho R T} \tag{3}$$

where c is polymer concentration in ppm, R is the gas constant, and T is the temperature. In the limit of $c \rightarrow 0$ for a truly dilute solution, eq.(3) would give the same relaxation time that is relevant for the dilute dumbbell model. This dumbbell relaxation time (τ) differs from the Rouse or Zimm longest relaxation

time ($\tau_1 = c_1\tau$) for a bead-chain model by a constant, $c_1 = 0.608$ and 0.422, respectively [21,22].

Fig. 1 shows the solution viscosity versus polymer concentration for the dilute and semi-dilute solutions of PS2 in TCP6. Initially, a linear relationship is obtained. However, near the critical concentration of 4500 ppm, the viscosity deviates positively from this linear relationship which is indicative of strong intermolecular interaction even in the equilibrium state. This is consistent with the earlier estimate that the 4500 ppm solution is at or near the critical concentration for domain overlap. The dependence of polymer relaxation time on the solution viscosity is also brought out by Chow *et al.* [13] who have shown that relaxation times estimated from coil-stretch experiments in opposing jet flows for semi-dilute solutions increase linearly with concentration. The effect of high concentration is such that a typical polymer molecule only feels the presence of neighboring ones as an apparent increase in viscosity. The estimate of polymer relaxation time from viscosity data via eq.(3) agrees well with the relaxation time calculated as the inverse of the onset eigenvalue of the velocity gradient tensor, $(\gamma\sqrt{\lambda})_{\text{onset}}$, for coil-stretch transition in the birefringence experiments presented later. Table 2 summarizes the polymer solution properties.

Table 2. Solution Properties (PS2) at $20°C$

concentration (ppm)	Solvent	η (poise)	τ (s)
100	LV	229*	0.21
1500	CW	14.8	0.26
1500	TCP6	14.3	0.13
4500	TCP6	23.0	0.17

* intrinsic viscosity $[\eta]$ (cc/gm)

From the viscosity measurements, the increase in zero shear viscosity for the

1500 ppm and 4500 ppm semi-dilute solutions compared to the mixed solvents is $\sim 27\%$ and $\sim 105\%$, respectively. However, there is only a 2-3 % increase for the dilute PS2 solution (100 ppm). Since the relaxation time for the polymer also depends on solution viscosity, shear viscosity measurements were also performed using a parallel plate rheometer which showed no shear thinning effect for all the solvents and polymer solutions in this study up to $\gamma \sim 10\ sec^{-1}$.

2.2 Homodyne Light Scattering

Homodyne light scattering is used to measure the velocity gradient in the flow field, and thus investigate the modifications of the flow field that are caused by the presence of the polymer. Fuller *et al.* [16,23] described the theory and application in the four-roll mill in detail. Dunlap and Leal [8] extended this work to the two-roll mill for dilute PS solutions (100 ppm). Here, we briefly discuss the experimental procedure and some important parameters for determining the absolute value of the velocity gradient.

Fig. 2 shows a schematic of the homodyne light scattering experiment. A monochromatic Argon-ion laser (Spectra-Physics model 165) at 488 nm was incident along a plane normal to the x-y plane of the 2-D flow at some angle $\theta/2$ to the normal z-axis. This defines the incoming wave vector $\mathbf{k}_i$. A photomultiplier tube was placed along the same plane at the same angle but on the opposing side of the z-axis for measuring the scattered light $\mathbf{k}_s$. Therefore, the scattering vector $\mathbf{q} = \mathbf{k}_i - \mathbf{k}_s$ always lies in the x-y (flow) plane, with a scattering angle θ, and an angle ϕ relative to the x-axis. Two $300\mu m$ pinholes separated by about 1 foot were placed in front of the photomultiplier tube to define the characteristic length of the scattering volume. The normal plane was chosen to be along the x-axis ($\phi = 0°$) for the 2-roll mill and along the extensional x'-axis ($\phi = 45°$) for the 4-roll mill. Thus, $\mathbf{q}$ is parallel to the local mean velocity so that $\mathbf{q} = q(1,0)$, where

$q = (4\pi n/\lambda_0)\sin\frac{\theta}{2}$. With this choice of $\mathbf{q}$, the only contribution of the measured velocity gradient is from the extensional component of the velocity gradient tensor $\frac{\partial u}{\partial x}$. The scattering angle θ is fixed at 25.5° (26.0° for the 1500 ppm PS2 in CW solution).

The resulting auto-correlation function for a Gaussian intensity distribution was given by Dunlap and Leal [8] as

$$F_2(\mathbf{q},t) = \frac{1}{2\pi^3}\exp\left[-\frac{1}{2}q^2\gamma^2L^2t^2A\right] \tag{4}$$

where L is a characteristic width of the scattering volume, and A is a function of λ, ϕ, θ, and α, with α being the ratio of a characteristic length of the scattering volume to its width L. For the specific choices of θ, p, and flow types λ in this study, A is equal to one in the two-roll mill flow and is approximately equal to one ($A = 0.95 + 0.26\ \alpha^2$) in the four-roll mill flow. The auto-correlation function is generated using a 64-channel Brookhaven Instruments BI2030 correlator which can correlate photon counts with a smallest sample time of $\sim 0.2\mu s$. The duration of each correlation was generally taken to be 1-3 sec.

We introduced PS Latex spheres of size 0.091 $\pm 0.0058\mu m$ from Dow Chemical as scattering particles. Although a slightly different size of 0.109 $\pm 0.0027\mu m$ Latex spheres were seeded in the 4500 ppm solution, this would only affect the calibration for the absolute value of the velocity gradient but not for relative values. Since the correlation function is very sensitive to noise and dust in the solution, the solvents were carefully filtered through a 0.22 μm Millipore filter. The measurements were made at the center plane of the flow field to avoid end effects. This was done carefully by aligning the incident and scattered light to cross at the half height of the flow device using a 5 mW He-Ne laser and a goniometer to give precision alignment and scattering angle measurements.

The absolute value for γ can be determined by calculating the half height time t_h from the Gaussian shape correlation function. This value for t_h is the time

for the correlation function to decay to half of its maximum value. Thus, eq.(4) gives

$$\gamma = \frac{\sqrt{2 \ln 2}}{q \ L \ t_h \sqrt{A}} \tag{5}$$

Since the auto-correlation F_2 depends on the Gaussian intensity profile of the beam, which would fluctuate from time to time on the order of days, calibration for absolute values for γ was based on the known linear relationship between γ and roller speed when no flow modification is present. It turned out, from the calibration, that the apparent value for L is about the size of the laser beam which is $\sim 160\mu m$ if A is assumed to be equal to one.

Since previous investigators [8] have made extensive measurements on the 2-roll and 4-roll mill using homodyne light scattering, we briefly discuss the apparatus and similar measurements for the solvent TCP6 in the next section.

2.3 Two-Roll and Four-Roll Mills

Flow devices to generate the two-dimensional (2-D) flow field $\mathbf{v} = \mathbf{\Gamma} \cdot \mathbf{r}$ as given in eq.(1) have been described in detail by Fuller and Leal (four-roll mill) [7], and Dunlap and Leal (two-roll mill) [8]. The four rollers in the four-roll mill (1.5 inches in both diameter and height) are enclosed in a square box (8 × 8 × 1.5 inches), and its dimension (and thus the gap width between rollers) is chosen such that the roller surface closely coincides with a hyperbolic streamline, corresponding to the velocity field in eq.(1) with $\lambda = 1$.

Fig. 3 shows schematic streamlines for several different flow types in the four-roll and the two-roll mill ($-1 \leq \lambda \leq 1$). Strong flows are essential for high chain extension, namely flows with $\lambda > 0$ so that the strain rate exceeds the vorticity. We are interested in the whole range of strong flows ($0 < \lambda \leq 1$). However, the four-roll mill cannot provide reliable 2-D linear flow for $0 < \lambda < 0.2$ [16], so

previous workers [8] have produced three sets of rollers for the two-roll mill which give flow types near simple shear with $\lambda = 0.094$, 0.485, and 0.019, respectively. An analyical solution for Newtonian fluids relating shear rate γ with roller speed ω for a co-rotating roller pair has been obtained by Dunlap and Leal [8] in the form

$$\gamma = \frac{A}{\lambda}\omega \tag{6}$$

where A is constant for a given roller size. They have shown good agreement with eq.(6) for a Newtonian fluid over the entire range of roller speeds available in the apparatus using homodyne light scattering and streakline photography [8].

Unfortunately, however, secondary flow occurs at the higher roller speeds that are necessary to achieve significant chain extension when the solvent is less viscous. Flow visualization studies were performed to investigate the stability of both flow devices. Lagnado [24] showed that end effects from the top and bottom glass plates of the four-roll mill started to disturb the 2-dimensionality of the flow at $Re \sim 5$ where $Re = r\omega d/\nu$ with r being the roller radius, ω the roller speed, d the gap width between adjacent rollers, and ν the kinematic viscosity. We have also performed a flow visualization study in the two-roll mill. Hollow glass beads ($\sim$100 μm) were seeded into a Newtonian liquid (glycerol) as scattering particles for streakline photography. Then, a thin sheet of light from a 300 watt projector lightbulb with variable intensity control was used to illuminate the vertical cross-section of the incoming asymptotic streamline which was located at an angle $\phi \sim \tan^{-1}\sqrt{\lambda}$ to the x-axis ($\phi \sim 17°$ for the $\lambda = 0.094$ roller pair). Next, a Polaroid camera with a macrolens was used to take streakline pictures with half- to one-second exposure time which turned out to be adequate to provide good streakline photographs. Similar end effects were observed. The critical Reynolds number for the two-roll mill with largest gap width (λ=0.094) is $Re_c \sim 15$ for onset of end boundary effects. Beyond that Reynolds number (Re_c), vortices developed near the top and bottom plates of the flow device inside the gap region and grew larger

with increasing shear rates. Lagnado *et al.* [25] showed that critical conditions for instability to set in for an *unbounded* linear flow depended on the eigenvalue of the velocity gradient tensor $\gamma\sqrt{\lambda}$. Combining the results above for $\lambda = 0.094$ with the results for with results for 4-roll mill ($\lambda = 1$), it is apparent that the onset of end effects also correlates with $\gamma\sqrt{\lambda}$ for these two flow types. If the roller speed ω used in the definition of Re is replaced by $\omega\sqrt{\lambda}$, we obtain a critical Reynolds number $Re\sqrt{\lambda} \sim 5$ in both the 4-roll and 2-roll mills.

Because of this onset of secondary flows from the top and bottom surfaces, it is necessary to use high viscosity solvents like CW and TCP6 to ensure a stable 2-D flow within the range of shear rate of interest. A series of viscosity measurements of different solvents for PS2 was performed and the mixed solvents actually used were chosen so that the flow would remain laminar and 2-D for γ greater than the critical value γ_c for high chain extension. The criteria for choosing a viscous solvent was based on the following conditions

$$Re \equiv \frac{r\gamma d}{\nu}\left[\frac{\lambda}{A}\right] \leq Re_c \tag{7}$$

$$\gamma\tau_1 = O(1) \tag{8}$$

$$\tau_1 = c_1\frac{(\eta - \eta_s)M_w}{c\rho RT} \tag{9}$$

where c_1 is a constant depending on the model relaxation time.

From the critical Reynolds number determined by visualization experiments, it is apparent that the two-roll mill is more stable than the four-roll mill. One explanation is that the gap-width to height ratio is smaller in the two-roll mill which inhibits disturbance growth or developing vortices near the top and bottom boundaries. Homodyne light scattering performed by previous workers on a Newtonian glycerol/water mixture with $\eta \sim 10$ poise, were used to characterize the flow field and to calibrate velocity gradient measurements for the semi-dilute PS2 solutions. Table 3 shows the characteristics of the flow devices reported by Dunlap and Leal [8].

In this study, experiments were performed only in the 4-roll mill and the 2-roll mill # 2. In order to distinguish polymer effects from the behavior of the solvents, homodyne light scattering was also performed here for the solvent TCP6. Fig. 4 shows the measured velocity gradient (relative value) versus the *Newtonian* velocity gradient $\gamma\sqrt{\lambda}$ at the stagnation point in both the 2-roll and 4-roll mill. The measured velocity gradient varied linearly with $\gamma\sqrt{\lambda}$ up to about $\gamma\sqrt{\lambda} \sim 45sec^{-1}$ ($Re \sim 4.3$) for the 2-roll mill. Then, γ deviates positively from linearity for larger roller speeds. However, linearity is preserved in the 4-roll mill up to $\gamma\sqrt{\lambda} \sim 32sec^{-1}$ where $Re \sim 10$. Therefore, the solvents can be considered to be Newtonian. We will later show that flow modifications induced by the polymer are distinctively different from boundary effects.

Table 3. Characteristic of the Flow Devices

Device		r*	Measured		Theory	
		(cm)	λ	γ/ω	λ	γ/ω
2-Rolls	# 1	2.906	0.09	4.7	0.094	4.66
	# 2	3.170	0.05	9.5	0.049	9.64
	# 3	3.361	0.02	25.0	0.019	26.12
4-Rolls		1.905	.2-1	0.64	—	0.678

* $r + \frac{d}{2} = 3.488$ cm (diagonally in 4-roll mill)

2.4 Steady State Flow Birefringence

Flow birefringence measurements have been applied extensively in shear flow, and reviews by Janeschitz-Krieg [26] and Peterlin and Munk [27] are useful in understanding some of the fundamental concepts. The level of birefringence is a measure of the conformation change of the macromolecular chain which has significant optical segment anisotropy. In particular, Peterlin [28] derived an expression

for the birefringence of a polymer solution in linear 2-D flows as

$$\frac{\Delta n}{nc} = 2\pi \left[\frac{(n^2+2)}{3n}\right]^2 \frac{N_A}{M_w} N(\mu_{\parallel} - \mu_{\perp}) \left[(< x^2 > - < y^2 >)^2 + 4 < xy >\right]^{\frac{1}{2}} \quad (10)$$

$$\cot 2\chi = \frac{< xx > - < yy >}{2 < xy >} \quad (11)$$

where Δn is the birefringence, n is the refractive index of the solution, c is the polymer concentration in gm/cc, N_A is Avogadro's number, M_w is the molecular weight, $\mu_{\parallel} - \mu_{\perp}$ is the difference in the intrinsic polarizability parallel and normal to a subunit of the polymer chain, $< \cdot\cdot >$ are the second moments of a distribution function for the end-to-end vector of a polymer chain, and χ is the (polymer) orientation angle between the principal axis of the refractive index tensor and the x-axis of the flow device. The above expressions neglect any contribution of form birefringence and are thus expected to be a good approximation only when the mean refractive indices of the polymer and solvent are similar in value and/or the solution is concentrated. Since the mean square end-to-end dimension of a polymer chain is $< r^2 >=< x^2 > + < y^2 > + < z^2 >$, birefringence data provides a measure of the degree of polymer extension assuming that no chain-folding exists. Previous workers [7,8] have found good agreement between flow birefringence experiments for dilute PS solutions and predictions using eqs.(10) and (11) in conjunction with the FENE dumbbell model. In the present study, we compare experimental data with a modified FENE dumbbell model that includes an intermolecular interaction term as proposed by Hess [19].

Birefringence experiments involve the measured light intensity which passes through the flow device between a crossed polarizer and analyzer. Fig. 5 shows a schematic of the experiment, and the relative orientation of the analyzer, polarizer, principal axis of polarization tensor of polymer, and the flow coordinates. The relationship between light intensity and birefringence is given by the following

expression [29]

$$I = I_0 \sin^2 2\theta \sin^2 \frac{\pi h \Delta n}{\lambda_0} \tag{12}$$

where I is the light intensity measured by a photodetector that is connected to a laser power meter, I_0 is the intensity of the incident light beam, θ is the angle between the polarizer and the principal optical axis of the polymer solution, h is the thickness of the birefringent zone (which is assumed to be the complete distance across the flow device $\sim$ 3.8 cm), and λ_0 is the wavelength of the light source which is 4880 Å for the Argon-ion laser used in the present study. The analog signal from the power meter is sent to a Metrabyte A/D converter (model DAS-8) in an IBM/AT computer for data averaging and analysis. Birefringence data is usually accurate to within 1% except at extremely high roller speed where local viscous dissipation would decrease the apparent viscosity of the solution, and thus reduce the relaxation time of the polymer. This would result in a horizontal shift of the birefringence curve when the data are plotted versus the dimensionless velocity gradient normalized by the relaxation time of the polymer.

By rotating the flow device to achieve maximum intensity (i.e., determine the orientation where θ is 45°), both the birefringence Δn and the orientation angle χ between the principal axis of refractive index tensor and the x-axis of the flow device can be determined (refer to Fig. 5b). This angle χ is consistent with the classical definition of the extinction angle for birefringence experiments in simple shear flow [30].

In order to calculate the contribution to birefringence from the polymer alone, a correction for the solvent contribution must be made. Philippoff [31] introduced the following relationship assuming that the orientation angle χ_s for the solvent is always 45°

$$\Delta n_p{}^2 = \Delta n^2 + \Delta n_s{}^2 - 2\Delta n_s \Delta n \sin 2\chi \tag{13}$$

$$\cos 2\chi_p = \frac{\Delta n}{\Delta n_p} \cos 2\chi \tag{14}$$

where the subscripts p and s refer to the polymer and solvent, respectively.

In the present case, the birefringence of the mixed solvents was measured, and χ_s was found to be 45° except at low roller speeds where $\chi_s < 45°$. In any case, the solvent contribution to solution birefringence is still negligible at low roller speeds. Therefore, eq.(13) was used to calculate the polymer contribution to the birefringence. Solvent birefringence is presented in Fig. 6 as Δn plotted versus the Newtonian rate of strain $\gamma(1+\lambda)/2$ which is proportional to the stress. The linearity of the data suggests that the stress-optical law is valid for these low molecular weight Newtonian solvents. We can define the stress-optical or Maxwell constant in a more general manner for linear 2-D flows as

$$\Delta n_s = C\eta_s(1+\lambda)\gamma \tag{15}$$

since the principal stress difference $\Delta p \propto \eta_s(1+\lambda)\gamma$ for our flow field [30,31]. The stress-optical constant (C) for the solvents, obtained by calculating the slope of the least-square fitted straight line in Fig. 6, is given in Table 1. Values of C for other solvents from previous workers are presented for comparison. The Maxwell constants obtained here are of the same order of magnitude as values for other organic solvents reported by Tsvetkov [32].

2.5 Transient Birefringence for Inception and Cessation of Flows

For time-dependent birefringence experiments, two measurements need to be performed to calculate $\Delta n(t)$ and $\chi(t)$ since both are unknown and varying with time. Osaki *et al.* [33] has previously done experiments in shear flow using two distinct orientations for the analyzer-polarizer combination relative to the flow axes. The same technique is employed here. First, we performed the experiments with the flow device rotated to an angle where the maximum intensity is obtained at steady state. Then, the polarizer and analyzer are rotated 45° with all other

parameters remaining the same as in the first experiment. The two experiments then correspond to the following time-dependent intensity equations

$$I_\theta(t) = I_0 \sin^2 2\theta(t) \sin^2 \frac{\pi h \Delta n(t)}{\lambda_0} \tag{16a}$$

$$I_{\theta+45^\circ}(t) = I_0 \cos^2 2\theta(t) \sin^2 \frac{\pi h \Delta n(t)}{\lambda_0} \tag{16b}$$

where θ is the relative orientation angle (same definition as in eq.(12)) for maximum steady birefringence in the first run, and $\theta + 45°$ is the relative orientation angle in the second run. The orientation angle χ is equal to the angle of the polarization vector relative to the x-axis minus the angle θ. An Metrabyte A/D converter board in an IBM/AT is used for data acquisition. The data is usually obtained at 200 Hz and averaged for 3-5 runs. Synchronization of data acquisition and the inception (or cessation) of flow is achieved by building a digital circuit into the A/D converter. When magnetic clutches are engaged/disengaged for inception/cessation of the flow, the digital circuit is triggered to send a TTL pulse of width $\sim 7\mu sec$ to the A/D converter to start data acquisition. Therefore, no significant time-lag exists between the start-up of flow and the initial data acquisition. In principle, some error in the measured intensity might arise from the slight difference in mechanical response of the motor-clutch units. Nevertheless, since the response time of the clutches is $\sim 10 - 20$ millisec and the motors are kept at a steady speed at all times, this error would be significant only when the time scale of the flow is comparable to the mechanical response time of the flow device which is estimated to be about 40 millisec.

Time-dependent results for both birefringence $\Delta n(t)$, and the orientation angle $\chi(t)$ (which differs from the relative orientation angle θ by a constant), can now be obtained by simply adding and dividing the two eqs.(16a) and (16b). When the polarizer is set at 0°, the angle of rotation of the device is fixed so that the steady birefringence is at a maximum. Thus, when the polarizer is at 45°,

the birefringence values tend to be much smaller at all times compared to the corresponding values at 0°. Osaki *et al.* [33] has pointed out that experimental error in intensity measurements for $I_{\theta+45°}$ would lead to a significant error in calculating the time-dependent extinction angle.

3. Results

Flow birefringence experiments were done in the four-roll mill (λ = 1.0, 0.5, 0.25) and for one pair of rollers in the two-roll mill (λ = 0.0485) for the semi-dilute polystyrene solutions. This provides a sequence of *strong* flows, with a range of ratio of the magnitude of the strain rate to the vorticity. A flow modification study, via homodyne light scattering, was also performed for λ =1.0 and 0.0485 to provide a correlation with the birefringence data. It should be noted that previous investigators reported no change in the flow for a dilute 100 ppm PS2 in LV, even though the birefringence is very strong. We first present the flow birefringence results, and these are then followed by the homodyne light scattering data. Results obtained earlier for the 100 ppm PS2 solution are also reproduced here for comparison.

3.1 Flow Birefringence

Flow birefringence is a common tool for study of flow-induced conformation changes for macromolecules, and numerous previous studies of polystyrene solutions have been done in both simple shear and extensional flows [6-8,11-16,29]. Pope and Keller [6] reported a linear dependence of the maximum birefringence on concentration in the range of 300-5000 ppm for a $M_w \sim 2 \times 10^6$ polystyrene sample. The critical concentration, i.e., $c^\star$, for their sample was $\sim$ 1.5%. However, their results show scattered data especially in the high shear region which was possibly due to instability of the sucking jet device they used. Another limitation of their experiments was the unknown thickness h of the birefringence zone.

Although polystyrene solutions with similar concentrations in the dilute to semi-dilute regime are studied here, our birefringence data is complemented with flow data in a well-characterized 2-D laminar flow by velocity gradient measurements and flow visualization studies.

Specific birefringence values (i.e., $\Delta n/c$) for different flow types are plotted in Fig. 7 as a function of $\gamma\sqrt{\lambda}$. The velocity gradient γ in this figure is uncorrected for deviations from Newtonian values. Instead, the correlations between roller speed and shear rate for Newtonian fluids were used. Later, we will show the experimentally measured velocity gradient data along with the birefringence results. For dilute polymer solutions, the specific birefringence for different concentrations would collapse to a single curve. However, Δn is no longer linear with c for the two semi-dilute concentrations of 1500 and 4500 ppm, which correspond to $c/c^{\star} \sim 0.33$ and 1.0, respectively. Since birefringence is related to the conformation of the polymer, a decrease of the of specific birefringence from linearity with concentration is an indication of inhibition of flow-induced stretching. This effect can only be ascribed to strong polymer-polymer interactions as the local effective (volumetric) concentration increases dramatically with increased length and concentration of polymer. We will discuss this inhibition effect in more detail in section 4.

The birefringence data in Fig. 7 shows that the onset velocity gradient $\gamma\sqrt{\lambda}$ for the apparent coil-stretch (C-S) transition for the 1500 and 4500 ppm PS2 in solvent TCP6 solutions is dependent on concentration. In particular, onset of stretching occurs at a value of $\gamma\sqrt{\lambda} \sim 5.0$ and 8.0 for the 1500 and 4500 ppm concentration respectively. The change in the onset velocity gradient is indicative of a change in the characteristic relaxation time of the polymer solution. The critical velocity gradient for onset of a C-S transition based upon birefringence experiments has been used for dilute solutions to give a reasonable estimate of the longest relaxation time for the polymer. Many birefringence experiments in pure

extensional flows have shown that onset occurred at $\gamma\tau \sim 1$ [6-8,34-37] . Specifically, Leal and coworkers [7,8] have shown both experimentally and theoretically that the condition

$$\gamma\sqrt{\lambda}\tau \quad \geq \quad 1 \tag{17}$$

must be satisfied for high chain extension in dilute solutions. Further, these investigators [7,8] showed that τ evaluated from birefringence data was in good agreement with the Zimm relaxation time [22] for dilute polymer solutions. In our case, the dependence of the onset shear rate on concentration can be accounted for in terms of the increase in solution viscosity and thus the relaxation time. In particular, relaxation times calculated from the inverse of the onset velocity gradient, $(\gamma\sqrt{\lambda})^{-1}$, agree with values determined from viscometry via eq.(3) (cf., Table 2). Thus, the semi-dilute concentrations used in this study do not appear to affect the correlation between onset shear rate and relaxation time.

This is clearly evident in Fig. 8 where the birefringence data from Fig. 7 is replotted versus the nondimensional eigenvalue of the velocity gradient $\tau\gamma\sqrt{\lambda}$, where τ is the relaxation time determined via viscometry. The 1500 ppm solution of PS2 in CW is also presented in Fig. 8. For both concentrations, the dimensionless onset strain rate $\tau\gamma\sqrt{\lambda}$ is approximately one, which is consistent with results for dilute and semi-dilute solutions by other investigators [8,11,12]. Clearly, the onset point scales with the characteristic relaxation time τ given by eq.(3). The slight differences between the two 1500 ppm solutions are presumably due to the higher molecular weight and polydispersity (high M_w tail) for the 1500 ppm solution in CW. However, all of the data for each concentration correlate well with $\tau\gamma\sqrt{\lambda}$ for various flow types λ down to the smallest value (λ=0.0485) which corresponds to an extension to vorticity ratio (s/ω) of only 1.1. At higher shear rates, the correlation of $\Delta n/c$ versus $\tau\gamma\sqrt{\lambda}$ for the 1500 ppm PS2 in TCP6 starts to break down. It can be seen that this occurs at $\tau\gamma\sqrt{\lambda} \sim 2.4$, which coincides with the point where a decrease in the slope of Δn versus shear rate occurs. This decrease

in slope is very likely a manifestation of a corresponding decrease in the velocity gradient relative to values for a Newtonian fluid, as we shall see in section 3.3. In particular, the decrease in birefringence slope definitely has nothing to do with any approach to saturation birefringence corresponding to full polymer extension.

In order to clarify this point, the PS2 data for the 100 ppm in LV, which does reach saturation at high shear rates [8], is included in Fig. 9 for comparison. All three solutions show an apparent saturation in birefringence, but at different birefringence levels which would not be expected if the polymer chains behave independently and are at full extension. Peterlin [28] showed that the birefringence for non-interacting fully extended polymer chains would give a saturation value of

$$\frac{\Delta n_\infty}{nc} = 2\pi \left[\frac{(n^2+2)}{3n}\right]^2 \frac{N_A}{M_w} N(\mu_\parallel - \mu_\perp) \tag{18}$$

From this prediction and experimental results for the saturation birefringence Δn_∞ for a dilute solution, a best fit value of N can be obtained, and this gives a good measure of the conformation change (extension) that a particular polymer sample is capable of undergoing. The linear chain of polystyrene has a segmental intrinsic optical anisotropy of $(\mu_\parallel - \mu_\perp) = -145 \times 10^{-23} cc$ [26]. Dunlap and Leal [8] thus showed that for the dilute PS2 (100 ppm) in LV, N$\sim$ 1200 assuming near complete extension of the polymer chains at the experimental value of saturation birefringence (see Fig. 14 in Ref. 8). Since the contour length R for a Gaussian chain is given by $R = Na$, where N is the number of statistical segments each of length a making up the chain, and the equilibrium end-to-end distance is $r \sim \sqrt{N}a$, this means that the maximum stretch ratio R/r ($\sim \sqrt{N}$) for complete extension of PS2 is $\sim$ 35.

For the semi-dilute (1500 and 4500ppm) solutions, the specific birefringence shows dramatically lower saturation values. Further, the saturation birefringence is no longer linearly increasing with concentration. Therefore, the values of saturation birefringence for the semi-dilute solutions clearly do not represent complete

extension, apparently due to local polymer-polymer interactions in the moderately deformed state. Indeed, using $N \sim 1200$ or $a \sim 16$ monomer units for one statistical segment, the measured saturation birefringence values for the 1500 and 4500 ppm solutions give an approximate chain extension of only 0.23 and 0.15 of the maximum attainable contour length ($r \propto \sqrt{\Delta n}$). In another words, the increase of concentration actually inhibits the achievable chain extension of the polymer presumably because of increased molecular interactions. This is, perhaps, the most important observation from the present study.

The breakdown in the correlation of birefringence with $\gamma\sqrt{\lambda}$ for the 1500 ppm solution in the 4-roll mill at high strain rates (cf., Fig. 7) may be a result of hydrodynamic or elastic instability. Dunlap and Leal [8] pointed out two phenomena that might cause a lowering of Δn in the 4-roll mill, relative to its value in the 2-roll mill at the same $\gamma\sqrt{\lambda}$. First, is hydrodynamic instability and/or three-dimensionality of the flow induced by vortex generation at the boundaries. The Reynolds number corresponding to the maximum birefringence ($\gamma \sim 30$ *or* $\omega \sim 44$) for the four-roll mill is ~ 7 which is just above the critical Reynolds number where end vortices start to creep into the local birefringent region. As this three-dimensional flow develops near the walls, the strongly birefringent layer becomes thinner (i.e., the vertical section at the stagnation region in which the flow remains two-dimensional becomes smaller) because polymer near the unstable wall region does not align or extend as efficiently as the polymer in the 2-D middle section. The birefringence values Δn calculated from the measured retardation assume that there is a vertical birefringence layer of length h, which we chose to be a constant, 3.81 cm, equal to the height of the rollers. Therefore, any non-birefringent region due to three-dimensionality in the end regions would reduce the measured retardation and thus reduce the apparent (averaged) value of Δn. For the more concentrated solution (4500 ppm), the Reynolds number (Re) is about 2 times smaller at the same strain rate than for the 1500 ppm solution,

assuming that the solution viscosity is used to calculate Re. This might be the reason that better correlation is obtained for the more concentrated case up to $\gamma\sqrt{\lambda} \sim 30$.

Another source of instability may come from viscoelastic effects due to the high Weissenberg number (Wi) associated with the flow. This disturbance is more localized and could not be detected by Dunlap and Leal [8] using only flow visualization. However, Lagnado *et al.* [25] predicted unstable flow of an Oldroyd type fluid in a 2-D linear flow at a critical Wi_c of O(1), where Wi $= \gamma\tau_1$, and τ_1 is a model relaxation time for the polymer. Some experimental evidence of flow instability for a viscoelastic fluid in a two-roll mill by Broadbent *et al.* [39] and in flow through a contraction by Muller *et al.* [40] appear to agree qualitatively with the theoretical prediction. The 2-roll mill data for the 1500 ppm solution also showed some fluctuation in the birefringence when $\gamma\sqrt{\lambda} > 30$. We stopped taking data beyond $\gamma\sqrt{\lambda} \sim 37$ at which birefringence started to fluctuate more. A Hewlett Packard model 3582A spectrum analyzer (0.02 Hz to 25.5 kHz) was used to look at the frequency spectrum of the unstable data, but no conclusive result was obtained except that the intensity sometimes fluctuates at a frequency equal to the inverse of the roller speed at high speeds. The Reynolds number at the maximum strain rate $\gamma\sqrt{\lambda}$ in the 2-roll mill is only $Re \sim 4$, which is considerably smaller than the critical Reynolds number (~ 15) for *inertial* instability of the two-roll mill. Hence, the instability observed may actually be induced by high Wi. In this regard, it is interesting to estimate the value of Wi in our experiments. For this purpose, we use a characteristic relaxation time $\tau_1 \sim 0.422\tau$ where τ is the experimental relaxation time (Table 2). The relaxation time τ_1 is the Zimm estimate of the longest relaxation time for a bead-chain model of a polymer molecule [22]. The Zimm model has a similar constitutive equation to one of the limiting forms of the Oldroyd type fluid (convected Maxwell model) studied by Lagnado *et al.* [25]. Using this estimate for the characteristic relaxation time, we calculate $Wi_c \sim 7.5$ at

the critical value of $\gamma\sqrt{\lambda} \sim 30(\gamma \sim 136)$. This seems qualitatively consistent with the possibility of a high Weissenberg number viscoelastic instability as suggested by the fluctuations of birefringence intensity for these low Reynolds number flows. Similar fluctuations also appear in birefringence for the 4500 ppm solution when $\gamma\sqrt{\lambda} > 30$ due to elastic instability.

Another important result from the flow birefringence experiments for the semi-dilute polymer solutions is that the width of the birefringent region broadens considerably with increasing concentration. Figs. 10(a) and 10(b) show the birefringence profile across the x′-axis (outgoing asymptote) and x-axis for two semi-dilute solutions in the 4-roll and 2-roll mills, respectively. The measurable birefringent region for the 4500 ppm solution is about twice the width of the 1500 ppm case which is also about twice that found earlier for the dilute solution (in which the birefringence zone was less than $0.02''$ in width). The decrease in Δn away from the stagnation point is typical of both the 2-roll and 4-roll mills, in which the polymer chains reside in the region of strong stretching only for a finite period of time. Another way to express the same idea is to note that the total strain experienced by a fluid element in one pass through the strong-flow region depends strongly on the proximity of the streamline to the dividing streamline that passes directly through the stagnation point. Therefore, Δn, which might be thought of being proportional to a characteristic dimension of the polymer, drops off rapidly away from the local stagnation region as is evident from Fig. 10. We have also plotted in Fig. 11 the birefringence across the x-axis in the 2-roll mill for x = 0 and $0.12''$ at $\gamma\sqrt{\lambda} = 14.82\ \text{sec}^{-1}$ which is approximately the critical strain rate for intermolecular interaction to affect the flow. The birefringence width and peak value appears unchanged even after the polymer leaves the stagnation region. The strain rate near this stagnation region is still strong enough to sustain the stretched conformation of the polymer. The measured velocity gradient at $x = 0.12''$ is only about 12% less than the value at the stagnation point as we will

show later in section 3.4.

Next, time-dependent birefringence data for inception and cessation of steady flow will be presented. The transient birefringence data for our semi-dilute solutions shows distinctively different behavior from either dilute or concentrated solution behavior.

3.2 Birefringence upon Inception and Cessation of Flow

First, transient birefringence data for the *solvent* TCP6 in 4-roll and 2-roll mill flows are shown in Fig. 12. No overshoot is observed up to a strain rate $\gamma\sqrt{\lambda}$ of $\sim$ 24 and 30 sec^{-1} for the two flow types λ = 1.0 and 0.049. A time scale characteristic of either the inception and cessation of flow for a Newtonian fluid is just the time for vorticity diffusion from the roller surface to the stagnation point. This characteristic time is $\sim d^2/\nu$. No other intrinsic (fluid) time scale is present for the Newtonian solvent.

For the polymer solutions, very interesting dynamical behavior is observed. Figs. 13(a) and 13(b) show time-dependent birefringence data for flow inception and cessation experiments for the 1500 ppm and 4500 ppm PS2 solutions in a pure extensional flow. Clearly, the birefringence data begins to show *overshoot* at some critical value of $\gamma\sqrt{\lambda}$. Such overshoots have not previously been shown to exist in the concentration regime between dilute and semi-dilute. It is evident in the 4500 ppm case, however, that the overshoot goes through a maximum, until no overshoot was again observed at the higher strain rates. The maximum per cent of overshoot relative to the steady value for the 1500 and 4500 ppm solutions is $\sim$ 34 and 39 % at $\gamma\sqrt{\lambda}$ = 26.0 and 11.8 respectively. Onset of overshoot occurred at a critical $\gamma\sqrt{\lambda}$ of $\sim$ 20 and 9.5, respectively, for the 1500 and 4500 ppm solutions. A lowering in the slope of the steady birefringence versus $\gamma\sqrt{\lambda}$ also occurs at these onset strain rates. This sudden decrease in $\Delta n/\gamma\sqrt{\lambda}$ is an indication of possible

flow modification. In the next section, any possible correlation of the overshoots in birefringence with flow modification will be discussed with the flow data.

Although the birefringence does not exhibit overshoot for dilute solutions in extensional flows, this type of overshoot phenomenon has previously been demonstrated for *concentrated* solutions. Indeed, Fuller and Leal [16] found similar overshoots in concentrated solutions ($\frac{c}{c^*} \gg 1$) of both polyox in water and polystyrene in TCP. They also predicted overshoots in the $\lambda = 1$ flow using a temporary entanglement network model with a conformation-dependent destruction function [17]. The observed overshoot phenomenon for the present semi-dilute solutions could again provide a window into the dynamics of entanglement creation and destruction. Although these solutions are not strongly entangled at equilibrium, one possible point of view is that enough topological entanglements can still exist so that the polymer chains are stretched as a temporary network at the inception of strong flow. This can occur only if the time scale of the deformation process (which is proportional to γ^{-1}) is much shorter than the time scale of the disentanglement process. Thus, the time scales for disentanglement are calculated to be 0.05 and 0.11 seconds for the 1500 and 4500 ppm solutions, respectively. At the start-up of flow, the deformed network gives overshoot in birefringence that is related directly to a high stress level that is supported in the temporary network of polymer chains. As the system reaches steady state, however, the temporary network breaks down and birefringence drops back to its steady state value. This disentanglement explanation of overshoots in extensional flow is essentially the same as the Fuller and Leal explanation for concentrated (highly entangled) solutions. While seemingly plausible, it does seem contradictory to the steady flow data obtained by Keller and coworkers [11-14], who claim to have demonstrated the existence of an *increasing* number of entanglements with *increasing* (high) strain rates for semi-dilute to moderately concentrated polymer solutions at steady state. One obvious difference between our work and the study of Keller *et. al.* [11-14]

is that the strain rates and concentrations used here are much lower but we are unable to understand how or why this should lead to a fundamental difference in the results.

Overshoot also appears in the two-roll mill at high strain rates for the semi-dilute solutions, cf., Figs. 14(a) and 14(b), though no overshoot was observed for the dilute 100 ppm solution even at the highest strain rate. The maximum percent of overshoot observed is $\sim$ 15 and 24 % at $\gamma\sqrt{\lambda} = 27.8$ and 14.8 sec^{-1} for the 1500 and 4500 ppm solutions, respectively. This percent of overshoot in the 2-roll mill ($\lambda = 0.049$) is relatively smaller than in the case of pure extensional flow. The reason for the smaller overshoot in the 2-roll mill case is not clear at this point. Since one distinction between the pure extensional flow ($\lambda = 1$) and the 2-roll mill flow is the existence of vorticity in the latter case, one might believe that the time-dependent orientation of the polymer could be the cause. Therefore, typical data for the orientation angle, $\chi(t)$, is plotted in Figs. 15(a) and 15(b) as a function of time for the 1500 ppm and 4500 ppm PS2 solutions, respectively. At inception of flow, the polymer is oriented near the principal strain axis ($\chi = 45°$), which is the direction of strain of the extensional component of the flow. As the polymer is being elongated, it is also being rotated and aligned with the direction of the steady state orientation at a time which lags slightly behind the time to achieve maximum birefringence (see Fig. 14). For some instances, the elongated polymers experienced large torque at flow inception resulting in undershoots in the orientation angle. This is evident in Fig. 15(a) for the 1500 ppm solution where a small amount of undershoot in χ ($\sim 2°$) exists. However, no undershoot is found for the more concentrated 4500 ppm solution at any of the shear rates studied. In order to investigate the effect of orientation of the extended polymer on the overshoot in birefringence, the *effective* strain rate experienced by the polymer as it reorients to the steady state is studied next.

The steady state orientation at high strain rates is near the direction of the

outflow axis with $\chi = \tan^{-1}\sqrt{\lambda}$. The effective strain rate, S_{eff}, experienced by the polymer for time-dependent flows can be shown to be

$$S_{eff}(t) = \gamma\frac{(1+\lambda)}{2}\sin 2\chi(t) \tag{19}$$

Therefore, even though the polymer would *initially* experience a maximum rate of strain as it elongates in the direction of the principal strain axis, it would then reorient towards the outflow axis with a monotonically decreasing effective strain rate down to $\gamma\sqrt{\lambda}$ in the 2-roll mill flows. Thus, at the *same value of* $\gamma\sqrt{\lambda}$, the initial strain rates experienced by the polymer in a 2-roll mill flow are always greater than those occurring in a pure extensional flow (Note that $\chi = 45°$ and $S_{eff} = \gamma\sqrt{\lambda}$ for the $\lambda = 1$ case at *all* times). This analysis suggests that *larger* overshoots should thus exist in the 2-roll mill flow if network deformation and subsequent flow-induced disentanglement is the primary mechanism for the overshoot to occur. However, our experimental data suggests otherwise. Thus, other effects such as the degree of flow modification must be invoked to explain this discrepancy. In the above results, we have assumed that the polymer has *no* effect on the flow, even at the highest values of $\gamma\sqrt{\lambda}$ where the maximum overshoots were observed. This indeed is true for the 4500 ppm solution, but not so for the less concentrated 1500 ppm solution, as we will see in the next section. Therefore, the time scale to modify the flow at inception may also be a key factor in the observed overshoot behavior. We will see later that significant inhibition of high strain rates induced by the polymer begins at a critical strain rate that coincides with values of $\gamma\sqrt{\lambda}$ for overshoots in birefringence in the less concentrated 1500 ppm solution.

On inception of flow, the rise time to reach maximum birefringence is inversely proportional to the effective strain rate $\gamma\sqrt{\lambda}$ for all cases. However, the characteristic relaxation time for birefringence, calculated from the exponential decay time at cessation of flow, only shows a small increase with increasing strain

rate. The value of this relaxation time at the highest strain rate is typically smaller than the calculated relaxation time from viscometric measurements. Some apparent overshoots were observed at the beginning of flow cessation. This small overshoot is possibly created by mechanical inertia of the clutches and motors when the clutches are disengaged at cessation of flows.

Little or no overshoot shows up at the highest shear rates. This could be attributed to the fact that the mechanical system of motors and clutches responds too slowly compared to the time scale of the overshoot which is proportional to $\frac{1}{\dot{\gamma}}$. Another experimental artifact that needs to be considered is the boundary effect, which intrinsically reduces the birefringence level. Thus, the absolute percent of overshoot at high shear rates may not be exact. Likewise, the steady state birefringence could be higher than the apparent value that is deduced from the measured light intensity by assuming that the birefringence magnitude is uniform across the layer. When the boundary effect creeps in, the true birefringence layer thickness is less than the solution thickness, and a smaller value of birefringence is deduced. It is our belief that this is not the case in the results that we obtained above because flow visualization did not show any significant deviation from 2-D flow over the complete range of experimental strain rates.

3.3 Flow Modification

The homodyne light scattering technique described earlier was employed to measure the velocity gradient in two flow types corresponding to $\lambda = 1.0$ and 0.049 in the 4-roll and 2-roll mills for semi-dilute PS2 solutions. The flow field was well-characterized by previous workers [8,16,23] for a Newtonian liquid (glycerol) using this light scattering technique. The absolute velocity gradient was found to depend linearly on roller speed except at some critical roller speed where instability set in. Dunlap and Leal [8] also showed the same linear relationship as the Newtonian

(glycerol) flow data between γ and ω for a 100 ppm solution of PS8 in LV at low shear rates below the γ_{onset} for polymer induced flow modification. In this study, flow data for the solvent TCP6 is also measured at the stagnation point for various roller speeds. With this solvent data, we can distinguish the polymer effect with no ambiguity.

In the two-roll mill, all realizable experimental roller speeds correspond to a Reynolds number well below the critical one determined from flow visualization experiments. Even though $Re \sim 10(> Re_c)$ at the highest strain rate used in the 4-roll mill, linearity in γ versus roller speed is still preserved for the Newtonian data which is less viscous than the polymer solutions. Therefore, we believe that we have avoided any large effect from vortex growth from the top and bottom boundaries. Any flow modifications are entirely due to molecular interaction and a corresponding viscoelastic effect. The scattering volume is located at the mid-plane between the top and bottom of the flow device so as to avoid *end* effects. This can be done by ensuring symmetry in the velocity gradient profile along the flow axis [8,23]. The polymer solutions still contain some dust particles even though the solvents were carefully filtered before use. Scattering from large dust particles obscured the smoothness of the correlation function. However, better Gaussian correlation curves were obtained by introducing a relatively large number of scattering particles ($\sim 50ppm$) and a longer duration time (1-3 sec) for the correlation, thus averaging out the scattering contribution from dust particles. The photon count was $\sim 4 \times 10^4$ $/sec$ which proved to be sufficient for good correlation with the above duration time. The laser intensity is operated at ~ 0.16 watt for all of the light scattering experiments and temperature is controlled to $\sim 20° \pm 0.04°C$. This stringent temperature control is necessary to ensure that the viscosity of the solution does not change significantly (which would in turn alter the relaxation time of the polymer solutions). In the velocity gradient data presented next, the vertical bar is the standard deviation of several data points

(and is sometimes even smaller than the symbol size). Under the same operating conditions, the light scattering data can be reproduced easily except at high shear where viscous dissipation and thus inertial effect introduces large fluctuations in the data.

Fig. 16 shows the measured velocity gradient at the stagnation point versus the Newtonian velocity gradient for the two semi-dilute polymer solutions for $\lambda = 1$ in the 4-roll mill. The velocity gradient for various roller speeds shows a dramatic decrease from the Newtonian result at a critical value $(\gamma\sqrt{\lambda})_c \sim 16$ and 14 s^{-1} for the 1500 and 4500 ppm solutions, respectively. Beyond this $(\gamma\sqrt{\lambda})_c$, the velocity gradient was reduced for both cases by up to 26-28 % from the Newtonian value. This effect was not observed for the dilute (100 ppm) solution of the same polymer sample. It is our belief that the onset of flow modification can clearly be related to molecular interaction due to chain stretching of the polymer. In particular, the decrease in the *slope* of Δn *vs* $\gamma\sqrt{\lambda}$ in Fig. 7 also occurs at $(\gamma\sqrt{\lambda})_c \sim 13$, which coincides quite closely with the onset of flow modification (induced by the polymers) for the 4500 ppm case. Since the apparent saturation birefringence levels for the 1500 and 4500 ppm solutions correspond only to 0.23 and 0.15 of the maximum contour length, this decrease in the *slope* of Δn *vs* $\gamma\sqrt{\lambda}$ is not due to an approach to maximum extension, rather, it is due to a marked change in the velocity gradient which is smaller than the expected Newtonian value. Even though the critical strain rate for the 1500 ppm solution is somewhat less than the value at which a lowering occurs in the slope of birefringence versus $\gamma\sqrt{\lambda}$, it can be explained by considering the effective concentration necessary to induce a flow effect and is discussed in section 4.1.

The velocity gradient cross-profile at $x' = 0$ in the 4-roll mill for a few strain rates is also shown in Fig. 17. The measured velocity gradient data for all strain rates and locations (y) are normalized by the Newtonian (solvent TCP6) value at the stagnation point at the lowest strain rate. The regions in which the flow is

modified extend beyond $\pm 0.3''$ for both semi-dilute solutions, which means that the flow is affected over a much broader region than was observed in the dilute PS8 ($M_w \sim 8.4 \times 10^6$) solution [8]. This *non-local* flow effect is also reflected in the broadness of the birefringence region in these semi-dilute solutions.

The velocity gradient data in the 2-roll mill for these solutions are also shown in Fig. 18 versus Newtonian $\gamma\sqrt{\lambda}$ at the stagnation point. The maximum per cent of decrease in the velocity gradient is about 20% for both concentrations. The critical velocity gradient $\gamma\sqrt{\lambda}$ for onset of flow modification is about 21 and 13 sec^{-1} for the 1500 and 4500 ppm solutions. By comparing these results with the 4-roll mill velocity gradient data, it can be seen that the values of $(\gamma\sqrt{\lambda})_c$ are about the same for the 4500 ppm solution in the two flow types ($\lambda = 1$ and 0.049), but that a similar correlation does *not* seem to exist for the less concentrated 1500 ppm solution. It is not clear why the critical $\gamma\sqrt{\lambda}$ does not correlate better in the 1500 ppm case, especially in view of the fact that the corresponding birefringence does correlate with $\gamma\sqrt{\lambda}$. We do note, however, that the birefringence region is much more localized for the 1500 ppm solution in the 2-roll mill, than for the 4500 ppm solution, or for the 4-roll mill, which may contribute to a delay to large $\gamma\sqrt{\lambda}$ values in observation of flow modification. Indeed, the cross-profile of the velocity gradient *across* the gap at x = 0 and $0.12''$ is shown in Figs. 19(a) and 19(b) for several strain rates, for the 1500 ppm solution in the 2-roll mill. These data show that the extent of the flow effect is only $\sim \pm 0.1''$ (note that the roller surfaces are at $\pm 0.125''$). Normalization of the measured velocity gradient is also done using the Newtonian (solvent TCP6) value at the center point for x = $0.0''$ and x = $0.12''$ at a low roller speed. A 26% decrease in velocity gradient is obtained away from the stagnation point at x = $0.12''$ and $\gamma\sqrt{\lambda} = 33.35 s^{-1}$. This larger flow effect shows that the polymer actually extends further after leaving the stagnation region even though the Newtonian velocity gradient at $x = 0.12''$ is actually smaller (about 12% lower than the value at the stagnation point, x=0).

With the above flow data, the question of a possible correlation of overshoots in birefringence with the existence of flow modification can now be addressed. In particular, it is our belief that the dynamical behavior of the birefringence in start-up flow observed in the previous section could be related to the inhibition of high strain rates observed here. We have previously suggested that a network-based disentanglement mechanism could account for the existence of overshoots in birefringence even for semi-dilute solutions. However, the disentanglement mechanism depends strongly on the initial amount of entanglements existing in the solution at equilibrium. Since the 1500 ppm solution only corresponds to 0.33 c^*, it is difficult to imagine that the network deformation and disentanglement mechanism is the only factor in this case. Another possibility may be that the overshoot of birefringence in this case is due, essentially, to an overshoot in the velocity gradient, which becomes more strongly inhibited once the polymer has time to become fully oriented and stretched to the degree possible in the particular solution. In fact, our results show that little or no flow modification exists at the critical values of $\gamma\sqrt{\lambda}$ for maximum overshoot in the 4500 ppm solution for either the 2-roll or 4-roll mill flows. Thus, it appears that the idea of network deformation and disentanglement is the only viable explanation for large overshoot in birefringence in this semi-dilute case (the flow field does not change at the values of $\gamma\sqrt{\lambda}$ that are relevant to the overshoot). However, there does appear to be a correlation between the onset values of $\gamma\sqrt{\lambda}$ for flow modification and the values of $\gamma\sqrt{\lambda}$ for overshoot of birefringence in the 1500 ppm solution. The maximum overshoot for the 1500 ppm solution in the 2-roll and 4-roll mill occurs at $\gamma\sqrt{\lambda} \sim 26$ and 28 $\sec^{-1}$, where we observe a 27% and 20% decrease in the velocity gradient, respectively, for steady flow. The primary conclusion from this is that it is critical to know the time-history of the velocity gradient at inception of flow if we are to clarify the mechanism for overshoot in birefringence. Our comparison for the transient birefringence with the flow data suggests that the time-history of the strain rate

experienced by the polymer may govern the dynamics of the polymer in the flow and subsequent flow modifications. Time-dependent measurements of the velocity gradient by the same technique of homodyne light scattering is currently being pursued in our laboratory.

4. Discussion

4.1 Concentration Effects on Flow Modification

In order to investigate the effect of concentration changes on the amount of flow modification, the measured velocity gradient is replotted in Fig. 20 versus the nondimensional velocity gradient $\tau\gamma\sqrt{\lambda}$. The amount of strain rate inhibition is generally larger in the *less* concentrated 1500 ppm solution for both flow types at the same value of $\tau\gamma\sqrt{\lambda}$. This is *unexpected* because one would expect that the flow modification effect should increase with increasing concentration. However, we notice from the birefringence results that increasing concentration also inhibits the high degree of chain extension that is necessary to produce the large stresses in the flow, that are essential to cause a decrease in the velocity gradient.

We can estimate the amount of polymer extension from the birefringence data by calculating the expected saturation birefringence Δn_∞ for each concentration based on dilute solution results from Dunlap and Leal [7]. They determined N=1200 for PS2. Using this value for N and adjusting the differences in refractive index and molecular weight for our PS2 solutions, we determined by using eq.(18) that $\Delta n_\infty \sim 6.8 \times 10^{-5}$ and 2.0×10^{-4} for full polymer extension in the 1500 and 4500 ppm PS2 solutions, respectively. Then, an effective volume concentration of spheres (ϕ_{eff}) with radius r_{eq} equal to half of the extended length for the polymer can be calculated as [8]

$$\phi_{eff} = \frac{4}{3}\pi {r_{eq}}^3 \frac{N_A}{M_w} c \qquad (20)$$

where $r_{eq} = \frac{1}{2}L\sqrt{\Delta n/\Delta n_\infty}$ is the equivalent radius of the extended chain, and L is the contour length ($\sim 4.5 \times 10^{-4} cm$). Fig. 21 shows the calculated effective concentration versus $\tau\gamma\sqrt{\lambda}$ in the 4-roll mill ($\lambda = 1.0$). The effective concentration of the 4500 ppm, ϕ_{45}, is higher than that of the less concentrated 1500 ppm, ϕ_{15}, up to $\tau\gamma\sqrt{\lambda} \sim 1.9$. However, beyond that point, ϕ_{15} is much larger than ϕ_{45} (up to 27%). The critical effective volume concentration ϕ_c for onset of flow modification can be determined by comparing the critical velocity gradient $(\tau\gamma\sqrt{\lambda})_c$ from Fig. 20(a) with the corresponding effective volume concentration from Fig. 21. We find $\phi_c \sim 170$ and 180 for the 1500 and 4500 ppm semi-dilute solutions, respectively. Thus, an effective critical effective volume concentration of $\sim 170 - 180$ correlates well with onset of flow modification for polymer solutions of different concentrations. This shows that the onset of flow modification depends strongly on both polymer concentration (amount of polymer) and configuration (effective chain length) of the polymer. The idea of a minimum effective volume concentration for an effect of polymer on flow gives good correlation with the actual occurrence of a flow effect in these experiments. However, the value of ϕ_c estimated from the semi-dilute solution experiments is O(10) times *less* than that of the dilute PS8 solution previously determined by Dunlap and Leal [8]. It is likely that this is due to experimental uncertainty in pinpointing the onset point for dilute solutions where the flow effect is *extremely* localized, but we will discuss this point in the next section.

Another noteworthy observation is that the magnitude of the effect of polymer on flow also correlates with the effective concentration. Using results from Fig. 20(a) and Fig. 21, an 11% reduction in velocity gradient for the 4500 ppm solution is achieved when $\phi = 220$ (at $\tau\gamma\sqrt{\lambda} = 3.3$). By comparison, a 9% velocity gradient reduction also occurs at the same effective concentration $\phi = 220$ (at $\tau\gamma\sqrt{\lambda} = 2.2$) in the 1500 ppm solution. This correlation of effective concentration with onset and magnitude of the flow modification for polymer solutions

of different concentrations has not been demonstrated previously. The presumption that an increase of concentration will automatically lead to a stronger flow effect needs to be considered carefully in different concentration regimes. Since ϕ depends both on concentration and polymer configuration (characteristic chain length), an increase of concentration alone cannot guarantee *a priori* that the flow modification will increase except for truly dilute solutions.

The large effective volume concentration required to induce a change in the flow is indicative of the necessity for strong hydrodynamic and possibly molecular interaction induced by the presence of stretched polymer chains, which are aligned locally near the stagnation region. We can also estimate the extra stress that is associated with the aligned polymer chains. By assuming that the stretched and aligned polymer acts as an elongated particle, we can use an equation due to Batchelor [42] to calculate the ratio of the normal stress contribution due to the elongated chains σ_p relative to that of the suspending fluid σ_s

$$\frac{\sigma_{\mathrm{p}}}{\sigma_{\mathrm{s}}} = \frac{\frac{4\pi}{9}\frac{\mathrm{N_A c}\rho}{\mathrm{M_w}}l^3}{\log\frac{2l}{\mathrm{r}}\log\frac{\mathrm{h}+2l}{\mathrm{h}} - \frac{3}{2}} \tag{21}$$

where $2l$ is the effective polymer chain length, $\mathrm{h} = \sqrt{\mathrm{M_w}/2l\mathrm{N_A c}\rho}$ is the lateral spacing between polymers, and r is the width of the polymer. It should be noted that $\sigma_p/\gamma\sqrt{\lambda}$ is the *Trouton viscosity* which is $3\eta_s$ for the Newtonian solvent in 3-D extensional flows. Fig. 22 shows the nondimensional polymer chain length $2r_{eq}/L$ calculated from birefringence results. The calculated stress ratio for the case of 1500 ppm PS2 in TCP6 at the onset of a flow effect is based upon the fact that the polymer is extended to about 20% of its maximum contour length when the onset of a decrease in $\gamma\sqrt{\lambda}$ is observed. If we assume that the polymer occupies about the same *volume* in the stretched and equilibrium states, the width of the polymer can be calculated to be r $\sim$ 157Å. We thus calculate the polymer axis ratio as $l/r \sim 31$ and the stress ratio to be 85 using eq.(21). (This estimate for the width

of the polymer, r, is later compared with model prediction from section 4.3 that gives $l/r \sim 28$ when $2l \sim 0.2L$, and thus justifies the assumption.) The calculated value of the stress ratio is also an order of magnitude smaller than reported earlier for the dilute PS8 case [8] at the point where both cases showed an order one flow effect. This seems to indicate two distinct interaction mechanisms for dilute and non-dilute polymer solutions.

One more comparison can be made regarding the issue of drag reduction. Zakin and Hunston [43] were able to demonstrate an effect of concentration changes for polystyrene 2M ($M_w \sim 2.4 \times 10^6$) in both poor and good solvent on the amount of drag reduction in turbulent pipe flow. Comparing the intrinsic viscosity of the polymer solutions, our solvent lies right in between the *good* and *poor* catagory. Adjusting for the slight difference in molecular weight and using the above effective volume concentration concept, our 1500 ppm PS2 in TCP6 is approximately equivalent to 1000 ppm of the 2M in a poor solvent (the 100 ppm PS2 in LV corresponds to $\sim 70ppm$ of 2M). The percent drag reduction is thus $\sim 25\%$ corresponding to our semi-dilute solution whereas the corresponding dilute solution only gives $\sim 6\%$ drag reduction from Fig. 2 in Ref. 43. This drag reduction result agrees in general with the flow modification data we obtained. The criteria of high chain extension and intense molecular interaction necessary for flow modification in the 2-D linear flow may be one reason for inhibition of turbulent momentum transfer by large eddies near the buffer region causing a reduction in drag at the wall in turbulent pipe flow. The less than linear increase of drag reduction with concentration could be a result of inhibition of polymer stretching, and thus of the magnitude of flow modification, as revealed by our birefringence and flow data.

The dynamics of polymer in the semi-dilute solutions is further discussed next using the idea of delocalization in birefringence as an attempt to explain the anomalous flow modifications discovered in our study.

4.2 Local and Non-Local Effects

As mentioned before, our use of the phrase *non-local* effect refers to the fact that the breadth of the birefringence region is many times that for the dilute case. Dunlap and Leal [8] found a minimum value of $\phi_c \sim 4000 - 6000$ for any flow modification to occur in dilute PS8 ($M_w \sim 8.42 \times 10^6$) solutions. However, the value of critical effective volume concentration for semi-dilute polymer solutions is an order of magnitude less than that of the dilute PS8 solutions. The fact that their 100 ppm PS2 solution exhibited no flow modification was attributed to the fact that the maximum value of ϕ_{eff} was only 2000 even in the fully stretched state. However, a significant flow effect occurs even when $\phi_{eff} \sim 200$ in semi-dilute solutions. Clearly, some additional factors must be important other than the *local* value of ϕ (*local* effect in here refers to the birefringence width of size similar to the size of the probing laser beam in the dilute solution). In the dilute case, since a high effective volume concentration exists only in a very small region around the extensional outflow axis, the increase in elongational viscosity only directly affects the flow very locally. Therefore, a measurable (averaged) effect only appears at a much higher ϕ_c in the dilute case. In the semi-dilute case, interaction of the polymer with the flow field occurs over a broader region. Rallison and Hinch [44] have done a local analysis of velocity gradient changes for dilute polymer solutions along the outflow stagnation streamline of a 4-roll mill using a nonlinear FENE dumbbell model. By assuming a thin region of high viscosity due to the polymer along the stagnation streamline, they found good agreement with the flow data of Dunlap and Leal [8] in the 4-roll mill. However, it appears that their method is not strictly applicable for semi-dilute solutions in which the birefringence zone is much larger than assumed in their analysis.

Next, we examine the extent of flow modification around the stagnation region. Comparing the flow effect with different concentrations at about the same

value of $\tau\gamma\sqrt{\lambda} \sim 3.3$ from Fig. 23, the decrease in velocity gradient is about 2 times larger for the less concentrated 1500 ppm than for the 4500 ppm at the stagnation point y = 0. However, the 4500 ppm solution shows a larger effect away from the stagnation point. This correlates with the fact that the birefringence region is much broader – about 2 times wider than in the 1500 ppm solution (see Fig. 10). Therefore, a larger non-local flow effect (strain rate inhibition) would be experienced because of the cumulative effect of high ϕ (indicative of high stresses) existing over a broader region in the more concentrated solution. This explanation is also discussed in Ref. 44. The existence of non-local flow modification is also shown by Müller *et al.* [14]. These investigators have shown that the pressure drop increase for $4 \times 10^6 M_w$ polystyrene solutions for pure extensional flow in an opposed-jet increases with concentration up to 1%. They further showed that delocalization of birefringence occurred at high strain rates which induced a large flow effect. The measured flow change by pressure drop across the opposed-jet is a macroscopic property averaged over the entire flow region. Therefore, the non-local birefringence would tend to affect the flow more in a global sense for higher concentration solutions in their study. Our velocity gradient measurement is pointwise (beam size is $\sim 160\mu m$) so that it is more sensitive to local effect, and enables us to detect the importance of inhibition of polymer extension due to increased concentration on reduction of local flow effect. The dynamics of the polymer for non-dilute polymer solutions as in our case will be discussed via model predictions in the following section.

4.3 Non-Dilute Dumbbell Models

The experimental birefringence data obtained above can be compared to certain theoretical models for better understanding of the rheological behavior of polymer molecules in semi-dilute solutions under strong flows. We are hopeful that this can provide evidence for distinguishing certain features necessary for the

molecular theory to mimic closely the response of the actual polymer to flows. The appropriate models should take into account intermolecular interactions between neighboring polymers. This interaction would exhibit a similar excluded volume effect (as in truly dilute solutions for segment-segment interactions in the same polymer chain) between polymers for non-dilute solutions. Network models [17,45] for concentrated polymer solutions are not applicable here because these models assume a highly entangled system of polymer chains, and no explicit dependence of rheological properties on concentration except, via its effect on junction density, is found. Reptation models as proposed by Doi and Edwards [46], are designed only for highly concentrated systems, and have clear limitations for application to semi-dilute flexible polymer solutions in elongational flow. For example, the elongational viscosity decreases monotonically when the strain rate is larger than a critical value, and this prediction contradicts many recent experimental observations for semi-dilute systems which show an initial monotonic increase in *effective* elongational viscosity with strain rate [13,14,47,48]. Thus, we do not consider these concentrated solution models for detailed comparison with our current experimental data.

Bird and DeAguiar [49,50] have proposed an *encapsulated* dumbbell (ED) model in which the effect of polymer-polymer interactions is to inhibit the mobility of polymer in the direction perpendicular to its backbone. This effect is introduced into the usual elastic dumbbell model as an anisotropic contribution in both the hydrodynamic friction and Brownian motion encountered by a test polymer molecule. This idea of anisotropy in bead friction was first introduced by Giesekus [51] to mimic the drag experienced by a deformed polymer coil, which should be at least qualitatively analogous to the anisotropic frictional force experienced in low Reynolds number flow by a nonspherical body such as an ellipsoid. Giesekus later used this concept to obtain a constitutive equation for concentrated polymer solutions and melts [52]. The ED model, as proposed by Bird and DeAguiar, con-

tains two parameters, namely σ and β, which govern the degree of anisotropy in the tensorial drag and Brownian motion, respectively. These parameters should presumably be a function of concentration and other molecular properties of the polymer system (though this is not mentioned in Refs. 49 and 50). From the steady state birefringence data obtained in the 2-roll and 4-roll mill flows, it is apparent that the polymer-polymer interactions for a semi-dilute solution have resulted in significant inhibition of the *stretching* of the polymer (Fig. 22).

DeAguiar [50] has obtained predictions for the mean square end-to-end length ($\langle\tilde{\mathbf{r}}\tilde{\mathbf{r}}\rangle$) of a polymer in uniaxial extensional flow with various values of the model parameters σ, β, and b. The parameter, b, in the ED model is a nondimensional quantity that is equal to $3N$ in the notation used here (note that we have determined previously that $N = 1200$ for the high M_w polystyrene used in the present study and this would suggest a value of 3600 for b). The general predicted trend is that the mean dimension of the polymer will increase with strain rate *more* rapidly with increasing values of σ. However, the range considered for b is only up to $b = 200$, while the range for σ is only down to 1/3 (note that σ must be less than one for concentrated solutions[50]). This limited range of parameters in their study does not allow a direct comparison with our current data. Therefore, the ED model prediction is again calculated numerically in the present study using the experimentally determined value for the parameter b (i.e., N in our case). We integrated numerically the second moment equations for the ED model, including the effect of finite transit times in the calculation to account for the fact that the polymer only resides near the stagnation region for a finite amount of time in the real extensional flow generated by 2-roll and 4-roll mills. This transient nature of the extensional flow (as seen by the polymer) has been pointed out by previous workers to be critical for model comparisons 7,8].

Following the approach of Ref. 7 with $l/D = 0.003$, and using the value of $N = 1200$ determined earlier from Ref. 8, the predicted root-mean-square end-to-

end length of the polymer is plotted versus nondimensional strain rate $\tau\gamma\sqrt{\lambda}$ in Fig. 24, with $\beta = 1$ and various values of σ for the 2-D extensional flow ($\lambda = 1$) in the 4-roll mill. We have neglected anisotropy in Brownian diffusion by taking $\beta = 1$ but this does not change the general behavior of the prediction except near the equilibrium state. This assumption of isotropy in Brownian motion is justified by the *fluctuation-dissipation* theorem suggested by Phan-Thien *et al.* [53], who have pointed out the *inconsistency* of having an independent degree of anisotropy in the frictional drag and Brownian diffusion force. From the results in Fig. 24, it is apparent that the polymer is predicted to extend to maximum contour length quite rapidly with increasing strain rate regardless of how small σ is. Indeed, the cases of $\sigma = 0.01$ and $\sigma = 0.001$ collapse to a single curve which is also the limiting solution for $\sigma \equiv 0$. The physical significance of $\sigma \rightarrow 0$ is that the polymer is restricted to *reptate* along its backbone for concentrated solutions. The dilute FENE dumbbell model is recovered for the case of $\sigma = \beta = 1$. Negative values of σ are not allowed in this ED model because physically unrealistic results ensue. The lack of a significant inhibition of polymer extension is not surprising because the ED model incorporates the effects of direct interaction between polymers only as an effective increased frictional resistance in directions perpendicular to the polymer backbone. The polymer can *reptate* and/or extend freely along the backbone in the *encapsulated* dumbbell model. Therefore, at high strain rates, the strong extensional component acting along the end-to-end length of the polymer simply dominates all other effects and the model predicts that the polymer extends in the *open-ended tube* to its maximum possible length. The prediction of the ED model is apparently in contrast to our limited birefringence data which shows strong inhibition of stretching with increasing concentration in the semi-dilute regime even at moderate strain rates. Although the ED model has shown some success with steady and transient (start-up) simple shear flows for semi-dilute polymer solutions [50], the model predictions in strong flow have not previously

been tested in detail (note that simple shear flow is a *weak* flow [2,3,15]). It is apparent that the ED model does not capture the inhibition of extension in *strong* flows that is characteristic of semi-dilute solutions.

An alternative dumbbell model which attempts to incorporate polymer-polymer interactions in an *ad hoc* way was proposed recently by Hess [19]. This is the so-called interacting dumbbell (IDB) model. In order to include polymer-polymer interactions for non-dilute polymer solutions, Hess [19] has introduced the concept of a *pairwise* (non-hydrodynamic) interaction among beads of different dumbbells. This led to a predicted $\sqrt{c}$ dependence in the slope of birefringence versus shear rate for polymer solutions in simple shear flow, which was shown to agree with birefringence results by Tsvetkov & Frisman [54] for semi-dilute poly-isobutylene solutions. The IDB model also predicted that the specific birefringence (plotted against the nondimensional velocity gradient) is inversely proportional to concentration in 2-D extensional flows, when the concentration dependence on the relaxation time is accounted for in the nondimensional velocity gradient (normalized by the relaxation time) [55]. This indicates that the absolute birefringence value should collapse to a single curve for different concentrations in the semi-dilute concentration regime, when plotted versus $\tau\gamma\sqrt{\lambda}$. Thus, the absolute birefringence for the semi-dilute polymer solutions is replotted versus *measured* values of $\tau\gamma\sqrt{\lambda}$ in Fig. 25. The measured eigenvalues of the velocity gradient tensor were obtained from the independent homodyne light scattering experiments, and thus represent the actual strain rate experienced by the polymer. The result shows a good correlation for the slope of birefringence versus $\tau\gamma\sqrt{\lambda}$ at the onset point, except for a slight shift in the abscissa. This shift could be the result of the difference between relaxation time by viscometry estimation and the dumbbell model relaxation time, τ_{db}. In view of the lack of a more general theory for semi-dilute solutions with $c \leq c^{\star}$, we proceed to compare our birefringence data with the FENE interacting dumbbell (FENE-IDB) model in more detail (i.e., quantitatively). The FENE

(finitely extensible nonlinear elastic) dumbbell uses a constant friction coefficient and *Warner* spring to describe the dynamical response of polymer in flows. Bird *et al.* [56] have shown that the FENE dumbbell is quite adequate in describing the behavior of dilute polymer solutions in shear flows and extensional flows.

The FENE-IDB model is a modified version of Hess's original IDB model which used a *Hookean* spring to describe the conformational diffusion of a deformed polymer chain back to equilibrium configuration. The Warner spring is essential for limiting the polymer extension to its maximum contour length especially in strong flows. Ref. 55 explains the development of the model in some detail, and presents predictions of rheological properties using this modified IDB model. In the present communication, we briefly discuss the main features of the model and then compare predictions with the steady birefringence data. The FENE-IDB model differs from the dilute FENE dumbbell model by an additional interaction force term. This interaction force is intended to take account of intermolecular forces among polymer chains which could include close contact forces and even topological entanglements when polymer concentration approaches the overlapping concentration, $c^{\star}$, at equilibrium. By using a mean field approximation, the interaction becomes an effective one-particle potential which acts upon a test dumbbell. There are two parameters, namely k_s and k_l, which describe the anisotropic interaction potential of the test dumbbell when it is oriented parallel and perpendicular to the main axis of the mean field created by neighboring polymers, respectively. For simplicity, we take $k_s = k_l$. No change in the results would occur, however, even for $k_l/k_s \sim \mathrm{O}(10)$ [55]. The dominant terms are governed by the parameter k_s.

In order to compare the experimental data with model predictions, we need to make a physically reasonable choice for the relaxation time of the polymer solution, τ_1, given by eq.(9). The (longest) Rouse or Zimm relaxation time will be used to determine τ_1 for the 1500 and 4500 ppm solutions from the viscometric

measurement of τ in Table 2 via eq.(3). The Rouse model [21] differs from the Zimm model [22] by neglecting hydrodynamic interaction between segments of the same polymer chain. The relaxation time predicted by these bead-spring (Rouse or Zimm) models should give a physically better estimate than the simple dumbbell model prediction from eq.(3) for polymer solutions. The Rouse or Zimm formula for the longest relaxation time is given by [21,22]

$$\tau_1 = \begin{cases} 0.608\tau, & \text{Rouse formula;} \\ 0.422\tau, & \text{Zimm formula.} \end{cases} \tag{22}$$

Peterlin [57] had also shown that the polymer expansion predicted by the dumbbell model is markedly larger than in the case of the Rouse or Zimm model by the same factor due to the difference in their relaxation times. Since the FENE-IDB model always predicts the onset velocity gradient to be at $\tau_{db}\gamma\sqrt{\lambda} = 1/2$ (τ_{db} is the IDB model relaxation time), and the measured onset point nondimensionalized by the relaxation times from viscometric data appears to be somewhat smaller than 1 (see Fig. 8), we conclude that the Rouse relaxation time is a better estimate for the semi-dilute solution data than the Zimm relaxation time. This is consistent with the idea of a hydrodynamic screening effect due to high concentration as suggested by other investigators [58,59]. In particular, the polymer in these solutions behaves like a *free-draining* chain due to hydrodynamic screening by neighboring polymers.

The only parameter left to be determined in the FENE-IDB model is the interaction parameter, k_s, which depends approximately linearly on the concentration (c) [19]. The simplest way to determine k_s is to compare the asymptotic value of the mean end-to-end length, $\langle r^2 \rangle^{\frac{1}{2}}$, at the largest value of $\tau_1\gamma\sqrt{\lambda}$ obtained in the experiment for the 1500 ppm solution, with the corresponding model prediction for various values of k_s. Then, the value of k_s for the 4500 ppm solution is assumed to be just three times the k_s value for the 1500 ppm solution. In this way, the interaction parameter is determined to be $k_s = 10$ and 30 for the 1500 and 4500 ppm solutions, respectively. The interaction parameter for the 100 ppm

is $k_s = 0$ which is equivalent to the dilute FENE dumbbell prediction, and the polymer relaxation time is taken from Ref. 8 to be $\tau_1 = 0.04$ sec. The model predictions are done by integrating the second moment equations as before with finite transit time included. Fig. 26 shows the predicted values for the square root of the specific birefringence ($\sim \langle r^2 \rangle^{\frac{1}{2}}$) for $\lambda = 1$ and 0.049, compared with the experimental data for the three dilute and semi-dilute solutions (100 ppm PS2 in LV, 1500 and 4500 ppm PS2 in TCP6). The experimental data is plotted using the *measured* velocity gradient for the case of $\lambda = 0.049$. This is representative of the data for all other flow types studied because the birefringence has been shown to correlate well with $\gamma\sqrt{\lambda}$.

The model predictions show excellent agreement with data for the semi-dilute solutions. The reason for the rather poor agreement in the dilute 100 ppm solution is likely due to the relatively high polydispersity sample used with $M_w/M_n = 1.30$, whereas the semi-dilute samples have a narrow molecular weight distribution of $M_w/M_n = 1.06$. Fuller and Leal [7] have pointed out the need to include polydispersity in the model *prediction* even for fairly narrow molecular weight distribution polymer samples. The birefringence data for the 100 ppm, which is reproduced from Dunlap and Leal [8], had been shown to agree well with the dilute FENE dumbbell model predictions when polydispersity is included in the model by means of data averaging with a log-normal distribution [8]. In the present analysis, no such averaging is performed. Instead the single value of $N = 1200$ is used for model comparisons with experimental results. This still gives good quantitative predictions as shown in Fig. 26 for our semi-dilute samples. The correlation of birefringence predictions with different flow types agrees with the *quasi-steady* data. Although only two semi-dilute solutions are compared, the overall agreement of model predictions with data leads us to believe that the FENE-IDB model provide a useful basis for modeling the dynamics of polymer solutions with concentration in the dilute to semi-dilute regime in strong flows.

Hess [19] had also shown good qualitative agreement with earlier experimental observations, such as steady birefringence, shear viscosity, and first normal stress coefficient, for simple shear flow.

From the above results, the concentration dependence of specific birefringence (plotted versus $\tau\gamma\sqrt{\lambda}$) is predicted to be c^{-1} for semi-dilute polymer solutions in 2-D extensional flows. This is quite surprising because it means that the absolute birefringence remains the same even if more polymer is introduced into the solution. However, the characteristic relaxation time for semi-dilute polymer solutions can be a strong function of polymer concentration. An approximate equation for τ as a function of concentration c can be derived using the Huggins' equation [60] and the dumbbell model prediction for the zero shear viscosity of the polymer solution η to be

$$\tau \;=\; \tau_0\,(1 \;+\; k_1[\eta]c) \tag{23}$$

where τ_0 is the characteristic relaxation time of the polymer in truly dilute solutions, k_1 is the *Huggins' coefficient*, and $[\eta]$ is the intrinsic viscosity. Since both k_1 and $[\eta]$ are independent of concentration, the relaxation time shows a simple relationship with c. Therefore, the actual concentration dependence of absolute birefringence from the FENE-IDB model prediction is $\Delta n \;\propto\; (1 + mc)$ with $m = k_1[\eta]$ being a constant. Therefore, experimental data should be compared with the knowledge of the characteristic relaxation time for high concentration solutions so that explicit concentration dependence of rheological properties can be determined (for example, the velocity gradient should be nondimensionalized by τ when comparing birefringence data for polymer solutions of different concentrations).

In spite of the good quantitative agreement between the FENE-IDB model predictions and the *steady state* birefringence data, transient predictions from the model do not give any overshoots in birefringence and this is in marked contrast

to the flow data presented earlier. The model only predicts a steady rise of birefringence to the final steady value with a characteristic time scale that is inversely proportional to $\gamma\sqrt{\lambda}$, for inception of extensional flow for any positive λ. The reason for failure of the FENE-IDB model for start-up of extensional flow is likely due to the fact that the IDB model neglects higher order interaction between polymers that contributes most to the overshoots in birefringence by entanglement formation and destruction mechanism. The value of the interaction parameter will no longer be a linear function of concentration. More importantly, the interaction force term will have complicated nonlinear terms which depend on higher order moments of the configuration tensor. This discrepancy is especially significant for high concentration solutions which would have many polymer-polymer interpenetrations at equilibrium to give rise to large overshoots in stress (or birefringence). This may be the case for the 4500 ppm solution as discussed in section 3.3 before. The overshoots in birefingence can then be explained qualitatively by the dynamics of network formation and destruction mechanism as proposed by the temporary network model [17].

A modified version of the FENE-IDB model was also tried including conformation dependent friction as is generally used for dilute solution models [7,8]. No overshoot in birefringence is found even for this FENE-IDB model with variable friction coefficient. This feature of variable friction (VF) can be incorporated into the FENE-IDB model by replacing γ with $\gamma\sqrt{N}r$ and multiplying the time-derivative terms by $\sqrt{N}r$ in eq.(11) of Ref. 53 for the IDB model, with $r = \langle r^2 \rangle^{\frac{1}{2}}$. The steady state prediction shows that the asymptotic value of specific birefringence, $\Delta n/\Delta n_\infty$, at intermediate velocity gradients is given by

$$\frac{\Delta n}{\Delta n_\infty} \sim \frac{N}{2{k_s}^2}(\gamma\sqrt{\lambda})^2 \tag{24}$$

This prediction shows that the birefringence depends on the square of the velocity gradient, $(\gamma\sqrt{\lambda})^2$, which disagrees with many experimental observations of a linear

dependence in strain rate with birefringence for semi-dilute polymer solutions in extensional flows at intermediate strain rates [16,37]. The present experimental results also show the same linear dependence in $\gamma\sqrt{\lambda}$ with birefringence. Since both Δn_∞ and k_s depend linearly with c, eq.(24) shows that the absolute birefringence decreases with increasing concentration ($\Delta n \propto c^{-1}$) which contradicts our experimental results shown in Fig. 25. All these results indicate that the VF feature could not properly mimic the hydrodynamic response of the polymer in semi-dilute solutions where hydrodynamic screening could be important.

5. Conclusion

The results we presented for flow birefringence and velocity gradient measurements of semi-dilute PS2 solutions show a distinctive effect of polymer concentration in this concentration regime. The flow birefringence data indicates that the onset strain rate is $(\tau\gamma\sqrt{\lambda})_{onset} \sim 1$ for the three concentrations studied including the dilute solution. Thus, the onset of stretching depends on concentration only through the characteristic relaxation time which is some linear function of concentration, $(1 + mc)$, for semi-dilute solutions. Flow birefringence for the three polystyrene solutions in this study correlates well with the eigenvalue of the velocity gradient tensor $\gamma\sqrt{\lambda}$ for various extensional flow types of $\lambda > 0$. The increase of steady birefringence with $\gamma\sqrt{\lambda}$ is shown to be linear initially, but the slope decreases at higher shear rates because of flow modification by an apparent increase in elongational viscosity. The specific birefringence is no longer independent of concentration in this semi-dilute regime. It is found to be inversely proportional to concentration when the data for the two semi-dilute solutions is plotted against the dimensionless shear rate $\tau\gamma\sqrt{\lambda}$ (note that τ is also a function of polymer concentration). This shows that high concentration would inhibit high chain stretching since birefringence provides a measure of polymer dimension.

When the steady flow birefringence is compared with predictions from ex-

isting molecular theories for semi-dilute polymer solutions, we find that the most appropriate choice is the FENE-IDB model. This modified version of Hess's model for interacting dumbbells provides excellent predictions for polymer conformation change in *strong (extensional) flows* for this concentration regime. The effect of concentration on the onset strain rate, the slope of the birefringence increase with $\gamma\sqrt{\lambda}$, and specific birefringence, can be captured explicitly by varying the interaction parameter, k_s, linearly with the concentration. The model predictions such as the linear increase of birefringence with strain rate also agree with observations by other investigators for semi-dilute polyethylene oxide solutions in extensional flows [6,16,37]. Our experimental data also suggest that a hydrodynamic screening effect exists in these semi-dilute solutions. The Rouse *free-draining* behavior is shown to provide better fit of model predictions with experimental data, than the *non-free-draining* model. However, the FENE-IDB model is inadequate in predicting the overshoots in birefringence for inception of extensional flows that are observed in the experiments. This overshoot in birefringence is believed to be the result of strong initial intermolecular interactions followed by disentanglement of the network at high strain rates. Since the FENE-IDB model neglects higher order interactions, the failure to predict overshoots due to network deformation and destruction is thus not surprising.

The main result in this study is that the concentration dependence of the flow effects induced by the different concentration polymer solutions is shown for the first time. Significant inhibition of high strain rate occurs in both the semi-dilute 1500 and 4500 ppm PS2 solutions whereas no measurable change is observed for the dilute 100 ppm solution. This effect is believed to be the result of high elongational viscosity in the birefringent region. The onset of flow modification corresponds to a high effective volume concentration of $\phi_c \sim 175$ for both semi-dilute solutions. This also represents an apparent increase in the normal stress difference of ~ 85 times that of the Newtonian solvent. These critical values are O(10) times less than

the corresponding critical values determined by previous workers in this laboratory for dilute PS8 solutions. The reason may be that the birefringent region is much broader in the semi-dilute case. This extended region of high stress by aligned and extended polymers can create stronger flow modification than in the dilute case. The correlation of the magnitude of the decrease in γ with ϕ_{eff} is also revealed by the local measurement of the velocity gradient for polymer solutions of different concentrations. This dependence of flow modification on ϕ leads to the opposing effect of high concentration on the magnitude of strain rate inhibition. High concentration would inhibit high chain stretching, but it would increase the local stress due to the increased amount of polymer present in the solution. That is the reason for larger local flow modification in the less concentrated 1500 ppm solution. This competing effect of increasing concentration on the changes to the flow may provide a new explanation (via the dynamics of the polymer in strong flows) for the inhibition of drag reduction by increasing concentration. The less than linear increase in drag reduction with concentration [9,18] is possibly due to the inhibition of polymer extension for semi-dilute polymer solutions in locally strong flow regions in the turbulent pipe flow.

Therefore, increasing the polymer concentration alone would not guarantee a *locally*, larger flow modification in this semi-dilute regime. However, the 4500 ppm solution shows *globally* larger flow effect extending away from the local stagnation region due to broader birefringent region. The above local and nonlocal effect is only detectable by the pointwise velocity gradient measurements in this study. Work is now directed towards obtaining experimentally the time-dependent velocity gradient measurement by a modified homodyne light scattering technique. This would allow us to clarify the origin of overshoots in birefringence and provide a basis for testing constitutive equations for polymeric fluids in flow.

References

[1] Toms, B. A., *Proc. 1st Int. Congr. Rheol.*, **2**, 135 (1948).

[2] Tanner, R. I., *A.I.Ch.E. Journal*, **22**, 910 (1976).

[3] Olbricht, W. L., Rallison, J. M., Leal, L. G., *J. Non-Newt. Fluid Mech.*, **10**, 291 (1982).

[4] Durst, F., Haas, R., Interlhal, W., *Rheol. Acta*, **21**, 572 (1982).

[5] James, D. F., Saringer, J. H., *J. Fluid Mech.*, **97**, 655 (1980).

[6] Pope, D. P., Keller, A., *Colloid & Polym. Sci.*, **256**, 751 (1978).

[7] Fuller, G. G., Leal, L. G., *Rheol. Acta*, **19**, 580 (1980).

[8] Dunlap, P. N., Leal, L. G., *J. Non-Newt. Fluid Mech.* **23**, 5 (1987).

[9] Berman, N. S., *Polymer Eng. & Sci.*, **20**, 451 (1980).

[10] Shenoy, A. V., *Colloid & Polym. Sci.*, **262**, 319 (1984).

[11] Gardner, K., Pike, E. R., Miles, M. J., Keller, A., Tanaka, K., *Polymer*, **23**, 1435 (1982).

[12] Keller, A., Müller, A. J., Odell, J. A., *Progr. Colloid & Polymer Sci.*, **75**, 179 (1987).

[13] Chow, A., Keller, A., Müller, A. J., Odell, J. A., *Macromolecules*, **21**, 250 (1988).

[14] Müller, A. J., Odell, A. J., Keller, A., *J. Non-Newt. Fluid Mech.*, **30**, 99 (1988).

[15] Leal, G. L., Fuller, G. G., Olbricht, W. L., *Prog. Astro. Aero.*, **72**, 351 (1980).

[16] Fuller, G. G., Leal, L. G., *J. Polym. Sci. Polym. Phys. Ed.*, **19**, 557 (1981).

[17] Fuller, G. G., Leal, L. G., *J. Polym. Sci. Polym. Phys. Ed.*, **19**, 531 (1981).

[18] Lumley, J. C., *Ann. Rev. Fluid Mech.*, Vol. I, 367 (1968).

[19] Hess, W., *Rheol. Acta,* **23**, 477 (1984).

[20] Dunlap, P. N., *private communication,* (1985).

[21] Zimm, B. H., *J. Chem. Phys.,* **24**, 269 (1956).

[22] Rouse, P. E., *J. Chem. Phys.,* **21**, 1272 (1953).

[23] Fuller, G. G., Rallison, J. M., Schmidt, R. L., Leal, L. G., *J. Fluid Mech.,* **100**, 555 (1980).

[24] Lagnado, R., Ph. D. Thesis, California Institute of Technology, Pasadena (1985).

[25] Lagnado, R. L., Phan-Thien, N., Leal, L. G., *J. Non-Newtonian Fluid Mech.,* **18**, 25 (1985).

[26] Janeschitz-Kriegl, H., *Adv. Poly. Sci.,* **6**, 170 (1969).

[27] Peterlin, A., Munk, P., *Physical Method of Chemistry,* eds. Weissberger, A., Rossiter, B., **1** (III C), pp. 271-384, John Wiley & Sons, N.Y. (1972)

[28] Peterlin, A., *Polymer,* **2**, 257 (1961).

[29] Janeschitz-Kriegl, H., *Polymer Melt Rheol. & Flow Birefringence,* Springer Verlag, New York (1983).

[30] Tsvetkov, V. N., Eskin, V. E., Frenkel, S. Ya., *Structure of Macromolecules in Solution,* Vol. 3, tr. & ed. C. Crane-Robinsin, National Lending Library for Sci. & Tech., Boston (1971).

[31] Philippoff, W., *Proc. IV. Intl. Congr. Rheol.,* E. H. Lee (ed.), Vol. 2, 1963, Interscience, N.Y. (1965).

[32] Tsvetkov, V. N., *Polymer Handbook,* eds. J. Bandrup and E. H. Immergut, Interscience, N.Y., p. V-75 (1966).

[33] Osaki, K., Bessho, N., Kojimoto, T., Kurata, M., *J. Rheol.* **23**, 457 (1979).

[34] Frank, F. C., Mackley, M. R., *J. Polym. Sci.*, **14**, 1121 (1976).

[35] Mackley, M. R., *J. Non-Newtonian Fluid Mech.*, **4**, 111 (1978).

[36] Farrell, C. J., Keller, A., Miles, M. J., Pope, D. P., *Polymer*, **21**, 1292 (1980).

[37] Pope, D. P., Keller, A., *Colloid and Polymer Sci.*, **255**, 633 (1977).

[38] Elata, C., Lehrer, C., Kalranovitz, A., *Israel J. Tech.*, **4**, 87 (1966).

[39] Broadbent, J. M., Pountney, D. C., Walters, K., *J. Non-Newtonian Fluid Mech.*, **3**, 359 (1978).

[40] Muller, S. I., Armstrong, R. C., Brown, R. A., Paper presented at the International Conference on Viscoelasticity of Polymeric Liquids, Grenoble, France (Jan. 1986).

[41] Geffroy-Aguilar, E., Leal, L. G., "*Flow Birefringence Studies in Transient Flows of a Two Roll Mill for the Test-Fluid M1*," *J. Non-Newt. Fluid Mech.*, to appear (1989).

[42] Batchelor, G. K., *J. Fluid Mech.*, **46**, 813 (1971).

[43] Zakin, J. L., Hunston, D. L., *J. Macromol. Sci.–Phys.*, **B18**, (4), 795 (1980).

[44] Rallison, J. M., Hinch, E. J., *J. Non-Newtonian Fluid Mech.*, **29**, 37 (1988).

[45] Phan-Thien, N., Tanner, R. I., *J. Non-Newt. Fluid Mech.*, **2**, 353 (1977).

[46] Doi, M., Edwards, S. F., *J. Chem. Soc. Faraday Trans. II*, **74**, 1789, 1802, 1818 (1978); **75**, 38 (1979).

[47] Binding, D. M., Walters, K., *J. Non-Newt. Fluid Mech.*, **30**, 233 (1988).

[48] Hudson, N. E., Ferguson, J., Warren, B. C. H., *J. Non-Newt. Fluid Mech.*, **30**, 251 (1988).

[49] Bird, R. B., DeAguiar, J. R., *J. Non-Newt. Fluid Mech.*, **13**, 149 (1983).

[50] DeAguiar, J. R., *J. Non-Newt. Fluid Mech.*, **13**, 161 (1983).

[51] Giesekus, H., *Rheol. Acta*, **5**, 29 (1966).

[52] Giesekus, H., *J. Non-Newt. Fluid Mech.*, **11**, 69 (1982).

[53] Phan-Thien, N., Manero, O., Leal, L. G., *Rheol. Acta*, **23**, 151 (1984).

[54] Tsvetkov, V. N., Frisman, E., *Acta Physicochim U.S.S.R.*, **20**, 61 (1945).

[55] Ng, R. C.-Y., Leal, L. G.,"*An Interacting FENE Dumbbell Model for Semi-Dilute Polymer Solutions in Extensional Flows,*" to appear (1989).

[56] Bird, R. B., Curtiss, C. F., Armstrong, R. C., Hassager, O., *Dynamics of Polymeric Liquids*, Vol. 2: Kinetic Theory, 2^{nd} ed., Wiley, New York (1987).

[57] Peterlin, A., *J. Chem. Phys.*, **39**, 224 (1963).

[58] Freed, K. F., Edwards, S. F., *J. Chem. Phys.*, **61**, 3626 (1974).

[59] Wang, F. W., Zimm, B. H., *J. Polym. Sci.: Polym. Phys. Ed.*, **12**, 1619, 1639 (1974).

[60] Billmeyer, F. W., *Textbook of Polym. Sci.*, Interscience Publishers, John Wiley & Sons, New York, p. 81 (1962).

[61] Ferry, J. D., *Viscoelastic Properties of Polymers*, John Wiley & Sons, Inc., New York (1970).

Figure Captions

Figure 1. Solution viscosity versus polymer concentration for PS2 in TCP6 solutions.

Figure 2. Schematic of the homodyne light scattering experiment with the two-dimensional flow in the x-y plane of the roll mill device. P represents the pinhole location, and F is a laser line filter ($488 \pm 7\ nm$).

Figure 3. Schematic streamlines for the linear two-dimensional flow with various flow type λ. The X-Y and X′-Y′ coordinates are used for experiments in the 2-roll and the 4-roll mill, respectively.

Figure 4. Measured velocity gradient γ (arbitrary value) versus the eigenvalue of the velocity gradient tensor, $\gamma\sqrt{\lambda}$ (theoretical Newtonian value), for the Newtonian solvent TCP6 in the 2-roll and the 4-roll mill.

Figure 5. Birefringence experiment: (a) schematic of experimental setup; (b) relative orientation of the analyzer, polarizer, principal axis of polarization tensor of polymer, and coordinate of the flow.

Figure 6. Flow birefringence of the solvents TCP6 and CW versus the Newtonian strain rate, $\gamma(1+\lambda)/2$.

Figure 7. Specific birefringence, $\Delta n/c$, versus eigenvalue of the velocity gradient tensor, $\gamma\sqrt{\lambda}$, for the 1500 and 4500 ppm solutions of PS2 in TCP6.

Figure 8. Specific birefringence, $\Delta n/c$, versus the dimensionless eigenvalue of the velocity gradient tensor, $\tau\gamma\sqrt{\lambda}$, for the 1500 and 4500 ppm solutions of PS2 in TCP6, and for the 1500 ppm solution of PS2 in CW (dashed line).

Figure 9. Specific birefringence, $\Delta n/c$, versus dimensionless eigenvalue of the velocity gradient tensor, $\tau\gamma\sqrt{\lambda}$, for the 100 ppm, 1500, and 4500 ppm PS2 solutions (same nomenclature as in Fig. 8).

Figure 10. Flow birefringence profile across the x′-axis (4-roll mill) and the x-axis (2-roll mill) for the semi-dilute PS2 solutions at $x' = x = 0$, for the two flow types: (a) $\lambda = 1.00$; (b) $\lambda = 0.049$.

Figure 11. Flow birefringence profile across the x-axis in the 2-roll mill for the 4500 ppm solution of PS2 at $\gamma\sqrt{\lambda} = 14.82\ \sec^{-1}$, and for $x = 0$ (□), $x = 0.12''$(×).

Figure 12. Flow birefringence of the Newtonian solvent TCP6 versus time for inception and cessation of steady extensional flows at the stagnation point: (a) $\lambda = 1.00$ (4-roll mill); (b) $\lambda = 0.049$ (2-roll mill).

Figure 13. Flow birefringence versus time for inception and cessation of steady pure extensional flows at the stagnation point in the 4-roll mill ($\lambda = 1.00$) for the semi-dilute solutions of PS2 in TCP6: (a) 1500 ppm; (b) 4500 ppm.

Figure 14. Flow birefringence versus time for inception and cessation of steady extensional flows at the stagnation point in the 2-roll mill ($\lambda = 0.049$) for the semi-dilute solutions of PS2 in TCP6: (a) 1500 ppm; (b) 4500 ppm.

Figure 15. Orientation angle, χ, versus time for cessation of steady extensional flows at the stagnation point in the 2-roll mill ($\lambda = 0.049$) for the semi-dilute solutions of PS2 in TCP6: (a) 1500 ppm; (b) 4500 ppm.

Figure 16. Measured velocity gradient γ (arbitrary value) versus the eigenvalue of the velocity gradient tensor, $\gamma\sqrt{\lambda}$ (theoretical Newtonian value),

in the 4-roll mill ($\lambda = 1.00$) for the semi-dilute solutions of PS2 in TCP6: (a) 1500 ppm (solvent TCP6 data represented by the squared symbol); (b) 4500 ppm.

Figure 17. Measured velocity gradient (relative values of γ) profile across the x′-axis at the stagnation point in the 4-roll mill ($\lambda = 1.00$) for the semi-dilute solutions of PS2 in TCP6: (a) 1500 ppm; (b) 4500 ppm.

Figure 18. Measured velocity gradient γ (arbitrary value) versus the eigenvalue of the velocity gradient tensor, $\gamma\sqrt{\lambda}$ (theoretical Newtonian value), in the 2-roll mill ($\lambda = 0.049$) for the semi-dilute solutions of PS2 in TCP6: (a) 1500 ppm (solvent TCP6 data represented by the squared symbol); (b) 4500 ppm.

Figure 19. Measured velocity gradient (relative values of γ) profile across the $x - axis$ in the 2-roll mill ($\lambda = 0.049$) for the 1500 ppm solution of PS2 in TCP6 at: (a) $x = 0''$ (roller surface located at $y = \pm 0.125''$); (b) $x = 0.12''$ (roller surface located at $y = \pm 0.14''$).

Figure 20. Measured velocity gradient γ (arbitrary value) versus the dimensionless eigenvalue of the velocity gradient tensor, $\tau\gamma\sqrt{\lambda}$ (theoretical Newtonian value), for the solvent and the polymer solutions, and for two flow types: (a) $\lambda = 1.00$ (4-roll mill); (b) $\lambda = 0.049$ (2-roll mill).

Figure 21. Effective volume concentration, ϕ, versus the dimensionless eigenvalue of the velocity gradient tensor, $\tau\gamma\sqrt{\lambda}$ (theoretical Newtonian value), for the polymer solutions in the 4-roll mill ($\lambda = 1.00$).

Figure 22. Dimensionless effective polymer chain length, $2r_{eq}/L(= \sqrt{\Delta n/\Delta n_\infty})$, calulated from the birefringence results in Fig. 9 plotted versus the

dimensionless eigenvalue of the velocity gradient tensor, $\tau\gamma\sqrt{\lambda}$, for solutions of various polymer concentrations.

Figure 23. Measured velocity gradient (relative values of γ) profile across the x′-axis in the 4-roll mill ($\lambda = 1.00$) for the 1500 ppm (dashed line) and the 4500 ppm (solid line) solutions of PS2 in TCP6 at the dimensionless shear rate: $\tau\gamma\sqrt{\lambda} \sim 0.44$ (□); $\tau\gamma\sqrt{\lambda} \sim 0.33$ (×).

Figure 24. Predictions of the ED model with $\alpha = \beta = 1$ for the root-mean-square end-to-end length of a dumbbell versus the dimensionless eigenvalue of the velocity gradient tensor, $\tau\gamma\sqrt{\lambda}$, and for various values of the parameter σ: $\sigma = 10,\ 2,\ 1,\ 0.1,\ 0.01,\ 0.001$ (from left to right of the graph).

Figure 25. Flow birefringence (absolute value), Δn, versus the dimensionless *measured* values of the eigenvalue of the velocity gradient tensor, $\tau(\gamma\sqrt{\lambda})_{\text{measured}}$, for the 1500 ppm (solid line) and the 4500 ppm (dashed line) solutions of PS2 in TCP6 (same symbols for different flow types are used as in Fig. 8).

Figure 26. Predictions of the FENE-IDB model for $\lambda = 1.00$ (solid line) and $\lambda = 0.049$ (dashed line) for various values of the parameter, k_s, along with representative flow birefringence data for solutions of various concentration: c = 0 ppm (□); c = 1500 ppm (△); c = 4500 ppm (×).

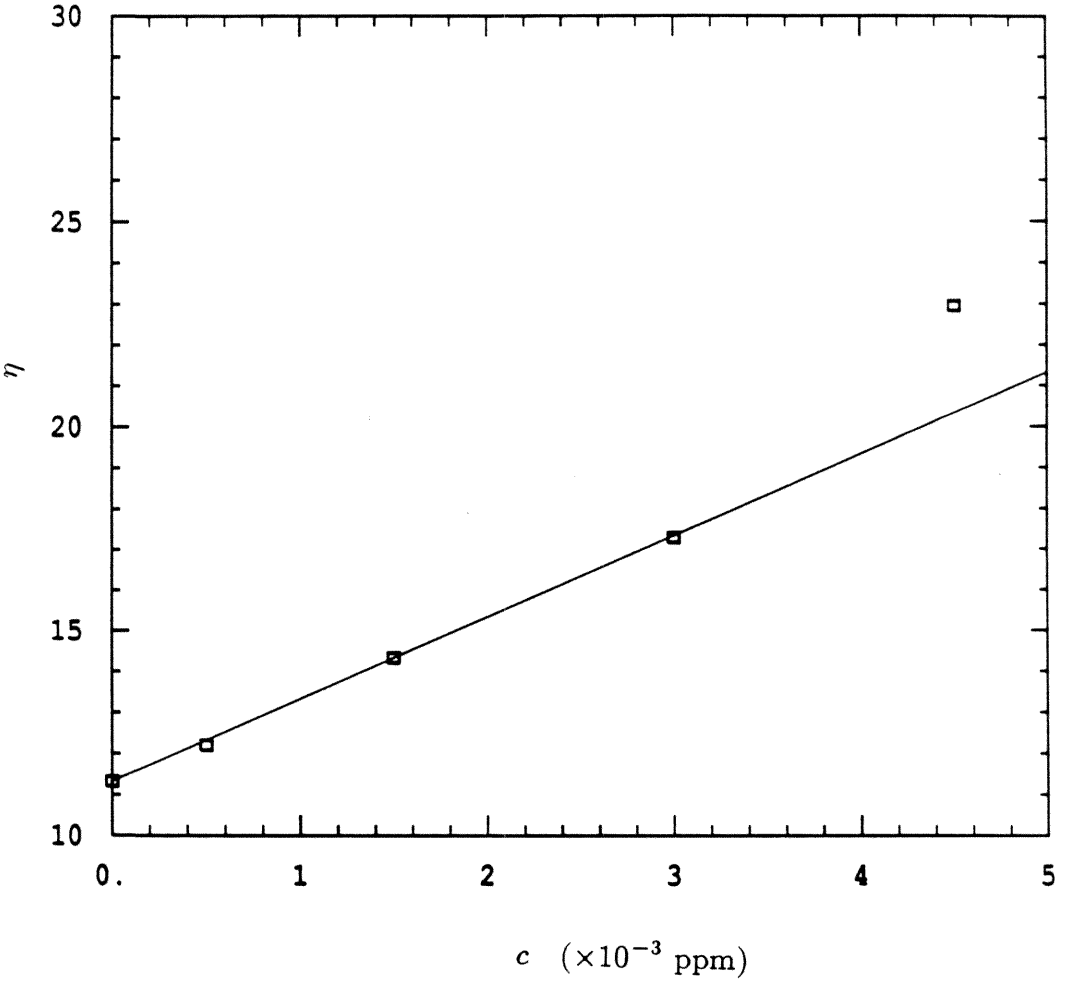

Fig. 1

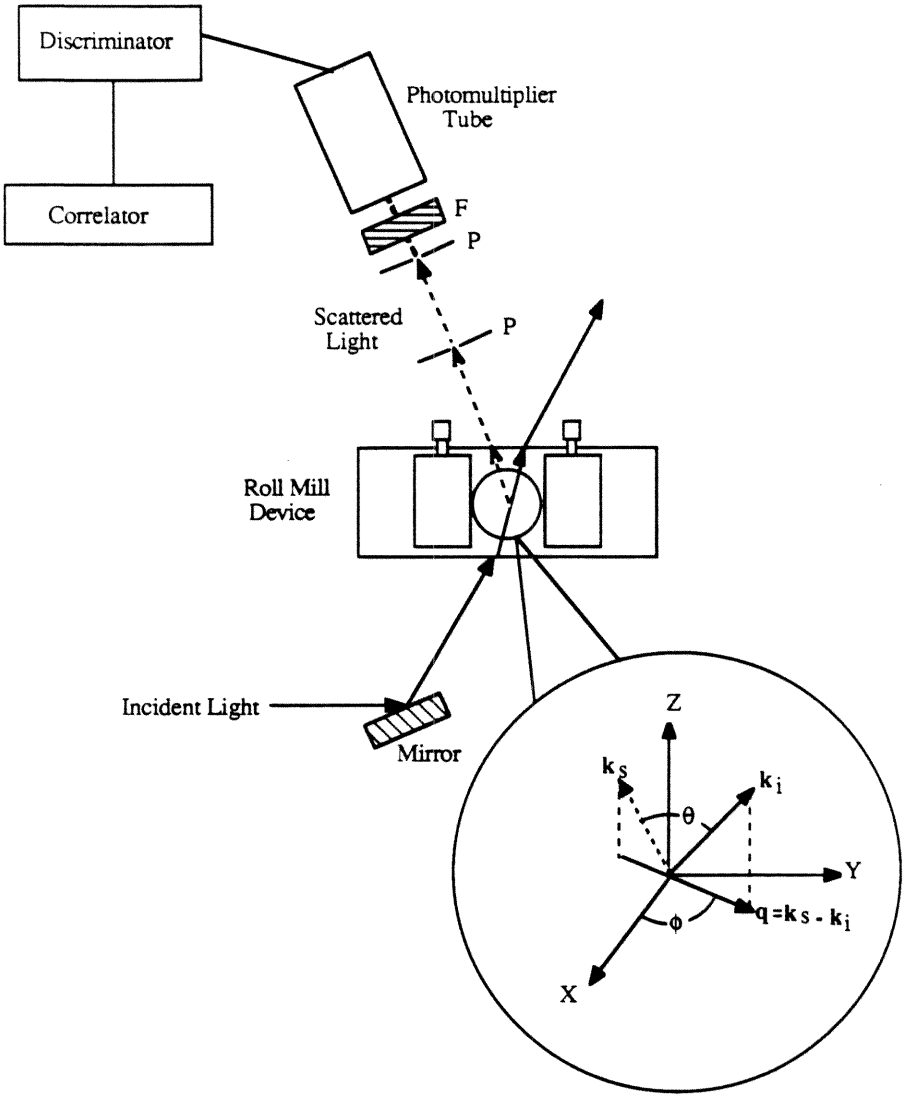
Discriminator
Correlator
Photomultiplier Tube
F
P
Scattered Light
P
Roll Mill Device
Incident Light
Mirror
Z
k_s
k_i
θ
Y
$q = k_s - k_i$
ϕ
X

Fig. 2

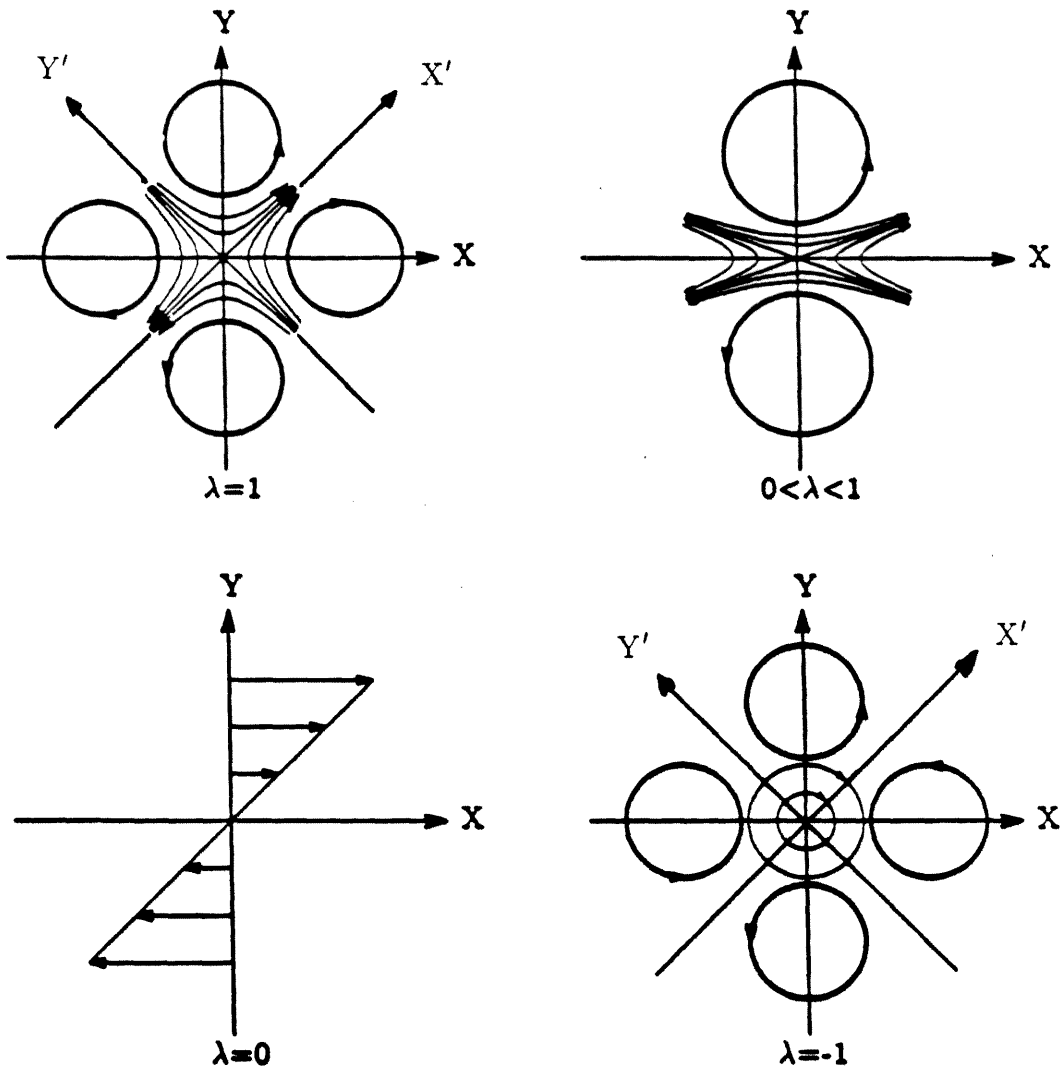

Fig. 3

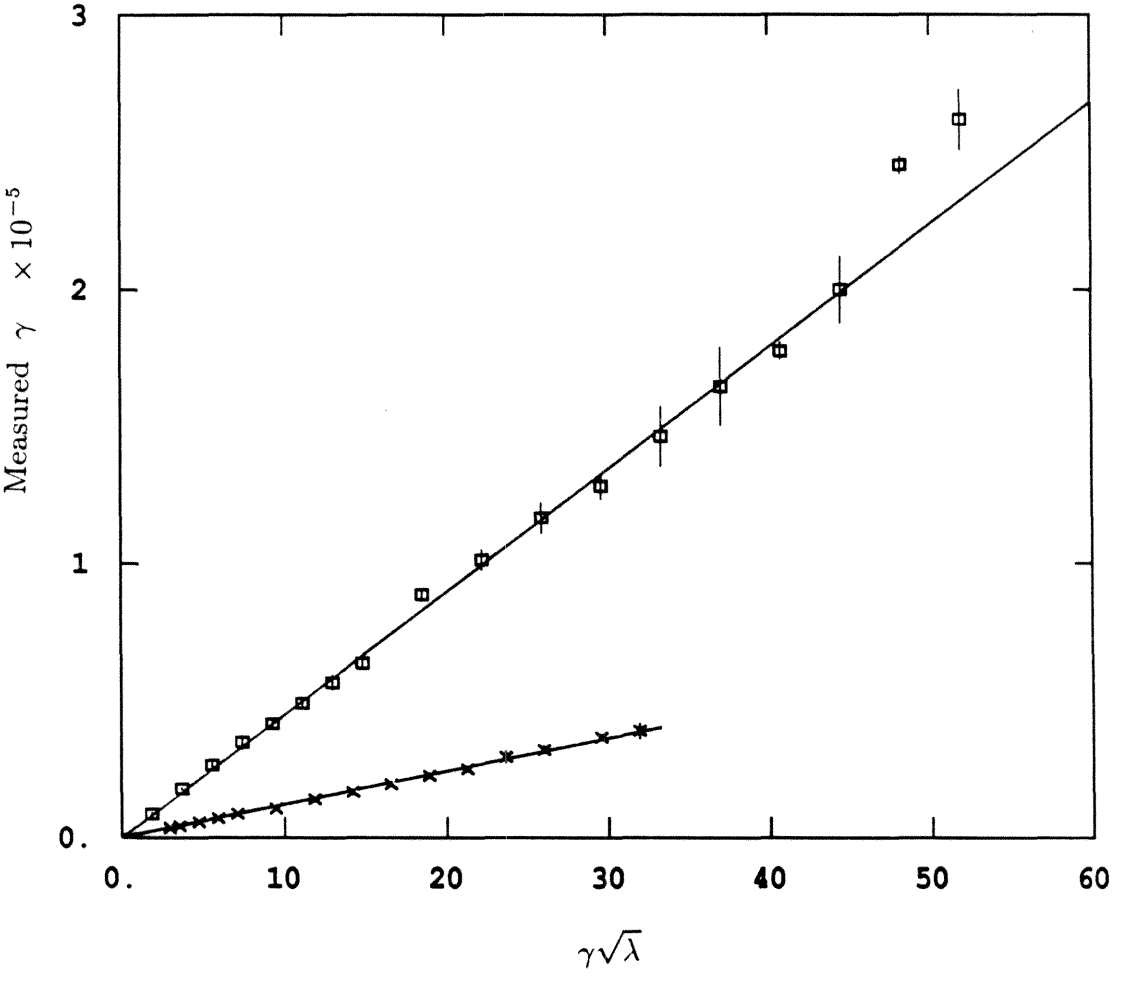
3
2
1
0.
Measured γ $\times 10^{-5}$
0.
10
20
30
40
50
60
$\gamma\sqrt{\lambda}$

Fig. 4

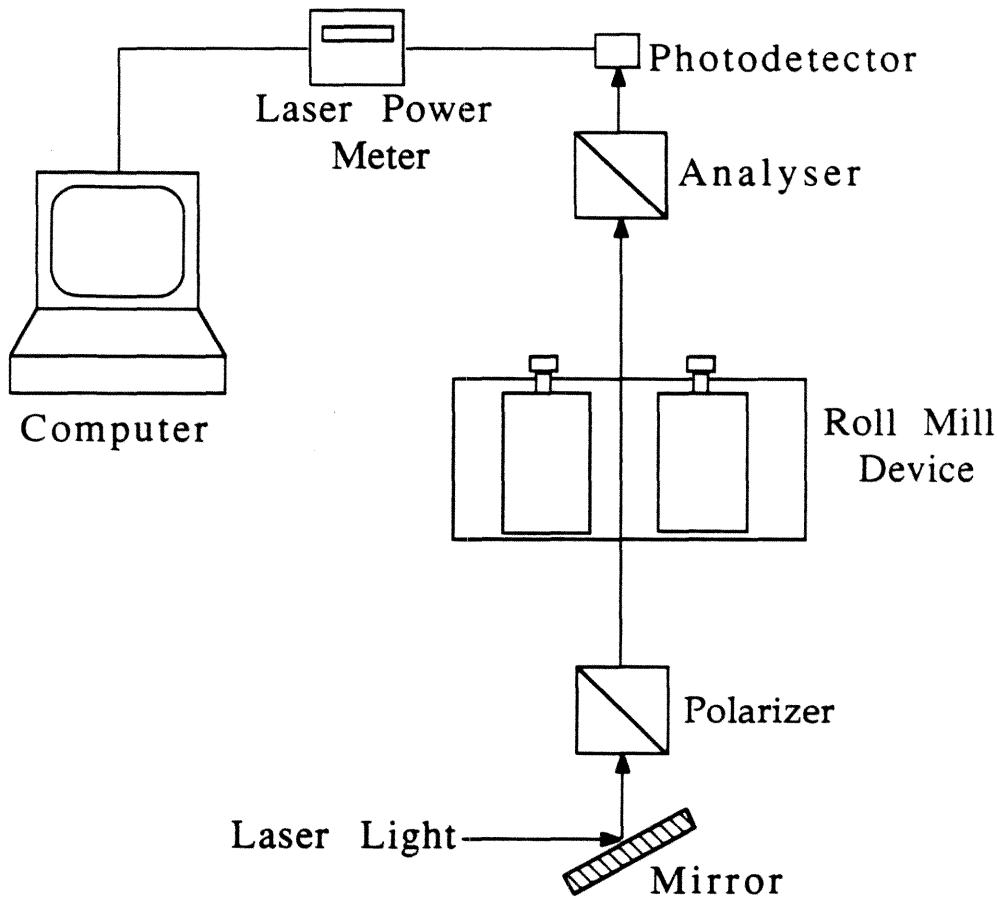
Photodetector
Laser Power Meter
Analyser
Computer
Roll Mill Device
Polarizer
Laser Light
Mirror

Fig. 5(a)

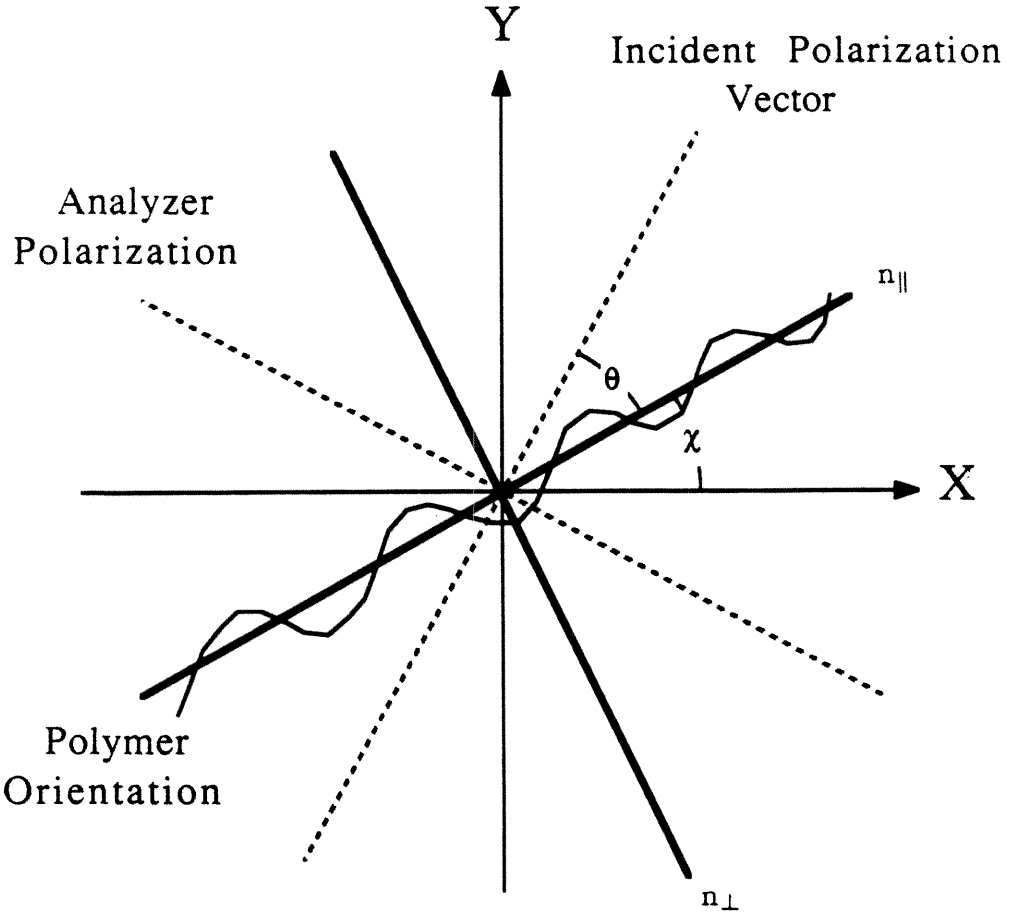
Y
Incident Polarization
Vector
Analyzer
Polarization
$n_{\parallel}$
θ
χ
X
Polymer
Orientation
$n_{\perp}$

Fig. 5(b)

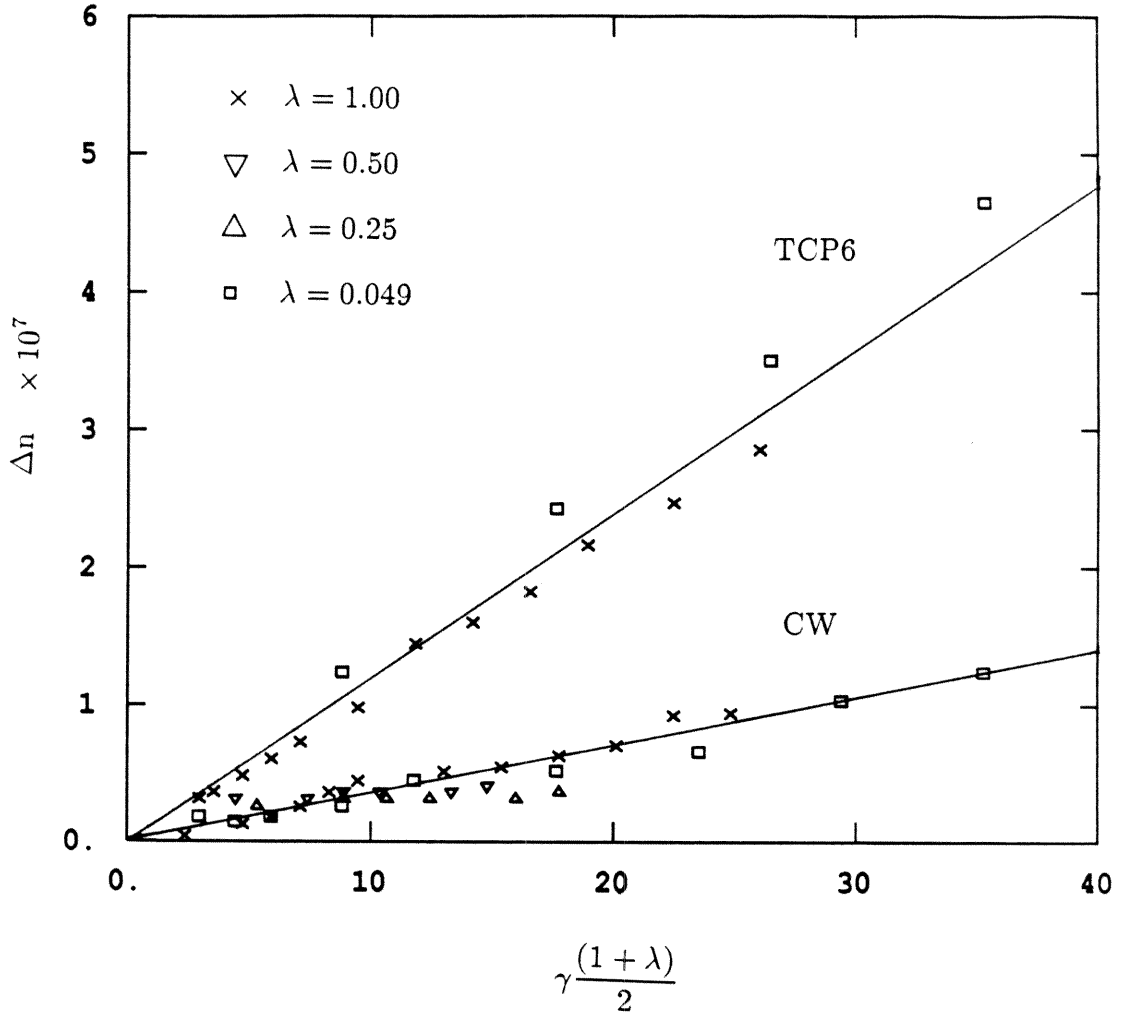

Fig. 6

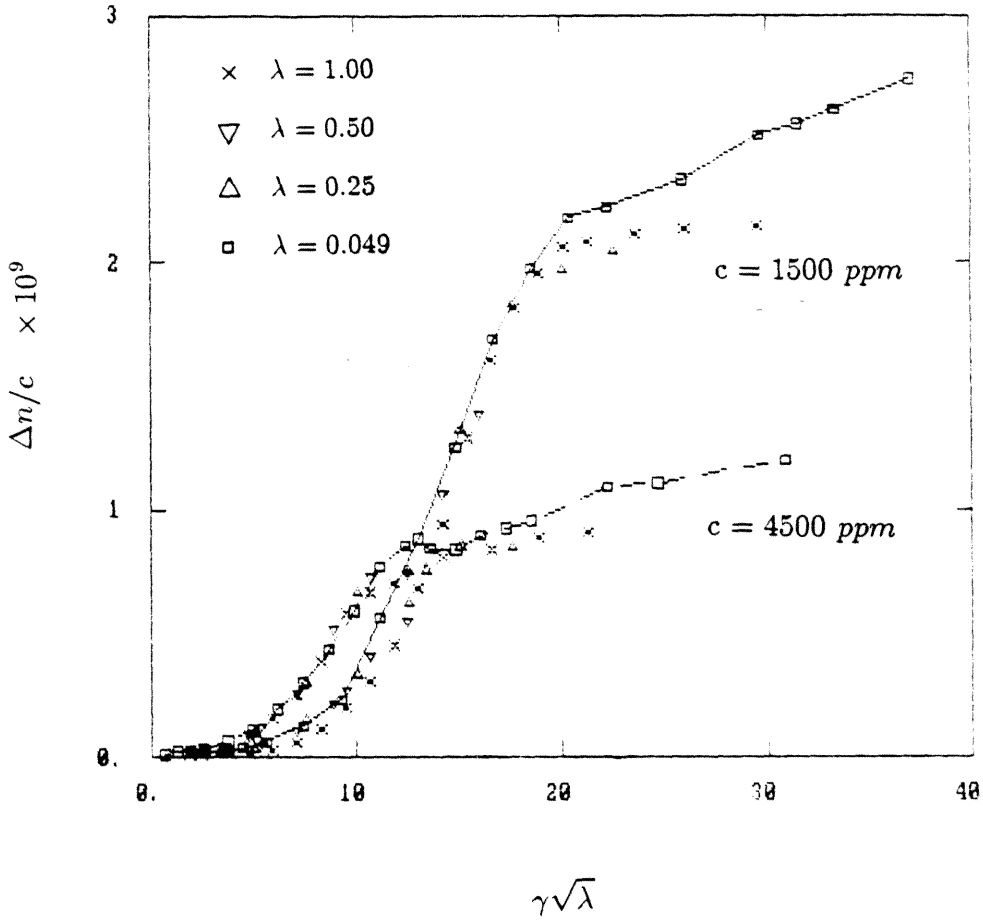
3
2
1
0.
0.
10
20
30
40
× λ = 1.00
▽ λ = 0.50
△ λ = 0.25
□ λ = 0.049
c = 1500 ppm
c = 4500 ppm
Δn/c × 10^9
γ√λ

Fig. 7

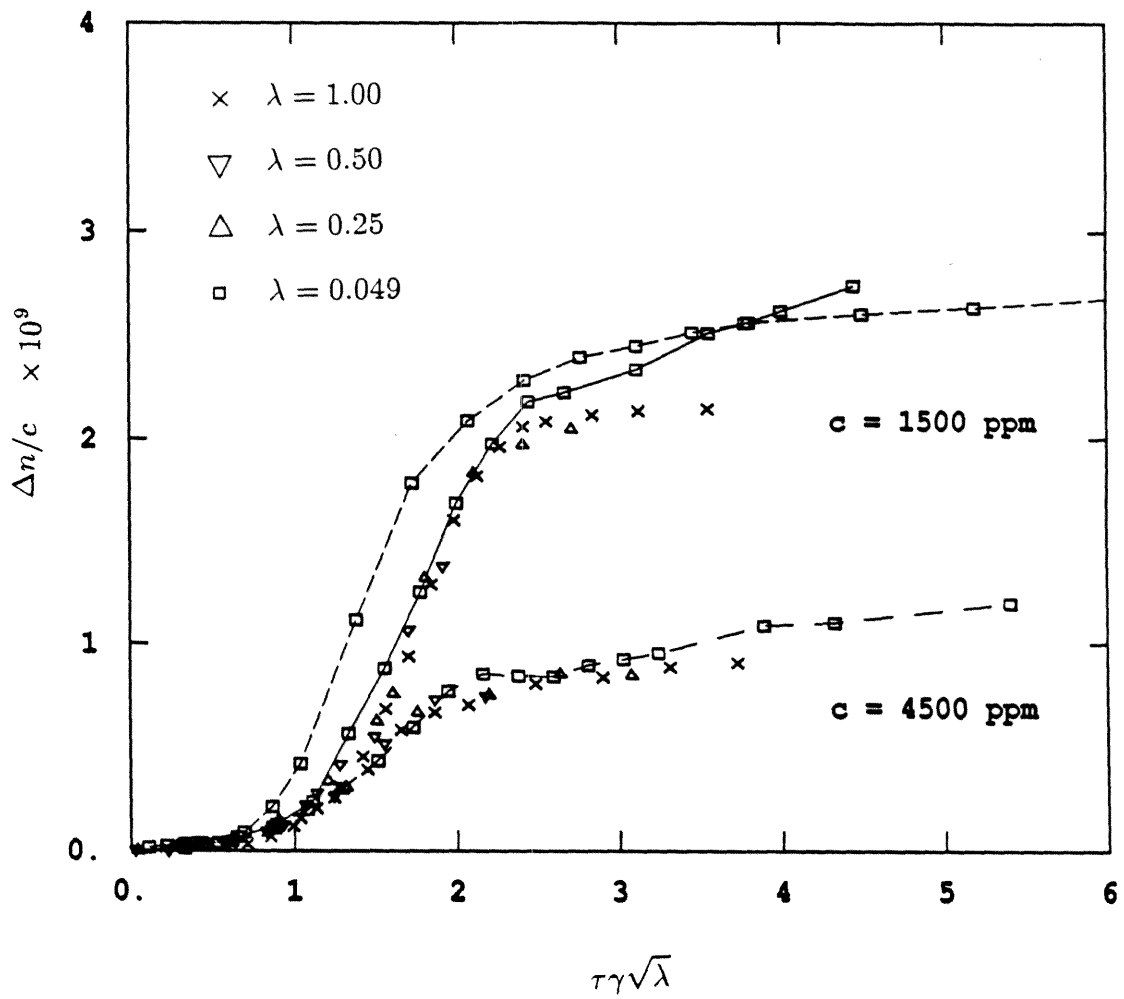
4
3
2
1
0.
0.
1
2
3
4
5
6
× λ = 1.00
▽ λ = 0.50
△ λ = 0.25
□ λ = 0.049
c = 1500 ppm
c = 4500 ppm
Δn/c × 10^9
τγ√λ

Fig. 8

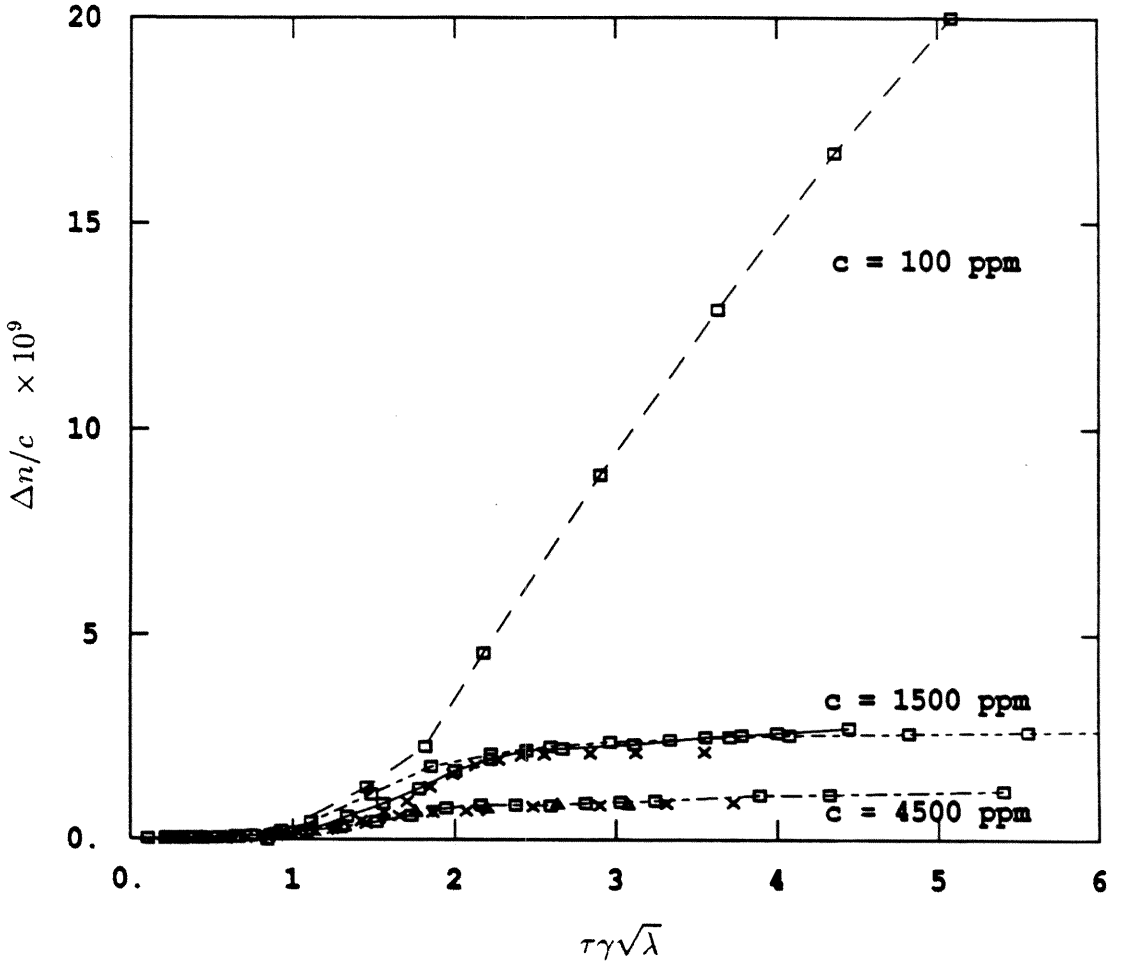
20
15
10
5
0.
0.
1
2
3
4
5
6
$\Delta n/c \times 10^9$
$\tau\gamma\sqrt{\lambda}$
c = 100 ppm
c = 1500 ppm
c = 4500 ppm

Fig. 9

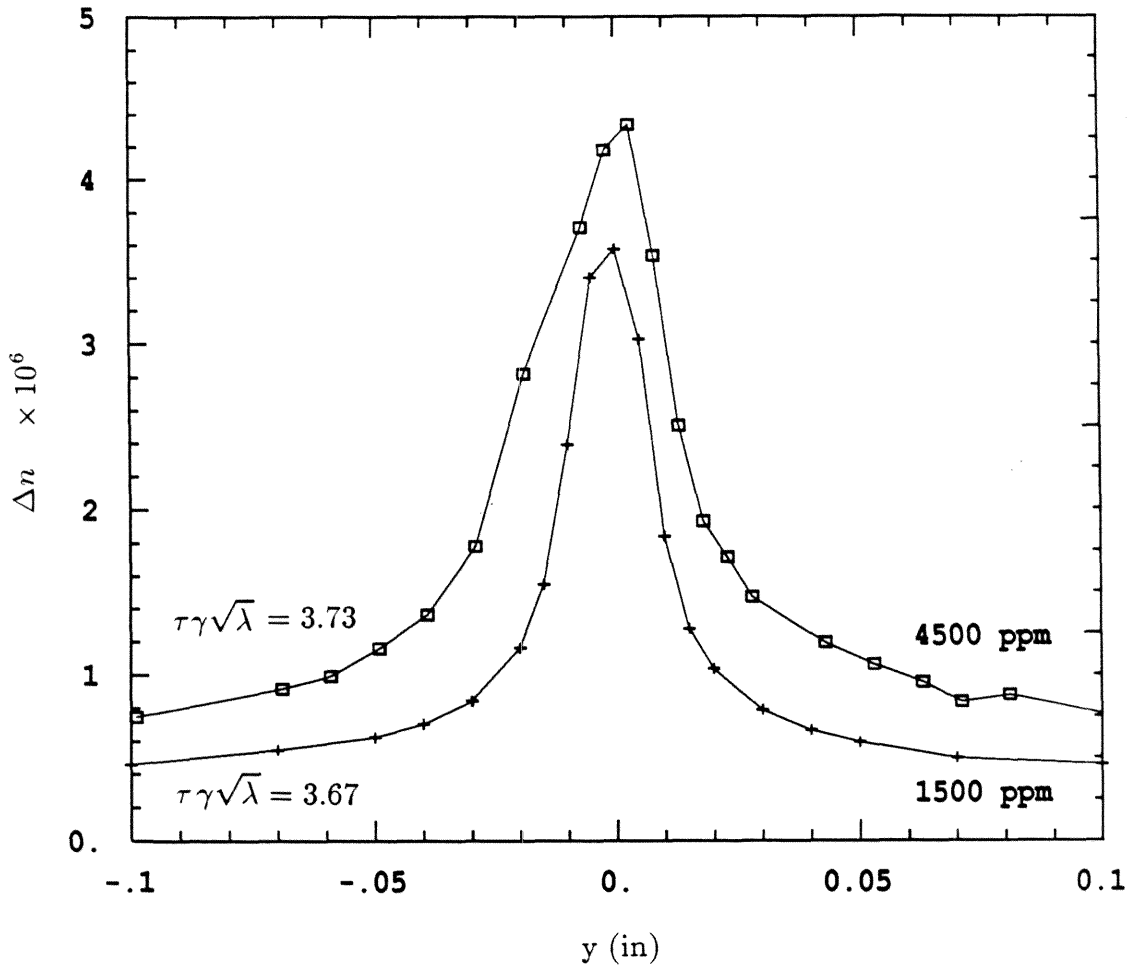
5
4
3
2
1
0.
$\Delta n \times 10^6$
$\tau\gamma\sqrt{\lambda} = 3.73$
4500 ppm
$\tau\gamma\sqrt{\lambda} = 3.67$
1500 ppm
-.1
-.05
0.
0.05
0.1
y (in)

Fig. 10(a)

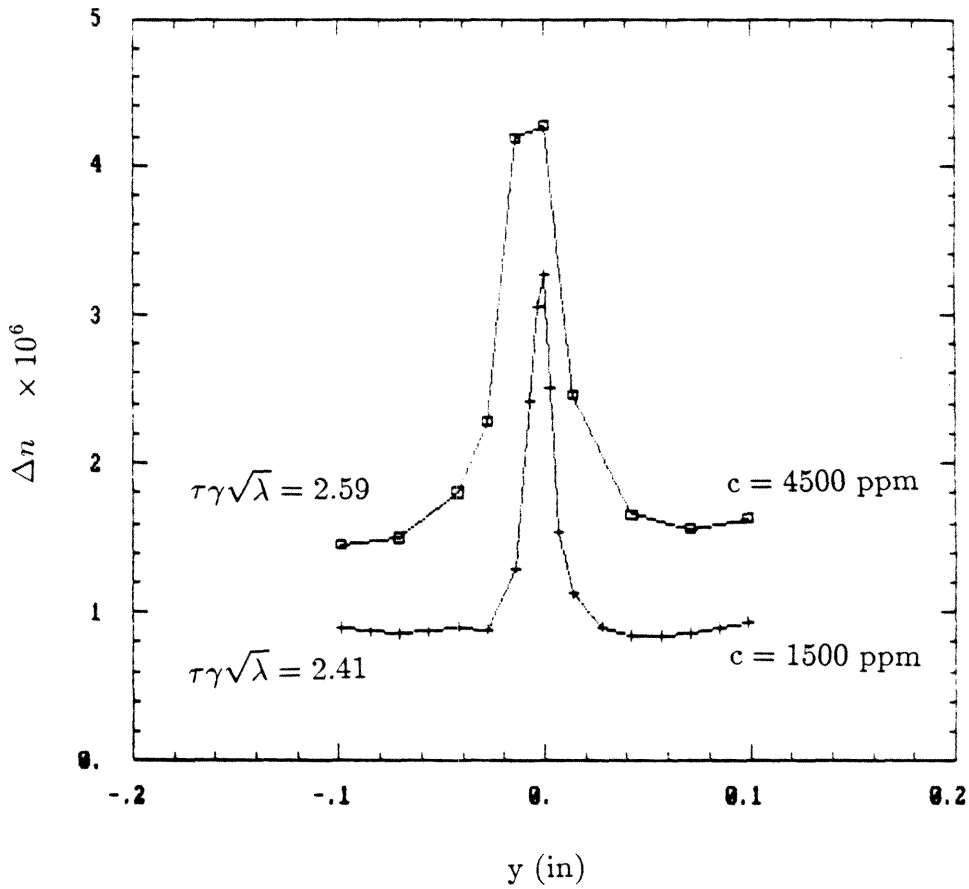
5
4
3
2
1
0.
$\Delta n \times 10^6$
$\tau\gamma\sqrt{\lambda} = 2.59$
c = 4500 ppm
$\tau\gamma\sqrt{\lambda} = 2.41$
c = 1500 ppm
-.2
-.1
0.
0.1
0.2
y (in)

Fig. 10(b)

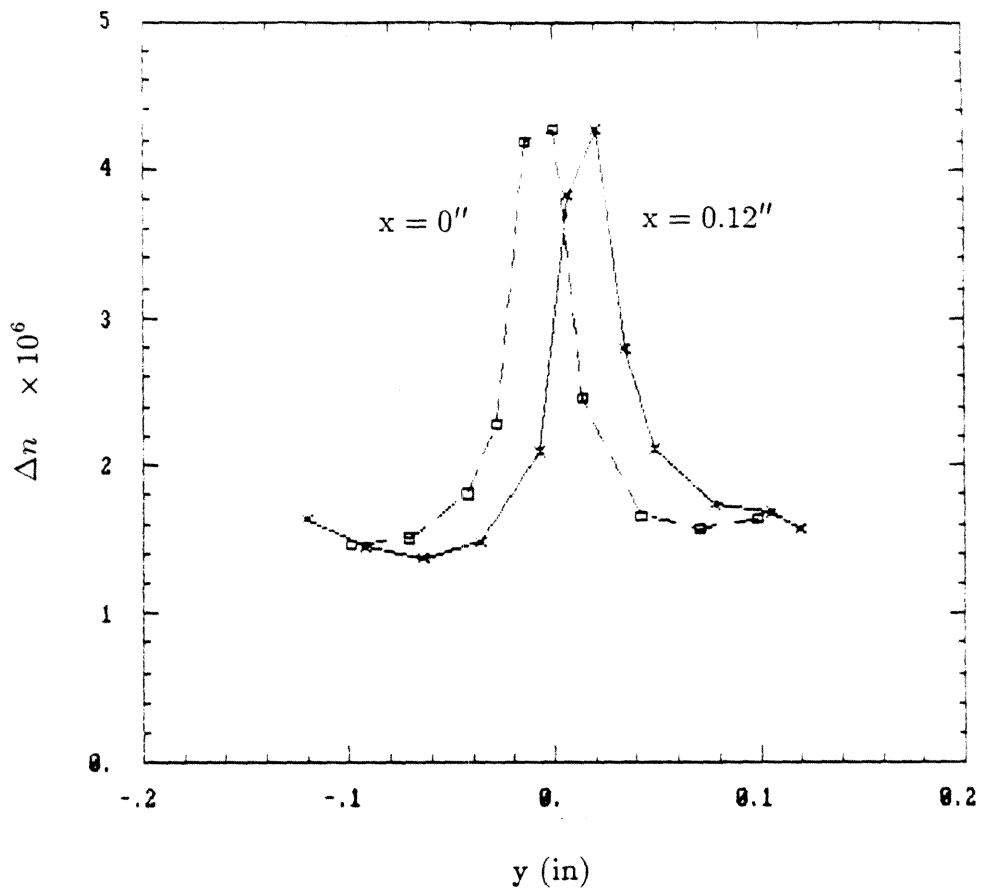

Fig. 11

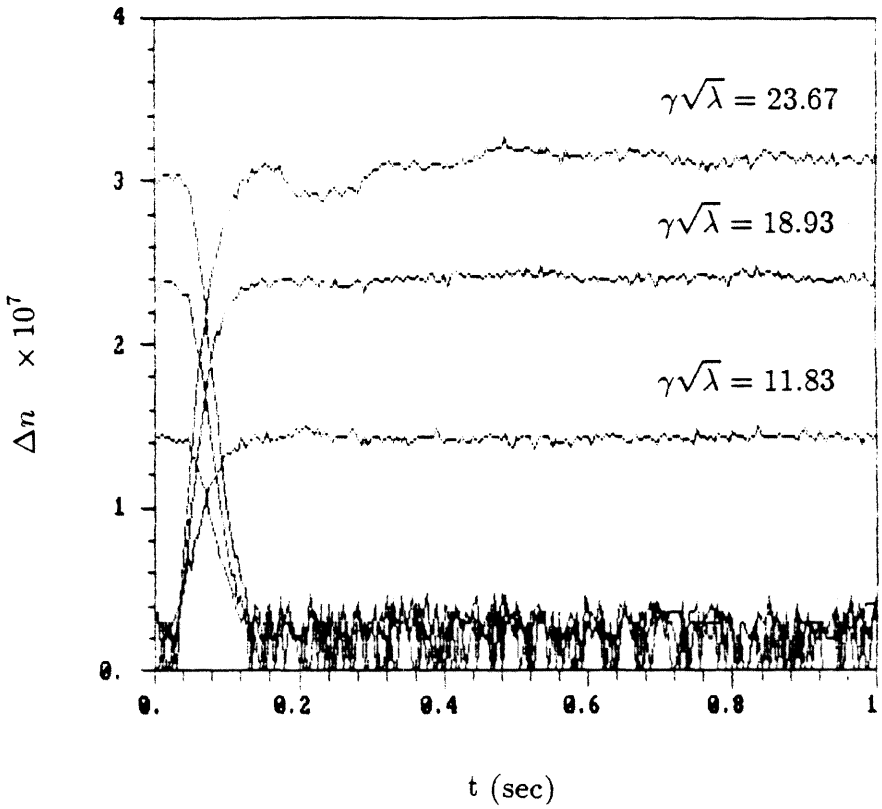
$\gamma\sqrt{\lambda} = 23.67$
$\gamma\sqrt{\lambda} = 18.93$
$\gamma\sqrt{\lambda} = 11.83$
$\Delta n \times 10^7$
t (sec)
0.
1
2
3
4
0.2
0.4
0.6
0.8

Fig. 12(a)

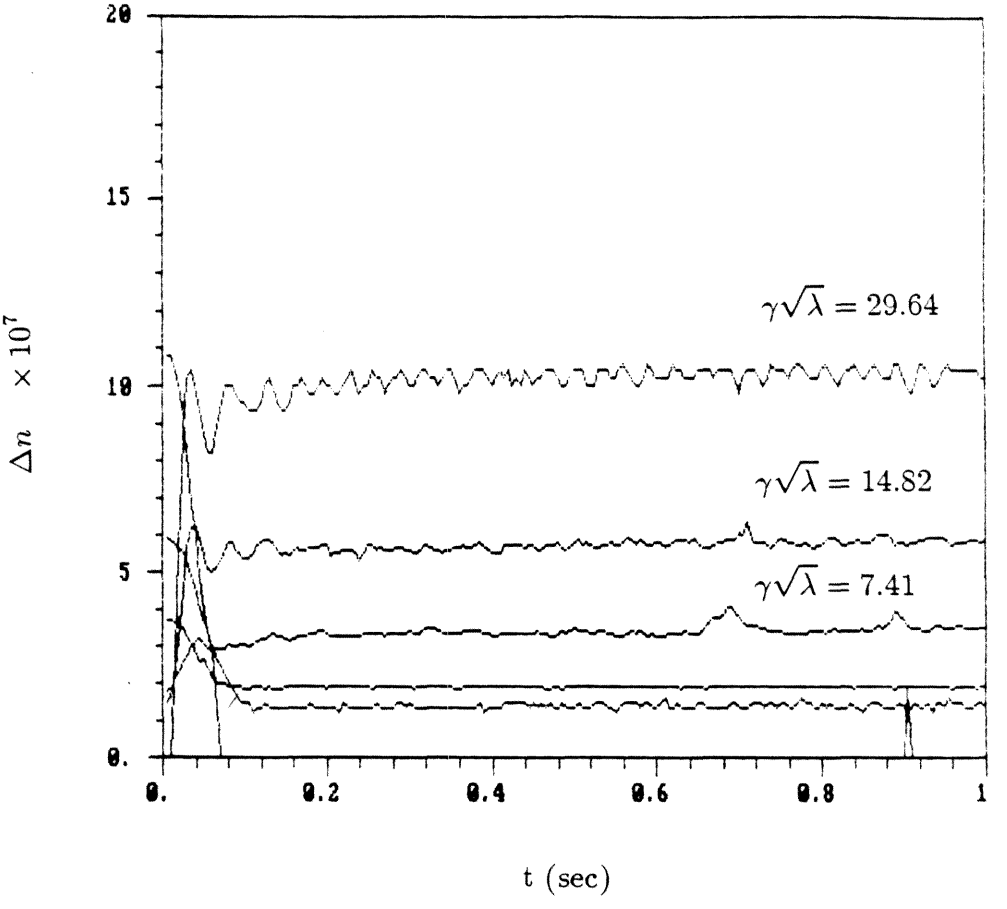
20
15
10
5
0.
0.
0.2
0.4
0.6
0.8
1
$\Delta n \times 10^7$
t (sec)
$\gamma\sqrt{\lambda} = 29.64$
$\gamma\sqrt{\lambda} = 14.82$
$\gamma\sqrt{\lambda} = 7.41$

Fig. 12(b)

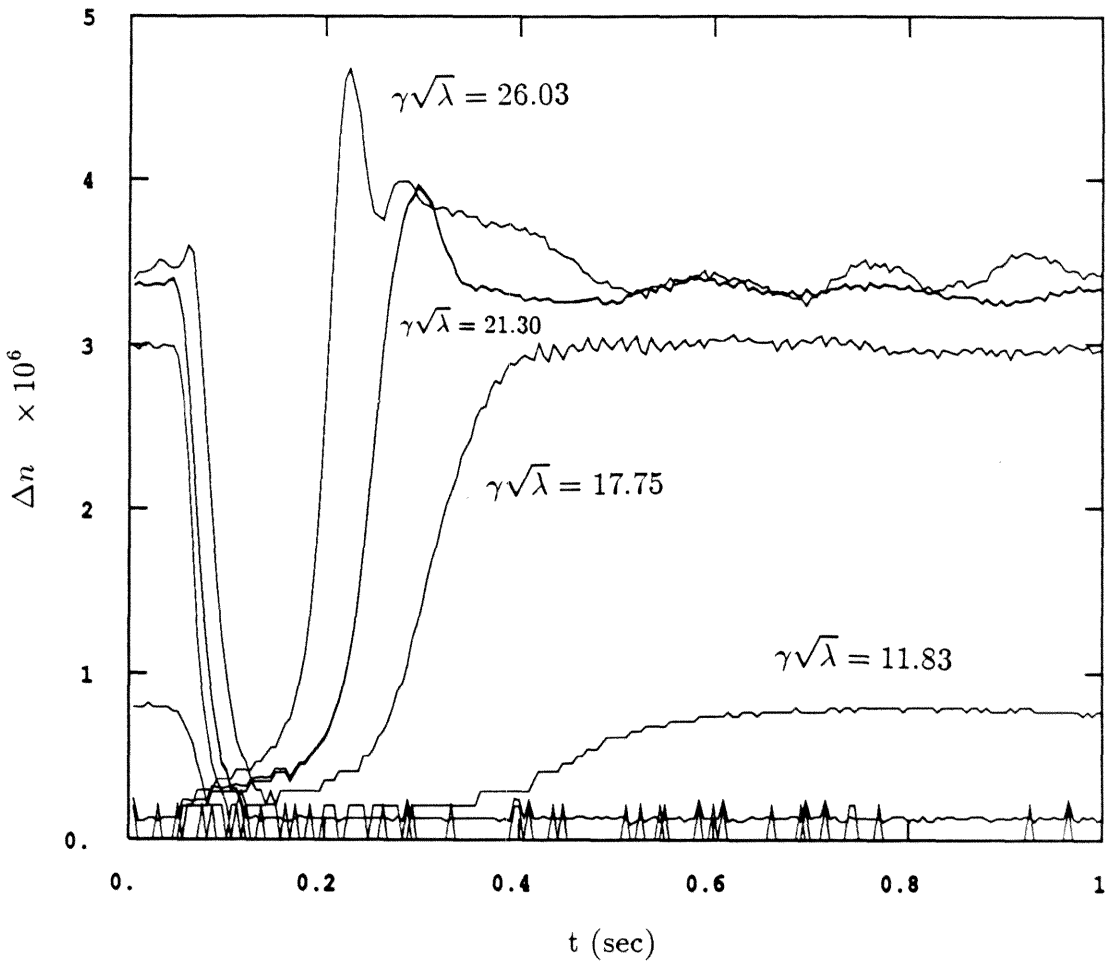
$\gamma\sqrt{\lambda} = 26.03$
$\gamma\sqrt{\lambda} = 21.30$
$\gamma\sqrt{\lambda} = 17.75$
$\gamma\sqrt{\lambda} = 11.83$
$\Delta n \times 10^6$
t (sec)
0.
1
2
3
4
5
0.2
0.4
0.6
0.8

Fig. 13(a)

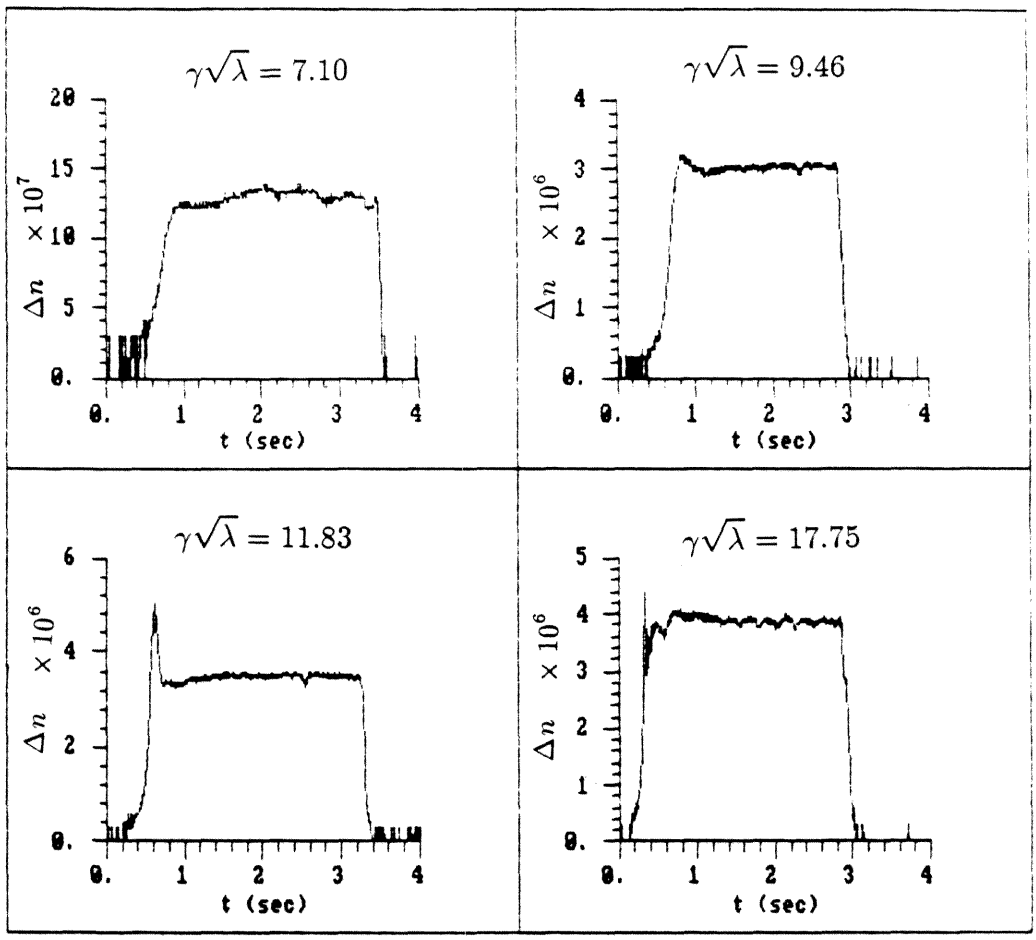
$\gamma\sqrt{\lambda} = 7.10$
$\Delta n \times 10^7$
t (sec)
$\gamma\sqrt{\lambda} = 9.46$
$\Delta n \times 10^6$
t (sec)
$\gamma\sqrt{\lambda} = 11.83$
$\Delta n \times 10^6$
t (sec)
$\gamma\sqrt{\lambda} = 17.75$
$\Delta n \times 10^6$
t (sec)

Fig. 13(b)

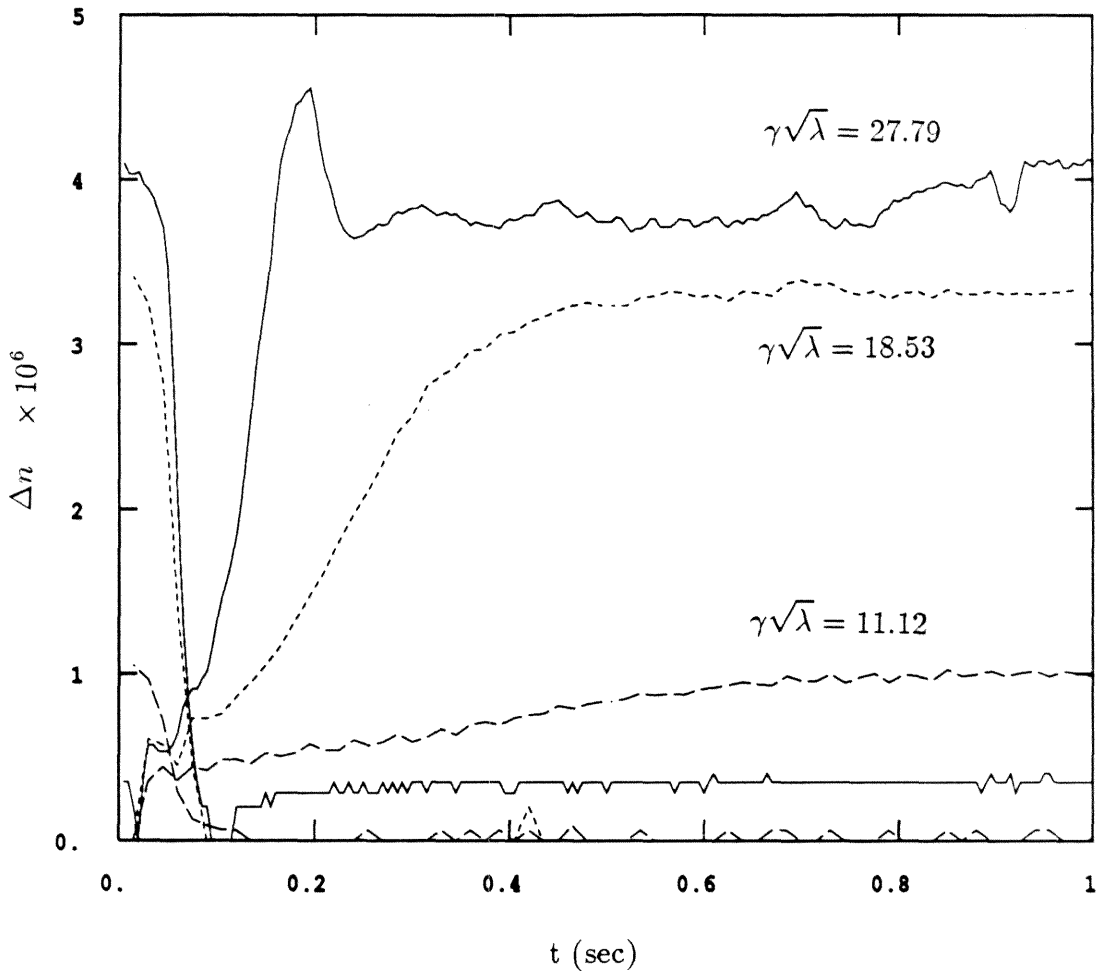
5
4
3
2
1
0.
$\Delta n \times 10^6$
$\gamma\sqrt{\lambda} = 27.79$
$\gamma\sqrt{\lambda} = 18.53$
$\gamma\sqrt{\lambda} = 11.12$
0.
0.2
0.4
0.6
0.8
1
t (sec)

Fig. 14(a)

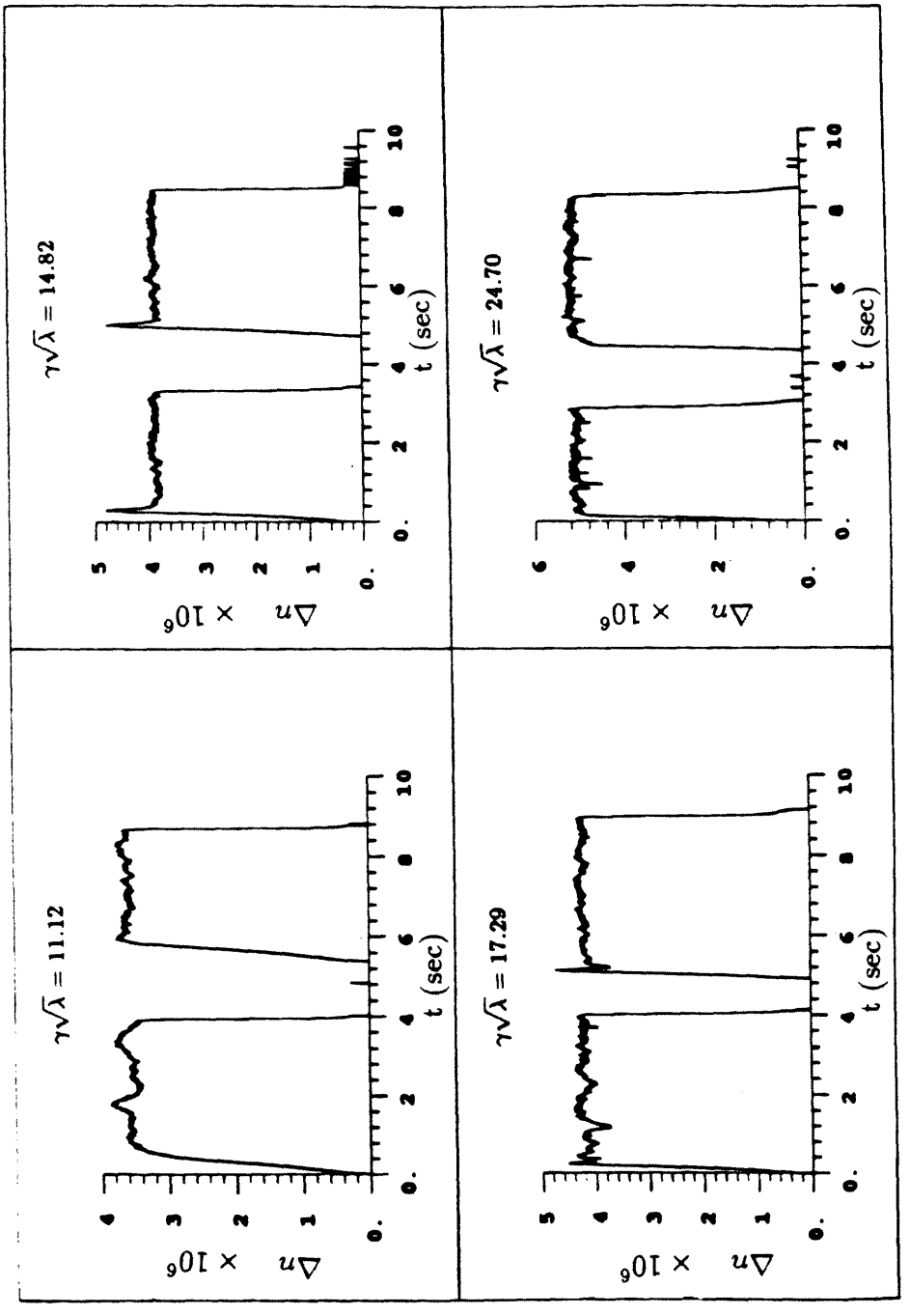
$\gamma\sqrt{\lambda} = 14.82$
$\gamma\sqrt{\lambda} = 24.70$
$\gamma\sqrt{\lambda} = 11.12$
$\gamma\sqrt{\lambda} = 17.29$
$\Delta n \times 10^6$
t (sec)

Fig. 14(b)

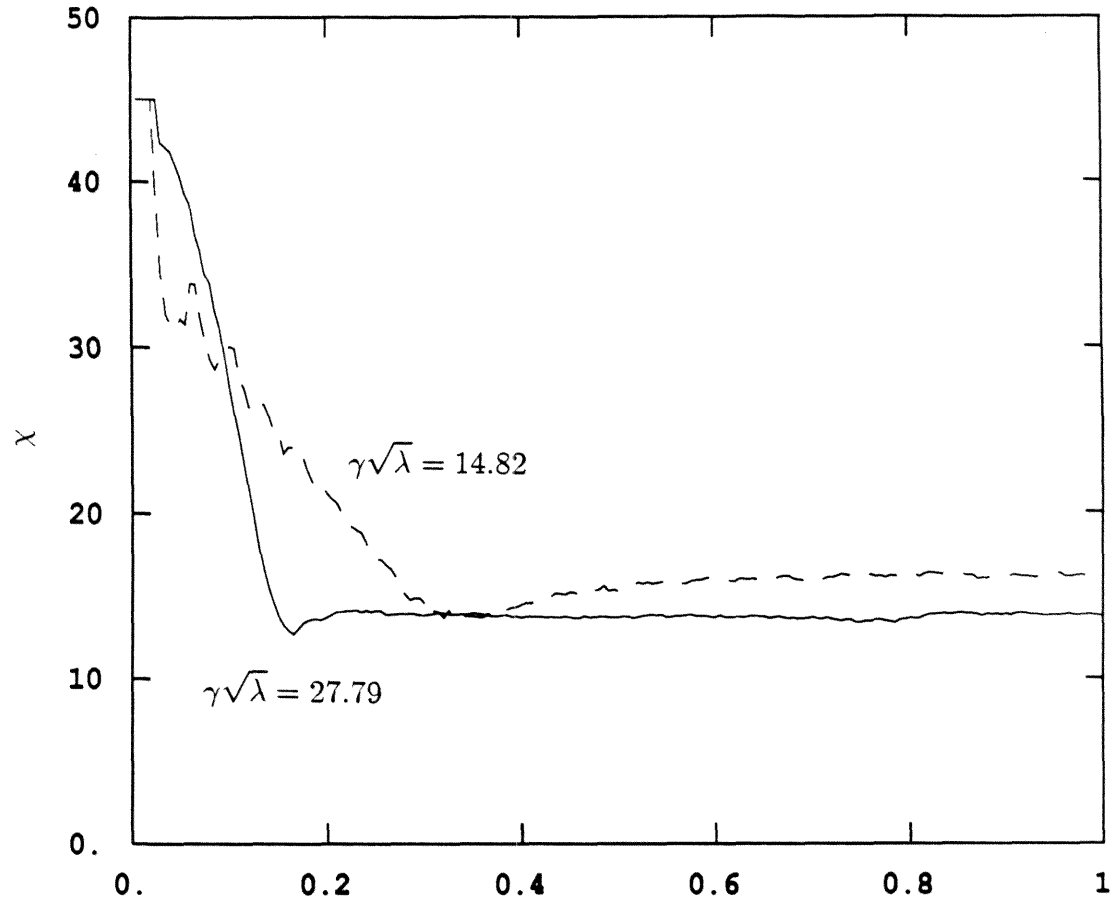
50
40
30
20
10
0.
0.
0.2
0.4
0.6
0.8
1
χ
$\gamma\sqrt{\lambda} = 14.82$
$\gamma\sqrt{\lambda} = 27.79$

Fig. 15(a)

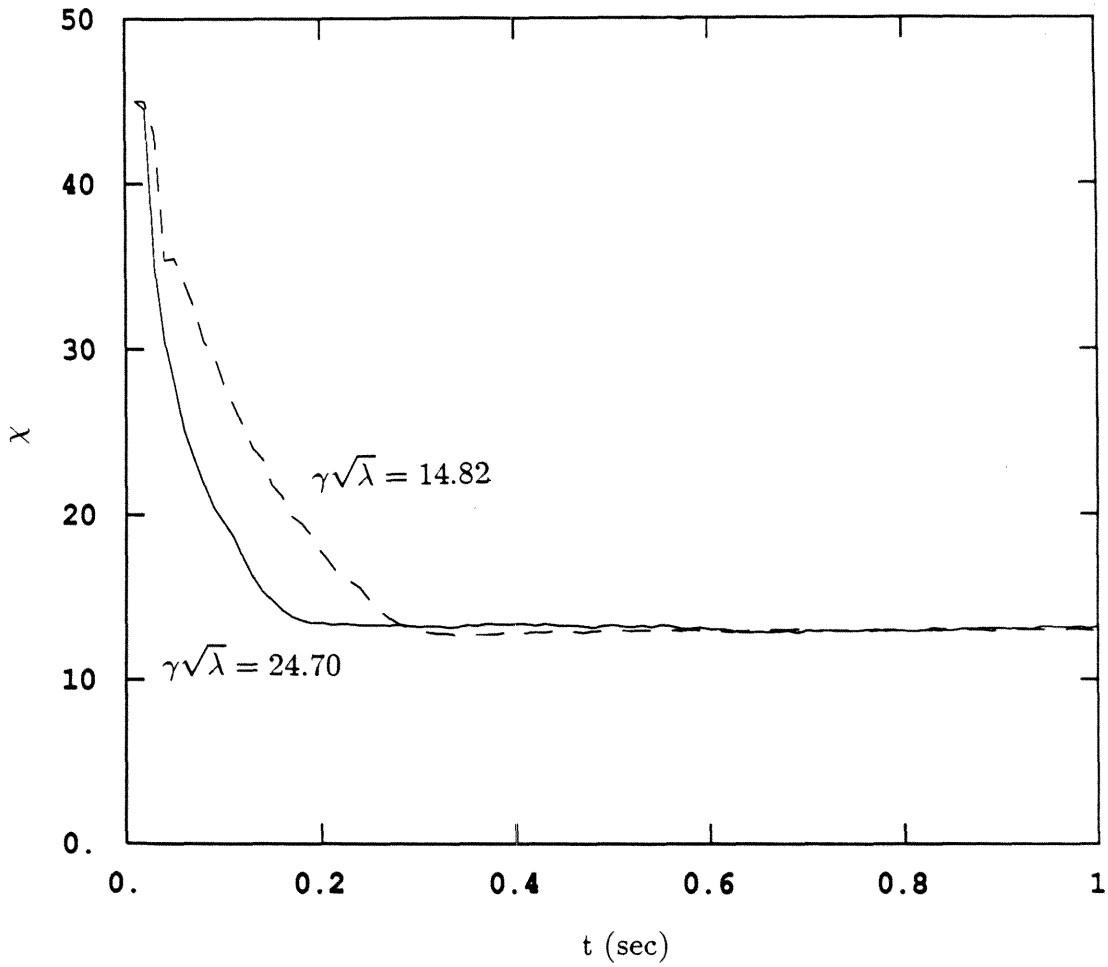
50
40
30
20
10
0.
χ
$\gamma\sqrt{\lambda} = 14.82$
$\gamma\sqrt{\lambda} = 24.70$
0.
0.2
0.4
0.6
0.8
1
t (sec)

Fig. 15(b)

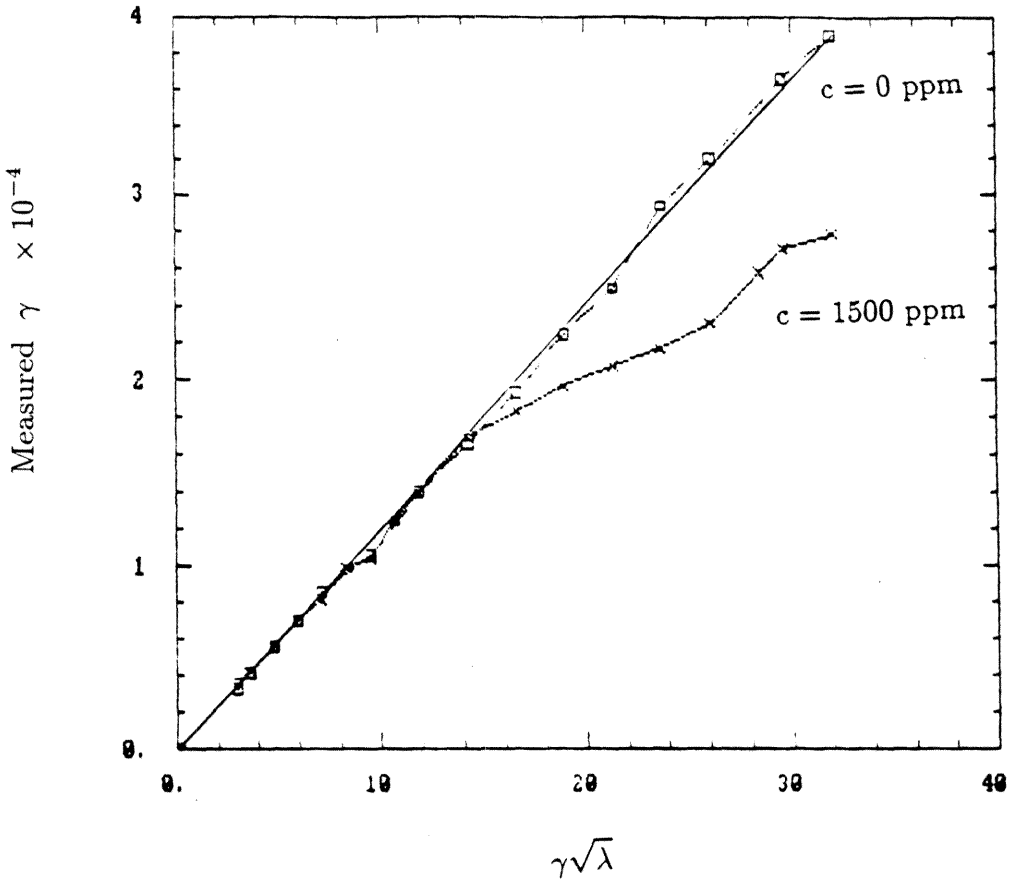
4
3
2
1
0.
0.
10
20
30
40
c = 0 ppm
c = 1500 ppm
Measured $\gamma \times 10^{-4}$
$\gamma\sqrt{\lambda}$

Fig. 16(a)

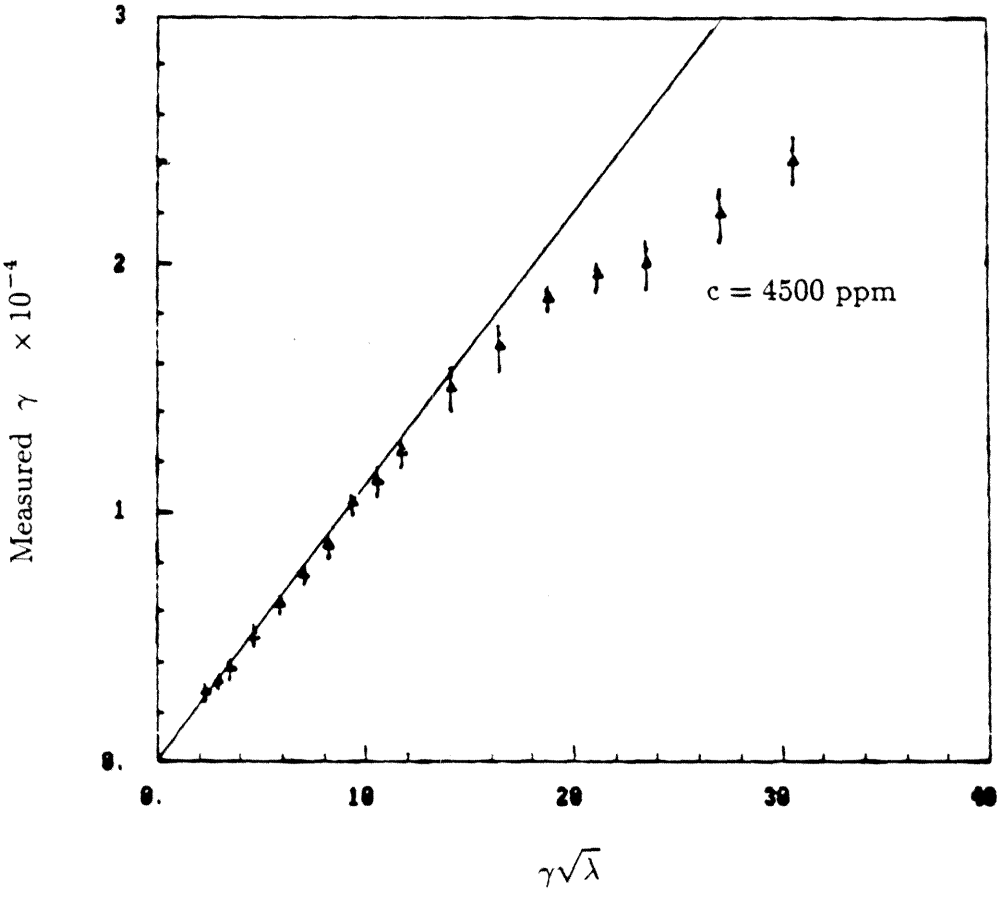

Fig. 16(b)

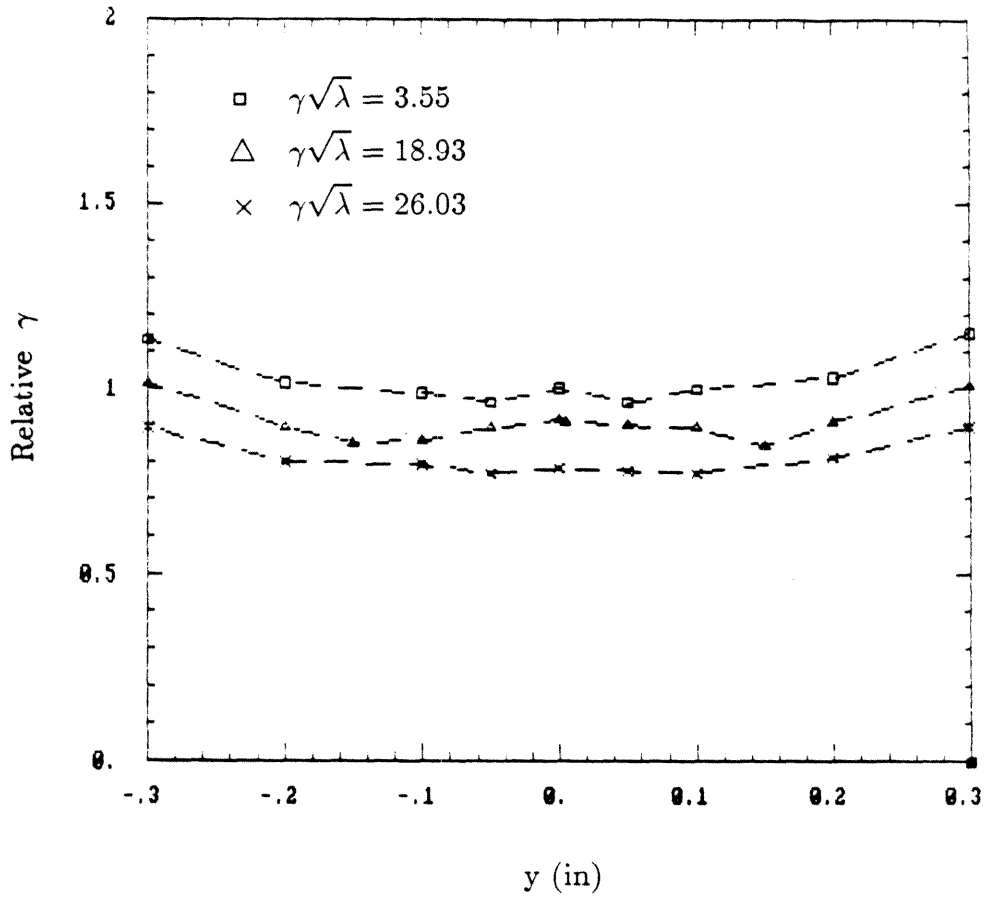

Fig. 17(a)

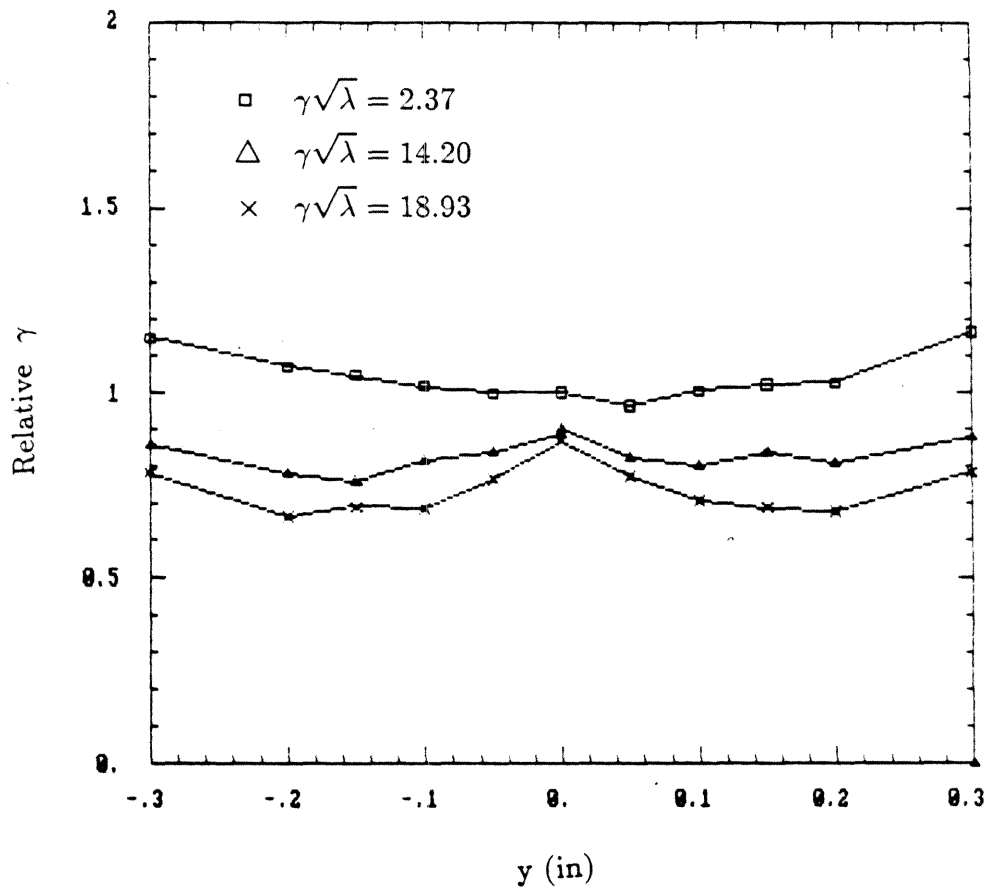

Fig. 17(b)

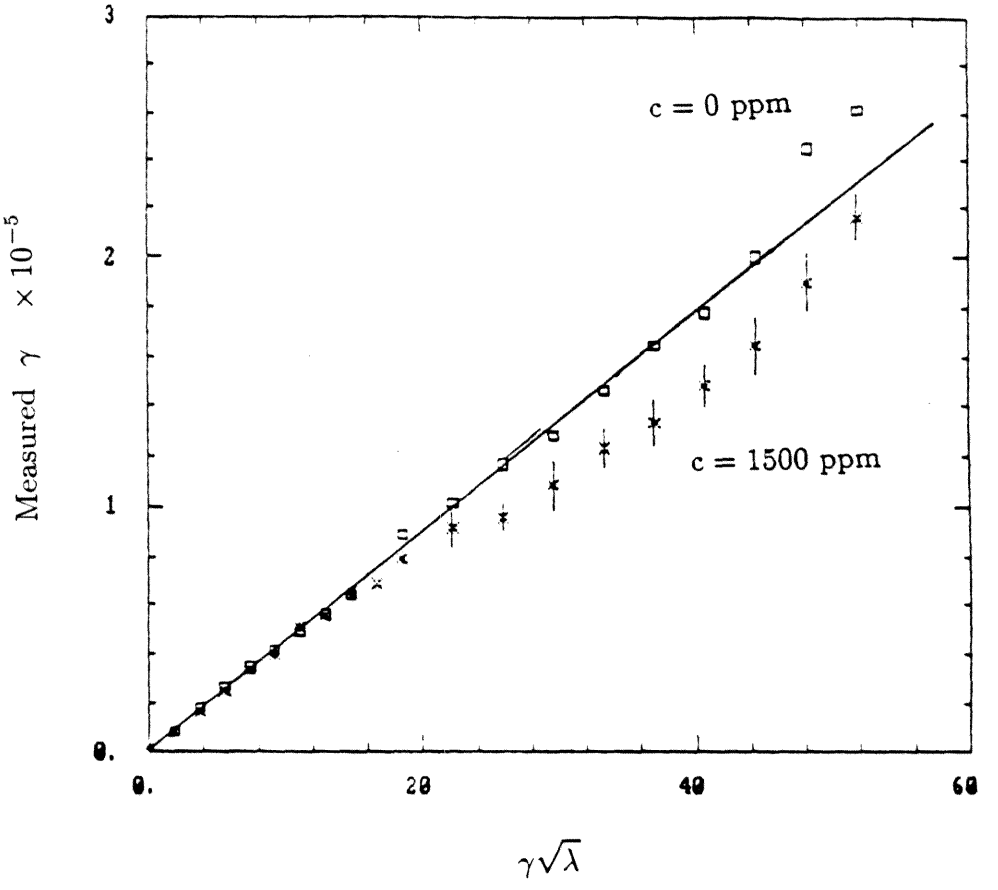
c = 0 ppm
c = 1500 ppm
Measured γ $\times 10^{-5}$
$\gamma\sqrt{\lambda}$
0.
1
2
3
0.
20
40
60

Fig. 18(a)

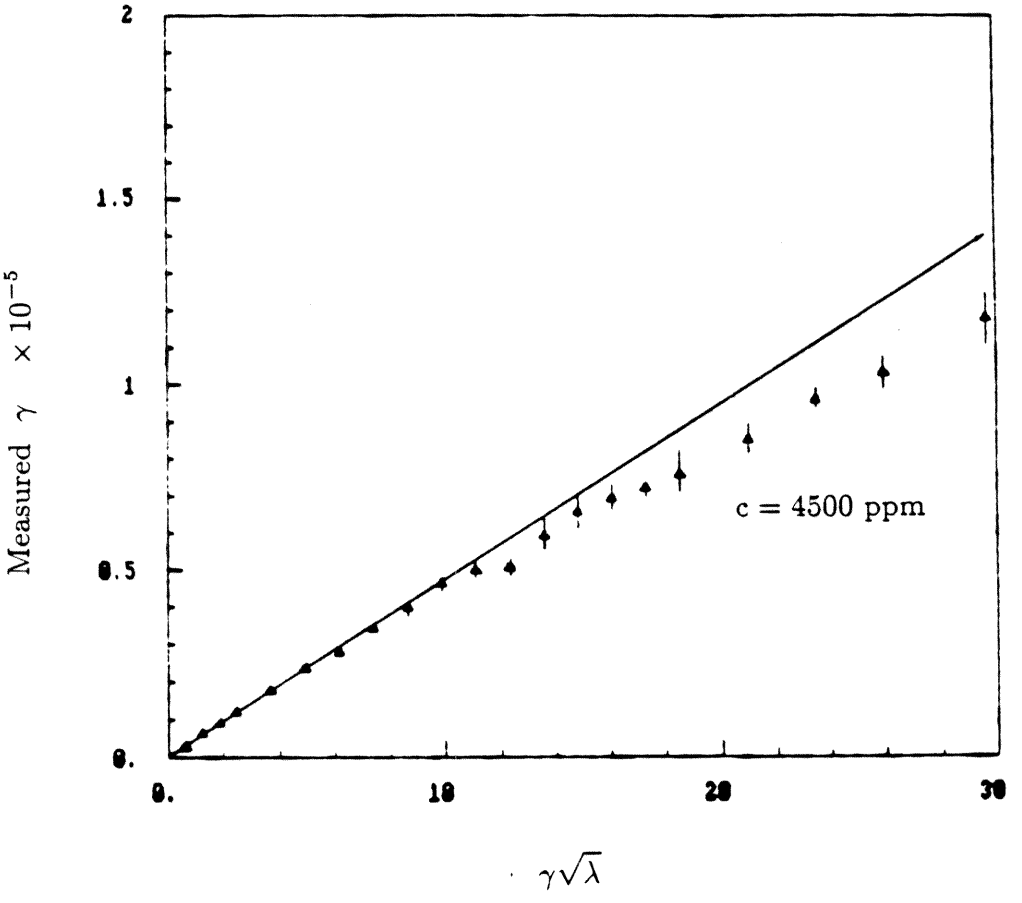
2
1.5
1
0.5
0.
0.
10
20
30
Measured $\gamma \times 10^{-5}$
$\gamma\sqrt{\lambda}$
c = 4500 ppm

Fig. 18(b)

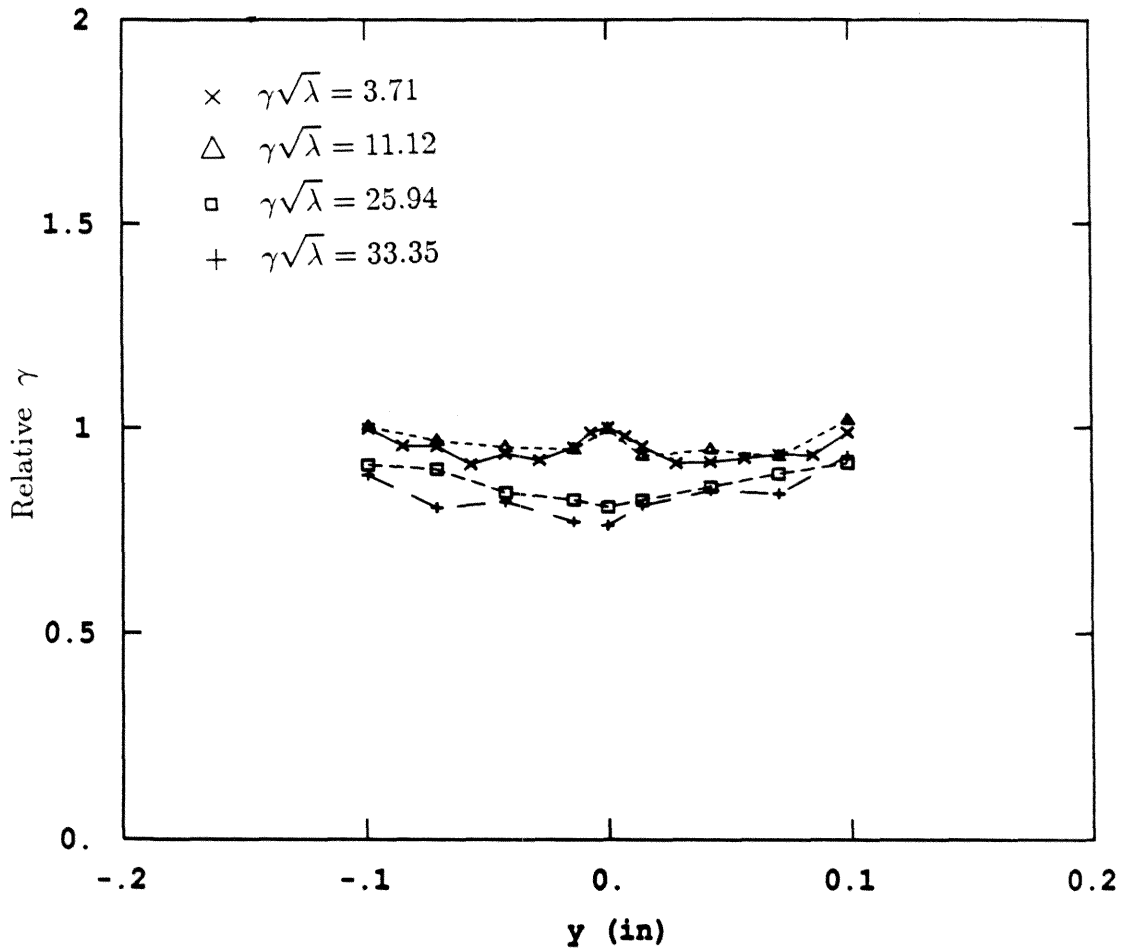

Fig. 19(a)

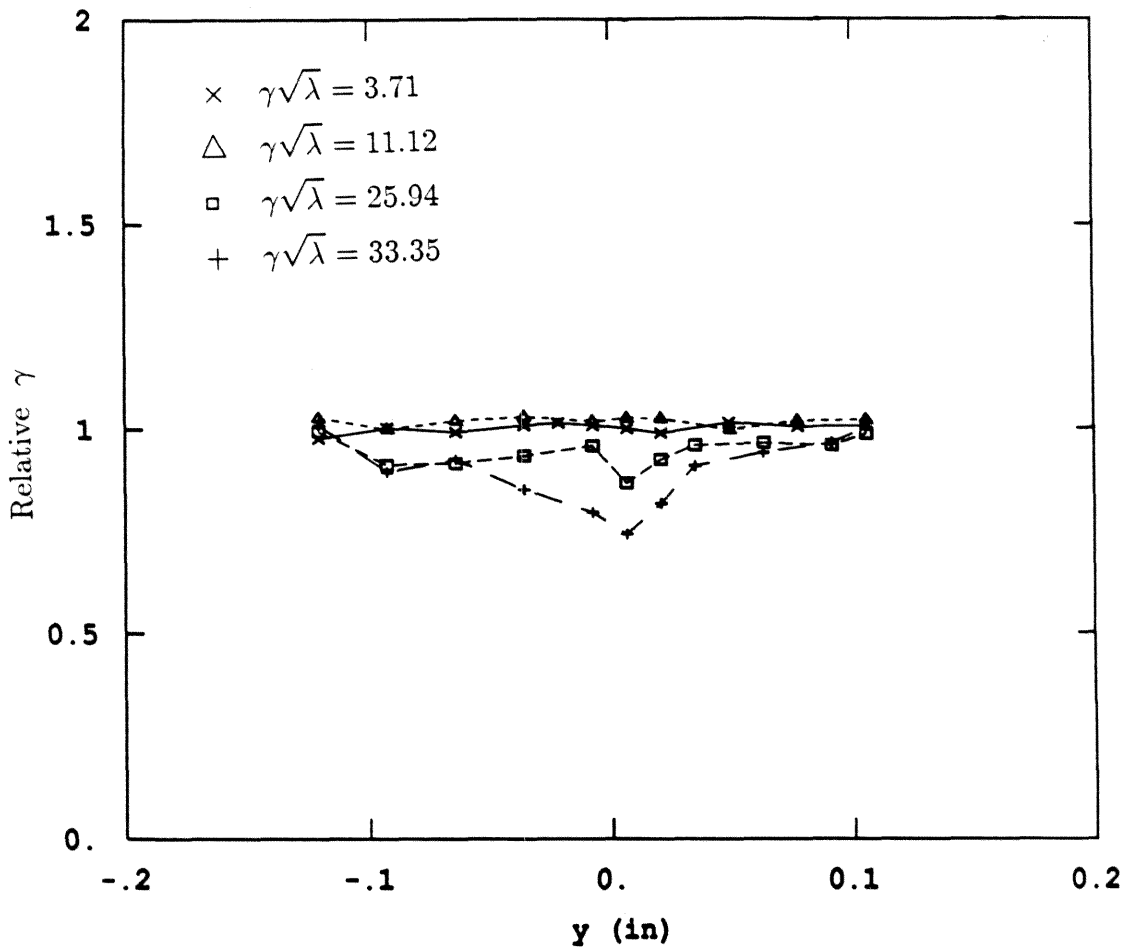
2
1.5
1
0.5
0.
Relative γ
$\times$ $\gamma\sqrt{\lambda} = 3.71$
$\triangle$ $\gamma\sqrt{\lambda} = 11.12$
$\square$ $\gamma\sqrt{\lambda} = 25.94$
$+$ $\gamma\sqrt{\lambda} = 33.35$
-.2
-.1
0.
0.1
0.2
y (in)

Fig. 19(b)

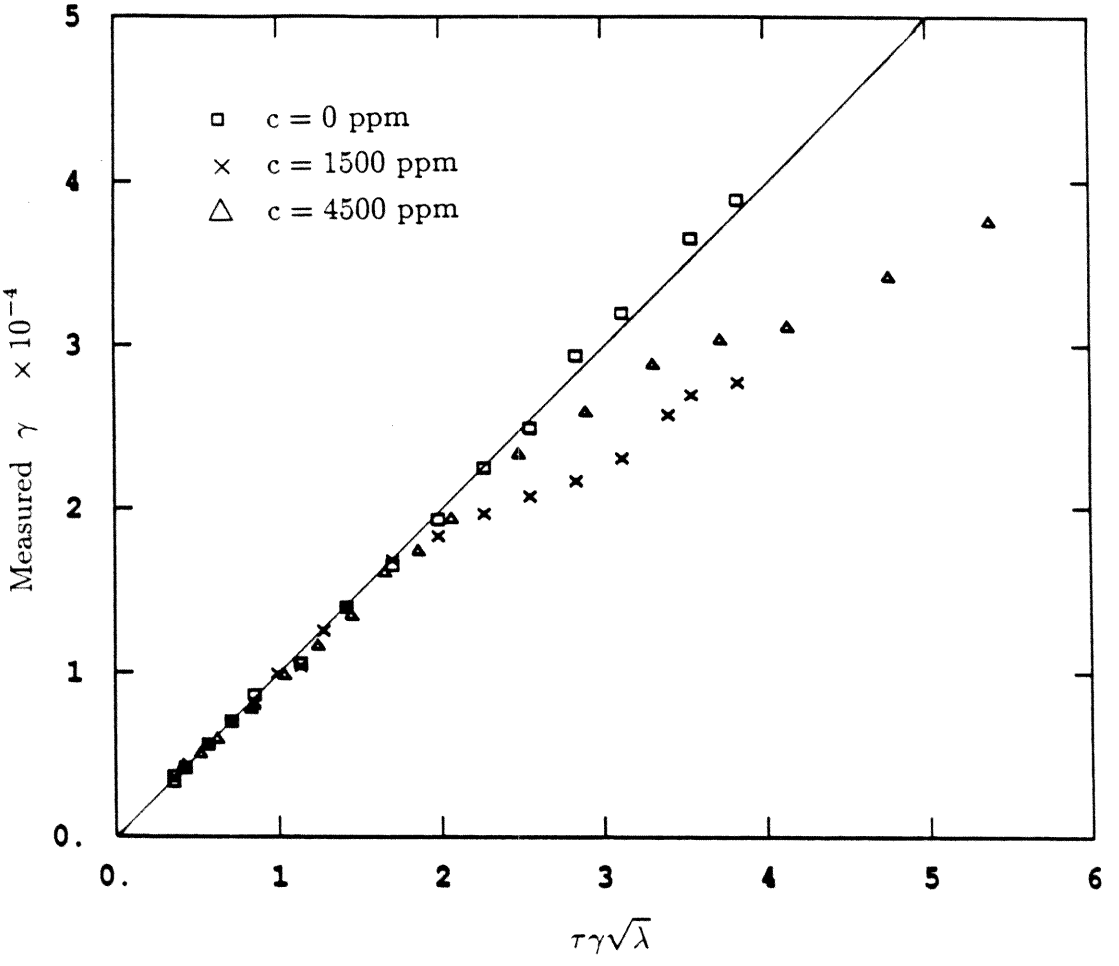
c = 0 ppm
c = 1500 ppm
c = 4500 ppm
Measured γ $\times 10^{-4}$
$\tau\gamma\sqrt{\lambda}$
0.
1
2
3
4
5
6

Fig. 20(a)

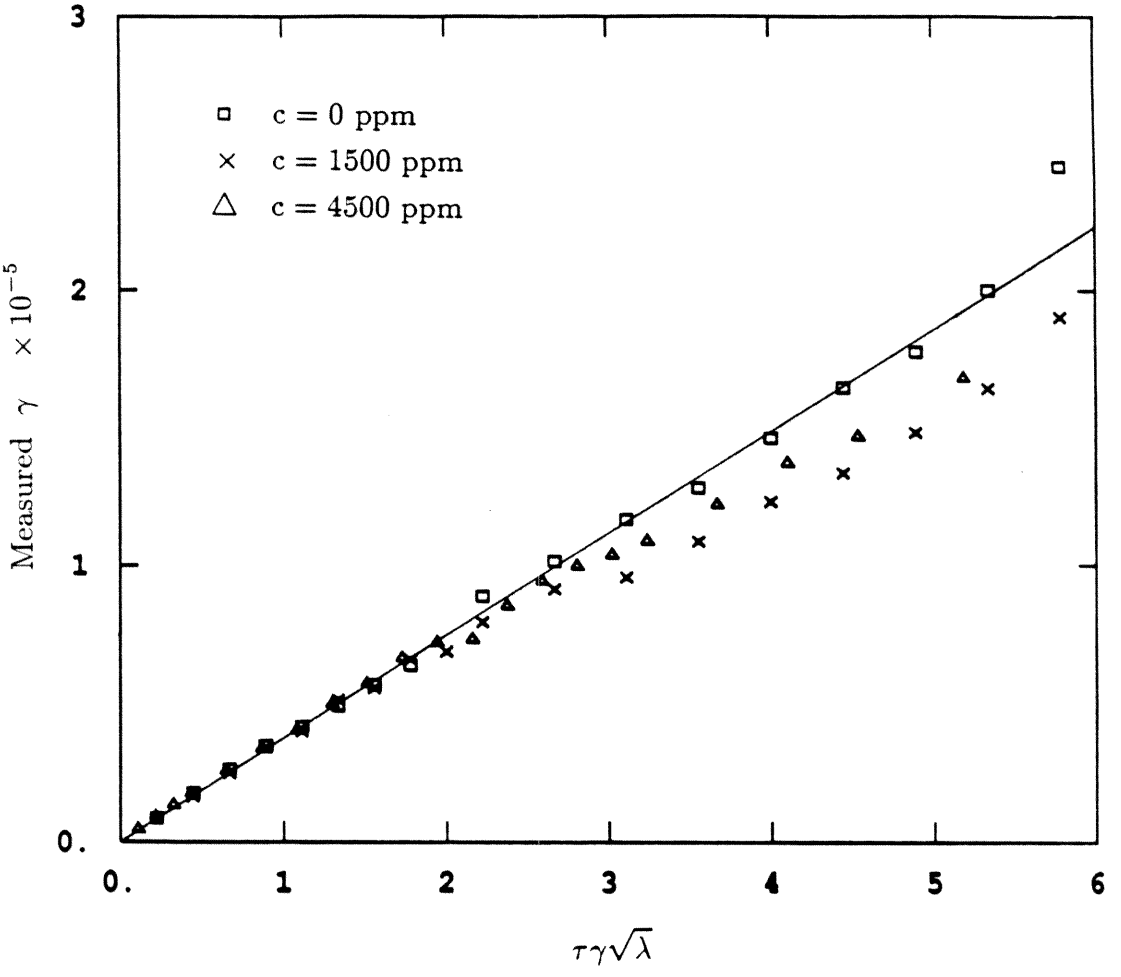
c = 0 ppm
c = 1500 ppm
c = 4500 ppm
Measured γ $\times 10^{-5}$
$\tau\gamma\sqrt{\lambda}$
0.
1
2
3
4
5
6
0.
1
2
3

Fig. 20(b)

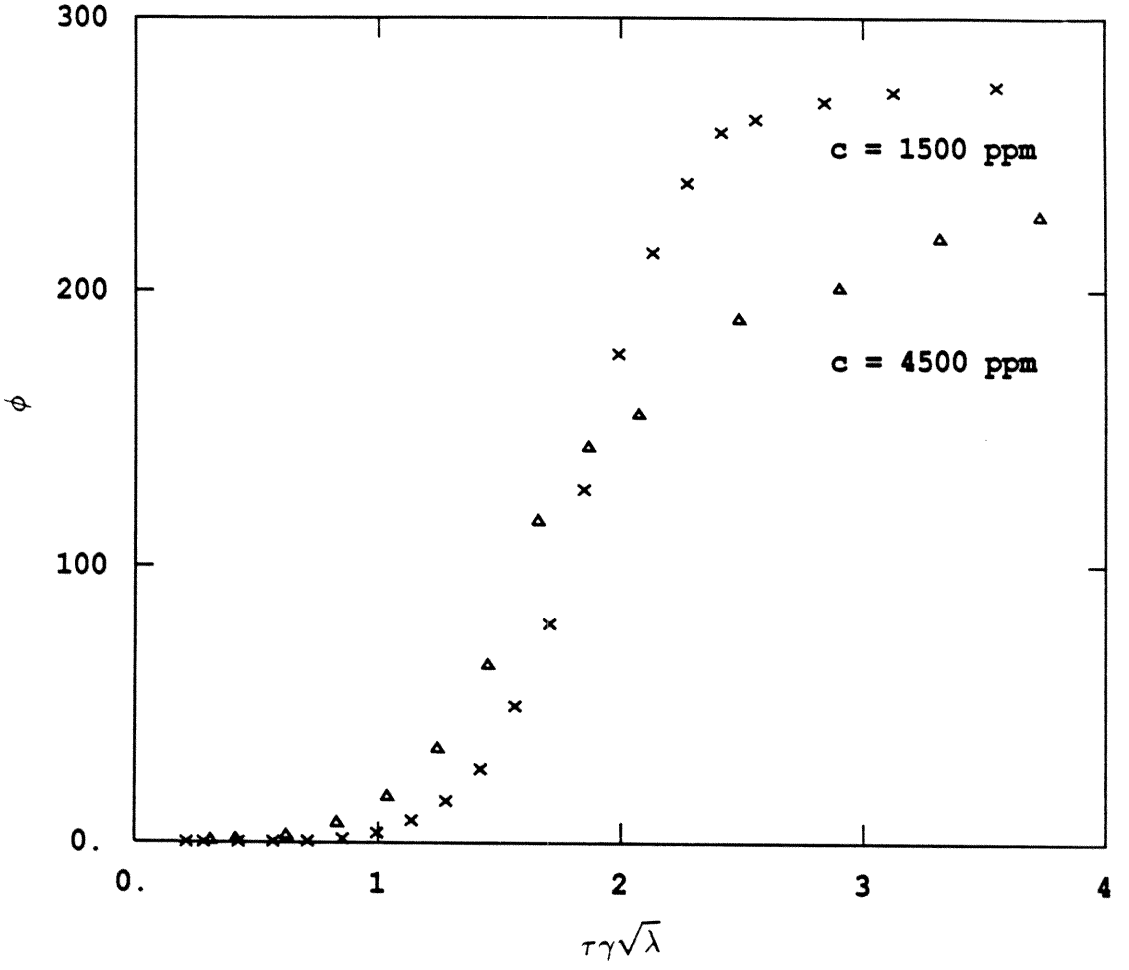
300
200
100
0.
0.
1
2
3
4
ϕ
$\tau\gamma\sqrt{\lambda}$
c = 1500 ppm
c = 4500 ppm

Fig. 21

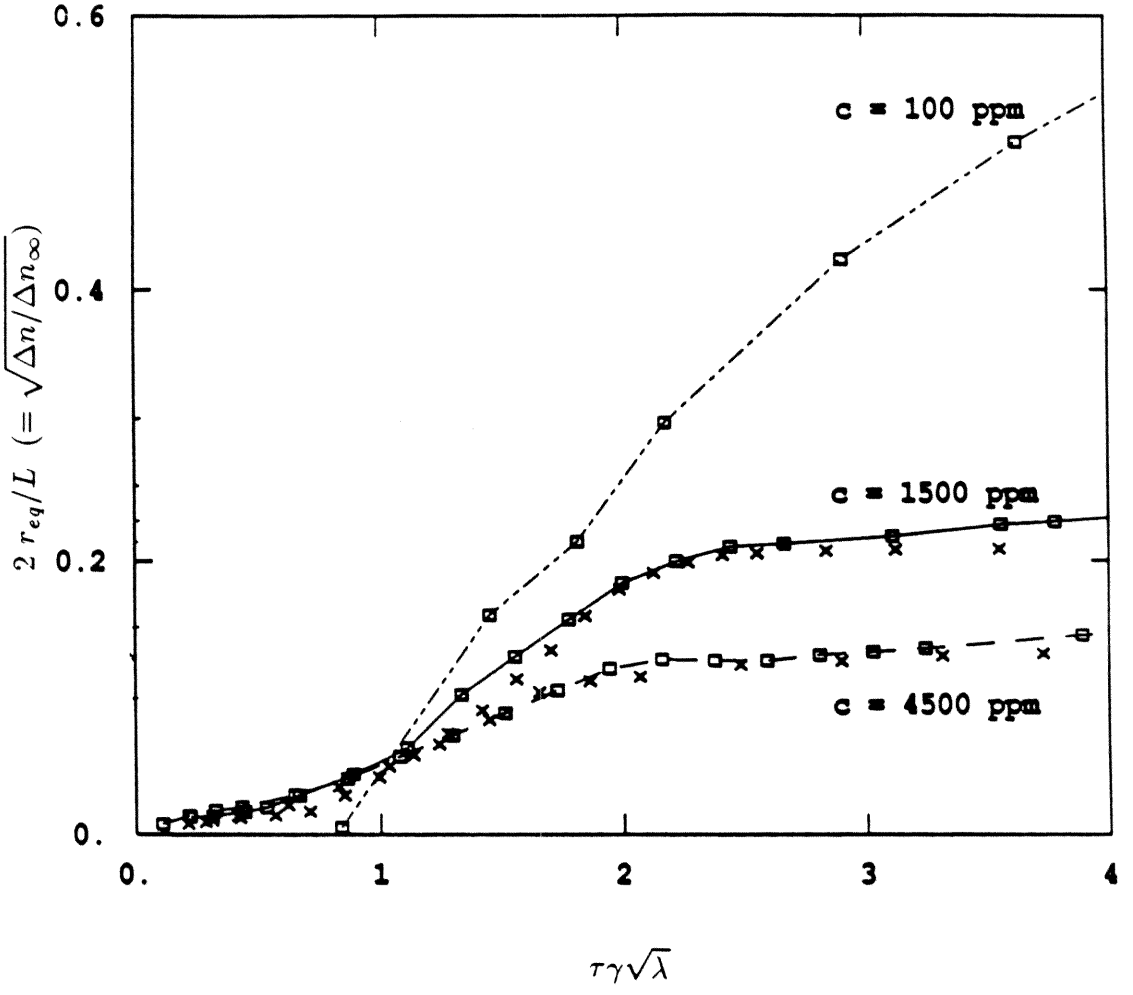
0.6
0.4
0.2
0.
0.
1
2
3
4
c = 100 ppm
c = 1500 ppm
c = 4500 ppm
$2\,r_{eq}/L\ (=\sqrt{\Delta n/\Delta n_\infty})$
$\tau\gamma\sqrt{\lambda}$

Fig. 22

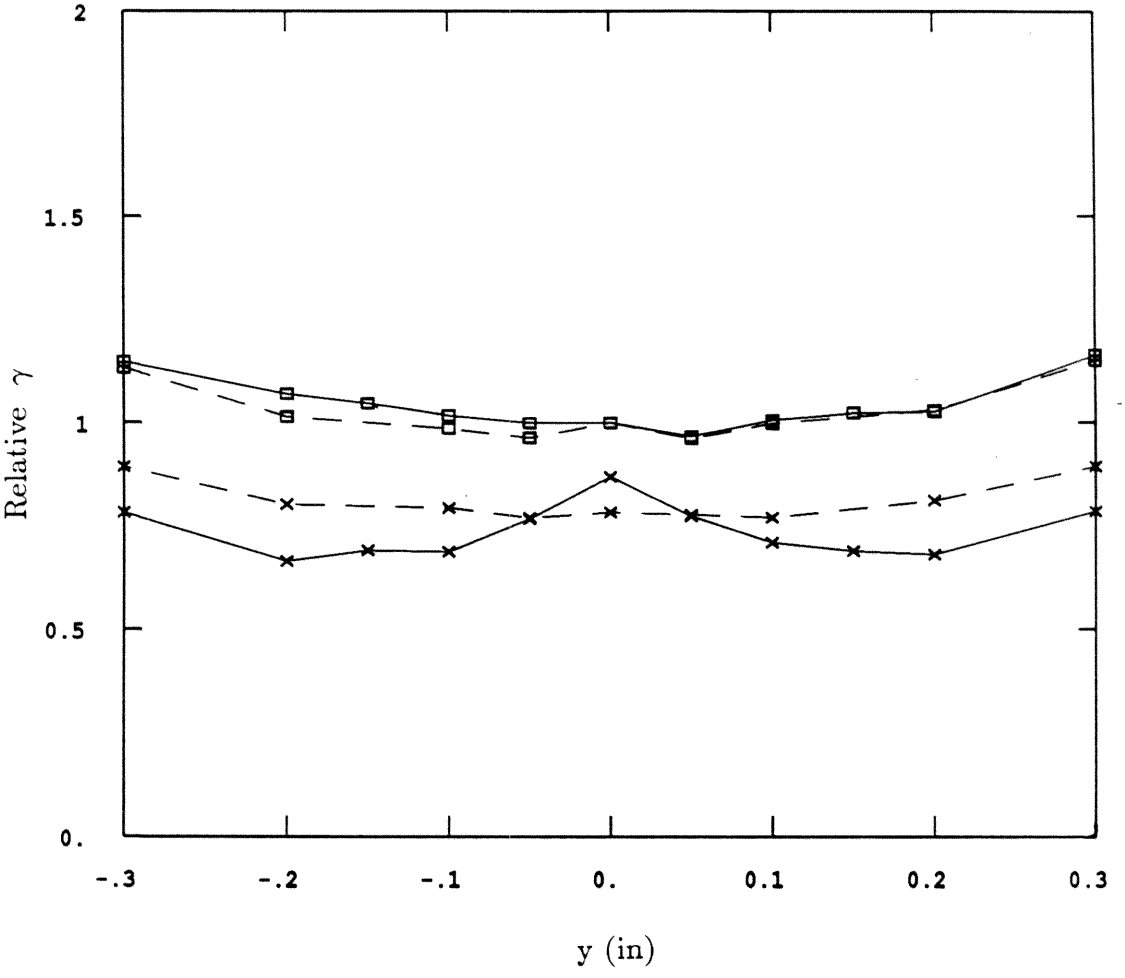

Fig. 23

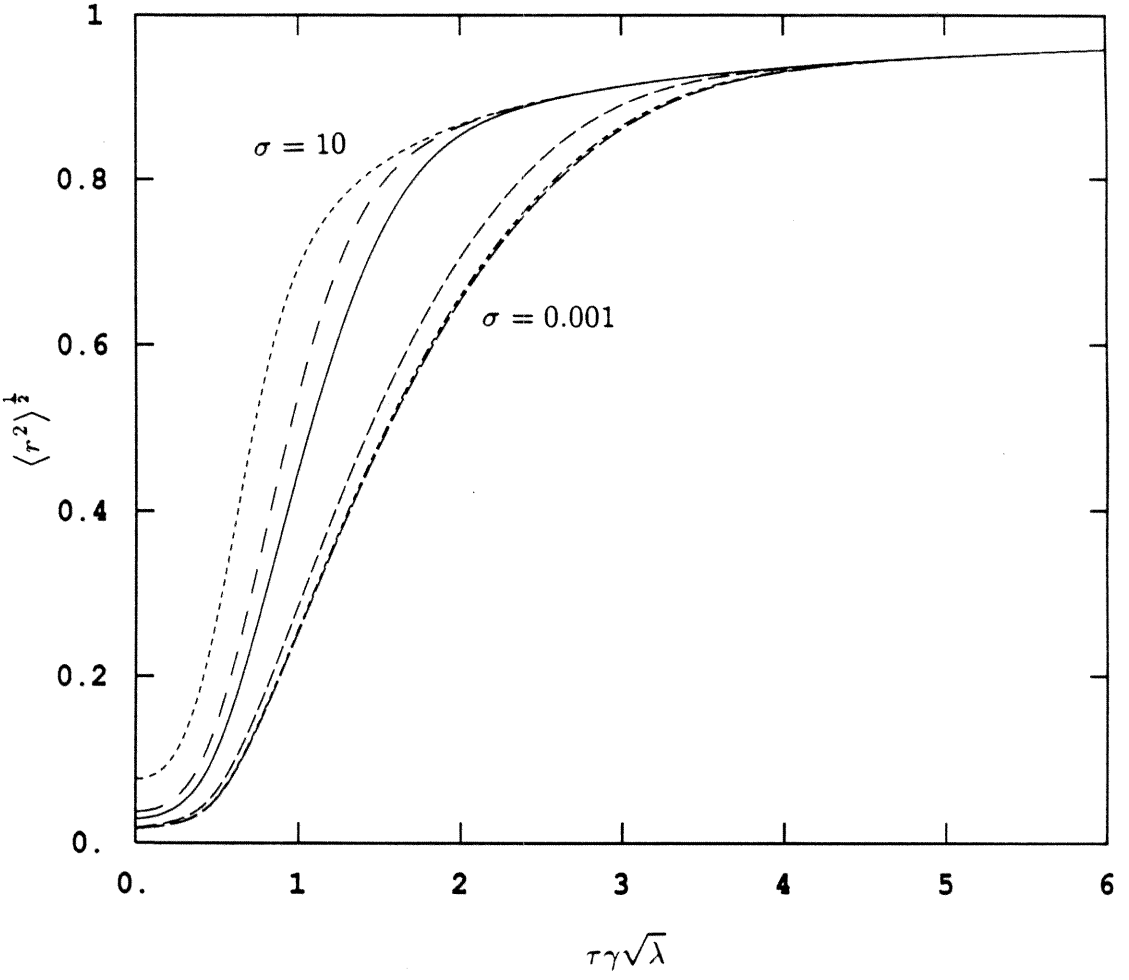
1
0.8
0.6
0.4
0.2
0.
0.
1
2
3
4
5
6
$\sigma = 10$
$\sigma = 0.001$
$\langle r^2 \rangle^{\frac{1}{2}}$
$\tau\gamma\sqrt{\lambda}$

Fig. 24

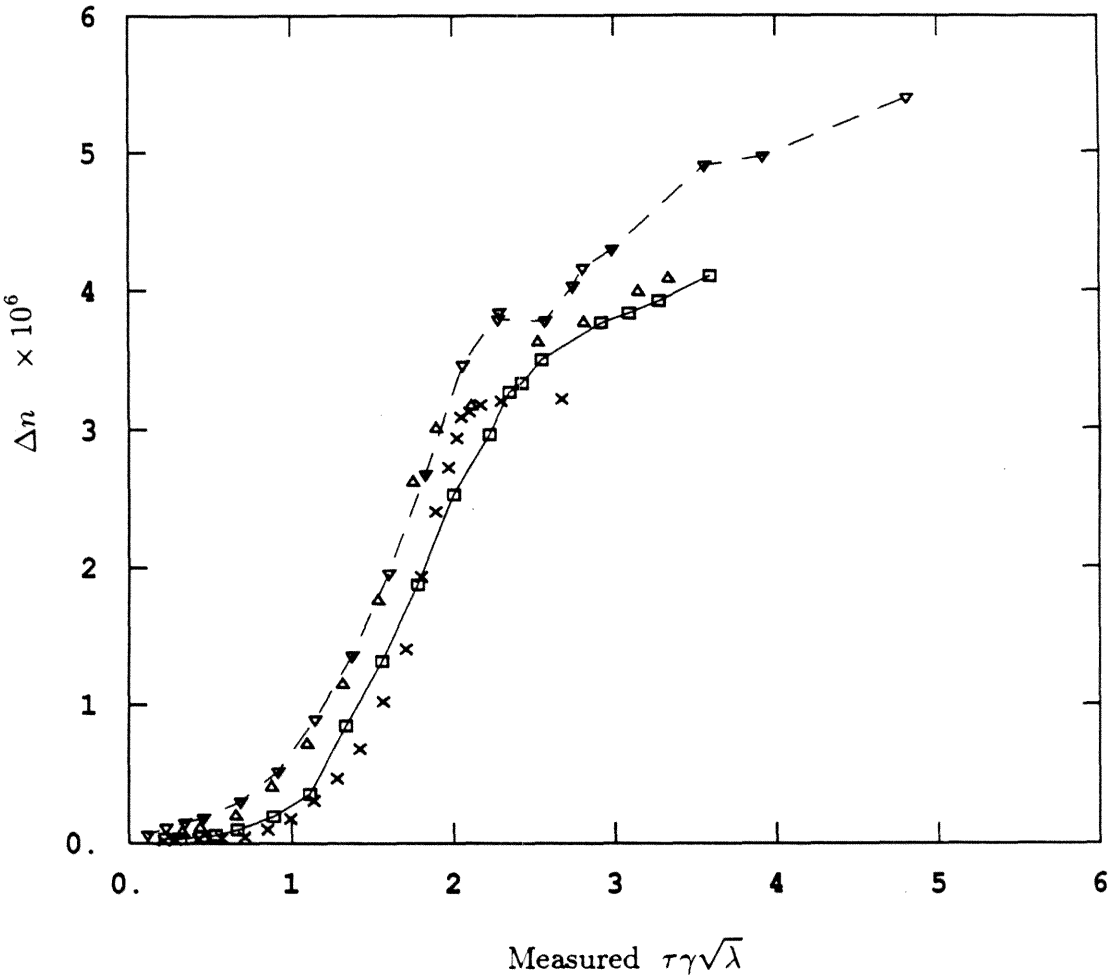
6
5
4
3
2
1
0.
$\Delta n \times 10^6$
0.
1
2
3
4
5
6
Measured $\tau\gamma\sqrt{\lambda}$

Fig. 25

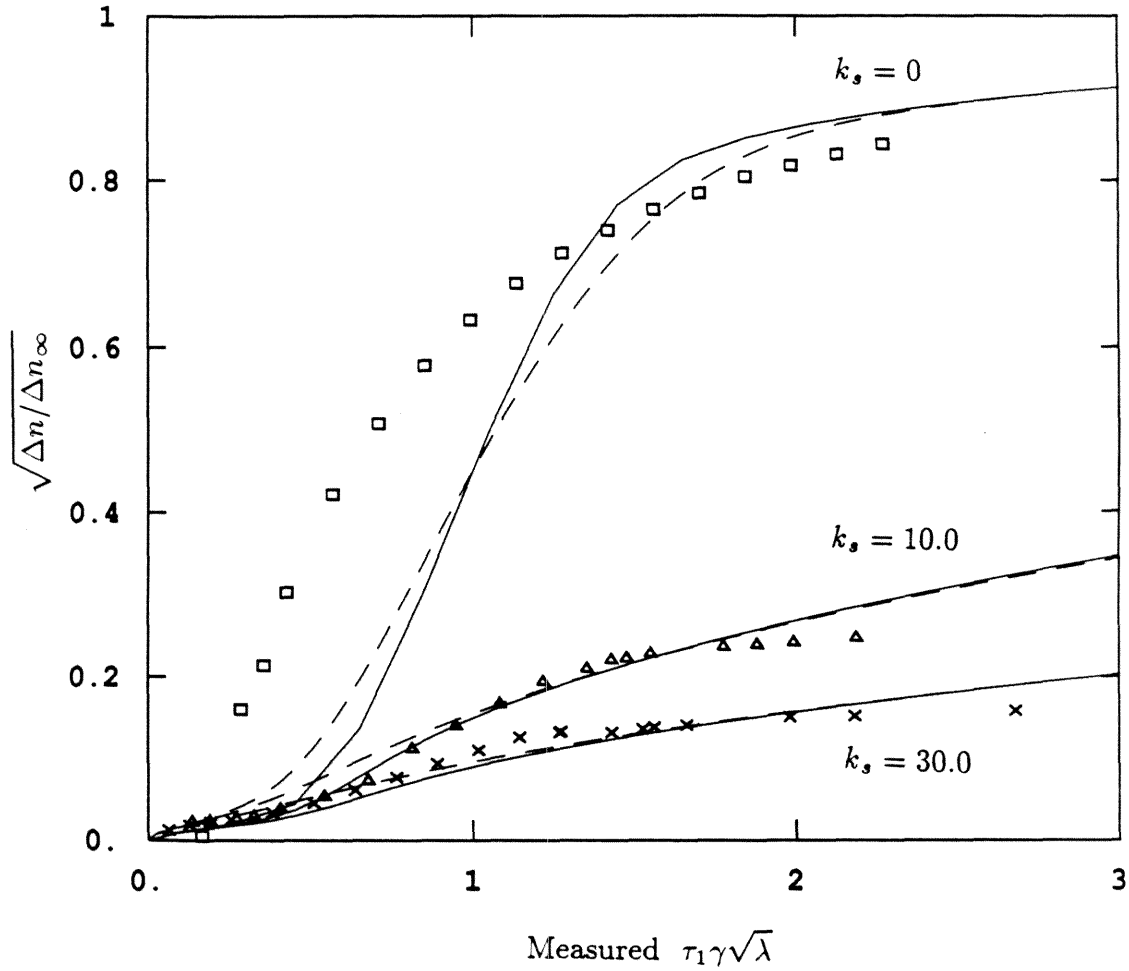
1
0.8
0.6
0.4
0.2
0.
0.
1
2
3
$\sqrt{\Delta n/\Delta n_\infty}$
$k_s = 0$
$k_s = 10.0$
$k_s = 30.0$
Measured $\tau_1 \gamma \sqrt{\lambda}$

Fig. 26

Chapter II

An Interacting FENE Dumbbell Model for Semi-Dilute Polymer Solutions in Extensional Flows

An Interacting FENE Dumbbell Model for Semi-Dilute Polymer Solutions in Extensional Flows

R. C.-Y. Ng*

Department of Chemical Engineering
California Institute of Technology
Pasadena, California 91125

and L. G. Leal†

Department of Chemical & Nuclear Engineering
University of California
Santa Barbara, California 93106

* Present address: Mobil Research and Development Corp., Dallas Research Laboratory, Dallas, TX 75244-4312, U.S.A.

† To whom all correspondence should be addressed.

Abstract

The effect of polymer concentration on the rheological properties of semi-dilute polymer solutions in extensional flows is studied with a *nonlinear* molecular theory. The theory is based on a elastic dumbbell model for interacting dumbbells proposed by Hess [16]. The elastic restoring force of a dumbbell is modeled by using a nonlinear *Warner* spring (FENE dumbbell) which replaces the linear *Hookean* spring originally in Hess's interacting dumbbell (IDB) model. The conformation change of polymer is shown to be a decreasing function of concentration. High concentration tends to inhibit large extension of polymer due to direct polymer-polymer interaction. The Hookean spring in the original IDB model has resulted in stretching of polymer chain beyonds its maximum contour length for large strain rates in extensional flows. When the nonlinear FENE dumbbell is incorporated into the IDB model, the defect of the Hookean spring disappears. A smooth transition of dilute solution behavior to semi-dilute solution behavior is obtained with this FENE-IDB model. The mean square end-to-end length of the polymer has the same prediction as the flow birefringence. The specific birefringence is proportional to c^{-1} for semi-dilute solutions when plotted versus the dimensionless eigenvalue of the velocity gradient tensor, $\theta\gamma'\sqrt{\lambda}$, but it is independent of concentration for dilute solutions as expected. For semi-dilute solutions, the characteristic relaxation time for the polymer, θ, is also a linear function of concentration. The flow birefringence is predicted to increase linearly with $\gamma'\sqrt{\lambda}$ in the semi-dilute solution regime for a wide range of shear rates. All these predictions agree qualitatively with some experimental observations [15,23,24].

1. Introduction

The dynamics of polymer molecules in shearing flows have been widely studied by modeling the polymer as an elastic dumbbell [1,2,3]. Bird and coworkers [4] have shown detailed derivations of the equations of change for polymer conformation and rheological properties of polymeric fluids using the dumbbell model. Although the dumbbell model is crude in the sense that the polymer molecule is modeled by just two beads connected by a spring (versus the bead-spring chain model such as the Rouse model [5]), it has proven successful in predicting the dynamical behavior of polymer solutions in both simple shear flows and extensional flows when compared with experimental data [6,7,8]. Most of the aforementioned models were applied to isolated polymer chains in a dilute polymer solution. When the concentration becomes larger, intermolecular interactions need to be considered.

Earlier molecular models such as the temporary network model, which originates from Yamamoto's network theory [9] for entangled polymer systems, describe the polymer-polymer interaction solely in terms of entanglement junction formation and destruction with various empirical formulae used to model the details of these processes [10,11]. There is no simple basis to account for concentration effects on the rheological properties of polymers within the context of the network model. Its application is restricted largely to concentrated polymer solutions and melts where the entanglement effect is dominant. The reptation model proposed by Doi and Edwards [12] has similar limitation in its applicability. In the reptation model, the interactions between polymers in a concentrated solution are effectively reduced to the description of the dynamics of a single *reptating chain* in a *tube*, though no detailed microscopic description is given of the interactions (or entanglements) of the *confined* single chain with other polymer molecules. Another proposal to describe non-dilute solutions is the encapsulated dumbbell model pro-

posed by Bird and DeAguiar [13,14]. This model also incorporates the reptation concept by describing the intermolecular interactions between a test chain and its neighbours with an anisotropic friction force and anisotropic Brownian mobility. However, it gives similar predictions to the dilute solution dumbbell model in extensional flow, and this result appears to disagree with recent experimental observations in our laboratory [15]. In summary, then, the utility of these existing molecular models for moderately concentrated polymer solutions is quite limited, especially in elongational flows where the polymer can be subjected to large deformations, and in the absence of any basis to account explicitly for the concentration dependence of the interaction of the test chain with other polymer molecules.

Recently, however, Hess [16] has proposed an interacting dumbbell (IDB) model for moderately concentrated (semi-dilute) polymer solutions which includes an explicit interaction force to account for concentration effects. The assumed existence and the form of the interaction principles are both *ad hoc*, but the mean field approximation for the resulting force on a *test* dumbbell is rigorous. The model leads to an explicit concentration dependence in the rheological functions such as birefringence and stress. It can also provide a description of transition in the dynamical behavior of a polymer solution as we go from dilute to semi-dilute solution concentrations. One limitation of the model, however, is that Hess used a linear *Hookean* spring to describe the *elastic* effect of the polymer in flows. In the dilute limit, this feature of the model is known to have limited application especially for modeling polymer dynamics in strong flows. In particular, the Hookean dumbbell is predicted to extend beyond its maximum contour length at high strain rates. This unrealistic result can be circumvented by replacing the linear spring with a nonlinear one. The nonlinear spring that will be used in the present study is the *Warner* spring [17] which has been discussed extensively in Ref. 3 for the finitely extensible nonlinear elastic (FENE) dumbbell model with constant friction coefficient and Warner spring. The Warner spring provides an infinitely large

spring force when the polymer is being stretched by the flow to near its maximum extension. Thus, the polymer can no longer extend beyond its maximum length. The purpose of this paper is to explore the effect of the Warner spring on the IDB model for polymer solutions with concentration in the dilute to semi-dilute regime. The type of flow field that we are interested in is the so-called *strong* flows in the sense that exponential stretching of the polymer is possible in these flows, which have a strain rate greater than vorticity.

Here, we will first examine the IDB model in homogeneous flows with a spring contribution given by either the Hookean or the Warner spring. The equation of change for the dumbbell configuration and the polymer stress tensor will be presented. Then, we will derive the rheological equations for general two-dimensional (2-D) linear flows ranging from pure rotational flow, to simple shear flow, and to pure extensional flow. Next, asymptotic and numerical results for the end-to-end length of the polymer and flow birefringence are presented for the IDB model with Hookean spring in 2-D extensional flows. The motivation for considering these 2-D *strong* flows is that this type of flow can be generated approximately in the 2-roll and 4-roll mill, so that comparison with experiments can be performed readily [8]. This part of the work is similar to Hess's results on uniaxial extensional flows. The difference is that the defect of the interacting Hookean dumbbell is clearly shown here but not in Hess's paper [16]. Finally, we will present asymptotic results for polymer conformation and flow birefringence using the IDB model with the nonlinear Warner spring (FENE-IDB model). This modified version of Hess's model for dilute to semi-dilute polymer solutions shows significantly improved predictions for the polymer dynamics in these strong flows. Numerical simulation is also presented for the birefringence and orientation of polymer in the same flows. The predictions agree in general with experimental results for semi-dilute polymer solutions in extensional flows by other investigators. Our results also show that a smooth transition from dilute to semi-dilute solution behavior can be obtained

with the improved model.

2. Development of the Model

Hess [16] has developed a dumbbell model with linear spring and constant bead friction for semi-dilute polymer solutions by incorporating the effect of finite concentration into the dilute dumbbell model via an interaction force term. The pair-wise interaction between beads of different dumbbells is modeled as a *conservative interaction potential.* By using a mean field approximation, an effective one-particle potential is obtained which depends on the end-to-end vector, $\mathbf{r}$, of a test dumbbell and on concentration. This interaction force is intended to account for all interactions among polymer chains which could include close contact forces or even topological entanglements when polymer concentration approaches the critical overlap concentration $c^\star$ at equilibrium. Since the model was derived by neglecting higher order terms in the multipole expansion for the interaction force, it should be applied to dilute to semi-dilute solutions whose concentrations are below the critical concentration $c^\star$.

The interaction force $\tilde{\mathbf{F}}_c$ acting on the test dumbbell by the external potential is then given by [16]

$$\tilde{\mathbf{F}}_c = -\frac{1}{2}\tilde{\nabla}\left(\tilde{\mathbf{r}}\cdot\tilde{\mathbf{E}}\cdot\tilde{\mathbf{r}}\right) \tag{1}$$

where

$$\tilde{\mathbf{E}} = (k_l\ \mathrm{tr}\tilde{\mathbf{C}})\ \mathbf{I} + (k_s - k_l)\ \tilde{\mathbf{C}}$$

and

$$\tilde{\mathbf{C}} = \langle\tilde{\mathbf{r}}\tilde{\mathbf{r}}\rangle.$$

Here, $\tilde{\mathbf{E}}$ is the interaction matrix, $\tilde{\mathbf{C}}$ is the configuration tensor averaged with the configuration distribution function, and k_s, k_l are two phenomenological parameters describing the anisotropic interaction potential of the test dumbbell when it

is oriented parallel and perpendicular to the main axis of the mean field respectively. In the above interaction potential, we have dropped an isotropic term which can be renormalized with the spring constant. Following Hess's analysis, we will assume that the interactions between the dumbbells are predominantly repulsive [16]. This assumption is similar to the existence of excluded volume effects for segment-segment interactions in the same polymer chain, in that both k_s and k_l are positive. For low concentrations, the dependence of the interaction parameters k_s and k_l is taken to be linear in the concentration as a first order approximation. Some experimental support for these assumptions has been given by Hess [16] using birefringence results of Tsvetkov and Frisman [18] for polyisobutylene solutions in shear flow. Furthermore, we assume $k_l \geq k_s$ so that the interaction is stronger when the test dumbbell is oriented perpendicular to the mean field orientation of the neighbouring dumbbells than parallel to the mean field. Hess [16] also observed that different coordinate systems are not equivalent in the mean field, therefore the main (principal) axis coordinates of the configuration tensor are used. This implies that

$$\langle \tilde{r}\tilde{r} \rangle_{ij} = 0 \qquad \text{if} \quad i \neq j. \tag{2}$$

All the vectors and tensors in this coordinate system are denoted by a tilde (˜).

With the interaction force given by eq.(1), we can perform a force balance on the beads of the dumbbell to obtain an equation of motion for the dumbbell. Besides the interaction force from eq.(1), other forces includes the usual Stokes' friction (constant friction coefficient) force, an entropic force due to Brownian motion, and either a Hookean or Warner spring force, which are described in great detail in Ref. 4. This equation of motion for the dumbbell can then be combined with the continuity equation for the configuration distribution function, $\psi(\tilde{\mathbf{r}}, t)$, for the end-to-end vector $\tilde{\mathbf{r}}$ to give eq.(3) below. The terms on the right hand side of eq.(3) represent the force contributions from the Stokes' friction, Brownian motion,

the spring force, and the interaction force, respectively. In the present analysis, we will examine both the linear (Hookean) and Warner spring (FENE dumbbell) for the interacting dumbbell (IDB) model in two-dimensional extensional flows. Following the same procedure as in Ref. 4, the following nondimensional diffusion (Fokker-Planck) equation for the configuration distribution function, $\psi(\tilde{\mathbf{r}}, t)$, for the dumbbell conformation can be easily derived as

$$\frac{\partial \psi}{\partial t} = -\tilde{\nabla} \cdot \left\{ \psi \left[\gamma \, \tilde{\mathbf{\Gamma}} \cdot \tilde{\mathbf{r}} - \frac{1}{6N} \tilde{\nabla} \ln \psi - \frac{1}{2} \zeta(\tilde{r}) \, \tilde{\mathbf{r}} - 2 \, \tilde{\mathbf{E}} \cdot \tilde{\mathbf{r}} \right] \right\} \tag{3a}$$

where

$$\zeta(\tilde{r}) = \begin{cases} 1, & \text{for Hookean spring;} \\ 1/(1-\tilde{r}^2), & \text{for Warner spring.} \end{cases} \tag{3b}$$

The above diffusion equation is nondimensionalized using $t = t'/\theta$, $r = r'/R$, $\gamma = \gamma'\theta$, and $k_i = (R^4/12NkT)\; k_i'; i = s, l$, where $R = Na$ is the maximum contour length of the polymer with N Gaussian subunits each consists of a monomers, $\theta = \xi_\circ R^2/12NkT$ is the Zimm relaxation time, kT is the Boltzmann temperature, $\xi_\circ$ is the Stokes' friction coefficient for a bead on the dumbbell, and $\gamma \tilde{\mathbf{\Gamma}} \cdot \tilde{\mathbf{r}}$ is the velocity field which is assumed to be linear in the velocity gradient with γ being the magnitude of the transpose of the velocity gradient tensor $\tilde{\mathbf{\Gamma}}$. All the primed variables are dimensional variables.

The equation of change for the second moment $\langle \tilde{\mathbf{r}} \tilde{\mathbf{r}} \rangle$ can now be obtained by multiplying eq.(3) with $\tilde{\mathbf{r}} \tilde{\mathbf{r}}$ and integrating over the configuration space. We get

$$\frac{d\langle \tilde{\mathbf{r}} \tilde{\mathbf{r}} \rangle}{d\, t} = \gamma \left(\mathbf{\Gamma} \cdot \langle \tilde{\mathbf{r}} \tilde{\mathbf{r}} \rangle + \langle \tilde{\mathbf{r}} \tilde{\mathbf{r}} \rangle \cdot \mathbf{\Gamma}^{\mathrm{T}} \right) - \zeta \langle \tilde{\mathbf{r}} \tilde{\mathbf{r}} \rangle + \frac{1}{3N} \mathbf{I} - 2 \left(\tilde{\mathbf{E}} \cdot \langle \tilde{\mathbf{r}} \tilde{\mathbf{r}} \rangle + \langle \tilde{\mathbf{r}} \tilde{\mathbf{r}} \rangle \cdot \tilde{\mathbf{E}}^{\mathrm{T}} \right). \tag{4}$$

The above equation for the FENE interacting dumbbell has been simplified using Peterlin's preaveraging approximation [19]. This preaveraging scheme is accurate when the configuration distribution function is strongly peaked and is exact for a delta function. For the Warner spring with a large value of N in a strong flow, the preaveraging approximation is applicable because the distribution function is

expected to be highly peaked [20,21]. Macroscopic properties such as birefringence and excess stress due to the polymer can then be calculated from the second moment $\langle \tilde{\mathbf{r}}\tilde{\mathbf{r}} \rangle$. The stress tensor, ${\tau_p}'$, neglecting the isotropic contribution can be expressed as [3]

$$ {\tau_p}' = n \langle (\mathbf{F_c} + \mathbf{F_s})\mathbf{r}' \rangle \tag{5} $$

where $\mathbf{F_c}$ and $\mathbf{F_s}$ are the external interaction force from neighbouring polymers and the spring force respectively, and n is the number of dumbbells per unit volume. The dimensionless stress tensor, $\tilde{\tau}_p = \tilde{\tau}_p' / \, 3nkT$, due to the polymers in the mean field approximation is thus given by

$$ \tilde{\tau}_p = N \left(\zeta \langle \tilde{\mathbf{r}}\tilde{\mathbf{r}} \rangle + 4\tilde{\mathbf{E}} \cdot \langle \tilde{\mathbf{r}}\tilde{\mathbf{r}} \rangle \right). \tag{6} $$

This excess stress tensor is diagonal in the principal axis coordinate system with its principal components represented by $\tilde{\tau}_i$, i=1, 2, 3. For pure extensional flow, the rheological function of interest is the elongational viscosity $\bar{\eta}$ which can be expressed as

$$ \bar{\eta} = \frac{\tilde{\tau}_1 - \tilde{\tau}_2}{\gamma}. \tag{7} $$

3. General Two-Dimensional Linear Flows

In this study, we are interested in two-dimensional linear flows described by the transpose of the velocity gradient tensor in the laboratory frame as

$$\mathbf{\Gamma} = \begin{pmatrix} 0 & 1 & 0 \\ \lambda & 0 & 0 \\ 0 & 0 & 0 \end{pmatrix} \tag{8}$$

where λ is a flow type parameter. The range of flow types $-1 \leq \lambda \leq 1$ covers the entire possible class of linear, two-dimensional flows from purely rotational flow ($\lambda = -1$) to pure extensional flow ($\lambda = 1$), with $\lambda = 0$ being simple shear flow. The representation of $\mathbf{\Gamma}$ in the principal axis coordinate system is facilitated by a coordinate transformation involving the rotation matrix $\mathbf{Q}$ in the flow plane as

$$\tilde{\mathbf{\Gamma}} = \mathbf{Q} \cdot \mathbf{\Gamma} \cdot \mathbf{Q}^{\mathrm{T}} \tag{9}$$

where

$$\mathbf{Q} = \begin{pmatrix} \cos\varphi & -\sin\varphi & 0 \\ \sin\varphi & \cos\varphi & 0 \\ 0 & 0 & 1 \end{pmatrix}$$

and φ is the orientation angle of the end-to-end vector for the test dumbbell relative to the laboratory frame. Thus,

$$\tilde{\mathbf{\Gamma}} = \begin{pmatrix} \tilde{\Gamma}_{xx} & \tilde{\Gamma}_{xy} & 0 \\ \tilde{\Gamma}_{yx} & \tilde{\Gamma}_{yy} & 0 \\ 0 & 0 & 0 \end{pmatrix} \tag{10}$$

where

$$\tilde{\Gamma}_{xx} = -(1+\lambda)\sin\varphi\cos\varphi$$

$$\tilde{\Gamma}_{xy} = \cos^2\varphi - \lambda\sin^2\varphi$$

$$\tilde{\Gamma}_{yx} = \lambda\cos^2\varphi - \sin^2\varphi$$

$$\tilde{\Gamma}_{yy} = (1+\lambda)\cos\varphi\sin\varphi.$$

Substituting the above velocity gradient into eq.(4), we obtain the following equation of change for the principal components of the configuration tensor $\tilde{C}_i$

$$\frac{d\tilde{C}_1}{d\,t} = (2\,\gamma\,\tilde{\Gamma}_{xx} - \zeta - 4\tilde{E}_1)\,\tilde{C}_1 + \frac{1}{3N} \tag{11a}$$

$$\frac{d\tilde{C}_2}{d\,t} = (2\,\gamma\,\tilde{\Gamma}_{yy} - \zeta - 4\tilde{E}_2)\,\tilde{C}_2 + \frac{1}{3N} \tag{11b}$$

$$\frac{d\tilde{C}_3}{d\,t} = (-\zeta - 4\tilde{E}_3)\,\tilde{C}_3 + \frac{1}{3N} \tag{11c}$$

where $\tilde{E}_i$, i=1, 2, 3, are the principal values of the interaction matrix given by

$$\tilde{E}_i = (k_s - k_l)\tilde{C}_i + k_l \sum_{i=1}^{3} \tilde{C}_i\ , \qquad i = 1,2,3. \tag{12}$$

The orientation angle φ can be determined from the condition given by eq.(2) for the off-diagonal components of the configuration tensor in the principal axis coordinate system as

$$\tilde{\Gamma}_{yx}\tilde{C}_1 + \tilde{\Gamma}_{xy}\tilde{C}_2 = 0. \tag{13}$$

Material functions in these flows are governed by the stress tensor due to the polymer. The stress tensor in the laboratory frame can be calculated from eq.(6) by using the inverse of the rotation matrix $\mathbf{Q}^{\mathrm{T}}$ to obtain

$$\tau_p = \mathbf{Q}^{\mathrm{T}} \cdot \tilde{\tau}_{\mathbf{p}} \cdot \mathbf{Q}. \tag{14}$$

4. Results for Two-Dimensional Extensional Flows

The range of flow types in this study is for $\lambda > 0$ which is in the strong flow region (with strain rate exceeding vorticity) necessary for high chain extension [22]. This class of flows can also be simulated quite accurately in the four-roll and two-roll mills so that a comparison of model predictions with experimental data such as flow-induced birefringence can be made. Predictions for semi-dilute polymer solutions using the interacting dumbbell model with a Hookean spring in uniaxial extensional flow have been obtained by Hess [16]. His analysis shows that the well-known singularity at $\gamma = 1/2$ from the linear spring assumption has been removed in the interacting dumbbell model. However, asymptotic results for the average end-to-end length still showed a linear increase with the velocity gradient γ at large extension rates. Thus, the polymer can extend beyond its maximum contour length at high values of γ. We have also performed an asymptotic analysis of the IDB model with Hookean spring in the steady two-dimensional pure extensional flow($\lambda = 1$). From eqs.(10) and (13), the orientation angle can be shown to be $\varphi = -45°$ for the $\lambda = 1$ hyperbolic flow. Since we are interested in high molecular weight polymer, which is essential for exhibiting non-Newtonian behavior in strong flows, we choose $N = 1200$ for all calculations. This high value of N corresponds to a polymer with molecular weight $\sim O(10^6)$ [8]. The asymptotic results for the average conformation of the polymer are similar to the case of uniaxial extensional flow. For large extension rates (i.e., $\gamma \gg 1$), the principal values of the configuration tensor are given by

$$\tilde{C}_1 \sim \frac{1}{2k_s}\gamma \tag{15a}$$

$$\tilde{C}_2 \sim \frac{k_s}{6N(k_s + k_l)}\,\gamma^{-1} \tag{15b}$$

$$\tilde{C}_3 \sim \frac{k_s}{6Nk_l}\,\gamma^{-1} \tag{15c}$$

and the root-mean-square end-to-end length of the dumbbell is given by

$$\langle r^2 \rangle^{\frac{1}{2}} = \langle \tilde{r}^2 \rangle^{\frac{1}{2}} = \left(\tilde{C}_1 + \tilde{C}_2 + \tilde{C}_3 \right)^{\frac{1}{2}} . \tag{16}$$

Since the extensional axis is in the 1-direction, the dominant component in the configuration tensor is $\tilde{C}_1$ with $\tilde{C}_1 \sim \langle r^2 \rangle \leq 1$. Another quantity of interest is the flow birefringence, Δn, which is given by

$$\frac{\Delta n}{B} = \tilde{C}_1 - \tilde{C}_2 \tag{17}$$

where B is proportional to polymer concentration, segmental optical anisotropy of the polymer molecule, and also depends on the refractive index of the solvent. For intermediate extension rates, if $3N \left(1 + 4k_s \langle r^2 \rangle\right) \langle r^2 \rangle \gg 1$ (which is always true for $N = 1200$ and $\gamma > 0.5$) and $k_s \sim k_l$, then

$$\langle r^2 \rangle \sim \frac{\Delta n}{B} \sim \frac{1}{2k_s}(\gamma - \frac{1}{2}). \tag{18}$$

In the limit of $\gamma \gg 1$, eq.(18) converges to eq.(15a). Since the maximum extension of the polymer corresponds to $\langle r^2 \rangle^{\frac{1}{2}} = 1$, it follows that the model fails if the following condition is not satisfied

$$k_s \quad \geq \quad \frac{1}{4}(2\gamma - 1) \quad . \tag{19}$$

The asymptotic prediction from eq.(18) shows that the mean-square end-to-end length of the polymer is inversely proportional to concentration (or k_s). At a fixed k_s value, the birefringence would increase linearly with the extension rate γ.

Exact results at all shear rates can be obtained numerically. We performed numerical calculations using the Hookean spring ($\zeta = 1$) in eqs.(11-13) for steady state two-dimensional extensional flows with $\lambda = 1$ and $\lambda = 0.049$. The steady state prediction for the root-mean-square end-to-end length, $\langle r^2 \rangle^{\frac{1}{2}}$, is shown in Fig. 1 for the Hookean IDB model (i.e., Hess's model) with various values of k_s (for

simplicity, we take $k_l = k_s$). The dilute non-interacting dumbbell case corresponds to $k_s = 0$. The singularity at $\gamma = 0.5$ is evident for the dilute Hookean dumbbell model. For the IDB model with linear spring, Fig. 1 shows that $\langle r^2 \rangle^{\frac{1}{2}} > 1$ for the cases of $k_s = 0.5$ and $k_s = 3$ even when the velocity gradients are of moderate values ($\gamma\sqrt{\lambda} < 7$) such that the condition from eq.(19) is violated. This is a defect of Hookean spring approximation which can be eliminated by using the nonlinear Warner spring, and will be discussed next. The onset velocity gradient for coil-stretch transition is only weakly dependent on concentration (i.e., upon k_s). Indeed, the onset velocity gradient for the range of concentration parameters k_s studied in Fig. 1 is essentially equal to 1/2 for all cases. Another noteworthy point is the correlation of the average end-to-end length of the polymer with the flow strength $\gamma\sqrt{\lambda}$ for the IDB model. For all the values of the interaction parameter studied, the correlation is excellent for all flow types down at least to the near shear flow case where $\lambda = 0.049$. The corresponding prediction for the absolute birefringence $k_s(\Delta n/B)$ is plotted in Fig. 2 versus $\gamma\sqrt{\lambda}$ for the pure extensional case (note that same results can also be obtained for other flow types with $\lambda \geq 0.049$). The absolute birefringence collapses into a single curve for the given range of k_s values (0.5 to 30) as predicted by eq.(18). The quantity $k_s(\Delta n/B)$ is called the absolute birefringence because both k_s and B are linear in concentration, so that $k_s(\Delta n/B)$ is just the solution birefringence, Δn, times a constant which is independent of concentration. However, since the Hookean IDB model still gives unrealistic predictions for arbitrary high values of shear rates or small values of the interaction parameter k_s, its usefulness is limited. Therefore, we will next present predictions for the IDB model with a nonlinear Warner spring.

The nonlinear Warner spring has been recognized as an essential feature for high chain stretching in strong flows by many investigators. Experimental results for dilute polymer solutions have shown that even this simple *ad hoc* form for the nonlinear elastic spring law can provide reasonable agreement between theoretical

prediction and experimental data such as birefringence in extensional flows [8]. We thus incorporate the Warner spring into Hess's IDB model. The resulting model was shown earlier to be the same as for the linear IDB model, i.e., the governing equations (11-13), but with the entropic spring contribution ζ given by

$$\zeta = \frac{1}{1 - \langle r^2 \rangle}. \tag{20}$$

An asymptotic analysis can again be performed for intermediate to large shear rates. The extension axis is assumed to be in the 1-direction which gives a negative value for the orientation angle, φ, because the convention of the rotation matrix for positive values of φ corresponds to anti-clockwise rotation. For large extension rates (or $\tilde{C}_1 \gg \tilde{C}_2$), the principal components of the velocity gradient tensor can be calculated approximately from eq.(13) to be

$$\tilde{\Gamma}_{xx} \;=\; -\tilde{\Gamma}_{yy} \;\sim\; \gamma\sqrt{\lambda}. \tag{21}$$

In the following analysis, the ratio of k_l/k_s is taken to be equal to one so that the dependence of $\langle r^2 \rangle$ or Δn on the interaction parameter (or concentration) can be illustrated in a simple asymptotic form. This would still give a reasonable approximation even for $k_l/k_s \sim O(10)$ because the dominating term is $\tilde{C}_1$ which can be O(10^3) times the values of $\tilde{C}_2$ or $\tilde{C}_3$ for intermediate shear rates. Another approximation is that we assume $3N(\zeta + 4k_s\langle r^2 \rangle)\langle r^2 \rangle \gg 1$ which is always true for $N = 1200$ and $\gamma > 0.5$ similar to the case of the linear IDB model. The large $\gamma\sqrt{\lambda}$ limit for $\langle r^2 \rangle$ can be shown from eqs.(11) to be

$$\langle r^2 \rangle \sim \frac{\Delta n}{B} \sim 1 - \frac{1}{2\gamma\sqrt{\lambda}}. \tag{22}$$

The Warner spring thus has restricted the extension of the dumbbell (polymer) to values that are less than or equal to its maximum contour length for any value of k_s. The minimum shear rates for eq.(22) to hold is given by

$$\gamma\sqrt{\lambda} \;\gg\; 2k_s. \tag{23}$$

For intermediate flow strength $\gamma\sqrt{\lambda}$, i.e., the condition from eq.(23) is not satisfied, and the following asymptotic limits for the averaged length of the polymer or specific birefringence can be shown

$$\langle r^2 \rangle \sim \frac{\Delta n}{B} \sim \frac{\gamma\sqrt{\lambda}}{2k_s}, \qquad \text{for} \quad \frac{1}{2} < \gamma\sqrt{\lambda} \ll 2(k_s - k_s^{\frac{1}{2}}) \; ; k_s > 1. \tag{24}$$

For larger shear rates, we obtained

$$\langle r^2 \rangle \sim \frac{\Delta n}{B} \sim \frac{\gamma\sqrt{\lambda}}{4k_s} + \frac{k_s - k_s^{\frac{1}{2}}}{2k_s}, \qquad \text{for} \quad 2(k_s - k_s^{\frac{1}{2}}) \ll \gamma\sqrt{\lambda} < 2k_s \; ; k_s > 1. \tag{25}$$

Since k_s is assumed to be proportional to the concentration c, the mean-square end-to-end length is predicted to be inversely proportional to c for small to intermediate shear rates. This means that an increase in the polymer concentration would actually inhibit stretching of the polymer. The above results also show that the slope of $k_s\langle r^2 \rangle$ versus $\gamma\sqrt{\lambda}$ would decrease from 1/2 to 1/4 with increasing shear rates at a fixed value of k_s. For small values of the interaction parameter, $k_s < 1$, the following asymptotic limits can be obtained

$$\langle r^2 \rangle \sim \frac{\Delta n}{B} \sim \begin{cases} \frac{1}{4k_s}\left[\gamma\sqrt{\lambda} + 2\left(k_s - k_s^{\frac{1}{2}}\right)\right], & \text{if} \quad 2k_s < \gamma\sqrt{\lambda} \ll 2(k_s + k_s^{\frac{1}{2}}); \\ 1, & \text{if} \quad 2(k_s + k_s^{\frac{1}{2}}) \ll \gamma\sqrt{\lambda} < \infty. \end{cases} \tag{26}$$

This case of $k_s < 1$ is almost the same as the dilute non-interacting dumbbell model prediction where the polymer end-to-end length approaches maximum extension rapidly with shear rate. The onset of stretching can be predicted by calculating the asymptotic limit for small shear rates (or $\langle r^2 \rangle_\circ \ll 1$). It can be shown that by ignoring the contribution from Brownian diffusion, which is only important at equilibrium, the following approximation is obtained

$$\langle r^2 \rangle_\circ \sim \frac{\Delta n}{B} \sim \frac{1}{2k_s}(\gamma\sqrt{\lambda} - \frac{1}{2}), \qquad \text{for} \quad \gamma\sqrt{\lambda} \sim \frac{1}{2}. \tag{27}$$

The onset velocity gradient is at $(\gamma\sqrt{\lambda})_o = (1 + 4k_s\langle r^2\rangle_o)/2$. This result is the same as in the case of the linear IDB model in the sense that the onset velocity gradient is only weakly dependent on concentration. Since $\langle r^2\rangle_o \ll 1$, the onset of stretching should occur at $(\gamma\sqrt{\lambda})_o = 0.5$ for finite values of the concentration (or k_s).

We have also calculated steady state predictions numerically using eqs.(11-13) and eq.(20) for several values of the interaction parameter k_s and a few different flow types. Fig. 3 and Fig. 4 show the predictions for $\langle r^2\rangle^{\frac{1}{2}}$ and the extinction angle $\chi(= -\varphi)$ versus flow strength $\gamma\sqrt{\lambda}$. It is apparent from Fig. 3 that the average length of the polymer tends to a much lower value when the concentration is high (i.e., larger k_s). The effect of high concentration tends to increase polymer-polymer interaction and this creates an additional constraint for unravelling of the coiled polymer away from equilibrium. This effect diminishes as k_s is decreased towards zero which represents the behavior of a truly dilute solution. When the concentration is extremely small so that $k_s = 0$, an unrestrained coil-stretch transition of the polymer conformation occurs. This coil-stretch transition occurs smoothly with increasing shear rate for the present constant-friction nonlinear IDB model. For the case of $k_s = 0.5$, the result is very close to the dilute limit, $k_s = 0$, which agrees with eq.(26) from the asymptotic analysis. In the dilute limit, the polymer would extend to near its maximum contour length rapidly at small shear rates. From the predictions, we could expect dilute solution behavior for all $k_s < 1$. The onset velocity gradient for all values of k_s studied is about $1/2$ as expected from eq.(27) which verifies the weak concentration dependence of the onset of stretching as predicted by the asymptotic analysis. The correlation of $\langle r^2\rangle^{\frac{1}{2}}$ with $\gamma\sqrt{\lambda}$ is excellent for all flow types down to $\lambda \sim 0.01$ which has a ratio of strain rate to vorticity (S/Ω) of only 1.02 (simple shear flow has $S/\Omega = 1$). The value for $\langle r^2\rangle^{\frac{1}{2}}$ for $\lambda = 0.001$ at a fixed value of $\gamma\sqrt{\lambda}$ is generally larger than that of the higher λ cases at all shear rates. Fig. 4 shows the predictions for the extinc-

tion angle, χ, with several values of k_s for the flow type $\lambda = 0.049$. It is obvious that the extinction angle is also weakly dependent on concentration. The value of χ decreases more slowly with increasing concentration from the equilibrium value of 45° corresponding to the principal strain axis to the outgoing flow axis, which corresponds to the principal eigenvector of the velocity gradient tensor. This angle for the outgoing flow axis can be approximated from eq.(13) to give

$$\chi \sim \tan^{-1}\sqrt{\lambda}, \qquad \text{if} \quad \tilde{C}_1 \gg \tilde{C}_2. \tag{28}$$

This limiting value for χ can be reached at a relatively small shear rate ($\gamma\sqrt{\lambda} \sim 1$) as is evident from Fig. 4. Thus, the polymer becomes aligned along the eigenvector of the velocity gradient tensor when the shear rate exceeds about one for all the cases studied here.

Next, we consider steady state birefringence predictions for the FENE-IDB model. In order to show the concentration dependence as calculated by asymptotic analysis, the value of the absolute birefringence ($k_s\Delta n/B$) is plotted versus the magnitude of the velocity gradient tensor $\gamma\sqrt{\lambda}$ in Fig. 5. Although we have only presented results for $\lambda = 1$, the correlation of birefringence with $\gamma\sqrt{\lambda}$ is the same as the $\langle r^2 \rangle^{\frac{1}{2}}$ correlation with $\gamma\sqrt{\gamma}$ (note that $\langle r^2 \rangle \sim \Delta n/B$ from eqs.(22-27) for the whole range of shear rates). The onset velocity gradient is 1/2 as expected from previous results for $\langle r^2 \rangle$. For the cases of $k_s < 1$, the absolute birefringence, which is just the solution birefringence times a constant independent of concentration, saturates at a value which is linear in k_s or concentration. This corresponds to dilute solution behavior as we have noted before. The initial slope of the curve for $k_s = 0.5$ is about 1/4 which is predicted by eq.(26). At higher values of $\gamma\sqrt{\lambda}$, the absolute birefringence approaches a maximum value which corresponds to complete extension of the polymer. This is almost equivalent to the non-interacting dumbbell model predictions for truly dilute polymer solutions.

On the other hand, the absolute birefringence collapses to a single curve for

various cases of $k_s \gg 1$, which correspond to semi-dilute solution behavior, at intermediate values of $\gamma\sqrt{\lambda}$. The slope of absolute birefringence versus $\gamma\sqrt{\lambda}$ is equal to one half which agree with the asymptotic results from eq.(24). At higher shear rates, the slope starts to decrease for the smaller $k_s = 3.3$ case, and is expected to decrease to a slope of 1/4 as predicted by eq.(25) for larger values of $\gamma\sqrt{\lambda}$. When the concentration is much higher, $k_s \gg 1$, the absolute birefringence is just linear to $\gamma\sqrt{\lambda}$ with a small positive deviation at higher shear rates. This deviation is governed by the concentration dependent term $(k_s - \sqrt{k_s})/2$ in eq.(25). If the concentration is extremely high, this deviation is minimum for finite shear rates and the prediction will then be governed by the asymptotic result in eq.(24). Therefore, by varying the interaction parameter k_s, which is approximately proportional to concentration, we can predict distinctive birefringence features for dilute to semi-dilute polymer solutions. The specific birefringence $\Delta n/B$ is independent of concentration for dilute solutions ($k_s < 1$). However, $\Delta n/B$ is inversely proportional to concentration for semi-dilute solutions ($k_s \gg 1$). For polymer solutions with concentration in the intermediate (dilute to semi-dilute) regime, we would have a more complicated concentration dependence which is governed by the asymptotic results from eqs.(22-25).

We can now compare the above predictions with experimental observations. The absolute birefringence predicted by the model shows a linear relationship with the dimensionless shear rate, $\gamma\sqrt{\lambda}$, for semi-dilute polymer solutions ($k_s \gg 1$) over a wide range of shear rates. This prediction agrees in general with flow birefringence of semi-dilute polyethylene oxide solutions measured by Fuller and Leal [23] and by Pope and Keller [24] for pure extensional flow in a 4-roll mill. Although their birefringence data showed a larger than linear dependence on concentration, this is not inconsistent with our predictions that the birefringence collapses to a single curve for different concentrations when plotted versus the dimensionless eigenvalue of the velocity gradient tensor, $\gamma\sqrt{\lambda}$. It is because the characteristic

relaxation time of the polymer can be a strong function of concentration for semi-dilute solutions. In dimensional form, $\gamma\sqrt{\lambda}$ is written as $\gamma'\sqrt{\lambda}\theta$, where $\theta = \theta(c)$. It can be shown that $\theta(c)$ is approximately given by

$$\theta = \theta_\circ(1 + mc) \tag{29}$$

where $\theta_\circ$ is the characteristic relaxation time of polymer in dilute solutions, m is a constant related to the intrinsic viscosity of the polymer solution, c is the polymer concentration. This equation is derived formally using the Huggins' equation [25] and the model prediction for the zero shear viscosity of the polymer solution. Higher order terms are truncated so that eq.(29) is only applicable to polymer solutions with concentration in the dilute to semi-dilute regime. This shows that a strong concentration dependence on the rheological properties is intrinsically included in the model for semi-dilute and concentrated polymer solutions. We also note that the FENE-IDB model predictions have been shown to agree in great detail with recent experimental results for flow birefringence of dilute to semi-dilute polystyrene solutions in 2-roll and 4-roll mill flows [15].

Inception of flow calculations are also attempted for the extensional viscosity versus time at various shear rates. However, no overshoot is found for the the same range of k_s and shear rates used in the steady state case. The extensional viscosity would increase monotonically from the equilibrium value of $2\eta_s$ (η_s is the zero shear solution viscosity) to the steady state value at a time which is inversely proportional to the shear rate $\gamma\sqrt{\lambda}$.

5. Concluding Remarks

The advantage of the FENE-IDB model for dilute to semi-dilute polymer solutions is that explicit concentration dependence can be obtained. By varying the interaction parameter k_s, which is proportional to concentration, we can obtain systematically dilute to semi-dilute solution behaviors. However, this model definitely oversimplifies all the interactions involved for concentrated solutions. The truncation of higher order terms in the interaction potential given by eq.(1) is a source of error for concentrated solution behavior. Hydrodynamic interaction is not considered here because its contribution should be negligible compared to the non-hydrodynamic forces described by the external interaction force in eq.(1) for semi-dilute solutions, where domain overlap of the polymer coils exists. The main result in this study is the inhibition of chain stretching by increased polymer-polymer interaction for high concentration solutions. The specific birefringence is inversely proportional to concentration for semi-dilute solutions and the dependence is less for lower concentrations. In the limit of truly dilute solution, the specific birefringence is, in fact, independent of concentration. Since the relaxation time of polymer is also a function of concentration, model comparison with experimental results should be performed with the shear rate being nondimensionalized by the solution relaxation time. Then, the above concentration dependence for flow birefringence can be shown explicitly.

Although the FENE-IDB model has its limitations because of many simplifications, we are able to show reasonable predictions for dilute to semi-dilute solution behavior in flows for a wide range of shear rates, flow types, and concentration regimes [15,23,24]. It is hopeful that this model can shed some light on the development of molecular theory for the entire range of concentration from dilute to concentrated polymer solutions. Another molecular model for concentrated polymer solutions has recently been developed by Hess [26], who has extended his concept of interacting polymer chains to obtain a *generalized Rouse theory* for

entangled polymeric fluids. The polymer chain is forced (by model assumptions) to *reptate* in the curvilinear direction along the polymer chain which has a similar effect to the original reptation model. However, the *generalized Rouse theory* can only be applied to the other limit of concentration for highly entangled systems. Work is warranted on the development of a molecular theory for polymeric solutions that can provide reasonable description of polymer dynamics in various types of flows and for the entire concentration regime ranging from infinitely dilute to concentrated polymer solutions.

References

[1] Peterlin, A., *J. Polym. Sci.: Polym. Lett.*, **4b**, 287 (1966).

[2] Tanner, R. I., *Trans. Soc. Rheol.*, **19**, 37, 557 (1975).

[3] Bird, R. B., Dotson, P. J., Johnson, N. L., *J. Non-Newt. Fluid Mech.*, **7**, 213(1980); errata **8**, 193 (1981).

[4] Bird, R. B., Curtiss, C. F., Armstrong, R. C., Hassager, O., *Dynamics of Polymeric Liquids*, Vol. 2: Kinetic Theory, 2^{nd} ed., Wiley, New York (1987).

[5] Rouse, P. E., *J. Chem. Phys.*, **21**, 1272 (1953).

[6] Mochimaru, Y., *J. Non-Newt. Fluid Mech.*, **9**, 179 (1981).

[7] Fuller, G. G., Leal, L. G., *Rheol. Acta*, **19**, 580 (1980).

[8] Dunlap, P. N., Leal, L. G., *J. Non-Newt. Fluid Mech.* **23**, 5 (1987).

[9] Yamamoto, M., *J. Phys. Soc. Jpn.*, **11**, 413 (1956); **12**, 1148 (1957); **13**, 1200 (1958).

[10] Phan-Thien, N., Tanner, R. I., *J. Non-Newt. Fluid Mech.*, **2**, 353 (1977).

[11] Fuller, G. G., Leal, L. G., *J. Polym. Sci. Polym. Phys. Ed.*, **19**, 531 (1981).

[12] Doi, M., Edwards, S. F., *J. Chem. Soc. Faraday Trans. II*, **74**, 1789, 1802, 1818 (1978); **75**, 38 (1979).

[13] Bird, R. B., DeAguiar, J. R., *J. Non-Newt. Fluid Mech.*, **13**, 149 (1983).

[14] DeAguiar, J. R., *J. Non-Newt. Fluid Mech.*, **13**, 161 (1983).

[15] Ng, R. C.-Y., Leal, L. G., "*Concentration Effects on Birefringence and Flow Modification of Semi-Dilute Polymer Solutions in Extensional Flows,*" to appear (1989).

[16] Hess, W., *Rheol. Acta*, **23**, 477 (1984).

[17] Warner, H. R., *Ind. Eng. Chem. Fundam.*, **11**, 379 (1972).

[18] Tsvetkov, V. N., Frisman, E., *Acta Physicochim U.S.S.R.*, **20**, 61 (1945).

[19] Peterlin, A., *Polymer*, **2**, 257 (1961).

[20] Dunlap, P. N., Leal, L. G., *Rheol. Acta*, **23**, 1 (1984).

[21] Phan-Thien, N., Manero, O., Leal, L. G., *Rheol. Acta*, **23**, 151 (1984).

[22] Leal, G. L., Fuller, G. G., Olbricht, W. L., *Prog. Astro. Aero.*, **72**, 351 (1980).

[23] Fuller, G. G., Leal, L. G., *J. Polym. Sci. Polym. Phys. Ed.*, **19**, 557 (1981).

[24] Pope, D. P., Keller, A., *Colloid and Polymer Sci.*, **255**, 633 (1977).

[25] Billmeyer, F. W., *Textbook of Polym. Sci.*, Interscience Publishers, John Wiley & Sons, New York, p. 81 (1962).

[26] Hess, W., *Macromolecules*, **21**, 2620 (1988).

Figure Captions

Figure 1. End-to-end length, $\langle r^2 \rangle^{\frac{1}{2}}$, vs. eigenvalue of the velocity gradient tensor, $\gamma\sqrt{\lambda}$, for $\lambda = 1$ (solid line) and $\lambda = 0.049$ (dashed line), and with various values of k_s for the Hookean IDB model, $N = 1200$.

Figure 2. Absolute birefringence, $k_s(\Delta n/B)$, vs. eigenvalue of the velocity gradient tensor, $\gamma\sqrt{\lambda}$, for the Hookean IDB model in pure extensional flow ($\lambda = 1$), and for values of the interaction parameter, $k_s = 0.5$ $\triangle$; 3.0 $+$; 5.0 $\bigtriangledown$; 10.0 $\times$; 30.0 $\square$, and for $N = 1200$.

Figure 3. End-to-end length, $\langle r^2 \rangle^{\frac{1}{2}}$, vs. eigenvalue of the velocity gradient tensor, $\gamma\sqrt{\lambda}$, for $\lambda = 1$ (solid line); 0.049 (broken-dashed line); 0.001 (dashed line), and for various values of k_s, for the nonlinear FENE-IDB model, $N = 1200$.

Figure 4. Extinction angle, χ, vs. eigenvalue of the velocity gradient tensor, $\gamma\sqrt{\lambda}$, for $\lambda = 0.049$, and for various values of $k_s = 0$ (solid line); 3.3 (interior dashed line); 10.0 (broken-dashed line); 30.0 (exterior dashed line), for the nonlinear FENE-IDB model, $N = 1200$.

Figure 5. Absolute birefringence, $k_s(\Delta n/B)$, vs. eigenvalue of the velocity gradient tensor, $\gamma\sqrt{\lambda}$, for the nonlinear FENE-IDB model in pure extensional flow ($\lambda = 1$), and for various values of the interaction parameter, k_s, and for $N = 1200$.

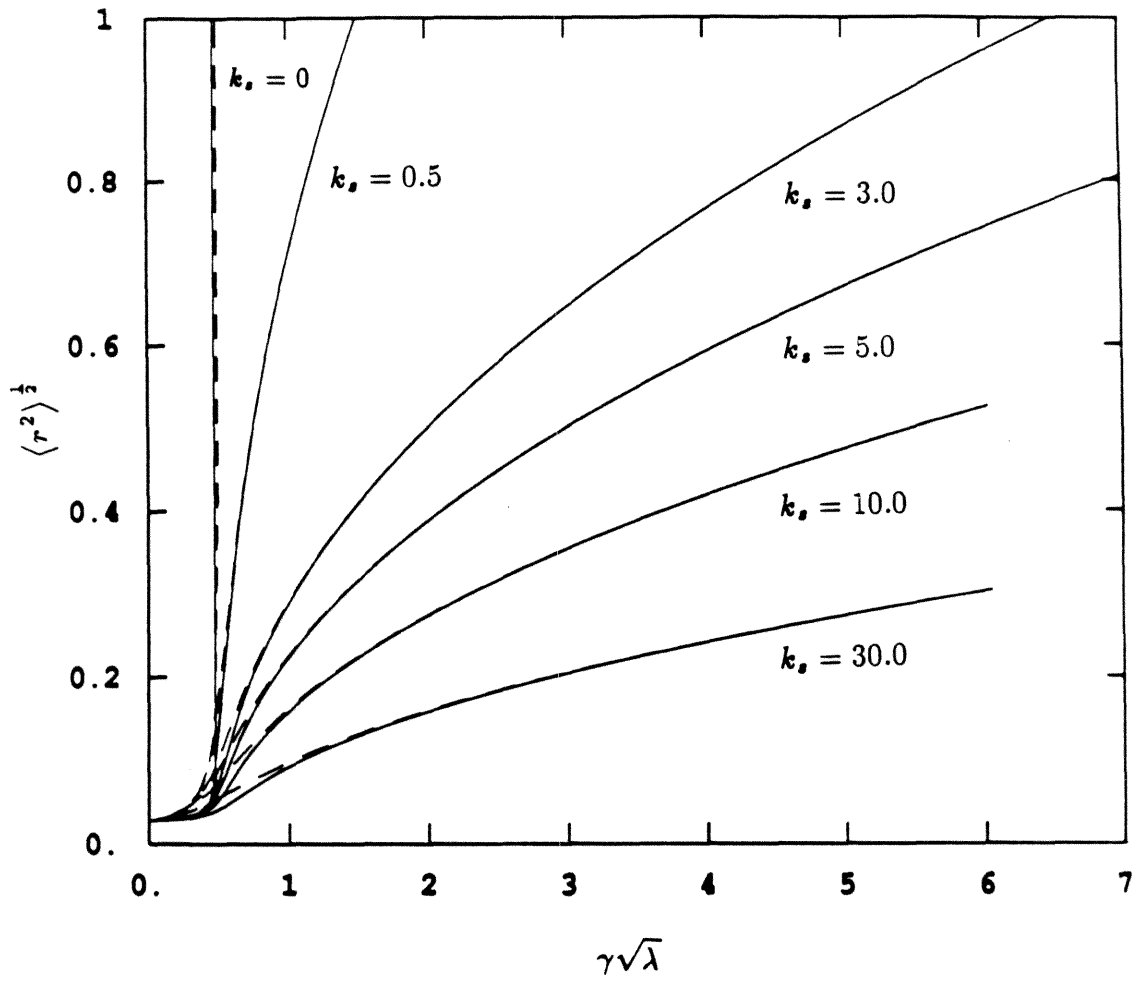
1
0.8
0.6
0.4
0.2
0.
0.
1
2
3
4
5
6
7
$\langle r^2 \rangle^{\frac{1}{2}}$
$\gamma\sqrt{\lambda}$
$k_s = 0$
$k_s = 0.5$
$k_s = 3.0$
$k_s = 5.0$
$k_s = 10.0$
$k_s = 30.0$

Figure 1.

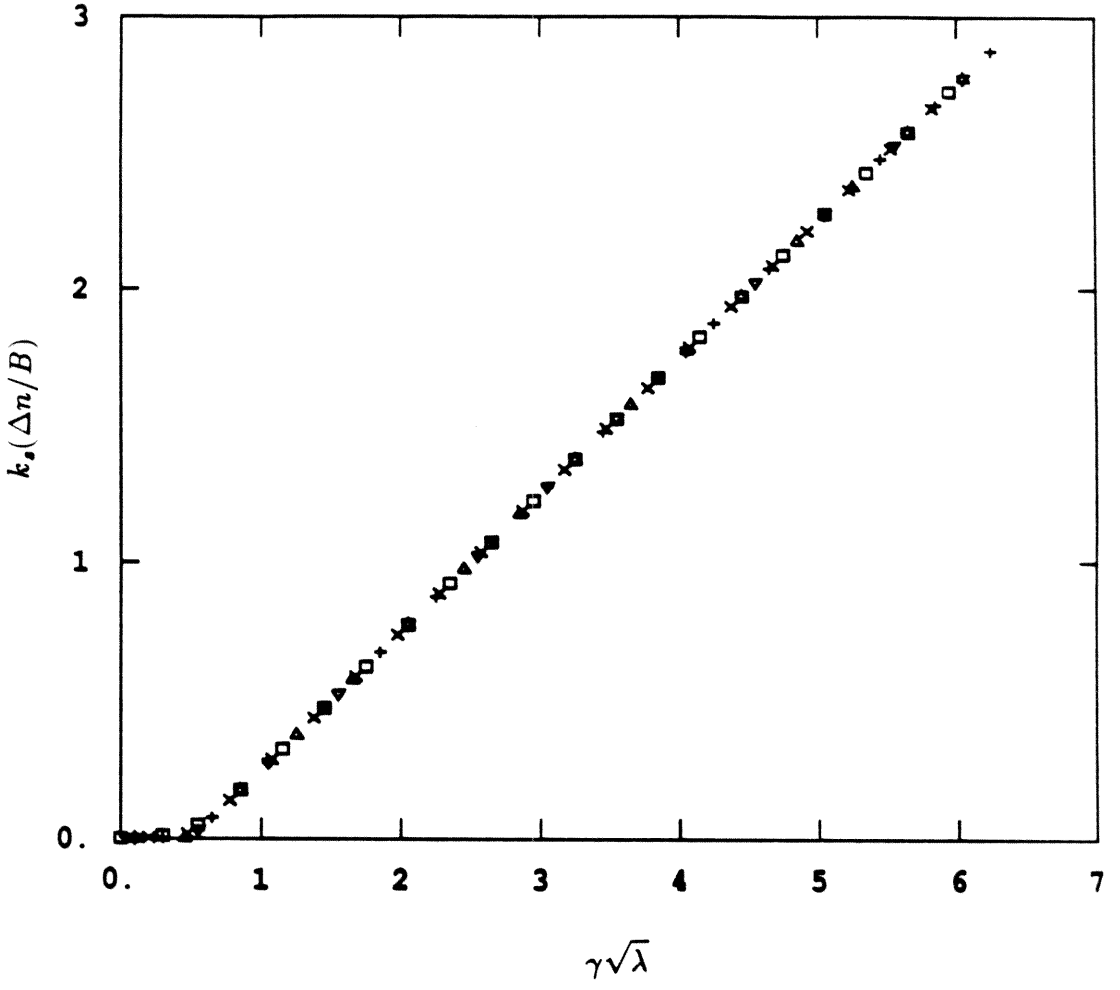

Figure 2.

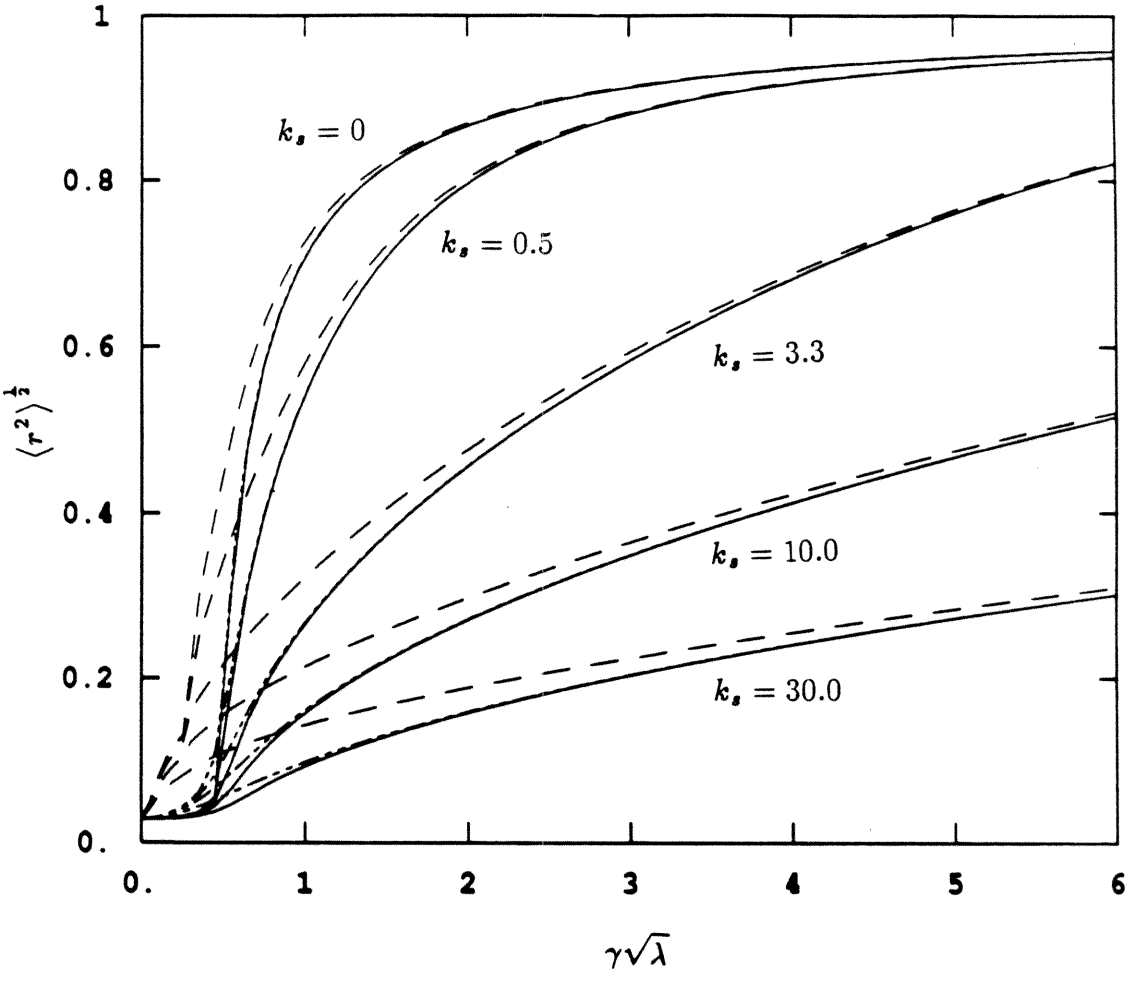
1
0.8
0.6
0.4
0.2
0.
0.
1
2
3
4
5
6
$\langle r^2 \rangle^{\frac{1}{2}}$
$\gamma\sqrt{\lambda}$
$k_s = 0$
$k_s = 0.5$
$k_s = 3.3$
$k_s = 10.0$
$k_s = 30.0$

Figure 3.

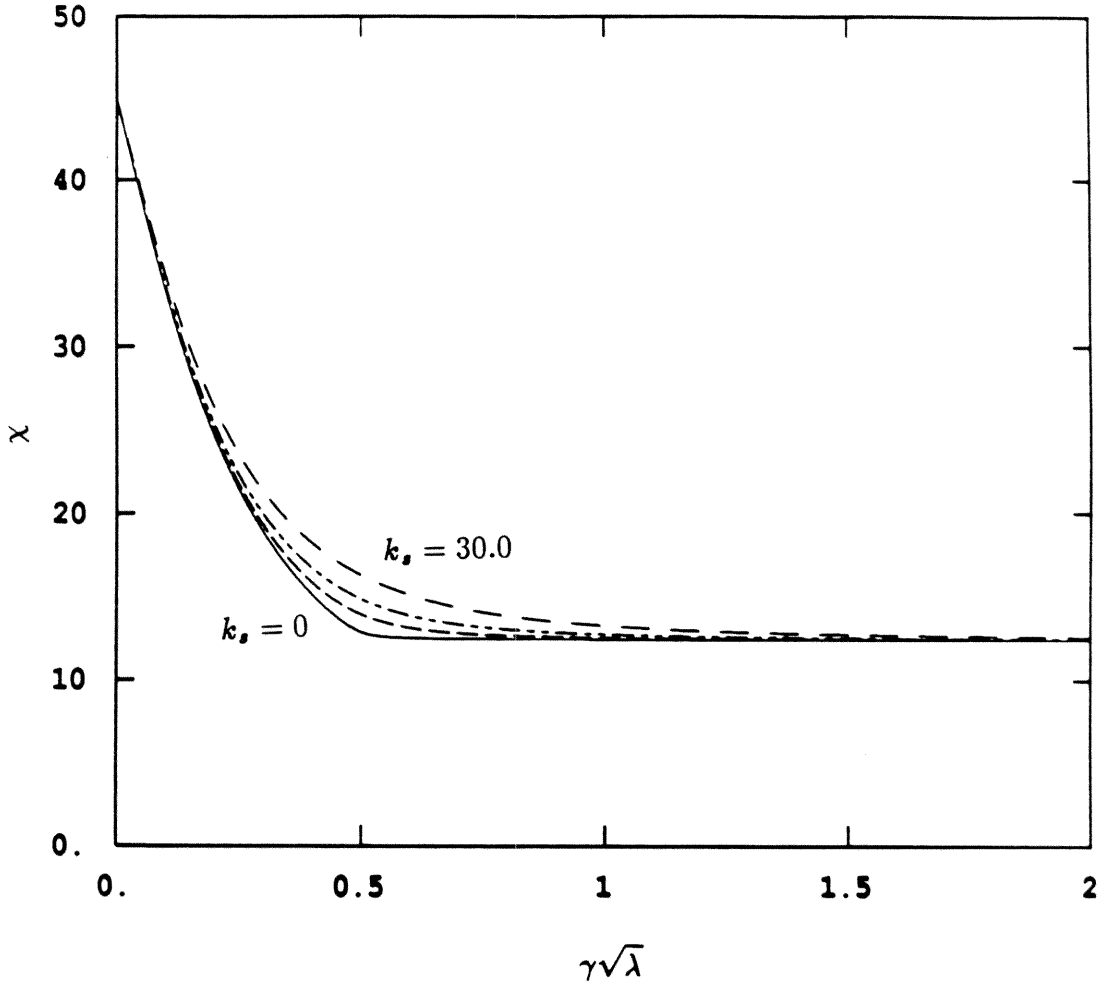

Figure 4.

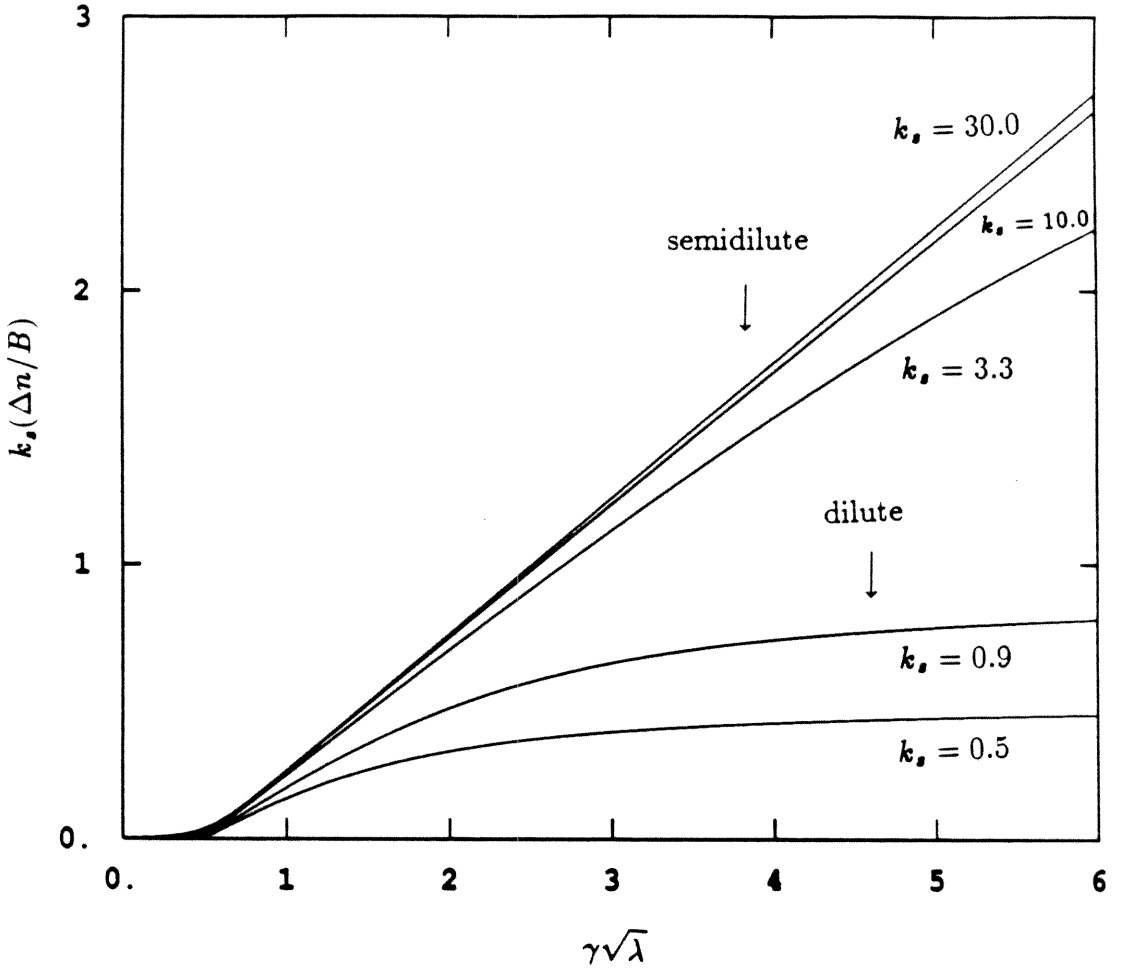
3
2
1
0.
0.
1
2
3
4
5
6
$k_s(\Delta n/B)$
$\gamma\sqrt{\lambda}$
$k_s = 30.0$
$k_s = 10.0$
$k_s = 3.3$
$k_s = 0.9$
$k_s = 0.5$
semidilute
dilute

Figure 5.

Part II: Chaotic Mixing in Time-Periodic Flows

Chapter III

Chaotic Mixing and Transport in a Two-Dimensional Time-Periodic Stokes Flow – the Blinking Two-Roll Mill (BTRM): I. Newtonian Fluids

Chaotic Mixing and Transport in a Two-Dimensional Time-Periodic Stokes Flow – the Blinking Two-Roll Mill (BTRM): I. Newtonian Fluids

R. C.-Y. Ng*,

Department of Chemical Engineering
California Institute of Technology
Pasadena, California 91125

D. F. James,

Department of Mechanical Engineering
University of Toronto
Toronto, Ontario, Canada M5S 1A4

and L. G. Leal†

Department of Chemical & Nuclear Engineering
University of California
Santa Barbara, California 93106

* Present address: Mobil Research and Development Corp., Dallas Research Laboratory, Dallas, TX 75244-4312, U.S.A.

† To whom all correspondence should be addressed.

Abstract

An apparatus, the *blinking two-roll mill* (BTRM), which can simulate a pair of blinking vortices, is built for the study of laminar mixing in two-dimensional time-periodic Stokes flows. This study is analogous to the study of chaos in a deterministic system (the flow). Particle advertion is shown to be either *regular* or *chaotic* depending on the characteristic period of oscillation, μ, for the BTRM flow. Efficient mixing is achieved *globally* in the flow device when $\mu \geq 0.5$. The essential proofs, such as the existence of Smale horseshoe structures or a positive Liapunov exponent, for chaos in the context of dynamical systems theory are revealed by the mixing experiments using flow visualization with dye tracer and quantitative measurements using a digital imaging technique. The quantitative measurements provide a better understanding of the mixing mechanisms and fluid transport properties in this time-periodic flow. The results can be compared qualitatively with theoretical studies of time-periodic vortex-pair flows by Aref [9] and Rom-Kedar *et al.* [10], and provide a basis for future comparisons with theoretical predictions for the specific flow.

1. Introduction

Laminar mixing of very viscous fluids is an important process in many chemical engineering applications such as polymer blending, low-shear mixing of biomaterials, and many reaction engineering problems. The primary goal of current research is to understand mixing mechanisms and to predict the ultimate characteristics of the product. Various techniques have been used in the past to correlate mixing mechanisms with the characteristics of the final (or intermediate) mixture. Some examples are: (a) Statistical measures of the degree of mixedness by Danckwerts [1] using the intensity and scale of segregation as a mixing index; (b) Dynamical measures by Calderbank [2], Uhl and Gray[3], and others [4] using empirical correlations between power consumption and mixing; (c) Deterministic approaches by Spencer and Wiley [5], Mohr *et al.* [6], using the concept of striation thickness and interfacial area as a measure of the quality of mixing. However, there is still not a complete theory that can bridge the gap betweem different complex mixing processes.

Recent efforts to study laminar mixing have relied on understanding the kinematics of two-dimensional (2-D) time-periodic laminar flows and its connection with dynamical systems theory [7,8]. The transition between regular and chaotic advection tor these relatively simple flows can serve as a model system for many mixing applications where fluid mixing is accomplished by stretching, orientation, and redistribution of fluid elements locally in the domain of interest, which can either be closed (batch mixing) or open domain (continuous mixing). The onset of chaotic advection here corresponds to exponential separation of two neighboring material points due to the stretching and reorienting of fluid elements and extremely efficient mixing. The purpose of this paper is to provide *physical* evidence and *quantitative* measurements of the characteristic features of chaotic particle motion for a specific mixing flow, known as the blinking two-roll mill.

In fact, many experimental and theoretical studies of mixing in 2-D chaotic flows have already provided a better understanding of the complex dynamics of chaotic mixing processes [7-15]. Theoretically, Aref [9] has done numerical experiments for a pair of blinking vortices (corotating) to show chaotic advection of tracer particles in this closed domain time-periodic flow. Khakhar *et al.* [8] also demonstrated chaotic behavior for Lagrangian particles in the *tendril-whorl* and *Aref-blinking-vortex* flow. Some measures of mixing characteristics were presented for these chaotic flows, namely the *Liapunov exponent* (a positive value implies exponential stretching of an infinitesimal material line as a long-time average) and the intensity of segregation (the ratio of root-mean-square concentration fluctuation of tracer particles at one location relative to the initial condition). These closed domain flows are relevant to certain batch mixing processes. Rom-Kedar *et al.* [10] and Wiggins [11] have studied a time-periodic model of a counter-rotating vortex pair (the oscillating vortex pair, or the OVP flow) which has an open flow domain. Transport and mixing of segregated fluids in different parts of the domain of the flow were predicted by analytical and numerical techniques via dynamical systems theory. Conversely, since the dynamics (in a *Lagrangian* framework) of particle (fluid element) motion in these flows is described by dynamical systems theory, certain important concepts in dynamical systems theory can be revealed by studying fluid mixing [7,11-14]. Indeed, some characteristic features of chaos in dynamical systems theory such as the Smale horseshoe [16-19], which is analogous to stretching and folding of fluid elements in fluid mixing, could be revealed by mixing experiments [7,14].

However, experimental studies of mixing in a physical system currently lag behind theoretical predictions. Some recent experimental works have shown encouraging results in relating chaotic mixing with dynamical systems theory predictions. Chaiken *et al.* [12] have experimentally demonstrated the existence of *Lagrangian turbulence* (chaotic advection) for a time-modulated (blinking) Stokes

flow between two eccentric cylinders. Ottino and coworkers [7,14] have done experiments on the motion of a Newtonian fluid in a cavity flow. Structures shown in their pictures clearly support certain theoretical expectations (such as the existence of Smale horseshoe structures) for chaotic mixing. Their work is similar in certain respects to the present study. Both the cavity and two-roll mill flows have two elliptic and one hyperbolic point in the steady flow configuration. One difference is that the flow structure in our apparatus (the two-roll mill) shows a close resemblance to Aref's blinking vortex flow [9]. In the present study, flow visualization and standard digital imaging techniques are used to investigate laminar mixing in a *blinking two-roll mill* (BTRM). We will present quantitative measurements by digital image processing to illustrate mixing and transport in chaotic flows.

The objective of the present work is to experimentally provide *physical* evidence of chaotic mixing, and to provide *quantitative* measurements of measurable quantities such as interfacial area, the area and regions of chaotic mixing, and fluid transport (redistribution of fluid elements) in various regions of the flow. There have been no other measurements of this type except from Ottino's group [7]. The analysis and measurements presented in this paper are an essential complement to a study of mixing processes via dynamical systems theory which is currently being pursued for the BTRM flow. In the next section, we will briefly discuss dynamical systems theory and its application to the present study.

2. Background on Dynamical Systems Theory

Theoretical criteria for the existence of chaotic motion of advecting particles in the flow include any one of the following properties (see Guckenheimer and Holmes [19]): (a) existence of a Smale horseshoe map; (b) positive Liapunov exponent; (c) transverse intersection of homoclinic or heteroclinic orbits. If the flow or the mapping exhibits any of the above characteristics, either locally or globally, then the long-time average behavior of an infinitesimal material line in the chaotic region is that it will stretch exponentially in the flow, and thus two neighboring particles will also separate exponentially on a long-time average. Many Hamiltonian dynamical systems show chaotic behavior when perturbed periodically [8-21]. In this paper, we will limit our discussion to two-dimensional laminar flows, which can always be modelled as Hamiltonian systems. In two-dimensional laminar flow, the velocity field **v**(x,y,t) in an Eulerian representation is related to the stream function ψ by

$$\mathbf{v}(x,y,t) = \left(\frac{\partial\, \psi}{\partial\, y} \ , \ -\frac{\partial\, \psi}{\partial\, x} \right) \tag{1}$$

where the stream function plays a role that is similar to an equipotential surface in Hamiltonian mechanics. The motion of particle (passive tracer) in this *flow* is governed by the set of differential equations in the Lagrangian form

$$\frac{d\, x}{d\, t} = \frac{\partial\, \psi}{\partial\, y} \tag{2a}$$

$$\frac{d\, y}{d\, t} = -\frac{\partial\, \psi}{\partial\, x} \tag{2b}$$

This is a Hamiltonian system whose Hamiltonian is just the stream function $\psi(x,y,t)$. For time-independent flows, this dynamical system has one degree of freedom and is integrable which means that a passive tracer particle in the flow will follow a smooth path along a streamline. The phase space, i.e., the 2-D flow plane, of this integrable system consists of streamlines of constant value. However, when the flow is time-modulated periodically, the time-dependent Hamiltonian with one

degree of freedom is then equivalent to an autonomous Hamiltonian with two degrees of freedom, and is likely to produce chaotic behavior [16,17]. The motion of a particle initially at $\mathbf{x}_o(x_o, y_o)$ reduces to an area-preserving map corresponding to the solution for eq.(2) with a given initial condition $\mathbf{x}_o$.

In order to identify certain important characteristics of the time-periodic system, it is best to study its Poincaré map rather than following particle trajectories at all times. The Poincaré map of the system can be represented experimentally by taking a snapshot of the positions of any passive particles, such as dye molecules, at each time period of the flow. This periodic flow visualization is the same as looking at the Lagrangian representation of the dynamics of particle trajectories in a time-periodic flow with a large number of initial conditions. By studying the physical analogue of the Poincaré map, structures such as islands, tendrils, and whorls near fixed points in the map can be shown to exist in mixing experiments. In addition, chaotic behavior can be identified experimentally via the existence of horseshoe structures, as predicted by the theory of dynamical systems.

In the present study, the time-dependent flow in the 2-roll mill is an analogue of Aref's blinking vortex flow [9]. The two rotating cylinders are alternately switched on and off, and thus qualitatively simulate the blinking vortices in Aref's system. The steady flow corresponding to the case under study is the corotating two-roll mill flow [22]. In an unbounded domain, this flow has a central hyperbolic point and two elliptic points (hypothetically at the centers of the rollers) on each side of it. Two homoclinic orbits are formed in this configuration which appear as a figure-eight-shaped separatrix. This separatrix can be thought of as a barrier to transport of materials in the sense that there is no advection across it in the steady flow configuration, and thus no mechanism for transport of material (aprart form diffusion) from the region inside to the region outside (or vice versa). Fig. 1 shows the schematic of the streamlines for the steady corotating flow. Since we are only interested in Stokes flows in which all inertial and acceleration effects can be

neglected, the time-periodic BTRM flow can be decomposed into a time-periodic counter-rotating pair of cylinders plus a steady corotating pair of cylinders. Thus, the streamfunction for the BTRM flow is just the superposition of the streamfunction for the steady corotating two-roll mill and the steady counter-rotating two-roll mill of equal strength

$$\psi \;=\; \psi_s(x,y)\Omega_s + \psi_p(x,y)\Omega_p(t) \tag{3}$$

where ψ is the streamfunction, Ω is a function of the roller speed defined below, and subscripts s and p represent the steady corotating and periodic counter-rotating cases respectively. For the blinking protocol, the two Ω's are given by

$$\Omega_s = \omega, \qquad t \geq 0 \tag{4a}$$

$$\Omega_p = \begin{cases} +\omega, & nT/2 \leq t \leq (n+1)T/2; \\ -\omega, & (n+1)T/2 \leq t \leq (n+2)T/2, \quad \text{for n = 0, 2,..} \end{cases} \tag{4b}$$

where ω is a constant roller speed, and T is the period. The linear relationship between the stream function and roller speed has been shown by Frazer [23] for the two-roll mill in an unbounded domain, and is consistent with the general expectations for Stokes flows. By perturbing the steady system with a time-periodic flow, homoclinic orbits will break apart. The stable and unstable invariant manifolds may then intersect transversely and consequently create a countable infinity of homoclinic points. This is one of the criteria for the presence of chaos [16,19].

Rom-Kedar *et al.* [10] and Wiggins [11] have studied a similar case of perturbing a counter-rotating vortex flow with a continuous sinusoidal straining field. In their study, transport of material is enhanced dramatically by formation of a heteroclinic tangle of the stable and unstable manifolds in the time-periodic field. Using the invariant property of these manifolds, the orientation preserving property of the Poincaré map, and the Melnikov technique, they were able to identify

important structures in the flow and quantify mixing via a procedure that they termed *lobe dynamics*. Transport of material through the separatrix is enhanced by the *tangling* of the stable and unstable manifolds that subsequently form the *lobes*. This behavior is common to many near integrable dynamical systems such as the time-dependent Duffing's equation. Fig. 2 shows a perturbed Poincaré map that results in tangle (or lobe) formation due to the transverse intersection of homoclinic orbits. Near the homoclinic points, the fluid is stretched, oriented, and even folded over itself after several periods. This leads to the possible formation of a Smale horseshoe which is a visual sign of chaos. This phenomenon was demonstrated vividly by the lobe or tangle dynamics [10,11]. Since our flow resembles the OVP in many aspects, we would expect similar behavior to occur in the BTRM flow.

In the next section, experimental details will be presented. In the section that follows, we try to illustrate the *possible* existence of a horseshoe map, which gives rise to chaotic particle motion, by examining the flow structures formed in the BTRM mixing experiment. These structures appear to be the physical analogue of the horseshoe map described above. The existence of this type of mapping is essential to efficient mixing. In addition, we will demonstrate the existence of exponential stretching of a blob of fluid for high frequency flows. This could be related to a positive Liapunov exponent for proof of the existence of chaotic mixing. Further, we will discuss the governing parameters for the existence of the morphological structures, material line and area stretching, and fluid transport between different regions of the BTRM flow.

3. Experimental Details

3.1 Apparatus

The flow device is a two-roll mill in a closed square box of 178x178 cm^2 similar to the one used in this laboratory for flow birefringence and visualization studies [22]. The rollers have a radius(R) of 1.91 cm and a height(H) of 3.81 cm. The gap width (2d) between rollers is 3.17 cm. A schematic for the experiment and a photograph for the flow device are shown in Figs. 3a and 3b, respectively. The flow device is made of acrylic walls with two glass plates at the top and bottom. In this configuration, flow visualization can be achieved in all directions. The rate of rotation of the rollers is controlled by Bodine electric motor controllers. The blinking two-roll mill configuration is realized by alternately engaging a electromagnetic clutch for each motor using computer-controlled switching. This switching is done using an IBM/AT computer with an I/O interface board to trigger a set of electromagnetic relays. The time for switching the rollers on and off is about 10-20 milliseconds, which is the response time ($<$ 10 ms) for the clutches operating at a maximum load, plus the operate or release time ($<$ 10 ms) of the electromagnetic relays. However, since the time for each *blinking* period is of the order of 1-40 sec, we assume that transient effects from the electronics can be neglected. It is observed from flow visualization by dye tracer that negligible mechanical inertia is present when disengaging the clutch to stop the roller. With this computer-controlled switching of the periodic motion for the rollers, we can simulate a blinking protocol similar to Aref's blinking vortex flow. The alternating rotation of the rollers is shown schematically in Fig. 4.

Flow visualization is carried out by injecting a blob of red dye Sudan IV, which is soluble in organic solvents such as the ones used here, into a clear, viscous organic solvent. Dye blobs can be placed either inside or outside the stagnation

streamline (the separatrix) of the steady flow by simply moving the injector (located near the side wall of the flow device to avoid disturbing the flow) to the desired strategic location at the beginning of the experiments (see Fig. 3a). Then, a 150 watt projector lamp is used to apply back lighting for the pictures with the aid of a reflector and a 45° angled first-surface mirror that are located in between the flow device. The pictures are captured by a high resolution Sony XC-77 monochrome CCD video camera and are recorded on a Panasonic 4-Head video cassette recorder during the entire course of the experiments. The recorded images can then be digitized by an ITT PCVision-Plus frame grabber using the IBM/AT and analyzed by Image-Pro II which is a utility software package by Media Cybernetics for image enhancement, analysis, and measurements.

3.2 Experimental Conditions

In order to ensure a Stokes flow and a high degree of two-dimensionality in the two-roll mill, viscous Newtonian solvents are used in this study. The Newtonian fluids for these mixing experiments are Chlorowax 45 (CW45), a chlorinated paraffin product from Diamond Shamrock, and 70/30 wt% of a mixed solvent of CW45 and tricresylphosphate (TCP). These fluids are chosen for their high viscosities and because they are effective solvents for polystyrene which is used for a companion study of mixing with polymer solutions, that is reported separately [24]. The molecular diffusivity of the dye in these organic solvents is estimated to be $O(10^{-8})cm^2/sec$ based on the known diffusivities for organic dye molecules in less viscous organic liquids. Therefore, we can ignore molecular diffusion and inertial effects in this study relative to mixing via kinematical evolution of material lines. Properties for the two fluids are shown in Table 1.

By using a 5 wt% Sudan IV red dye dissolved in the same suspending fluid, good monochrome contrast is obtained with the back lighting setup which is similar in certain respects to the more sophisticated shadowgraph imaging. The suspend-

ing fluid, which is contaminated with dye from a previous experiment, can still be used after thorough mixing. Indeed, after several minutes of mixing, the suspending fluid again appears in the video image as a uniformly bright background whereas a freshly injected dye blob appears as a dark spot that has a significant difference in grey scale for image analysis (the frame grabber has a resolution of 256 grey levels). In this way, many sets of experiments can be run without draining the flow device every time dye is introduced into the solution. This is the primary reason for using a monochrome (black and white) digital imaging technique instead of a color one.

Table 1. Newtonian Fluid Properties at $20°C$

Fluid	η (poise)	ρ (gm/cc)
CW45	190.0	1.30
CW45/TCP	44.9	1.26

The initial conditions for all experiments are as close to identical as possible, with a 0.4-0.5 cc blob of red dye injected near the center of the gap between the rollers at about the half-height of the flow device. Experimental results are reported at $20°C$ which is the controlled temperature in our laboratory. Local temperature increase due to viscous dissipation in the solution is found to be negligible by examining the flow structures both from the top and side view. For the investigation of transport rates reported in section 4.3, the initial condition is an annulus of dye between roller #2 and the left stagnation streamline (i.e., the separatrix). It is important to inject the dye at about half height of the flow device to minimize boundary effects associated with the finite vertical dimension of the flow device. Since the Reynolds (Re) and Strouhal (S) numbers govern the characteristics of the flow, we would like to keep both of these parameters as low

as possible to reduce inertial and transient effects respectively and to preserve two-dimensionality in this flow device. These characteristic nondimensional parameters are defined as follows

$$Re = \frac{R\,\omega\,d}{\nu} \tag{5a}$$

$$S = \frac{d}{R\,\omega\,T_{\frac{1}{2}}} \tag{5b}$$

where R is the roller radius, ω is the roller speed, d is the half gap width between the two rollers, ν is the kinematic viscosity, and $T_{\frac{1}{2}}$ is the half period which is the time of rotation for one roller in the blinking cycle (period). The range of experimental values is $Re = 0.03$–1.5 and $S = 0.01$–0.24. Most of the experiments that revealed important structures in the BTRM flow are performed at Re or $S \sim O(10^{-2})$. The condition for neglect of transient effect due to vorticity diffusion is $T_{\frac{1}{2}} \gg d^2/\nu$. Although $T_{\frac{1}{2}}$ is 1 to 40 sec, which is much larger than the largest value of $d^2/\nu = 0.07$ in our experiments, we still observed some evidence of transient effects for high frequency flows. Later, we will discuss these observed effects due to high ReS in the enclosed two-roll mill device.

4. Results and Discussions

In the next few subsections, flow visualization and *quantitative* measurements of the digitized image of the flow structures will be presented to demonstrate chaotic behavior for Lagrangian particles (passive dye tracer) in the flow. The length and area of mixing represented by stretching and redistribution of a blob of dye in both the regular and chaotic flow regimes are measured to show the distinct measurable differences between these flows. Furthermore, fluid transport through the stagnation streamline (i.e., the separatrix) and mixing characteristics via *tangle dynamics* in this BTRM flow will also be discussed. The results presented are for experiments in the Newtonian fluid CW45 unless otherwise stated.

4.1 Regular and Chaotic Mixing

For steady laminar flow in the two-roll mill, the flow is deterministic (which is also true for time-periodic cases for 2-D Stokes flows) and *integrable.* Since the BTRM is a closed domain flow enclosed in a box, tracer particles represented by the red dye should traverse along a closed streamline and stay in this orbit for all times. Fig. 5 shows streamline patterns for three possible steady flow protocols in our apparatus. The corotating two-roll mill and the single-roller flows correspond to the limiting cases in the general time-periodic or blinking flow with $T_{\frac{1}{2}} = 0$ and $T_{\frac{1}{2}} = \infty$ respectively. The counter-rotating flow can be interpreted as a large periodic perturbation that is added to the steady corotating case to generate the BTRM protocol by virtue of the linearity and quasi-steady nature of the Stokes equations describing the flow as shown previously. Mixing is inhibited due to the existence of the invariant manifolds (for example, the separatrix in the steady corrotating flow) which restricts the convective transport of fluids from one region to another. These steady flows or *integrable* systems can be classified as *regular mixing* where the stretching of material lines is at best linear with time and a particle trajectory is deterministic (the pathline is the same as a steady

streamline). However, for time-periodic flows (likely to be nonintegrable as shown later), such as the blinking protocol described earlier, material lines can experience exponential stretching as a consequence of the formation of the Smale horseshoe, and this gives rise to chaotic particle advection. Therefore, by introducing a time-periodic modulation of the steady case, the mixing of fluid may go through a transition from regular to chaotic behavior, depending upon the frequency and amplitude fo the modulation. The critical parameters which determine the mixing characteristics of dye with the suspending fluid in the BTRM are the half period $T_{\frac{1}{2}}$, the roller speed ω, and the total mixing time t'. The BTRM device is capable of generating a large region of chaotic mixing at large critical periods and/or roller speeds. The nondimensional characteristic parameters are the dimensionless period of oscillation μ, and total dimensionless mixing time t (or number of periods of time $T_\circ$), defined as

$$\mu = \frac{\omega T_{\frac{1}{2}}}{\omega_\circ T_\circ} \tag{6a}$$

$$t = \frac{t'}{T_\circ} \tag{6b}$$

where ω is the roller speed in rad/sec, $T_{\frac{1}{2}}$ is the half period in sec, and $T_\circ$ is a characteristic time for a particle to travel one revolution along a closed steady streamline near the center of the gap between the rollers at a roller speed of $\omega_\circ$ when one roller is rotating. Experimentally, we determined $T_\circ$ to be $\sim$ 40 sec for a roller speed $\omega_\circ$ of 1.75 rad/sec (this is almost the lowest roller speed accessible in our apparatus and provides a $O(10^{-2})$ Reynolds number). The value of μ corresponds to the number of revolutions of a fluid element near the center of the device in a half period of time. The mixing characteristics are almost identical for a fixed value of μ with various combination of T and ω. The reason for the present choice of μ and t nondimensional parameters is so that a qualitative comparison can be made with predictions from Aref's blinking-vortex flow [9]. Aref [9] has

predicted that a transition from regular to chaotic particle motion should occur when μ (in his case) increases from zero to about one. The size of the chaotic region is also predicted to increase with increasing μ until the entire flow domain became *globally chaotic.*

In the present study, similar results are observed. Intricate structures of stretching and folding of material lines are obtained as the flow strength parameter μ is increased. Figs. 6 and 7 shows two time sequences of pictures for $\mu = 0.05$ and 0.50, respectively, both at $\omega = 1.75$ rad/sec. The dye blob is placed initially near the center of the device. If we compare the pictures at t=5, a distinct difference in the mixing structure is evident. For the case of small flow strength which has a short blinking period of 4 seconds, fluid elements represented by the red dye can only be stretched linearly and stay near the unperturbed stagnation streamline. However, a small degree of folding and exponential stretching still occurs *locally* near the hyperbolic fixed point such that a particle trajectory is not necessarily deterministic. This is the case of *transition* to chaotic behavior because the folding and stretching action still do not form a complete horseshoe. However, when structures resembling the horseshoe map occur at or near hyperbolic points in the stronger flow with a period of 40 seconds ($\mu = 0.50$), the particle path becomes chaotic as we will show later. This leads to a large region of efficient mixing as is apparent from the pictures at large times. After 15 periods, the dye is dispersed quite thoroughly in a relatively large region spanning the entire experimental zone of observation (which is the size of the mirror).

Morphological structures such as *tendrils* and *whorls* arise naturally in those chaotic systems which have both hyperbolic and elliptic fixed points in the unperturbed configuration [20]. Berry *et al.* [20] in the study of a quantum map proposed to call the spiral structure near an elliptic fixed point a *whorl* and the wiggling manifolds near a hyperbolic fixed point a *tendril.* We have also observed structures resembling the tendrils around the central hyperbolic fixed point for

the BTRM flow. Fig. 8 shows clearly the tendril-like structure near the central hyperbolic fixed point for the fast blinking case with a 4-second period. For higher flow strengths, these tendrils will grow and intermingle with each other to form the observable structures analogous to the Smale horseshoe map from dynamical systems theory. Chien *et al.* [14] have demonstrated the existence of such structures in their cavity flow experiment by examining carefully the characteristics of the striations at the expected location of the horseshoe. In order to ensure that the observed structure was indeed the physical manifestation of a horseshoe map, they verified that the experimental construction satisfied all of Moser's conditions [17]. The properties of the structures satifying Moser's conditions were given by Chien *et al.* [14] as: (a) the existence of a quadrilateral S with hyperbolic points at opposing vertices that is formed by intersection (transversally) of the streamlines from the forward and inverse map after several periods of the flow; (b) the forward striations in S should be the images of the inverse striations (this rule also applys to the top and bottom of the striations); (c)the forward and inverse map must produce thinner striations which lie inside the striations produced by the map from one period before.

Following the above procedure for identifying possible horseshoe structures, the evolution of the striations from a dye blob initially in the BTRM is examined carefully to search for a candidate for a horseshoe. Since most of the dynamics of the system are governed by hyperbolic fixed points of low order [7], the search is concentrated on the central portion of the flow (between the two cylinders) where periodic points of a hyperbolic nature are likely to exist. With the aid of the 4-Head HQ Video Cassette Recorder, we examine the motion of the dye filament at a very slow speed to determine whether Moser's conditions are satisfied. A sequence of pictures for $\mu = 1.0(T_{\frac{1}{2}}=40$ sec) at various times is shown in Fig. 9 to show the increase in number of striations inside the location of a horseshoe candidate. The candidate horseshoe took more than one period to form because

the initial blob location is not the same as that for the horseshoe. The dyed fluid has to travel to the horseshoe location before the structure appears in the pictures. For every other period forward in time, more striations, which are thinner (not darker in grey level) than those from previous cycle, move to the horseshoe location. Therefore, we determine that the candidate for a horseshoe is formed in one period from $t = 1.5$ to $t = 2.5$ as shown in Fig. 9. Next, the dye pattern (forward map) at $t = 2.5$ and its mirror image (backward map) is superimposed in the picture shown in Fig. 10. The intersection of the striations is indicative of transverse crossing of the streamlines of the forward and backward map at the location of the horseshoe candidate. The picture thus reveals the existence of a quadrilateral with characteristics that satisfy most of the required conditions for horseshoe formation except for the hyperbolic property of the vertices that cannot be determined from experiments. This horseshoe (if indeed the vortices of the quadrilateral is hyperbolic) is a period 1 horseshoe. From the appearance of the horseshoe map, the flow is guaranteed to be chaotic.

The same technique is also applied to other cases of lower period flows, $\mu < 1$. By studying the video carefully, we determine that the transition to chaotic behavior occurs at about $\mu = 0.125$ (i.e., no horseshoe can form for $\mu < 0.125$). For intermediate values of period, $0.125 < \mu < 1.0$, the period for a candidate horseshoe increases with decreasing value of μ. The period 1 horseshoe disappears in these intermediate period (or flow strength) flows because the striations for the forward and backward map do not intersect at all. This observation is analogous to predictions by Khakhar *et al.* [8] in the study of their Aref-blinking-vortex flow. These investigators found that bifurcation of periodic points from hyperbolic, elliptic, or parabolic type to other types and periods occurred when the characteristic flow strength was varied between 0.5 to 10.0. For mixing purposes, it is desirable to have a low period horseshoe map so that efficient mixing can be achieved rapidly. In the BTRM, a period 1 horseshoe appears for $\mu > 0.5$.

Therefore, it is apparent that an optimum flow strength for efficient mixing exist in this flow in the range $0.5 < \mu \ll \infty$. However, islands of unmixed fluid or regular regions still exist even for intermediate values of μ as shown in Fig. 11, that are probably due to the presence of an incomplete horseshoe map [7] where the stable and unstable manifolds just fail to intersect.

4.2 Area of Chaotic Mixing and Liapunov Exponent

As mentioned before, the area of chaotic mixing (area refers to the area of dye coverage) depends on both the flow strength μ and the total mixing time, t. By increasing either the roller speed or the period of blinking, the motion can go through a transition from regular to chaotic, and subsequently to globally chaotic behavior. For various roller speeds ω, the area of mixing (nondimensionalized with the area of a roller) is plotted against μ in Fig. 12 where μ is a measure of flow strength (i.e., the number of revolutions a fluid element traverses along the center streamline between the rollers in a half period). The total time of mixing is $t = 25$, which is equivalent to a physical time of 1000 sec. Although most of the mixing of dye and suspending clear fluid is completed after the first 10 periods (40-sec each), we chose this large mixing time so that the density of dye in the measured area is fairly homogeneous. We can actually quantify the degree of homogeneity by analyzing and comparing grey levels at different locations within the mixed area. The region of chaotic mixing increases rapidly as the flow strength increases from zero. Then, the size of the chaotic area gradually levels off because it is approaching the side walls of the apparatus. This behavior is qualitatively similar to results from Aref's simulation of the blinking vortex flow [9]. By increasing the period of oscillation, μ, to some optimum number $\mu_c > 0.125$, we can achieve chaotic mixing in this device. This optimum period has to be much less than total mixing time such that we do not approach the limit of $T_{\frac{1}{2}} \to \infty$ which gives regular mixing behavior (only one cylinder is rotating in this case).

As we can see from Fig. 13, data for different periods but the same μ appear to scatter more at low μ values. For $T_{\frac{1}{2}}$= 1 sec and $\mu < 0.25$, the dye area tends to spread radially outward even though the Reynolds number is still less than one. This is probably because the boundary effect is significant for high frequency flows and the particle motion is no longer slowly varying. The Strouhal number is between 0.05 to 0.24 in these cases. Lagnado [25] has studied both experimentally and theoretically the stability of steady hyperbolic flows. Experimental results showed that steady flow in the four-roll and two-roll mill is 2-D for $Re < 5$. However, Lagnado's study concentrated locally only on the central region, and it is not clear whether secondary flows due to boundary effects might occur in the outer regions for similar or even smaller Reynolds number. In the BTRM experiments, the Reynolds number is always less than 1.5. From the data shown in Fig. 12, it is apparent that the results do not depend on the Reynolds number (proportional to the roller speed ω) because the transient effect (dyed fluid being pushed radially outward) occurs at different values of ω. However, this effect does depend rather strongly on the characteristic frequency, ReS (inversely proportional to the half period), because it is evident from Fig. 13 that this effect is most significant for the fast blinking case of $T_{\frac{1}{2}} = 1$ sec for different cases of μ. Experimentally, we observe that no secondary flow develops in the BTRM as long as $ReS < 0.04$. In particular, for $ReS < 0.04$, the depth of the dye (less than 0.5 cm) remains constant during the course of the experiment when observed from the side of the transparent flow device. However, a significant increase in the depth of the dyed region (from less than 0.5 cm to approximately 1.0-1.5 cm) is observed for $ReS > 0.04$. Another related observation is based on the sharpness of the *holes* or unmixed regular regions such as the one shown in Fig. 11, for $ReS < 0.04$. During the course of an experiment, the fact that these islands (holes) stay as a clear unmixed region again suggests strongly that the flow must be 2-D. Therefore, the kinematic of the flow field (Stokes flow) would determine the dynamics of a material line or blob

for the period of time as long as the flow is still two-dimensional for slowly varying flows.

In dynamical systems theory, one criterion for chaotic behavior is the existence of a positive Liapunov exponent for the average rate of stretching of an infinitesimal material line. In the BTRM flow, the rate of stretching of a blob of dye shows qualitative behavior that is consistent with the onset of chaotic flows. In Fig. 14, the area of dye is plotted against the total mixing time t. The dimensionless time is equivalent to the number of 40-sec periods. In the two steady cases of regular flows ($\mu = 0$ and $\mu = \infty$), stretching of the dye blob is only *linear* in time. Mixing is extremely poor in these steady cases. However, exponential stretching occurs in the blinking protocol for μ=0.25 and 0.5. A semi-log plot is shown in Fig. 15 from which a positive exponent for the rate of increase in area of mixing for the blinking cases can be measured for the first few periods. This exponential rate of stretching of fluid elements creates thin striations rapidly in the first few periods. The exponent starts to decrease at long times because part of the dye has moved to regions of mostly linear stretching in the outer part of the domain near the side walls. Interfacial contact length (or interfacial surface area per unit depth) between the dyed and the clear fliud also increases exponentially with time as shown in Fig. 16. The results for $t < 10$ are measured from the digitized pictures directly. However, we estimate the contact length for $t \geq 10$ by dividing the total area of mixing by the thickness of a typical striation. The reason is that it is very difficult to measure the perimeters (length on both sides) of the striations when they are too thin to be distinguished via the digitized data. These striations also overlap each other at higher periods which makes measurements from the digitized image impossible except for the total area measurement. The results in Fig. 16 are comparable to Aref's results on rate of chord length stretching in a blinking-vortex flow where exponential rate of stretching is observed for chaotic systems [26]. The exponent is analogous to the Liapunov exponents for

infinitesimal portions of the blob in the mapping of the BTRM flow averaged over long time. This exponential generation of interfacial surface area is what make the chaotic flows so efficient for mixing.

4.3 Transport of Blob of Passive Tracer

Transport of fluid is important in the context of mixing where good mixing is desirable at all locations of the device. In the steady corotating flow (μ=0), convective transport of material is inhibited by the existence of invariant manifolds which make up the homoclinic orbits (the separatrix). By time-modulating the steady case to the blinking protocol in this study, materials can be transported across the separatrix (the stagnation streamline) via the *lobe dynamics* mechanism described in the earlier study by Rom-Kedar *et al.* for the OVP flow [10].

The integrable system (steady flow) considered here is the corotating two-roll mill. A large amplitude perturbation (i.e., the time-periodic counter-rotating flow) is added to the steady case which makes the particle motion chaotic. The stream function (i.e., the Hamiltonian) of the blinking protocol is represented by eqs.(3) and (4), and has the same form as a time-periodic Hamiltonian with one degree of freedom. Thus, the present system is expected to result in *tangling* (in the notion of dynamical systems theory) of the stable and unstable manifolds and thus via the lobe dynamics mechanism in an enhanced rate of fluid transport. In fact, we observe structures in the BTRM flow that show a qualitative resemblance to those predicted theoretically in the OVP flow by Rom-Kedar *et al.* [10].

The time-periodic (blinking or piecewise continuous) BTRM flow has a characteristic frequency which is $1/T$. Rom-Kedar *et al.* [10] have shown that lobe area increases with decreasing frequency for the OVP flow up to some large period. In the BTRM flow, similar results are observed. Dye patterns resembling the *lobes* are formed possibly due to the *tangling* of the stable and unstable manifolds that emanate from the central hyperbolic point, when the period is greater than

zero but still less than the total mixing time. Fig. 8 clearly shows the formation of lobes near the hyperbolic fixed point for $T = 4$ sec ($\mu = 0.05$). For this fast blinking case, the lobes formed are very small and only a small amount of fluid is transported from the region inside the separatrix to the region outside at each period (a dye blob is placed inside the right homoclinic orbit initially). This *lobe* structure is almost identical to the *tendrils* found in Aref's blinking vortex flow [8,25]. When the period is being increased, however, the size of the lobes becomes larger. Fluid patch inside one lobe will be stretched and folded when it *hops* over to another lobe that is nearer to the hyperbolic fixed point at the next period of time. One should note that these lobes are constructed by the Poincaré map so that we are marching in discrete time period in the phase space. In the flow visualization experiments, the lobe structures traced out by the dyed fluid show the dynamics of the unstable manifolds in the chaotic flows. Fluid transport across the separatrix is greatly enhanced by this mechanism of lobe dynamics.

We have also performed quantitative measurements of the amount of fluid transported from the region inside the separatrix to the region outside. In order to measure this transport rate, a thin layer of dye is placed in the annular region between the right roller and the corresponding homoclinic orbit (i.e., the separatrix) that encloses the roller. This is done by placing a thick line of dye inside the right separatrix and running the experiment with μ=0 (one-roller rotating) for a few minutes until a homogeneous area of dye has filled in the annulus region, that is labelled as region B. The annular region on the left is labelled as region A whereas the outer region is C. Fig. 17 shows the a time sequence of pictures for $\mu = 0.25$ to show the dyed fluid being transported from one region to another. The measurements are performed from the digitized pictures by superimposing the separatrix from the steady case with the pictures from the blinking cases to identify dyed fluids in different regions. For the cases of $t = 0.5$ and $t = 1.5$ in Fig. 17, the *lobe* structure that emanates from the right separatrix provides the

primary mechanism for fluid transport. Fig. 18 shows the measured area of fluid transport from region B to the outer region C for two different flow strengths. It is apparent that fluid transport is greatly enhanced by increasing the value of μ. The amount of fluid transport to the outer region for $\mu = 0.50$ is two times that for the case $\mu = 0.125$ at $t = 2$. Thus, the fluid transport by the so-called *lobe* dynamics in the BRTM flow determines the extent of the region of chaotic mixing.

4.4 Reversibility of Chaotic Flows and Sensitivity to Initial Conditions

For integrable systems such as the steady (or time-independent) corotating, counter-rotating, and *Couette* flows, the particle trajectories coincide with the streamlines on which they are initially located. Neglecting inertial and transient effects, these steady flows must be reversible which is a consequence of the linearity of Stokes equation describing the flow. Fig. 19 shows a time sequence of reversibility experiments for $\mu = 0.05$ which is in the transition regime to chaotic mixing. The dye blob, that is initially placed near the central hyperbolic point, is being stretched and wrapped around the separatrix forward and backward for 10 periods. The dye reverts back almost precisely to its original shape except for a small filament emanating from the stagnation point where most of the folding and stretching of dye occurs.

For large flow strength where chaotic mixing is present, the flow is not reversible after even two periods. The reason for irreversiblity of the flow is the presence of Smale horseshoe structure where neighboring fluid elements separate exponentially in time. Any small disturbance in the flow, such as mechanical vibration or inertia at the moment of switching on and off the motors, in the flow would alter particle trajectories, by a large amount. This effect would then be amplified due to the presence of the Smale horseshoe. Fluid elements would no longer reverse along their original trajectory when the flow is reversed. Similar results were shown by Khakhar *et al.* [8] in a computer-simulated experiment

where the disturbance arose from numerical error because of finite accuracy in the computer.

Another observation regarding the sensitivity to initial conditions in chaotic flows is shown in Figs. 20a and 20b. Two identical blinking flow experiments for the case of $\mu = 0.125$ are performed with the inital dye blobs being placed at distinct locations. In the first case (Fig. 20a), regular mixing occurs when the position of the dye blob is outside the region of chaotic mixing. Dye tracer only advects along streamlines with little or no mixing. However, when the dye blob is positioned near the central hyperbolic point which is within the chaotic mixing region, efficient mixing is achieved as shown in Fig. 20a. This is the reason that the preceeding mixing experiments were all carried out with the same initial location for the dye blob so that essential features of the mixing experiments inside the chaotic region are retained.

5. Concluding Remarks

The chaotic advection of a fluid particle is observed in the 2-D time-periodic BTRM flow when the characteristic period of oscillation, μ, is larger than about 0.125. Morphological structures resembling the Smale horseshoe are revealed by the mixing experiments and thus suggests chaotic mixing in the flow. This chaotic flow provides efficient mixing over a large region of the flow device, which can be achieved by either increasing the roller speed or the time period for the alternate rotation of the cylinders. The digital imaging technique is essential for obtaining quantitative measurements of the rate of stretching of the dye blob, and of the rate of fluid transport in different domains of the flow device. The exponential rate of increase of interfacial contact length of the dye blob can be related to a positive Liapunov exponent in the context of dynamical systems as another proof for chaos. Some unmixed regions (islands) are also observed that might be the result of resonant structures when the period of the fixed point in the island is a

multiple of the characteristic period of the flow. These islands can also exist due to an incomplete horseshoe [7].

The main accomplishment of this study is to provide quantitative measurement of mixing properties (area of mixing and fluid transport rates) in chaotic flows. These mixing properties are related qualitatively to theoretical predictions for chaos using dynamical systems theory. By applying dynamical system theory in the context of laminar mixing or vice versa, we are one step closer to a better understanding of the dynamical behavior of the time-periodic flows that occur in many mixing applications. We are currently in the process of obtaining detailed theoretical predictions of transport rates, lobe structure, area of mixing, etc., for both an unbounded two-roll mill, and for a two-roll mill in a box of the same lateral dimensions used here. The theoretical framework of nonlinear dynamics shows that the phenomena observed are *robust* in the sense that we should expect only quantitative, rather than qualitative differences, due to the idealizations inherent in the assumptions of a quasi-steady, two-dimensional Stokes flow that are built in to the theory. However, the present study will provide the first quantitative comparison between theory and experiment, from which to see how important those differences may be.

References

[1] Danckwerts, P. V., *Appl. Sci. Research,* **A3**, 279 (1952).

[2] Calderbank, P. H., *Trans. Inst. Chem. Eng.*, **36**, 443 (1958).

[3] Uhl, V. H., Gray, J. B., eds., *Mixing: Theory and Practice*, Vol. I, Academic Press, New York (1966).

[4] Uhl, V. H., Gray, J. B., eds., *Mixing: Theory and Practice*, Vol. II, Academic Press, New York (1967).

[5] Spencer, R. S., Wiley, R. M., *J. Colloid Sci.*, **6**, 133 (1951).

[6] Mohr, W. D., Saxton, R. L., Jepson, C. H., *Ind. Eng. Chem.*, **49**, 1855, 1857 (1957).

[7] Ottino, J. M., Leong, C. W., Rising, H., Swanson, P. D., *Nature,* **333**, 419 (1988).

[8] Khakhar, D. V., Rising, H., Ottino, J. M., *J. Fluid Mech.*, **172**, 419 (1986).

[9] Aref, H., *J. Fluid Mech.*, **143**, 1 (1984).

[10] Rom-Kedar, V., Leonard, A., Wiggins, S., "*An Analytical Study of Transport, Mixing and Chaos in an Unsteady Vortical Flow,*" *J. Fluid Mech.*, to appear (1989).

[11] Wiggins, S., *Nature,* **333**, 395 (1988).

[12] Chaiken, J., Chevray, R., Tabor, M., Tan, Q. M., *Proc. Roy. Soc. Lond. A.*, **408**, 165 (1986).

[13] Chaiken, J., Chu, C. K., Tabor, M., Tan, Q. M., *Phys. Fluids,* **30**, 687 (1987).

[14] Chien, W.-L., Rising, H., Ottino, J. M., *J. Fluid Mech.*, **170**, 355 (1986).

[15] Khakhar, D. V., Chella, R., Ottino, J. M., *Adv. Rheology,* **2**, (Fluids), 81 (1984).

[16] Lichtenberg, A. J., Lieberman, M. A., *Regular & Stochastic Motion*, Springer Verlag, New York (1983).

[17] Moser, J., *Stable and Random Motions in Dynamical Systems*, Princeton University Press (1973).

[18] Doherty, M. F., Ottino, J. M., *Chem. Eng. Sci.*, **43**, 139 (1988).

[19] Guckenheimer, J., Holmes, P., *Nonlinear Oscillations, Dynamical Systems, and Bifurcations of Vector Fields*, Springer-Verlag, New York (1983).

[20] Berry, M. V., Balazs, N. L., Tabor, M., Voros, A., *Ann. Phys.*, **122**, 26 (1979).

[21] Khakhar, D. V., Franjione, J. G., Ottino, J. M., *Chem. Engng. Sci.*, **42**, 2909 (1987).

[22] Dunlap, P. N., Ph. D. Thesis, California Institute of Technology, Pasadena (1986).

[23] Frazer, R. A., *Phil. Trans. Roy. Soc.*, **A225**, 93 (1925).

[24] Ng, R. C.-Y., James, D. F., Leal, L. G., "*Chaotic Mixing and Transport in a Two-Dimensional Time-Periodic Stokes Flow – the Blinking Two-Roll Mill (BTRM): II. Dilute Polymer Solution,*" to appear (1989).

[25] Lagnado, R., Ph. D. Thesis, California Institute of Technology, Pasadena (1986).

[26] Aref, H., Tryggvason, G., *Physica*, **12D**, 59 (1984).

Figure Captions

Figure 1. Schematic streamlines for the steady corotating two-roll mill flow.

Figure 2. A perturbed Poincaré map with transverse intersection of homoclinic orbits leading to homoclinic tangles (or lobes).

Figure 3. Experimental equipment for the BTRM flow: (a) schematic of experiment; (b) photograph for the flow device.

Figure 4. Roller speed versus time for the two rollers, with $T_{\frac{1}{2}}$ being the half period, and $\omega_1 = \omega_2$ for the BTRM experiments.

Figure 5. Streamline patterns for three possible steady flow protocols in the two-roll mill: (a) corotating ($\mu = 0$); (b) one rotating cylinder ($\mu = \infty$); (c) counter-rotating.

Figure 6. Dye patterns in the BTRM experiment for $\mu = 0.05$, $T_{\frac{1}{2}} = 2$ sec, and at various times: (a) t = 0, (b) t = 5, (c) t = 10, and (d) t = 15 (total mixing time = t $\times$40 sec).

Figure 7. Dye patterns in the BTRM experiment for $\mu = 0.50$, $T_{\frac{1}{2}} = 20$ sec, and at various times: (a) t = 0, (b) t = 5, (c) t = 10, and (d) t = 15 (total mixing time = t $\times$40 sec).

Figure 8. Tendril-like structure near the central hyperbolic fixed point for $\mu = 0.05$, $\omega = 1.75$ rad/sec, and $T_{\frac{1}{2}} = 2$ sec.

Figure 9. A sequence of pictures for $\mu = 1.0$ and $T_{\frac{1}{2}} = 40$ sec for the CW/TCP solution at various times: (a) t = 1.0; (b) t = 1.5; (c) t = 2.0; (d) t = 2.5; (e) t = 3.0. The arrow indicates possible location of a horseshoe.

Figure 10. A superimposed picture of the dye pattern (forward map) and its mirror image (backward map) for the case of $t = 2.5$ in Fig. 9. Note

that the possible horseshoe formation along the central region with transverse intersection of streamlines.

Figure 11. Islands of unmixed fluid or regular regions (bright patches of clear fluid at some distance away from the upper and lower side of the rollers) inside the chaotic mixing area at the total mixing time $t = 15$ and two cases of μ: (a) $\mu = 0.125(T_{\frac{1}{2}} = 1 \text{ sec}, \omega = 17.45\text{rad/sec})$; (b) $\mu = 0.50(T_{\frac{1}{2}} = 20 \text{ sec}, \omega = 1.75\text{rad/sec})$.

Figure 12. Area of mixing (dye coverage) A, normalized by A_R (area of the roller), versus the characteristic period μ in the CW/TCP solution at various roller speeds ω(rad/sec): $\omega = 1.745(*)$; $\omega = 4.363(\bullet)$; $\omega = 8.725(+)$; $\omega = 17.450(\triangle)$.

Figure 13. Area of mixing (dye coverage) A, normalized by A_R (area of the roller), versus the characteristic period μ in the CW/TCP solution for various half period $T_{\frac{1}{2}}$(sec): $T_{\frac{1}{2}} = 1(\circ)$; $T_{\frac{1}{2}} = 2(\triangle)$; $T_{\frac{1}{2}} = 4(+)$; $T_{\frac{1}{2}} = 8(\bullet)$; $T_{\frac{1}{2}} = 20(*)$. The solid line is for the fast blinking case of $T_{\frac{1}{2}} = 1$ sec to illustrate increase in mixing area due to transient effect.

Figure 14. Area of mixing (dye coverage) A, normalized by A_R (area of the roller), versus dimensionless time t (physical time $t' = 40 \times$ t sec) in the CW/TCP solution for various values of the characteristic period: $\mu = 0.00(\times)$; $\mu = 0.25(+)$; $\mu = 0.50(\triangle)$; $\mu = \infty(\square)$.

Figure 15. A semi-log plot of the area of mixing (dye coverage) A, normalized by A_R (area of the roller), versus dimensionless time t (physical time $t' = 40 \times$ t sec) in the CW/TCP solution for various values of the characteristic period that would result in chaotic mixing: $\mu = 0.25(+)$;

$\mu = 0.50(*)$. The case for CW45 solution at $\mu = 0.50(\triangle)$ is shown here to illustrate similar results for fluids of different viscosities.

Figure 16. Interfacial contact length L (interfacial surface area per unit depth) versus dimensionless time t (physical time $t' = 40 \times$ t sec) in the CW/TCP solution for $\mu = 0.50$ and $T_{\frac{1}{2}} = 20$ sec.

Figure 17. A sequence of pictures for $\mu = 0.50$ and $T_{\frac{1}{2}} = 20$ sec at various times: (a) t = 0.00; (b) t = 0.50; (c) t = 1.00; (d) t = 1.50. Inset shows the different regions inside and outside the separatrix.

Figure 18. Fluid transport into region C (A_C), normalized by the area of annulus of dye in region B (A_{B_o}) at t = 0, versus dimensionless time t for the CW/TCP solution for two cases of μ: $\mu = 0.125$ (dashed line, $\times$); $\mu = 0.50$ (solid line, $\triangle$).

Figure 19. A sequence of pictures for $\mu = 0.05$ and $T_{\frac{1}{2}} = 2$ sec at various times t (physical time $t' = 40 \times$ t sec): (a) t = 0.0; (b) t = 1.0; (c) t = -1.0. Note that negative value of t indicates a backward transform for the experiment, i.e., the rotation direction and order of rotation for the two rollers are reversed.

Figure 20. Different initial conditions for $\mu = 0.125$, $T_{\frac{1}{2}} = 5$ sec, and total mixing $t' = 600$ sec: (a) initial dye blob inside the chaotic mixing region; (b) initial dye blob outside the chaotic mixing region (at the bottom left corner).

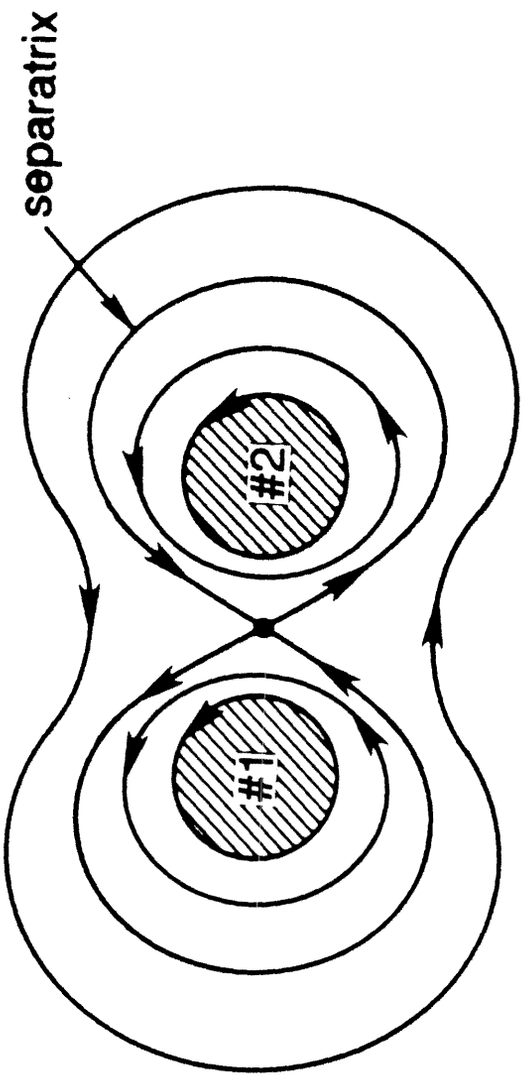

Fig. 1

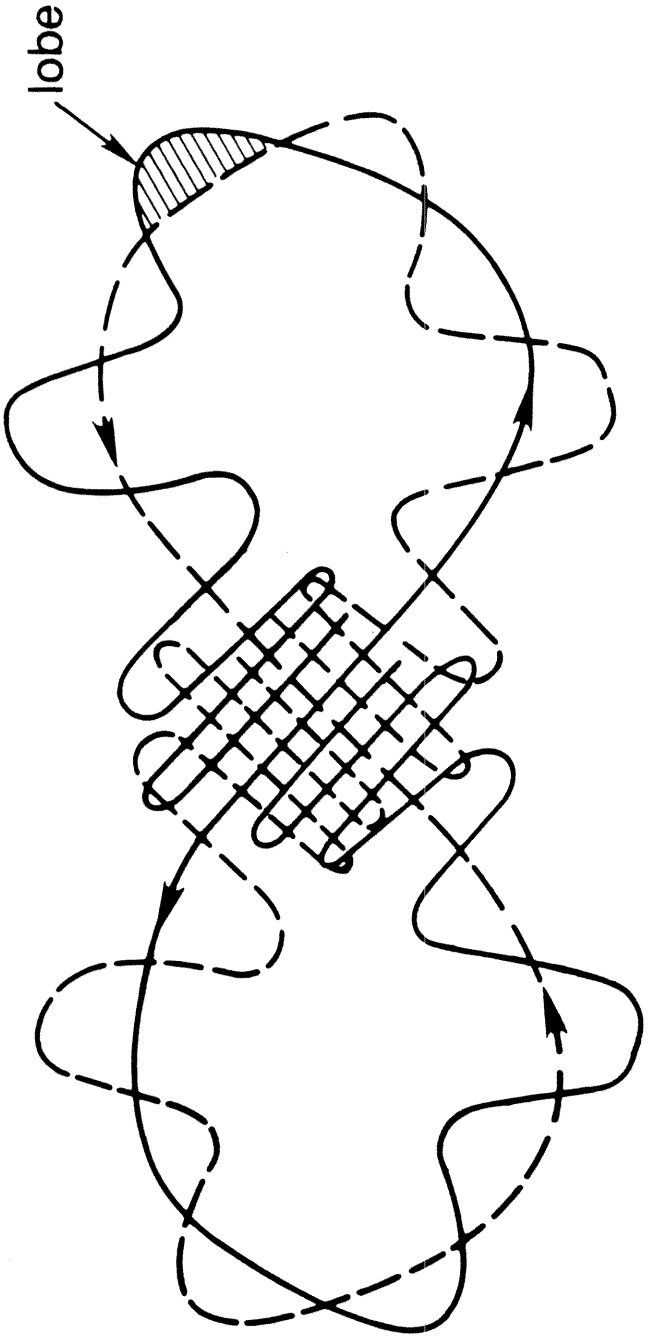

Fig. 2

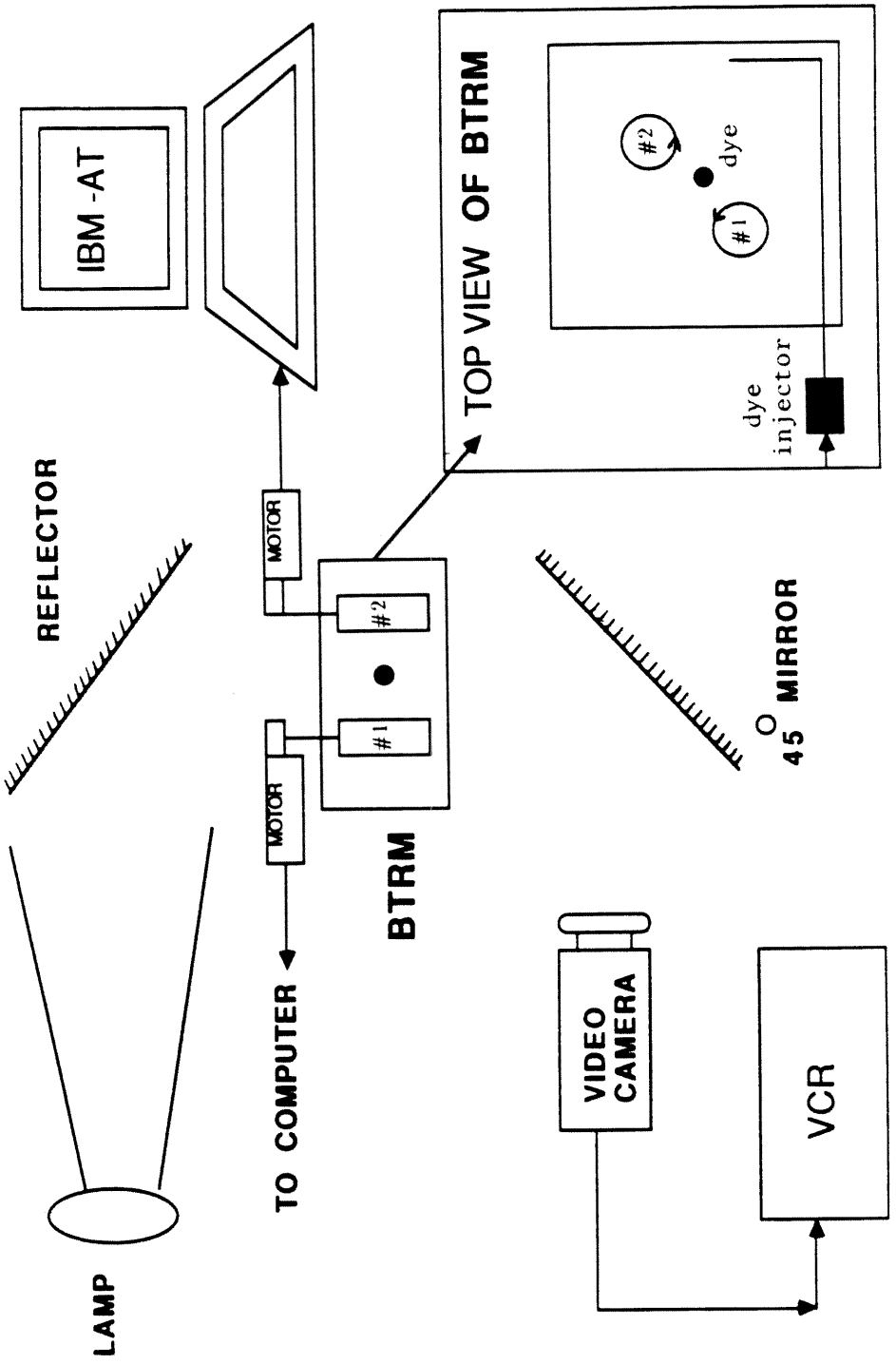
IBM -AT
REFLECTOR
MOTOR
TOP VIEW OF BTRM
#2
dye
#1
dye
injector
#2
#1
MOTOR
BTRM
45° MIRROR
LAMP
TO COMPUTER
VIDEO
CAMERA
VCR

Fig. 3(a)

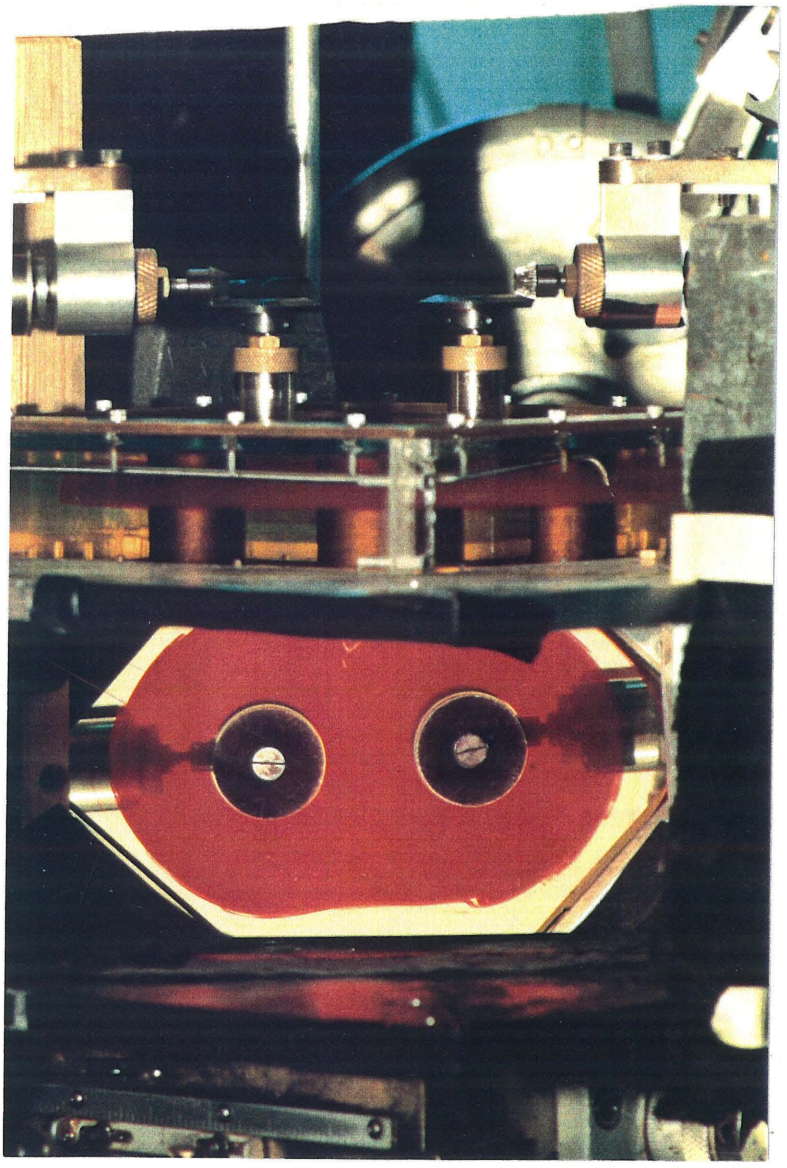

Fig. 3 b

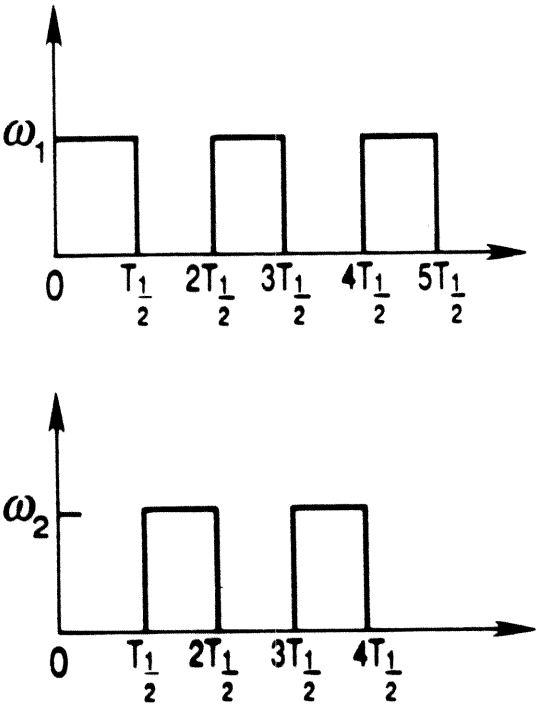
ω_1
0
$T_{\frac{1}{2}}$
$2T_{\frac{1}{2}}$
$3T_{\frac{1}{2}}$
$4T_{\frac{1}{2}}$
$5T_{\frac{1}{2}}$
ω_2
0
$T_{\frac{1}{2}}$
$2T_{\frac{1}{2}}$
$3T_{\frac{1}{2}}$
$4T_{\frac{1}{2}}$

Fig. 4

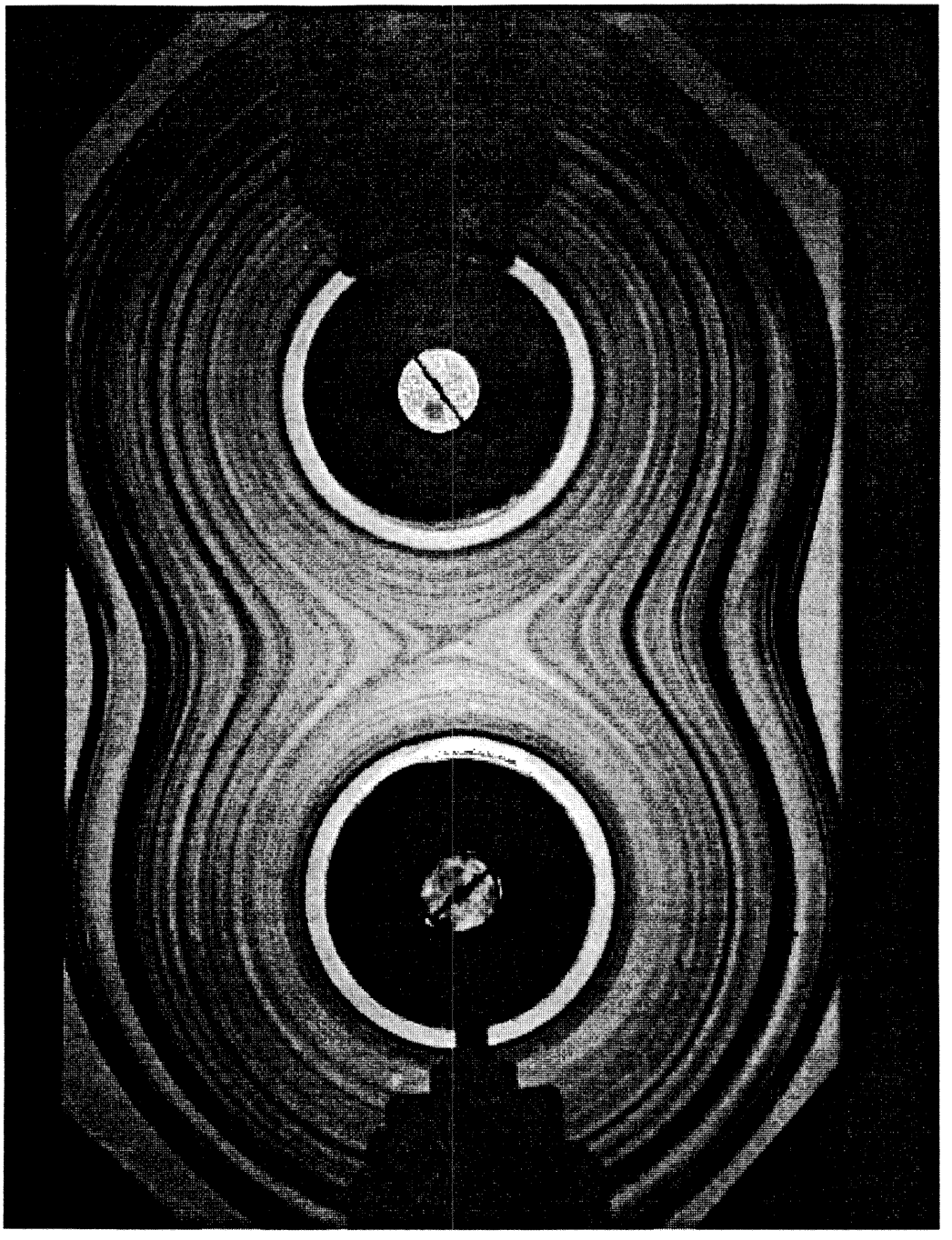

Fig. 5(a)

Fig. 5(b)

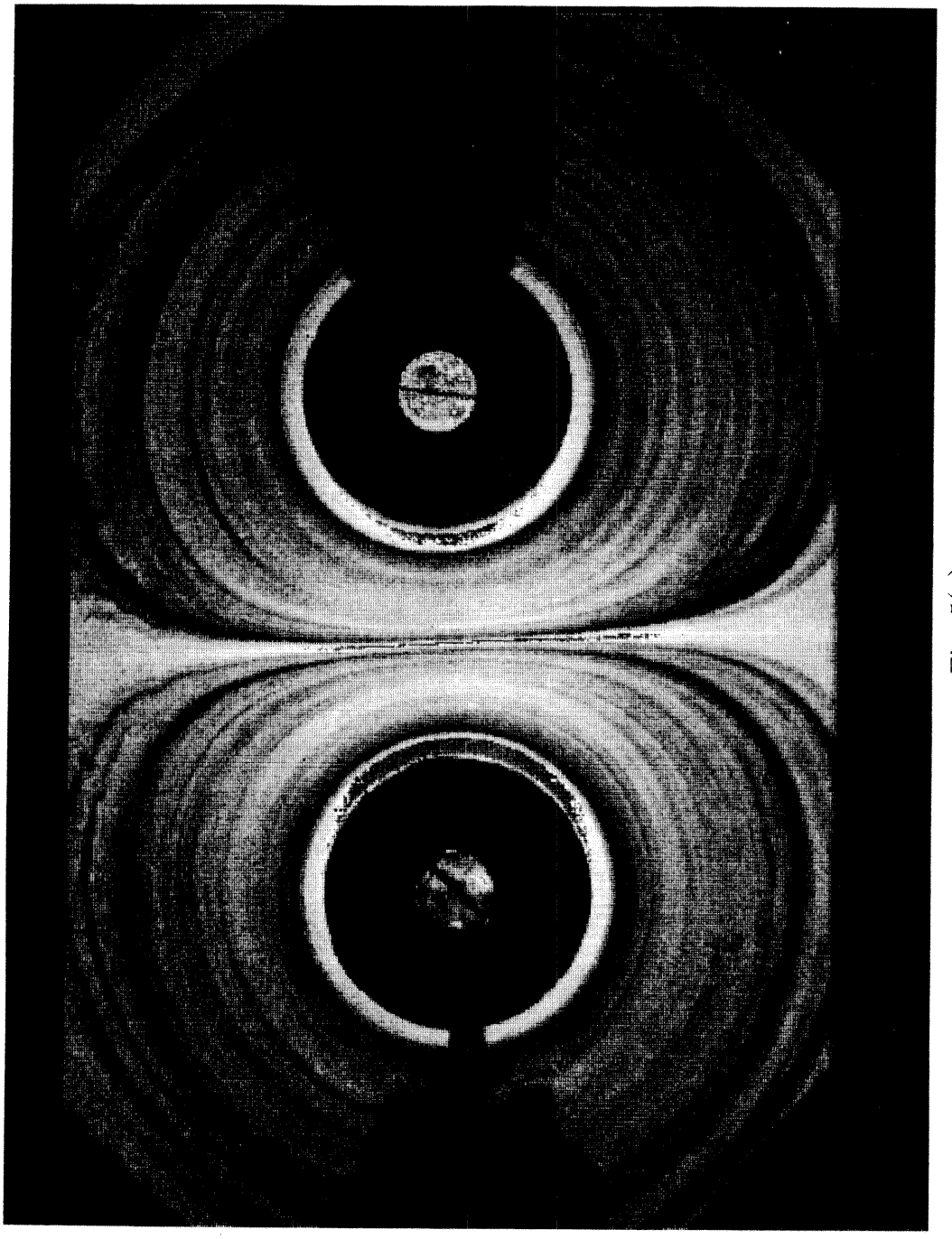

Fig. 5(c)

(a)

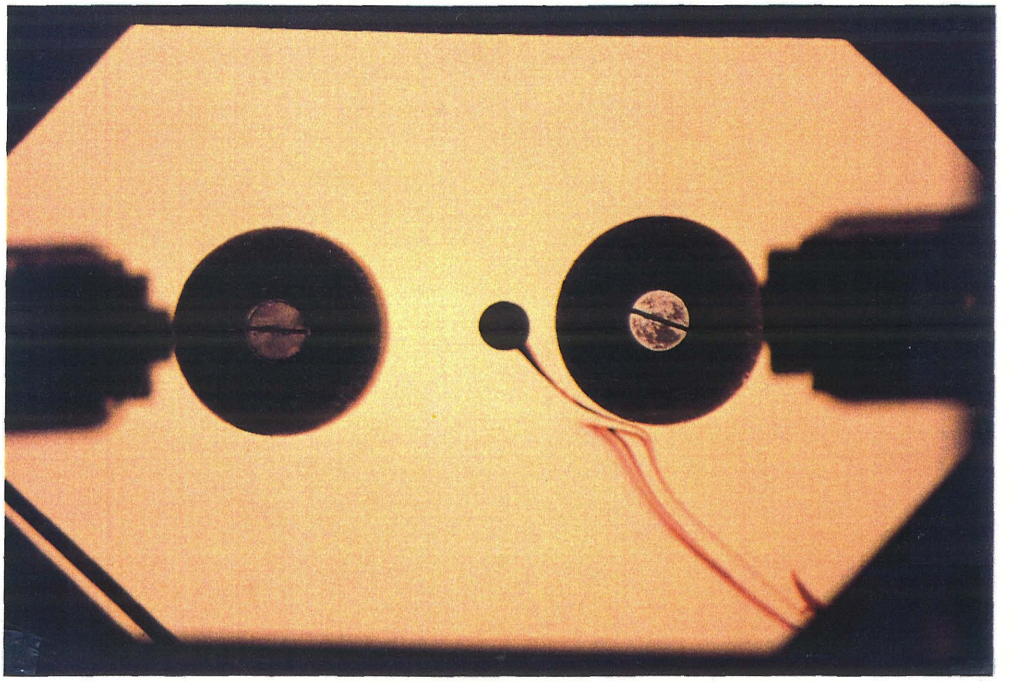

(b)

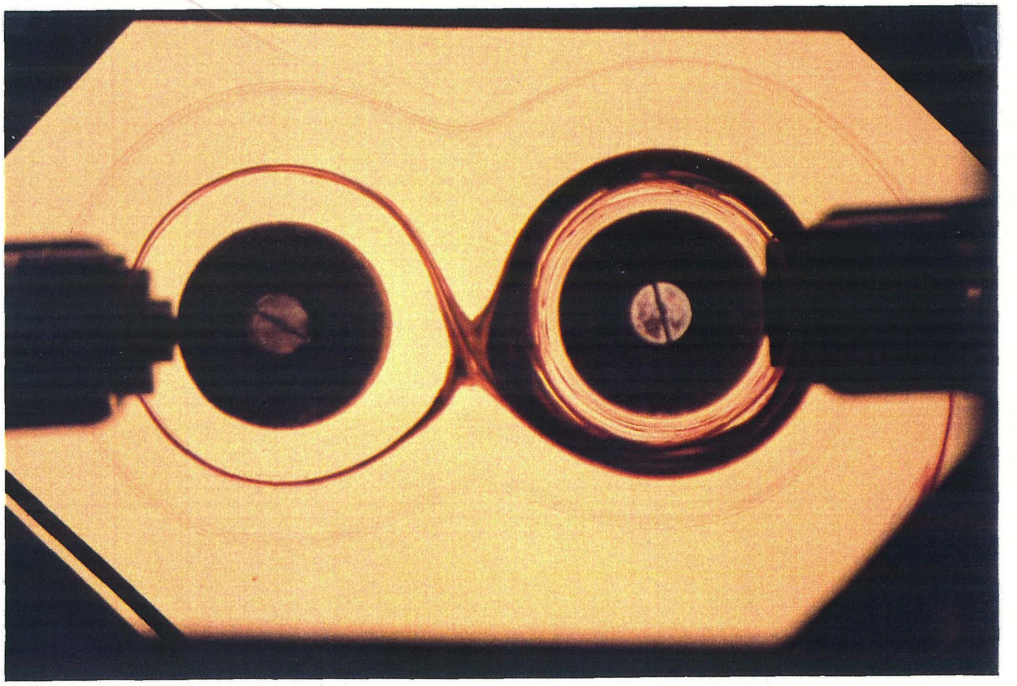

Fig. 6

(c)

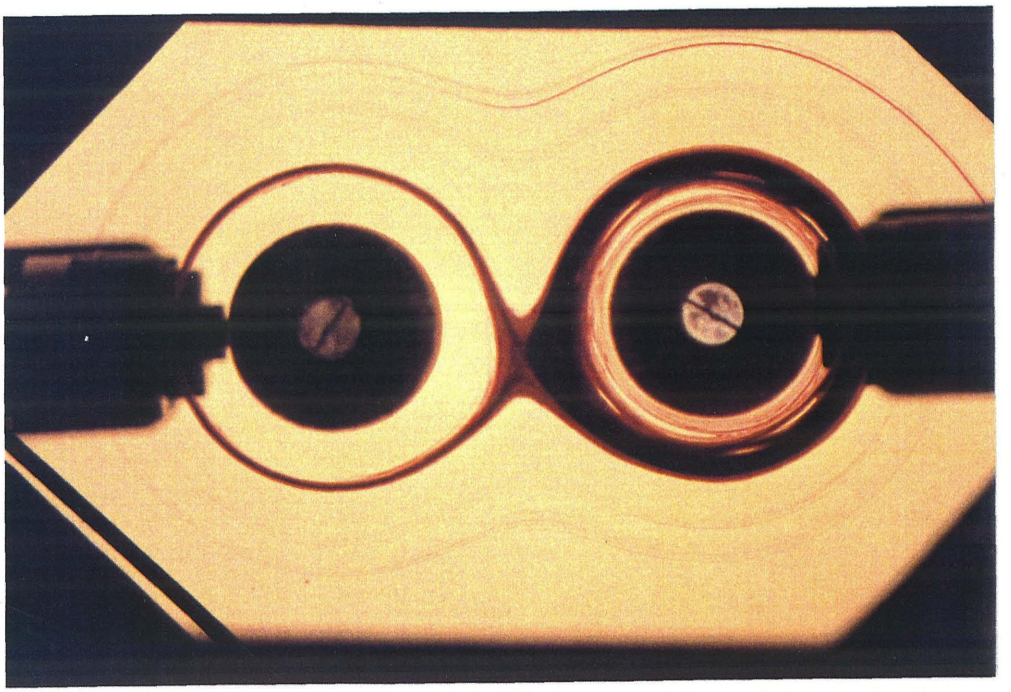

(d)

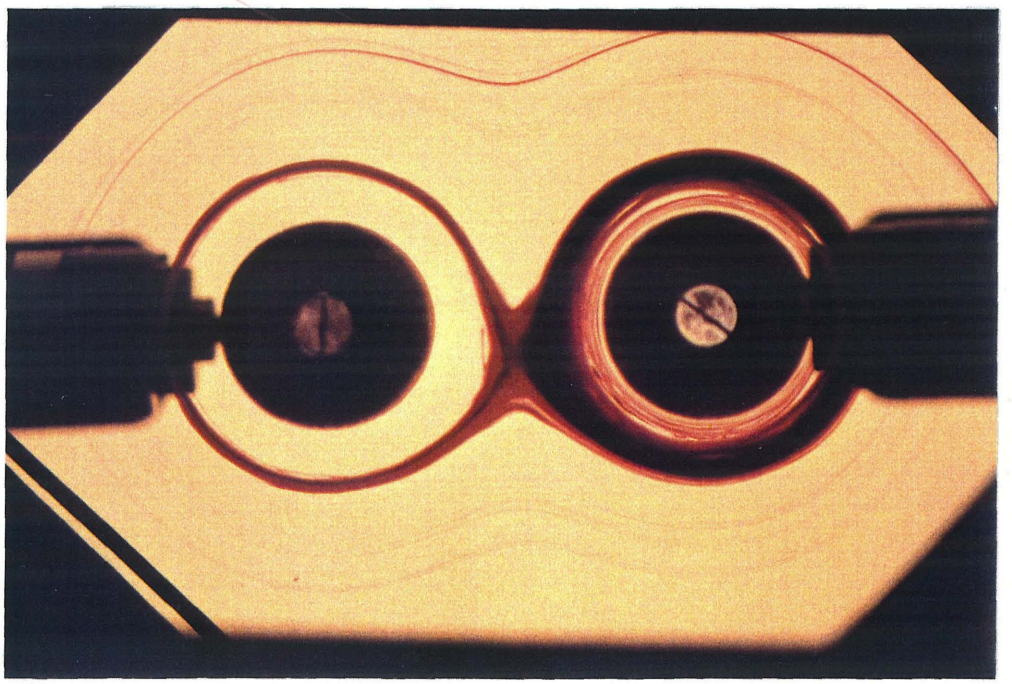

Fig. 6

(a)

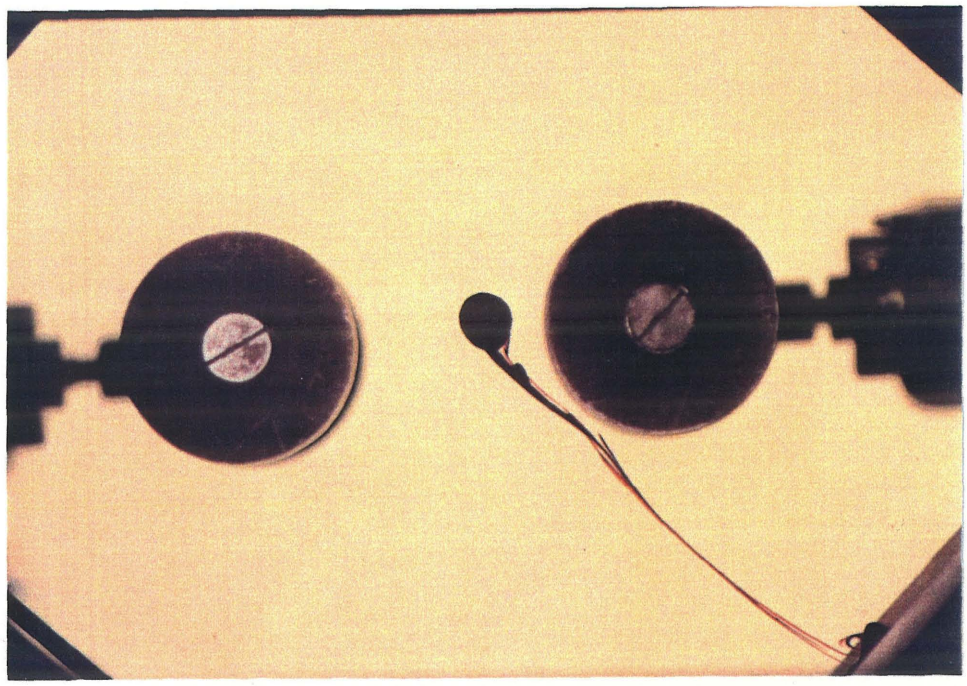

(b)

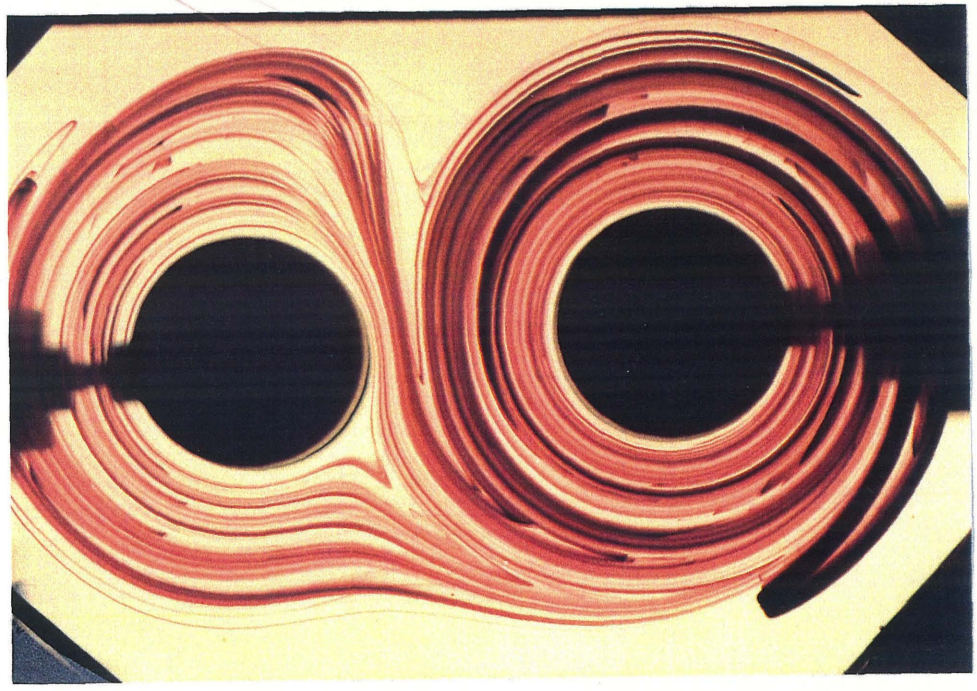

Fig. 7

(c)

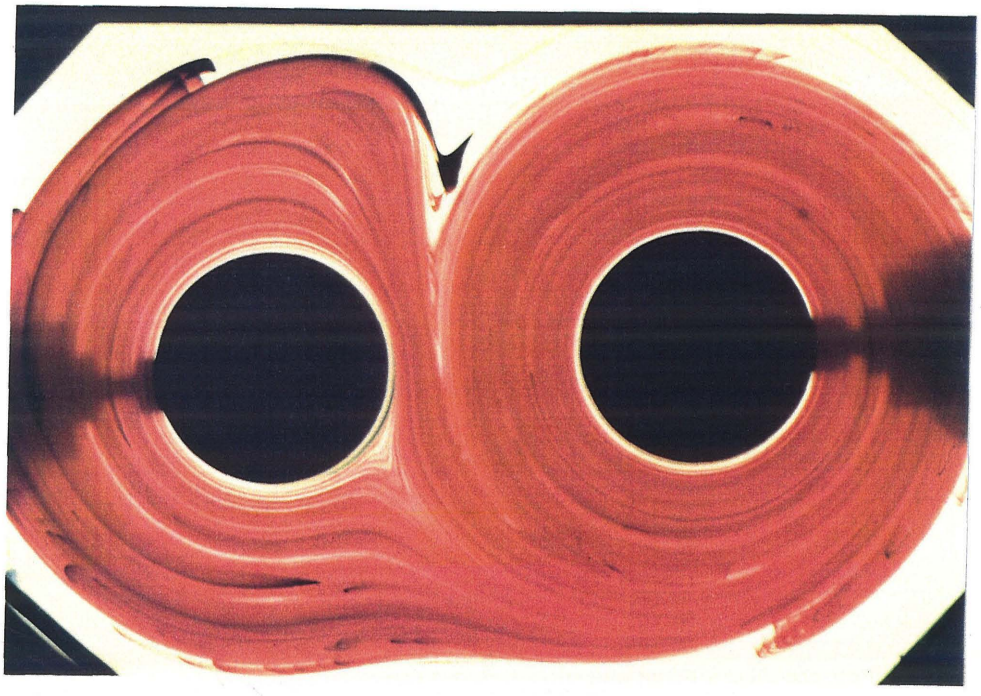

(d)

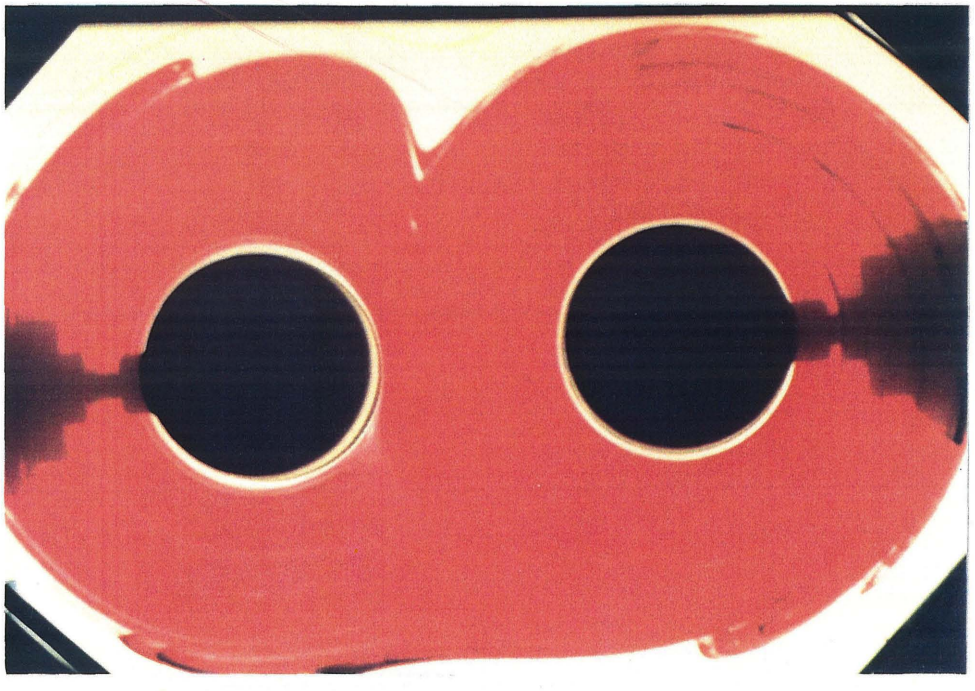

Fig. 7

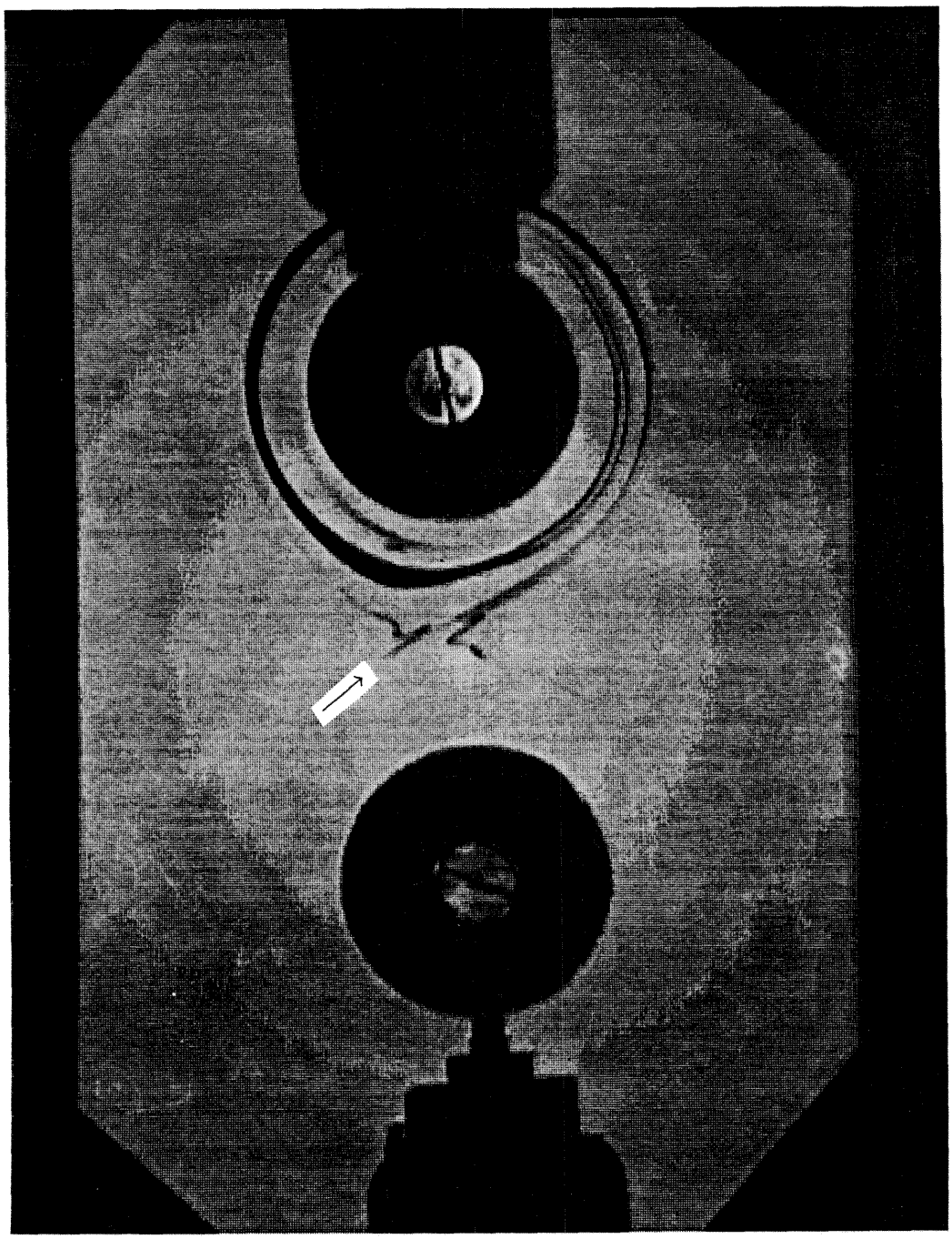

Fig. 8

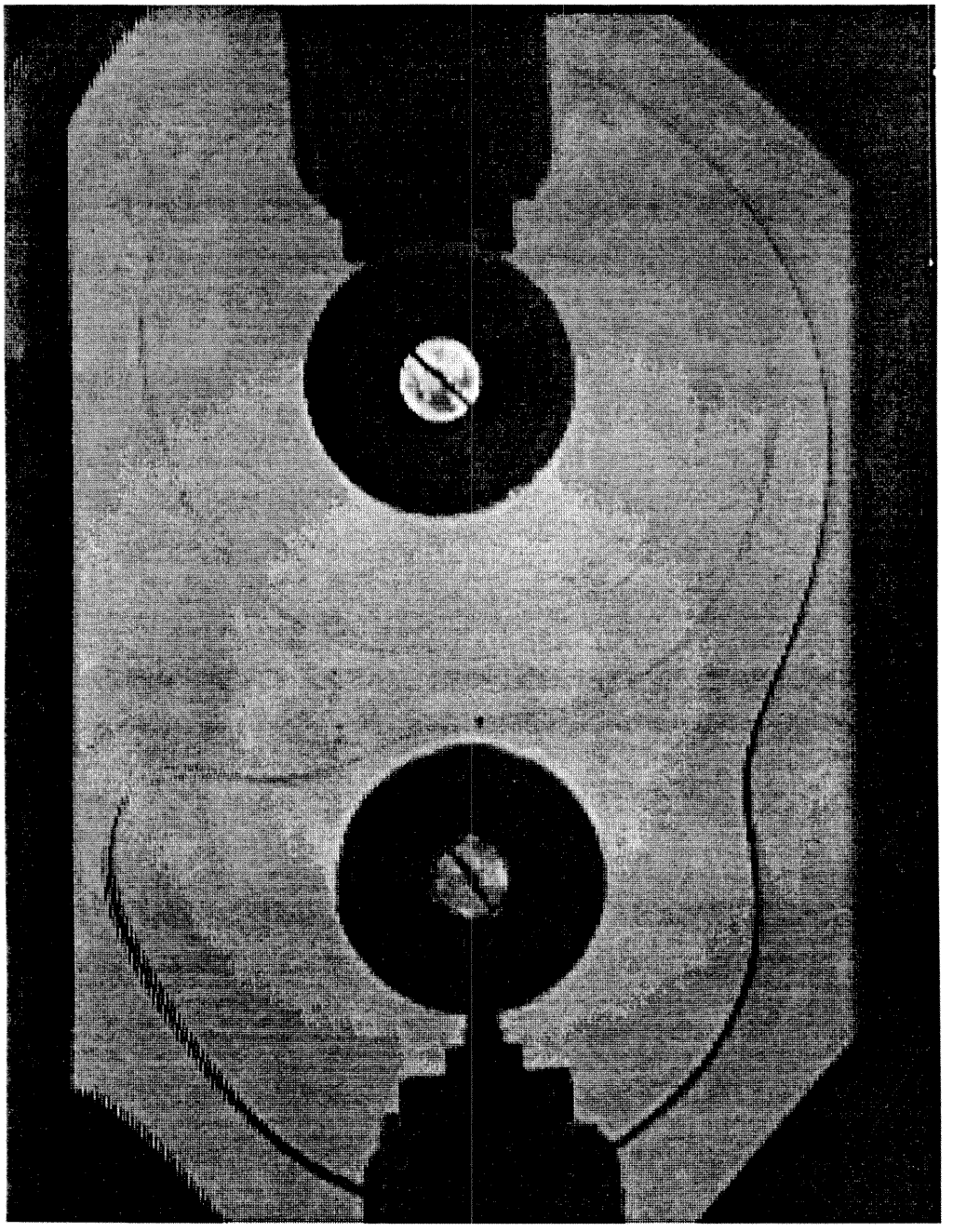

Fig. 9(a)

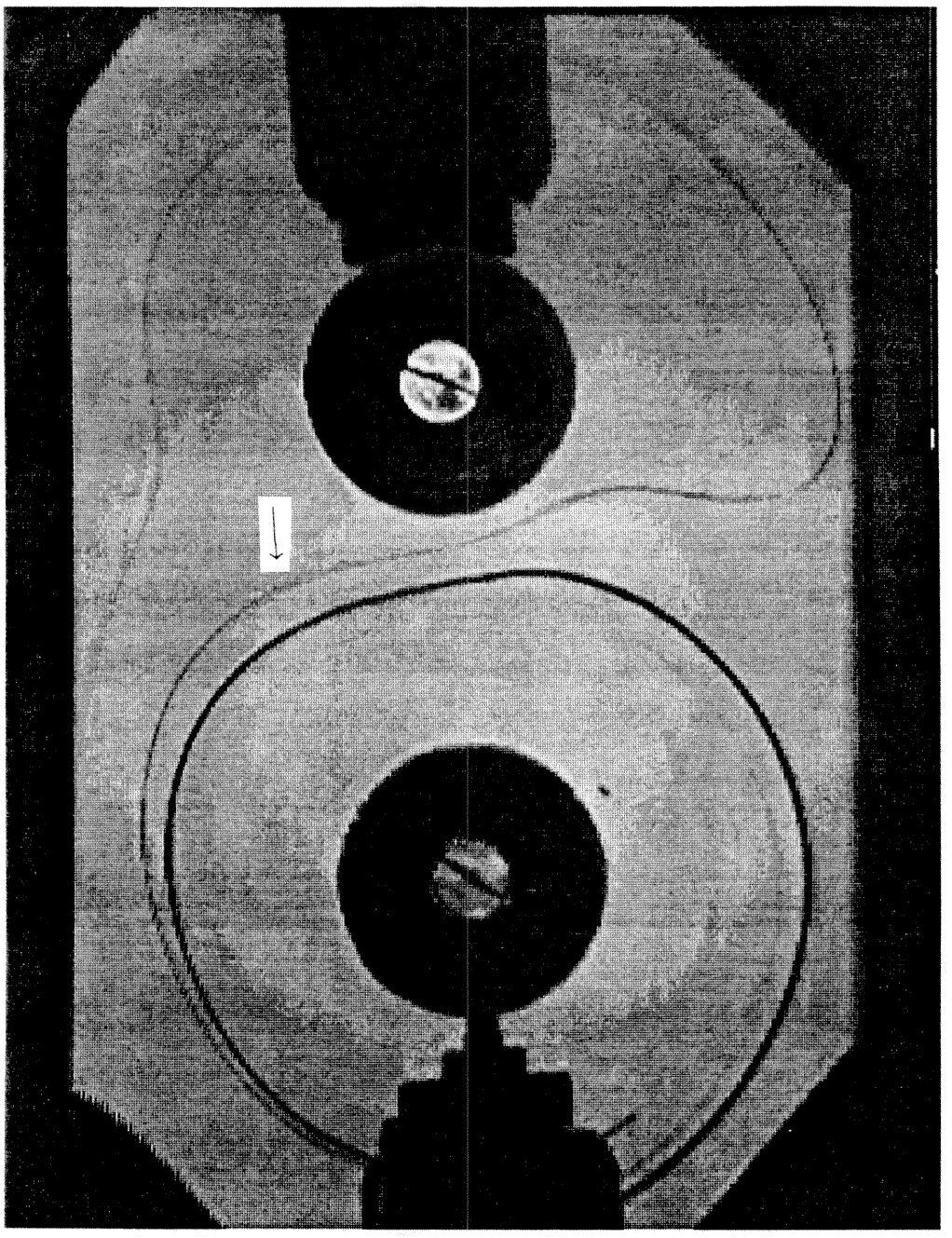

Fig. 9(b)

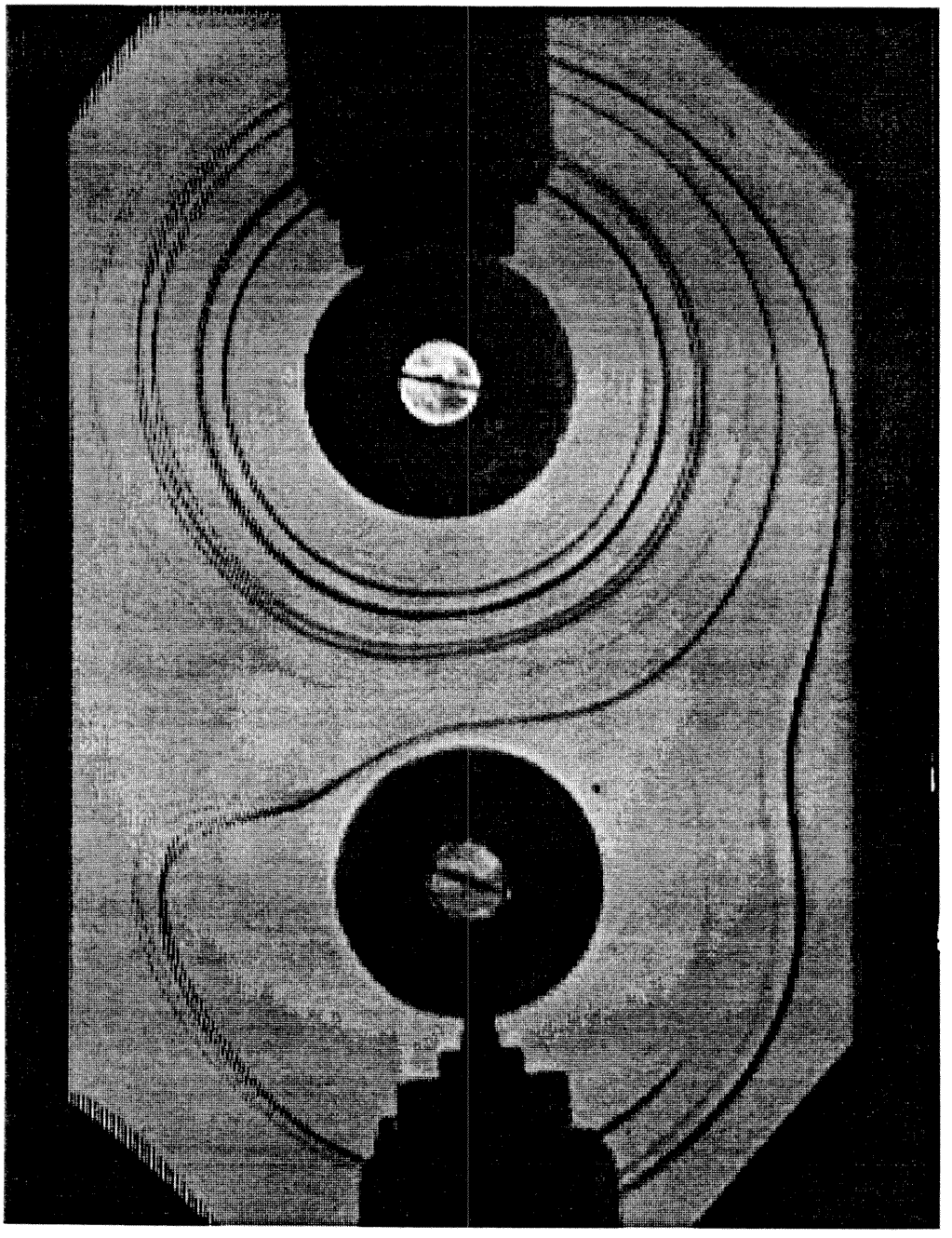

Fig. 9(c)

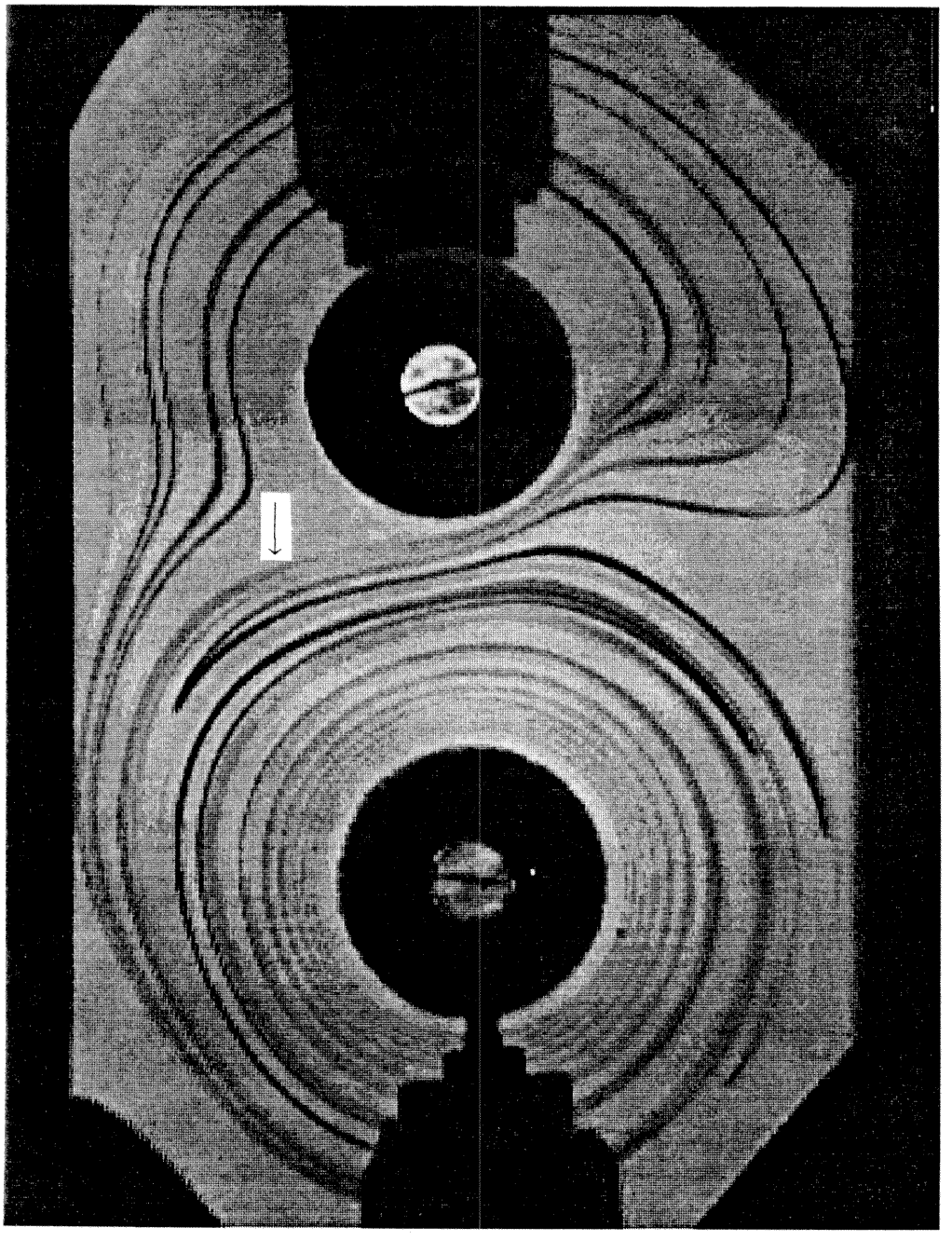

Fig. 9(d)

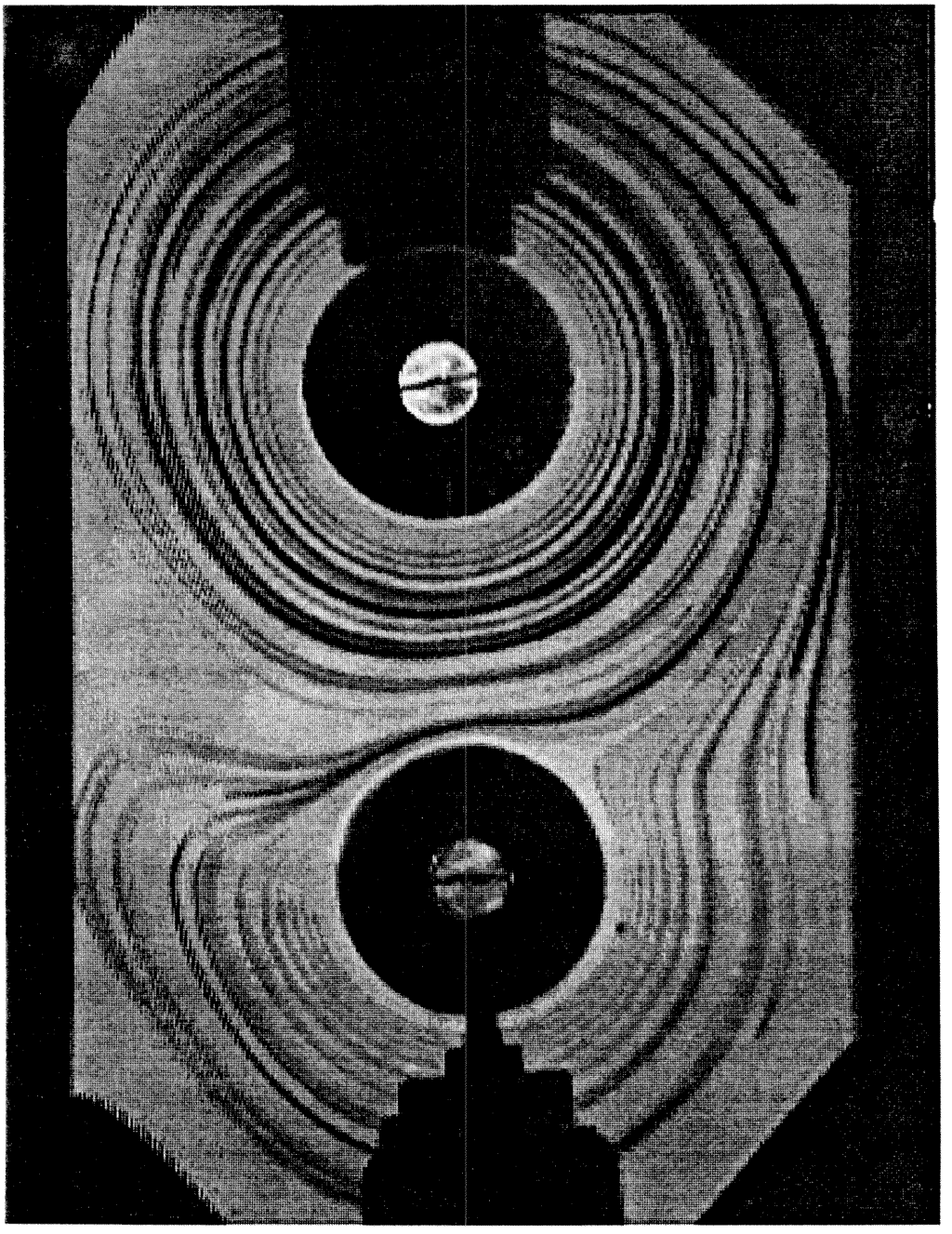

Fig. 9(c)

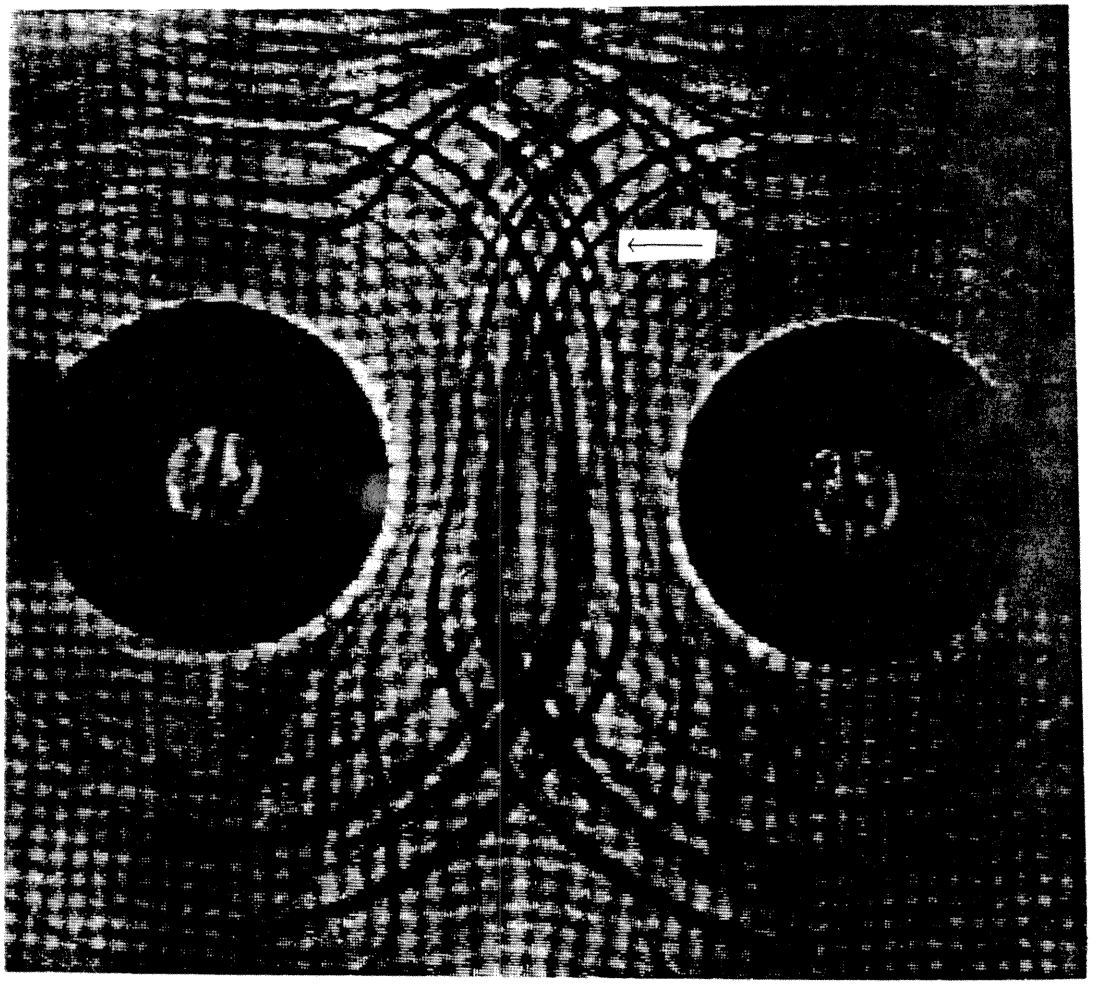

Fig. 10

(a)

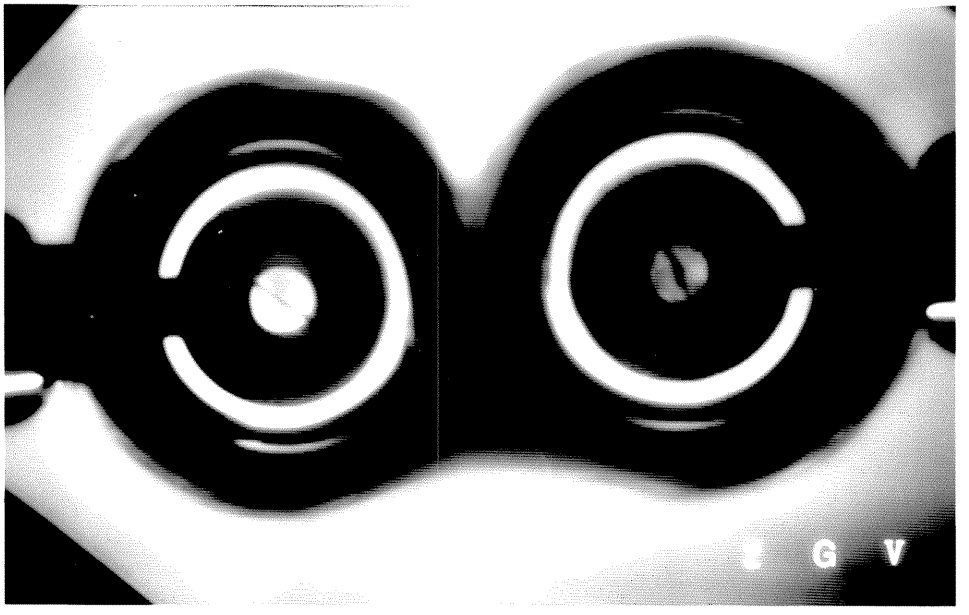

(b)

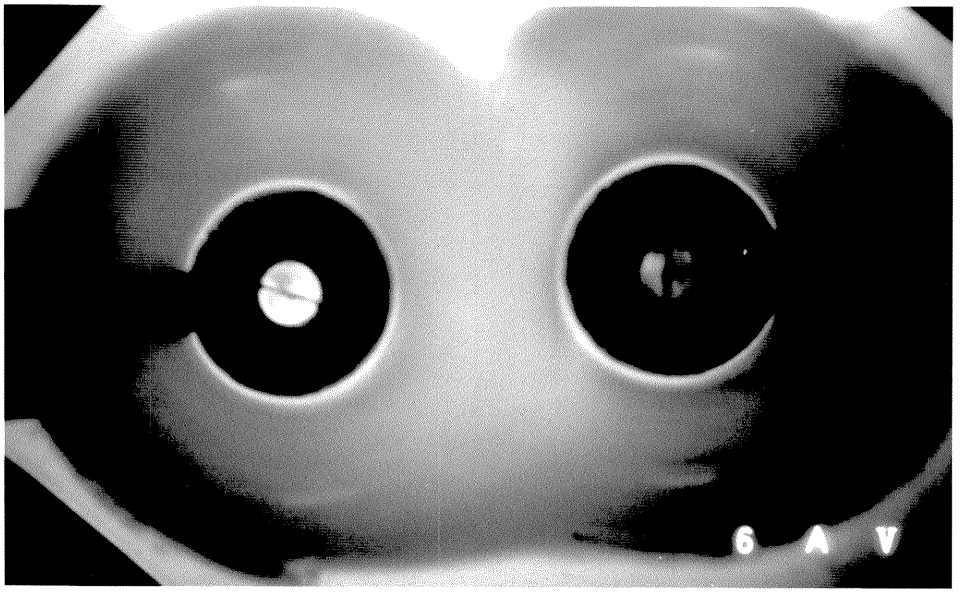

Fig. 11

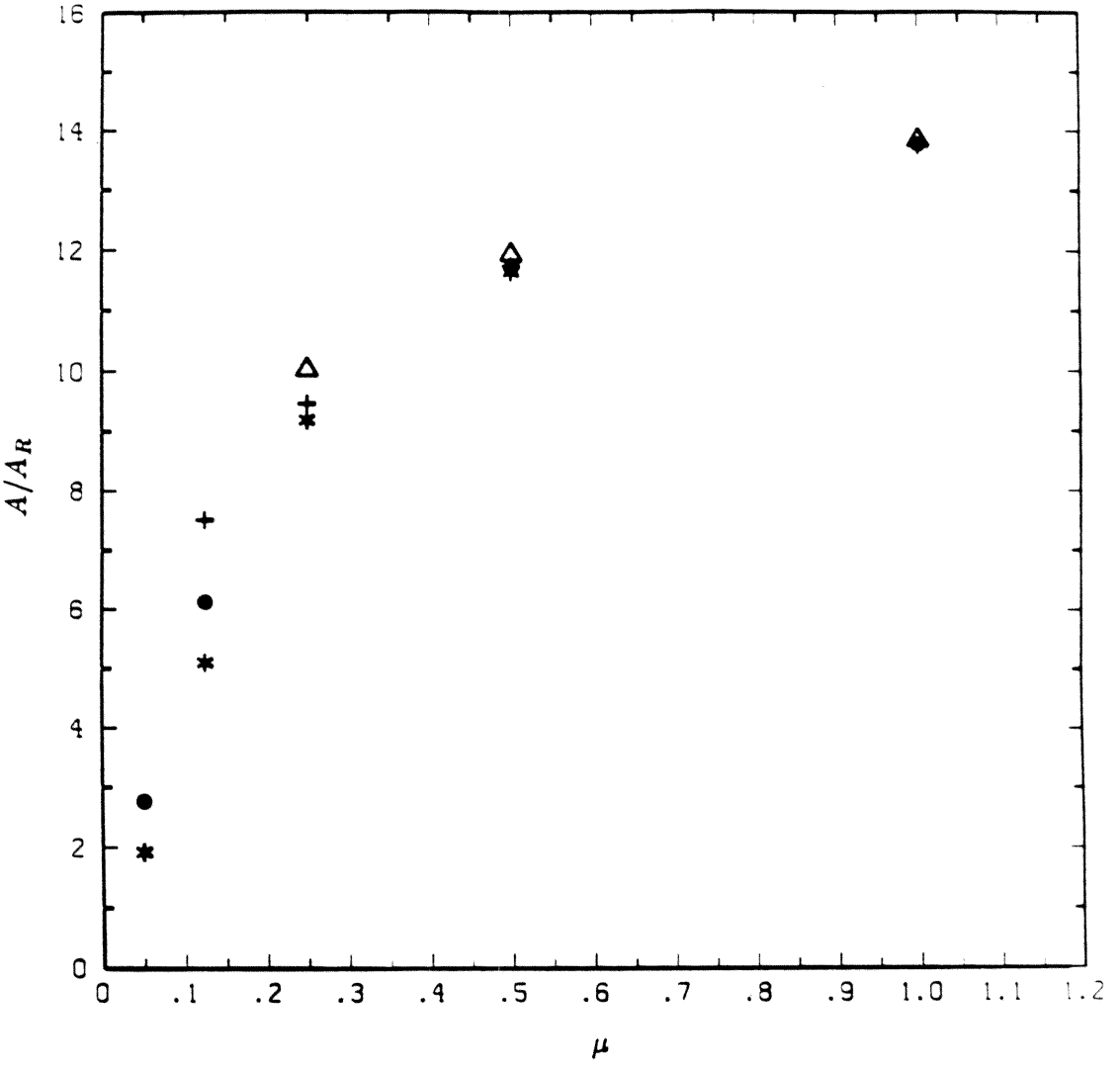

Fig. 12

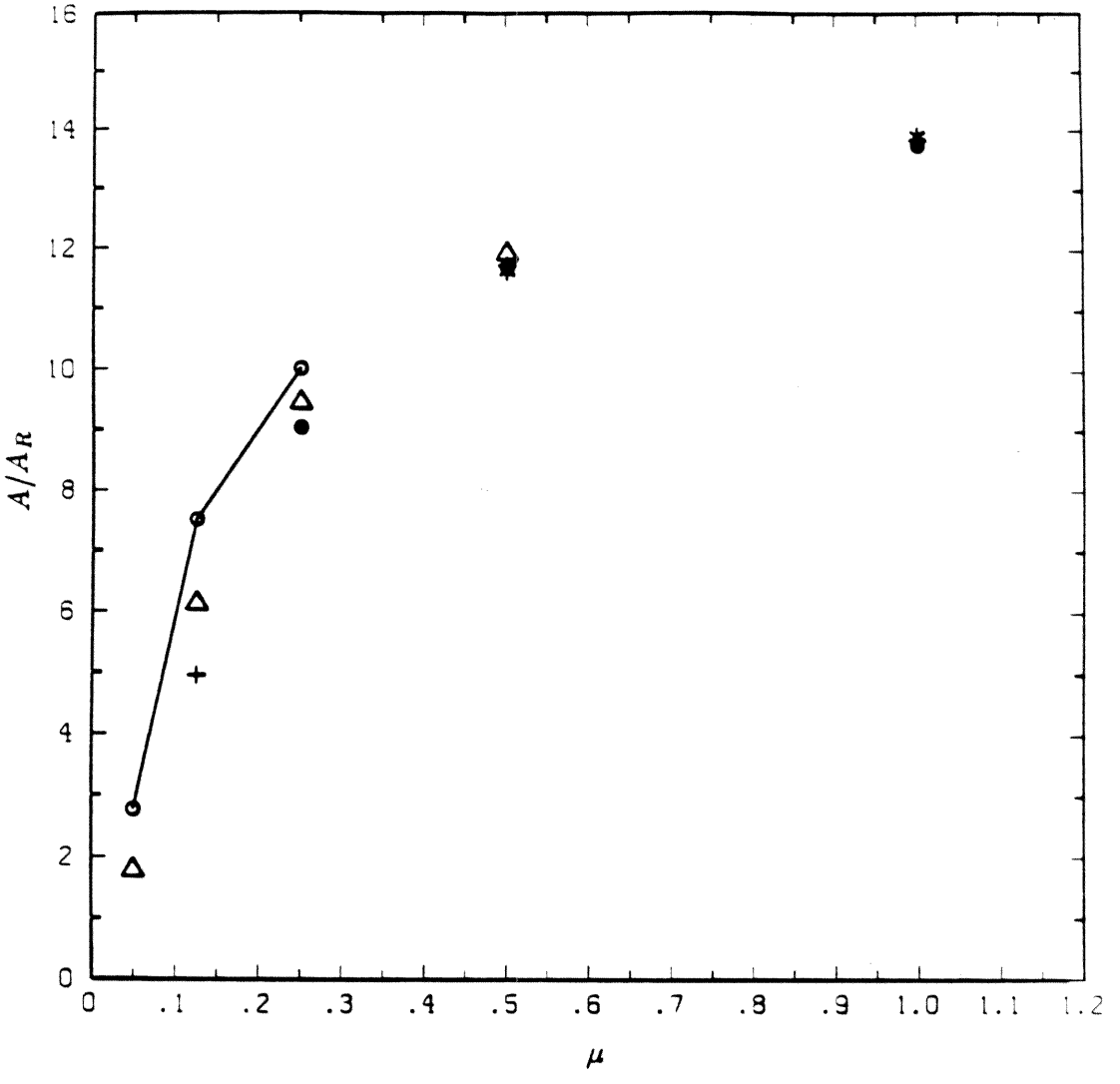

Fig. 13

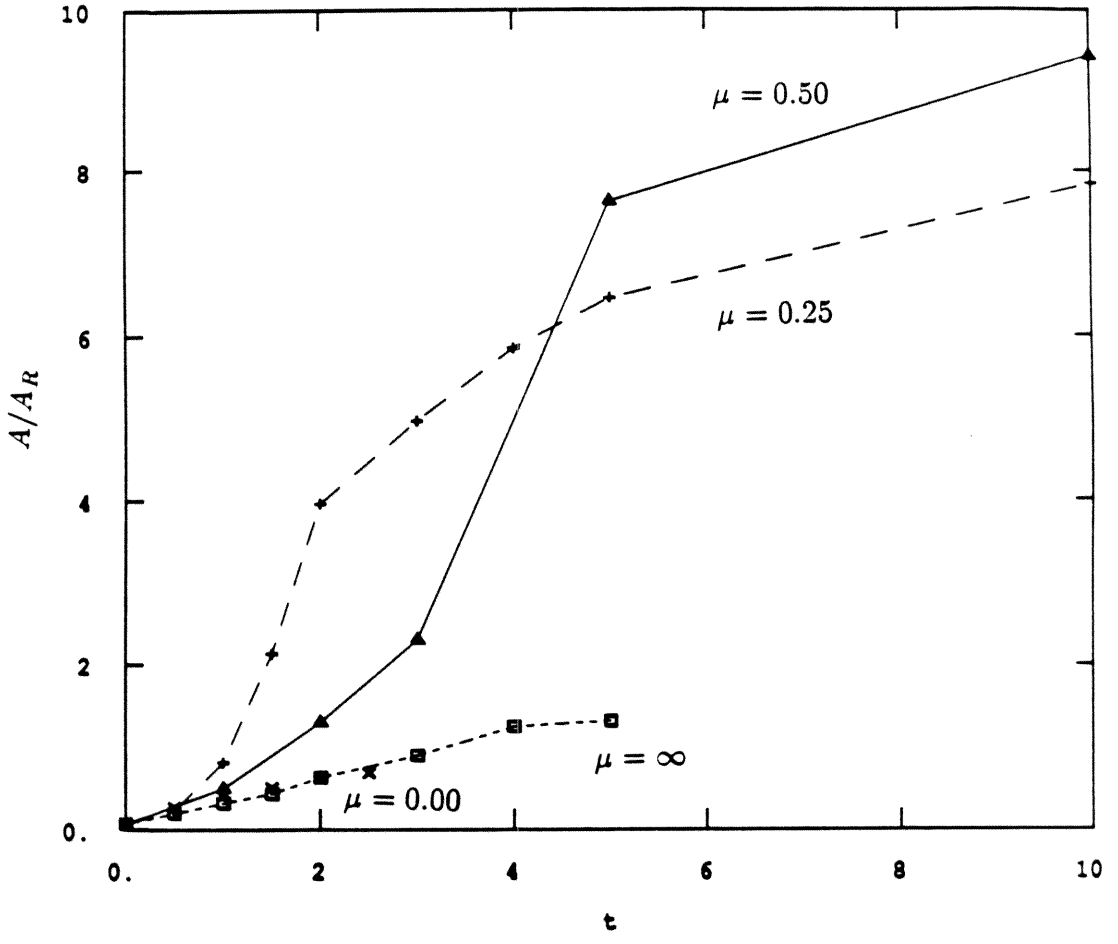

Fig. 14

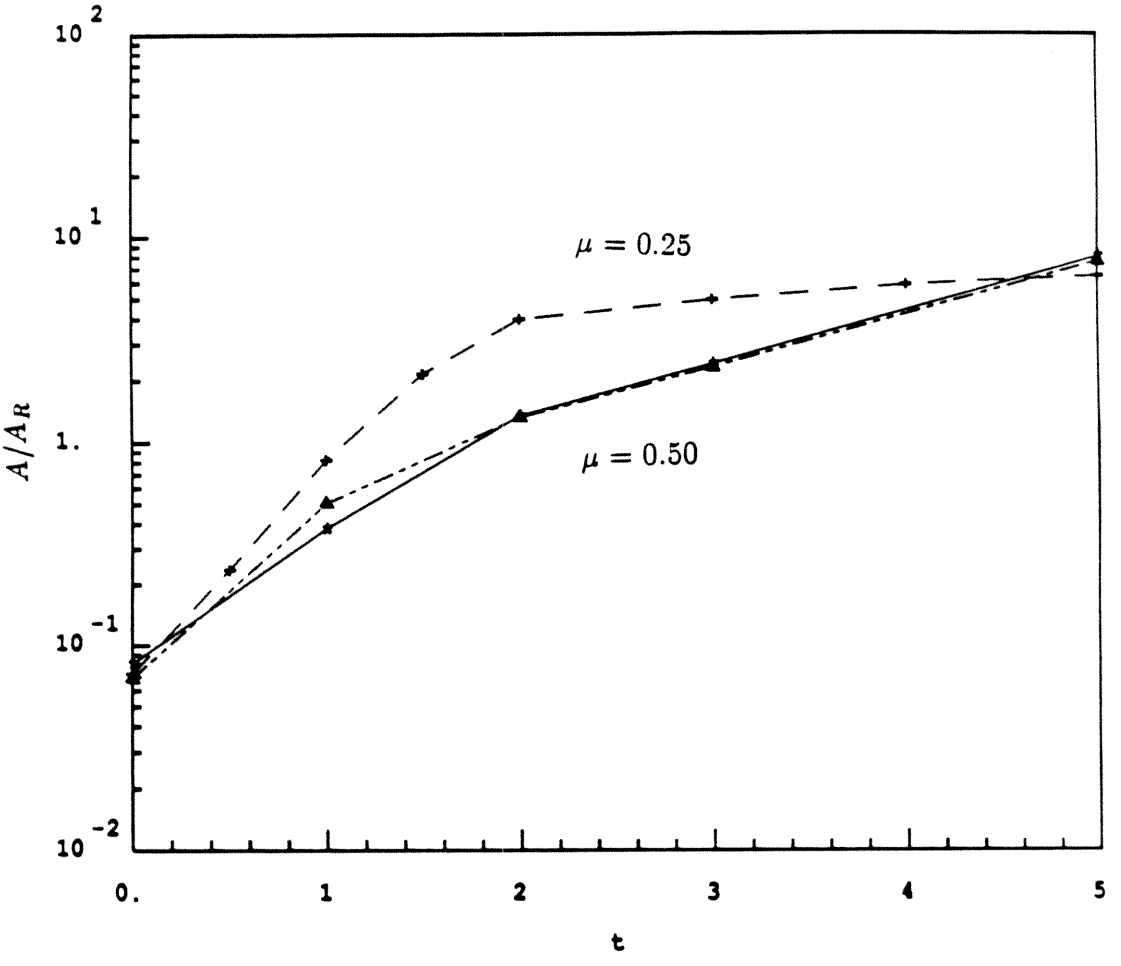

Fig. 15

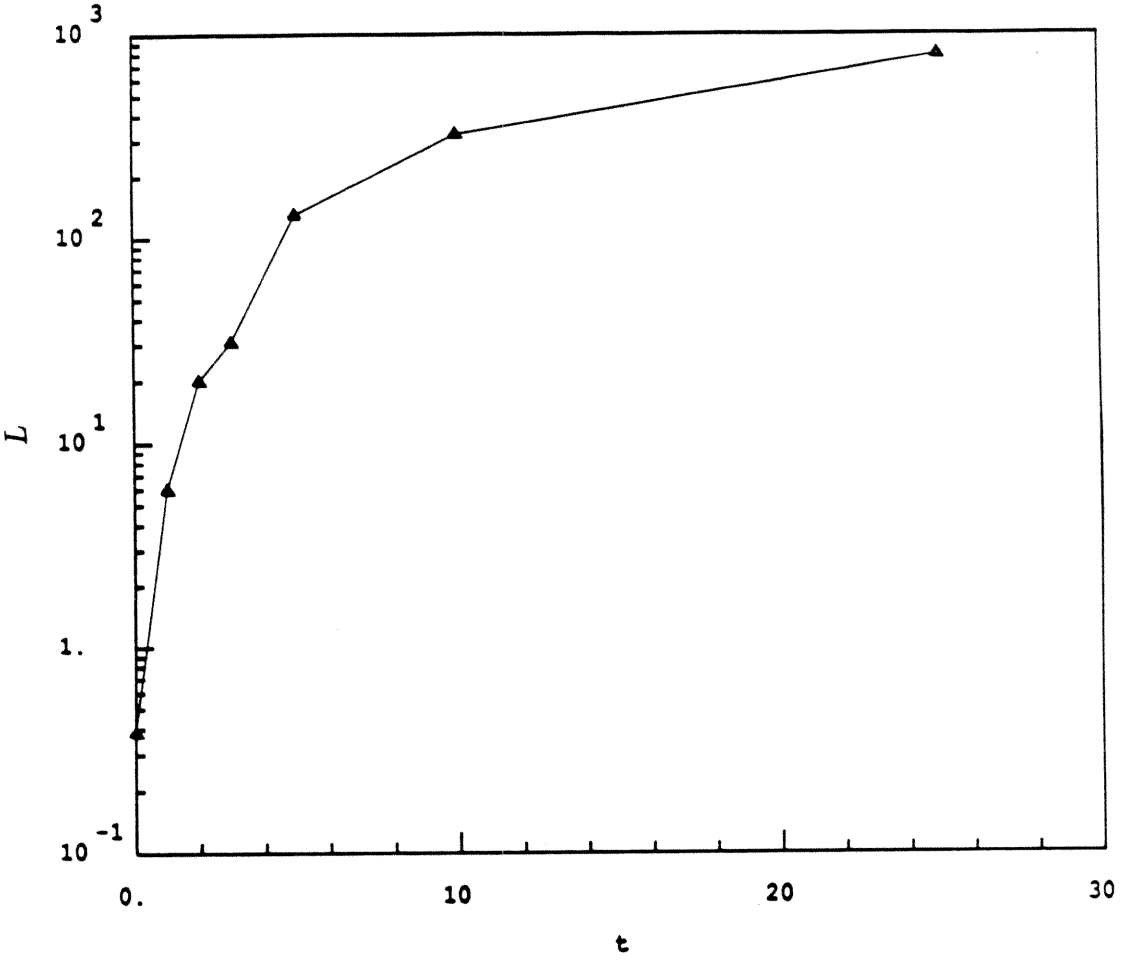

Fig. 16

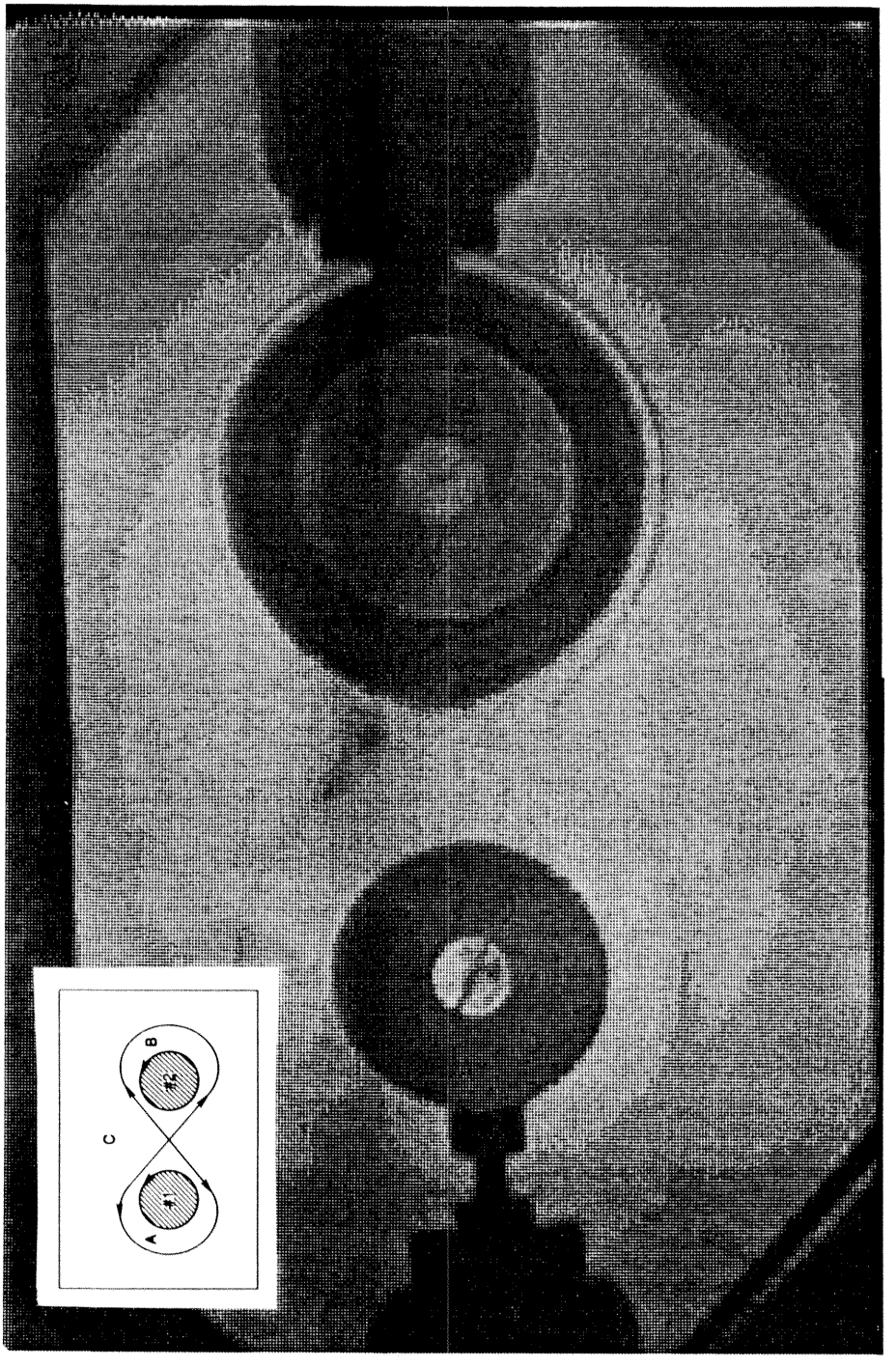

Fig. 17(a)

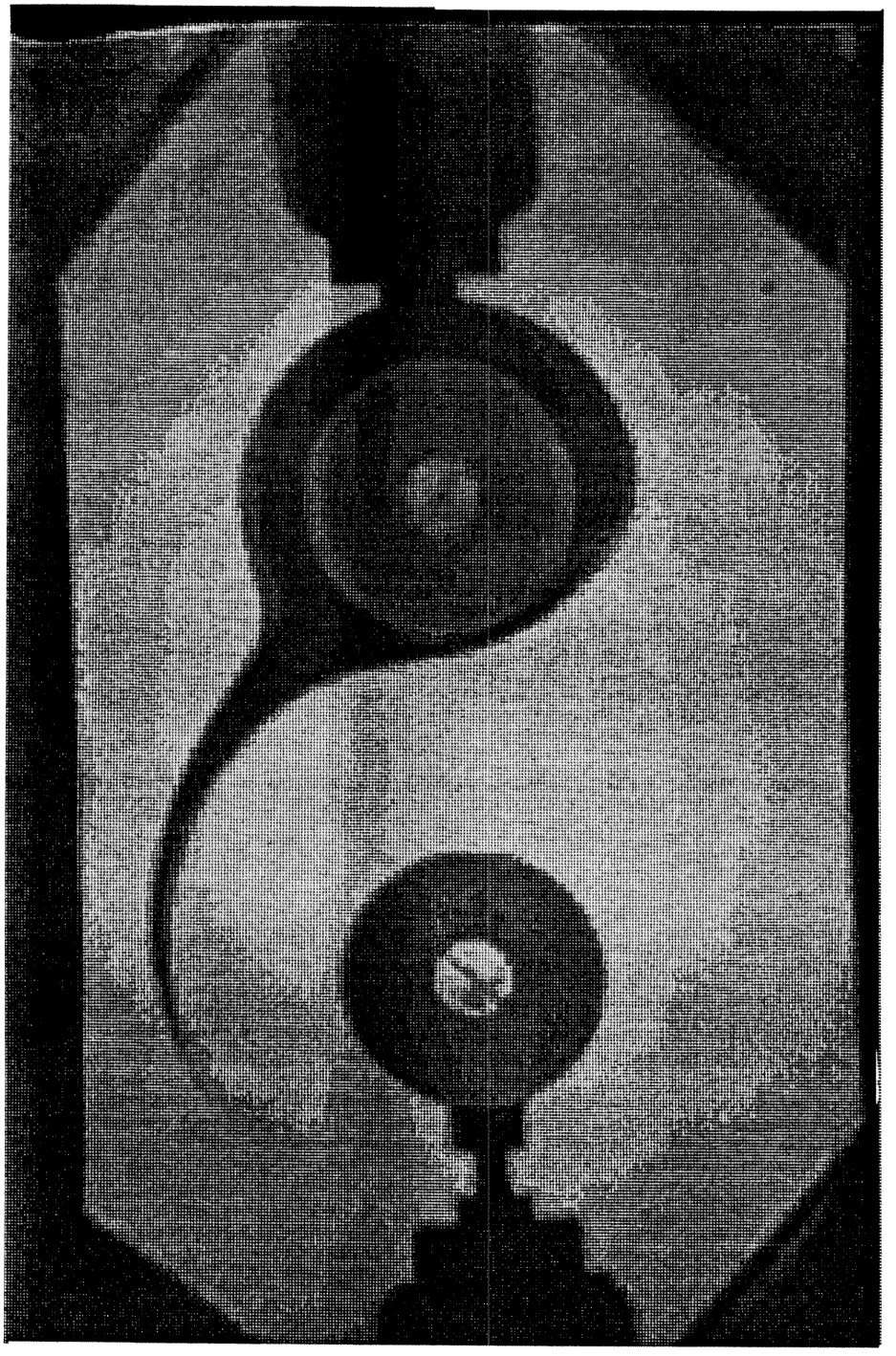

Fig. 17(b)

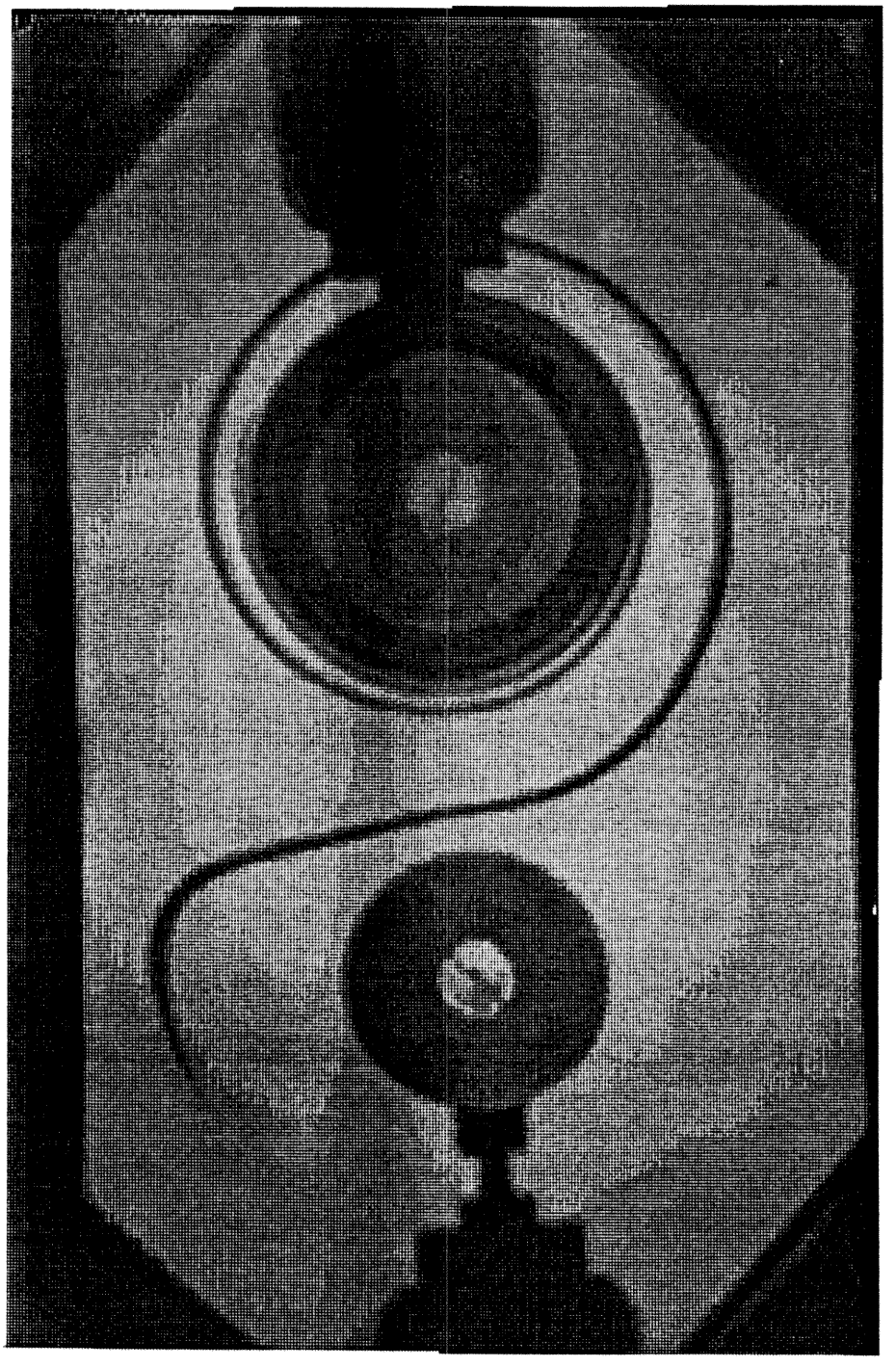

Fig. 17(c)

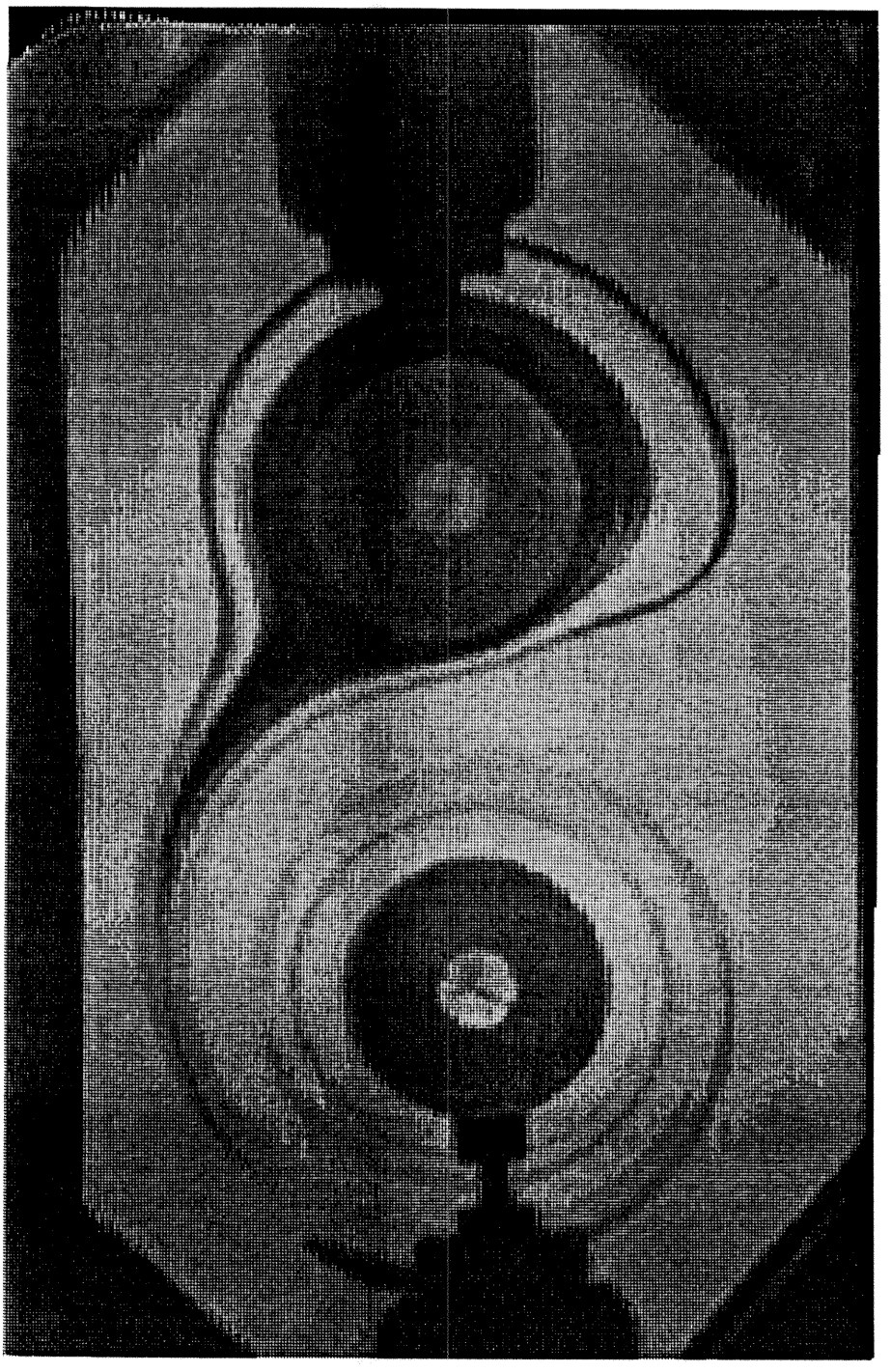

Fig. 17(d)

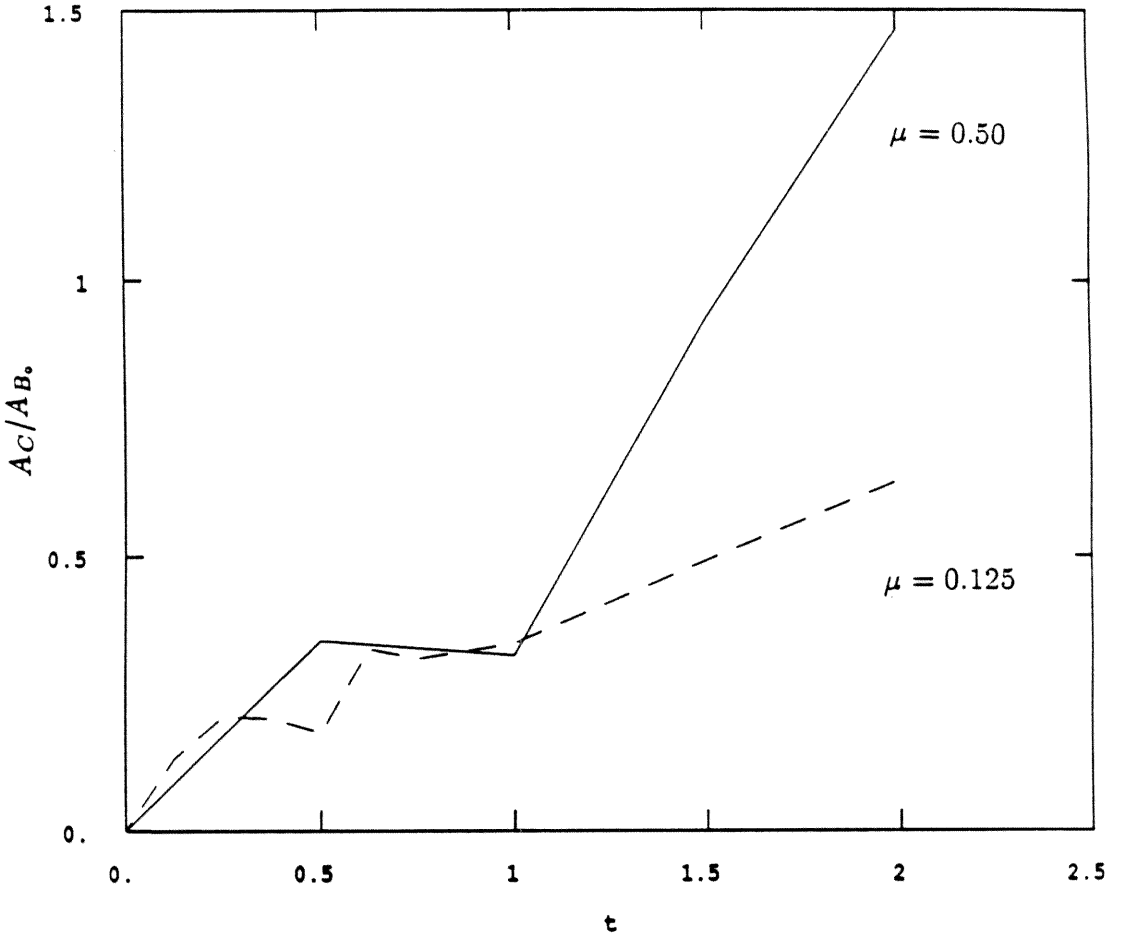

Fig. 18

(a)

(b)

(c)

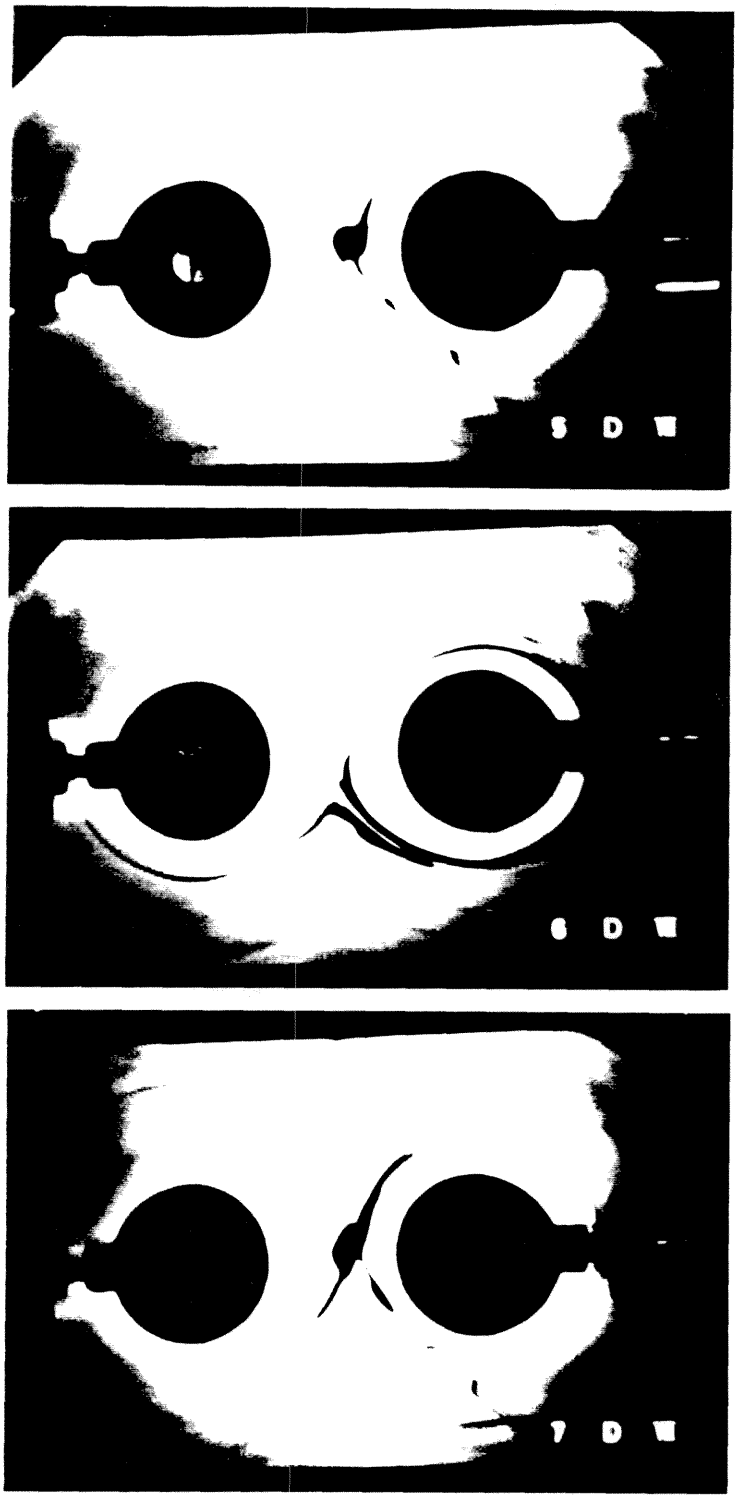

Fig. 19

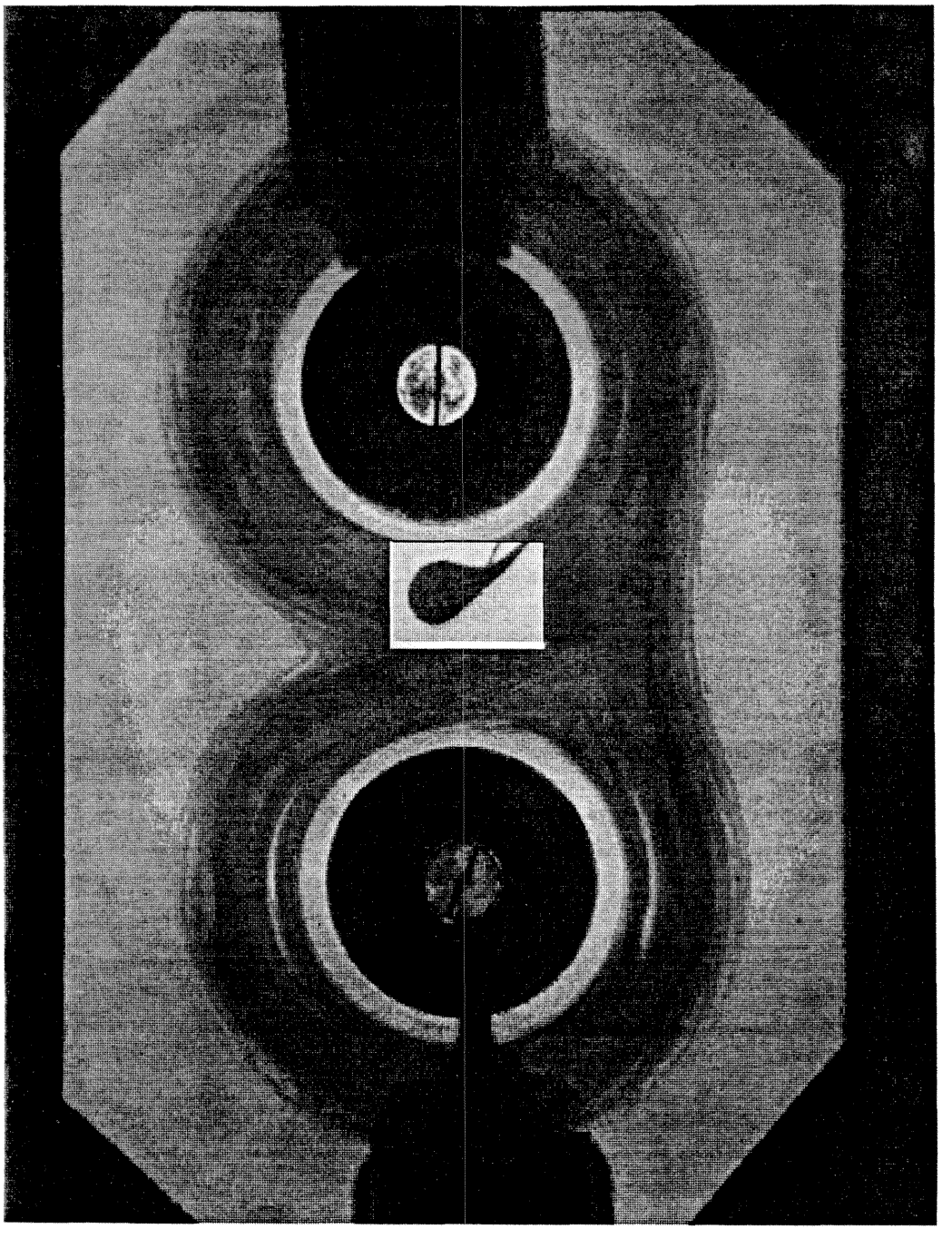

Fig. 20(a)

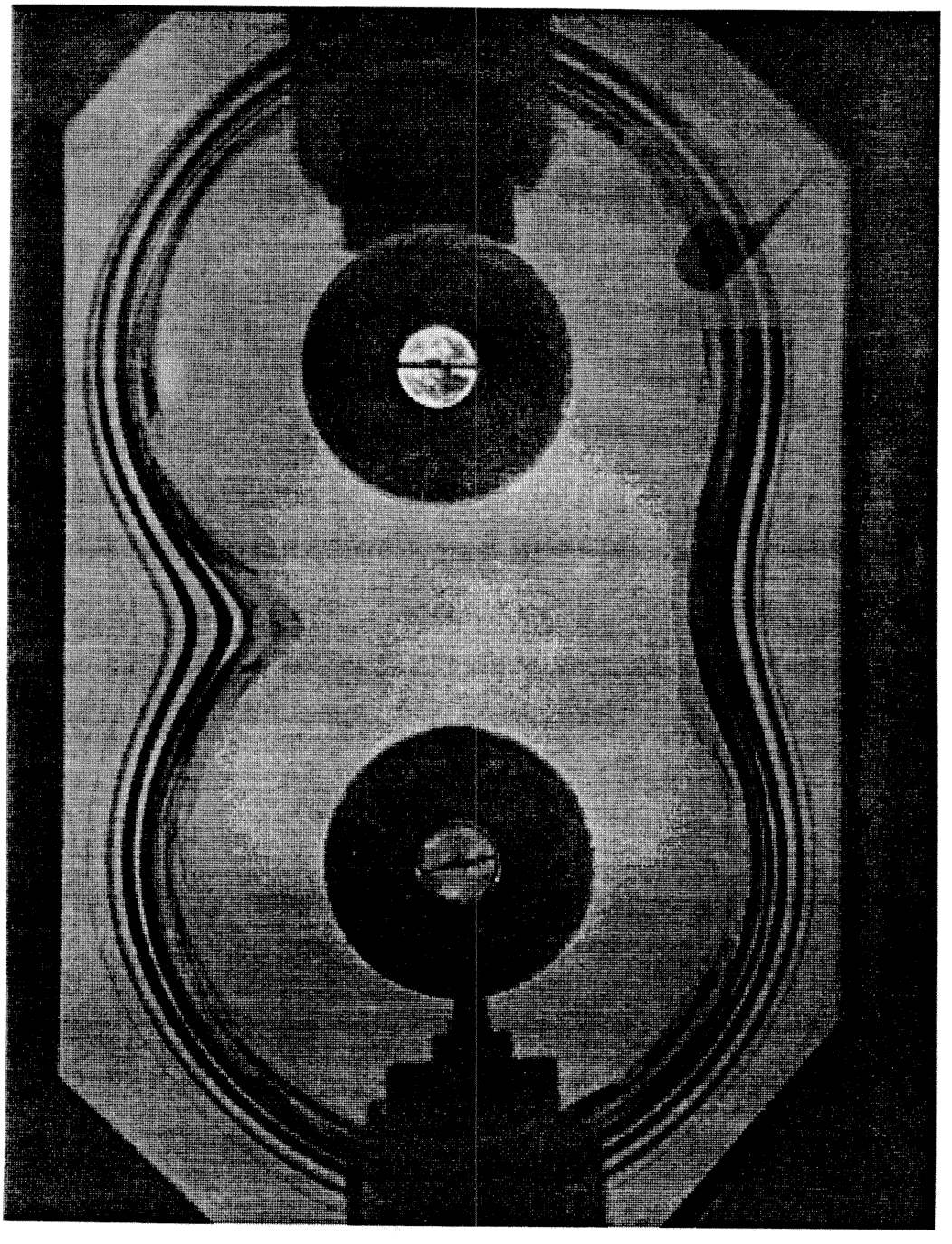

Fig. 20(b)

Chapter IV

Chaotic Mixing and Transport in a Two-Dimensional Time-Periodic Stokes Flow – the Blinking Two-Roll Mill (BTRM): II. Dilute Polymer Solution

Chaotic Mixing and Transport in a Two-Dimensional Time-Periodic Stokes Flow – the Blinking Two-Roll Mill (BTRM): II. Dilute Polymer Solution

R. C.-Y. Ng*,

Department of Chemical Engineering
California Institute of Technology
Pasadena, California 91125

D. F. James,

Department of Mechanical Engineering
University of Toronto
Toronto, Ontario, Canada M5S 1A4

and L. G. Leal†

Department of Chemical & Nuclear Engineering
University of California
Santa Barbara, California 93106

* Present address: Mobil Research and Development Corp., Dallas Research Laboratory, Dallas, TX 75244-4312, U.S.A.

† To whom all correspondence should be addressed.

Abstract

The chaotic mixing and fluid transport properties of a dilute polymer solution in a two-dimensional time-periodic Stokes flow are compared with those of the Newtonian solvent. This time-periodic flow is generated in a *blinking two-roll mill* (BTRM) apparatus that was described in a companion paper for the Newtonian fluid case [7]. The BTRM flow has been demonstrated to produce chaotic particle advertion when the characteristic period of oscillation, μ, is larger than 0.125 [7]. The results for the polymer solution also show similar features for chaotic mixing. However, the area of mixing and the rate of fluid transport in the polymer solution. show an O(1) decrease when compared with the corresponding Newtonian results. The polymer-induced flow effect is revealed in the mixing experiments using flow visualization with dye tracer and quantitative measurements via digital imaging technique. The onset of the polymer effect on the flow occurs at a critical Deborah number of $(De)_c \sim 2$. This high Deborah number effect may be related to the large deformation of polymer in the BTRM flow where the polymer experiences a succession of *strong* and *weak* flows at different time intervals. The residence time of the polymer in the extensional region will determine the extent of modification of the flow by the polymer. This mechanism may explain the fact that the largest decrease in the area of mixing is obtained in high frequency flows in the BTRM.

1. Introduction

Dilute polymer solutions have been shown to exhibit non-Newtonian fluid behavior in *strong* flows [1,2]. Strong flows correspond to flows that are capable of inducing large deformation of the polymer molecules. Specifically, a linear polymer chain in a strong flow would be stretched exponentially in time. The strong flow criterion has been discussed in detail by Tanner [3] and more recently by Olbricht *et al.* [4]. Some observable examples of non-Newtonian effects for dilute polymer solutions in extensional flows are the large pressure drop increase that occurs in flow through porous media [5] and in sink flow [6]; and polymer-induced flow modifications in stagnation flows of various geometry [1,2]. Those flows that have been studied to date are typically steady from an Eulerian point of view, though the polymer molecules experience a time-dependent flow history in a Lagrangian framework. furthermore, in the cases where the flow can be characterized in detail (i.e., neither turbulent nor porous media flows), the region of interaction between the polymer and the flow is extremely localized.

The present study is intended to provide experimental evidence of non-Newtonian effects for a dilute polymer solution in a time-periodic (or blinking) two-roll mill. The steady flow in a co-rotating two-roll mill has been well-characterized by previous investigators in this laboratory [2]. Indeed, Dunlap and Leal [2] have studied both polymer conformation and flow in this system, demonstrating that strong birefringence and a local inhibition of large strain rates can occur near the stagnation point and along the outflow symmetry axis. The blinking two-roll mill differs in interesting and important ways from the steady flow, provided that the *strength* of the flow is sufficient to undergo a transition from regular to chaotic motions, and those differences offer an opportunity to understand dilute solution dynamics in a framework that is much more directly relevant to the major technological application of dilute solutions in polymer drag reduction. First, from the Lagrangian frame of reference seen by a polymer molecule, the flow is alter-

natively *strong* and mostly *weak*, and this is much more like the environment seen by a polymer in a turbulent flow. Second, the region of the flow domain where the flow is strong on average, in the sense that there is an exponential separation of material points, is substantial – in fact the region covers the whole of the two-roll mill for a high enough roller speed or a long enough period for blinking. Finally, in spite of the complexity of particle paths in the flow, it can be simulated completely, either analytically or numerically for a Newtonian fluid, or (presumably) numerically in the case of a dilute solution model. Hence, detailed comparisons between model predictions and experimental observations should ultimately be possible, thus allowing a much more demanding test of the capabilities of existing models in time-dependent, spatially complex flows, that is much more relevant to turbulent flows than anything studied heretofore, but without the impossible complexity of fully developed turbulence.

In this paper, we take only the first step of studying some overall flow and mixing characteristics of the BTRM flow for a dilute polymer solution that can be compared with a companion study of similar phenomena for a Newtonian fluid. Later, we shall report on more detailed measurements of polymer conformation and flow, in a framework that is philosophically comparable to our earlier studies of dilute solution behavior in steady flows, in anticipation of comparisons between model predictions and experimental observations that were alluded to above.

The flow generated in the two-roll mill is a two-dimensional laminar flow (the Reynolds number is kept below O(1) for all experiments), and the velocity field $\mathbf{v}$(x,y,t) in an Eulerian representation is related to the stream function ψ by

$$\mathbf{v}(x,y,t) = \left(\frac{\partial\, \psi}{\partial\, y} \;,\; -\frac{\partial\, \psi}{\partial\, x} \right) \tag{1}$$

where the stream function plays a role that is similar to an equipotential surface in Hamiltonian mechanics. The motion of particle (passive tracer) in this *flow* is

governed by the set of differential equations in the Lagrangian form

$$\frac{d\,x}{d\,t} = \frac{\partial\,\psi}{\partial\,y} \tag{2a}$$

$$\frac{d\,y}{d\,t} = -\frac{\partial\,\psi}{\partial\,x} \tag{2b}$$

This is a Hamiltonian system whose Hamiltonian is just the stream function $\psi(x, y, t)$. For time-independent flows, this dynamical system has one degree of freedom and is integrable which means that a passive tracer particle in the flow will advect along a streamline or a pathline. Phase space of this integrable system consists of streamlines of constant value. However, when the flow is time-modulated periodically, the time-dependent Hamiltonian with one degree of freedom is then equivalent to an autonomous Hamiltonian with two degrees of freedom, and is likely to produce chaotic behavior [9,10]. The previous mixing study in the BTRM flow for a Newtonian fluid has already demonstrated the existence of chaotic mixing behavior via flow visualization and various *quantitative* measurements. These characteristic features of chaotic particle motion agree qualitatively with predictions from dynamical systems theory.

In the present study, flow visualization and standard digital imaging techniques are used to investigate the effect of *polymer* on the mixing characteristics in the time-periodic BTRM flow. Significant deviation from the Newtonian result is observed in mixing experiments for the polymer solution when the Deborah number (a measure of the viscoelastic effect of the polymer that will be defined later in section 3.1) is large enough to affect the flow.

2. Experimental Details

2.1 Apparatus

The flow device is the same blinking two-roll mill (BTRM) that was used in the earlier study of chaotic mixing for a Newtonian fluid. Details of the apparatus, the flow visualization technique, and the digital image processing are described in Ref. [7]. A schematic for the experiment is shown in Fig. 1. The two alternately rotating rollers, are switched on and off periodically by computer-controlled switching, and thus simulate quantitatively a pair of blinking vortices similar to Aref's blinking-vortex flow [11]. The periodically alternating rotation of the rollers # 1 and #2 is shown schematically in Fig. 2. At any instant of time, one of the rollers is rotating at a constant speed and the other roller is stationary. The direction of rotation is counter-clockwise for both rollers. Flow visualization is performed by injecting a blob of red dye into the solution which is pale yellow in color. Then, the dye patterns from the mixing experiments are captured by a Sony XC-77 monochrome CCD video camera and recorded on a Panasonic 4-Head video cassette recorder. These recorded images can be digitized by an ITT PCVision-Plus frame grabber using an IBM/AT computer and then analyzed by Image-Pro II (a utility software package by Media Cybernetics) for image analysis and quantitative measurements.

2.2 Experimental Conditions

The polymer solution used in this study is prepared by first dissolving a high molecular weight polystyrene sample (PS2) of $M_w \sim 1.86 \times 10^6$ (manufactured by Pressure Chemical Co.) in tricresylphosphate (TCP). This polymer has a narrow molecular weight distribution of $M_w/M_n = 1.06$. The polymer took about a week to dissolve completely in the solvent TCP with gentle heating and stirring.

This solution is then mixed thoroughly with a high viscosity solvent, Chlorowax-45 (CW45), to increase the solution viscosity. This is important for minimizing boundary and inertial effect. The final composition of the mixed solvent is 70/30 wt% of CW45/TCP. The polystyrene concentration is 1500 ppm by weight in the mixed solvent.

The reason for choosing this concentration is because the same polymer sample in a different solvent has been shown to inhibit high rate of strain in *steady* two-dimensional extensional flows at a polymer concentration of 1500 ppm [12]. Since the previous study [7] has demonstrated that exponential stretching of material lines occurs in the BTRM flow, it is suggested that the polymer molecules can be deformed significantly enough to have an effect on the flow. The 1500 ppm PS2 in CW45/TCP solution is characterized by measuring the zero shear viscosity of both the solution and solvent. These measurements are performed using a Ubbelohde capillary viscometer. The characteristic relaxation time τ for the polymer can be obtained from the measured viscosity via the relationship [13]

$$\tau = \frac{(\eta - \eta_s)M_w}{c\rho RT} \tag{3}$$

where η is the viscosity of the polymer solution, η_s is the solvent viscosity, c is the polymer concentration in ppm, ρ is the solution density, R is the gas constant, and T is the temperature. Table 1 summarizes the properties of the polymer solution and the solvent.

Table 1. Solution Properties at $20°C$

Fluid	η (poise)	ρ (gm/cc)	τ (sec)
CW45/TCP	44.9	1.26	-
1500 ppm PS2	55.1	1.26	0.41

The increase in zero shear viscosity due to the presence of the polymer in the solvent is about 23%. Since the polymer relaxation time depends on the solution viscosity, any shear thinning effect would consequently reduce the characteristic relaxation time. Therefore, shear viscosity measurements are also performed using a parallel plate rheometer. The result shows constant solution viscosity for both the solvent and the polymer solution for shear rates up to $\gamma \sim 6.3\ \mathrm{sec}^{-1}$.

The dye solution used for flow visualization is a 5 wt% Sudan IV red dye dissolved in the same suspending fluid (i.e., the polymer solution). The dye is used in lieu of tracer particles, and provides a Lagrangian representation of the dynamics of particle trajectories in the time-periodic flow for a large number of initial conditions. The initial conditions for all mixing experiments (section 3.1) are as close to identical as possible, with a 0.4-0.5 cc blob of red dye injected near the center of the gap between the rollers at about the half-height of the flow device. For investigating the fluid transport in different regions of the flow (section 3.2), the initial condition is an annulus of dye between roller #2 and the left stagnation streamline. At each time period, the dye pattern represents the Poincaré map in dynamical systems theory. By studying the the dye pattern experimentally at each time period, the results in the mixing experiments can be related to many characteristic features of *chaotic mixing* [7,14,15]. It may be noted that the molecular diffusivity of the dye in the organic solvent is estimated to be about $O(10^{-8})\mathrm{cm}^2/\mathrm{sec}$, and thus diffusion can be neglected during the course of each experiment, which is typically less than 1000 sec. It follows that the final characteristics of the dye pattern will be determined solely by the kinematics of the flow. In order to facilitate comparisons with existing theory from nonlinear dynamics for chaotic flows, as well as future comparisons with detailed simulations of the 2-roll mill flow, it is important that the Reynolds (Re) and Strouhal (S) numbers be kept as low as possible. The primary reason is to preserve two-dimensionality and to avoid transient effects in the flow device. These dimensionless parameters

are defined as follow:

$$Re = \frac{R\,\omega\,d}{\nu} \tag{4a}$$

$$S = \frac{d}{R\,\omega\,T_{\frac{1}{2}}} \tag{4b}$$

where R is the roller radius, ω is the roller speed, d is the half gap width between the two rollers, ν is the kinematic viscosity, and $T_{\frac{1}{2}}$ is the half period which is the time of rotation for one roller in a cycle (period). The range of experimental values is $Re = 0.15$–1.5 (based on the solvent viscosity) and $S = 0.01$–0.24. The condition for neglecting the start-up and relaxation transients due to vorticity diffusion when the cylinders are started and stopped is $T_{\frac{1}{2}} \gg d^2/\nu$. Although $T_{\frac{1}{2}}$ is 1 to 40 sec, which is much larger than the value of $d^2/\nu = 0.07$ in our experiments, we still observed transient effects for high frequency flows (i.e., $T_{\frac{1}{2}} \sim 1$ sec) in the Newtonian solvent. However, this transient effect is greatly reduced in the polymer solution as we will observed in the next section.

In the next section, results for the area of mixing and fluid transport in the BTRM flow for the polymer solution will be presented and compared with the Newtonian case. Similar mixing behavior is observed but the efficiency of mixing is reduced due to viscoelastic effects (high Deborah number) in the polymer solution.

3. Results and Discussion

3.1 Area of Chaotic Mixing

The general qualitative features of *chaotic* mixing in the BTRM flow are not changed by the presence of the polymer in the Newtonian solvent. The mixing characteristics of dye with the suspending polymeric fluid are still governed by the half period $T_{\frac{1}{2}}$, the roller speed ω, and the total mixing time t'. The dimensionless characteristic parameters are the flow strength (or dimensionless period of oscillation) μ, and total mixing time t (or number of periods of time $T_\circ$), defined as

$$\mu = \frac{\omega T_{\frac{1}{2}}}{\omega_\circ T_\circ} \tag{5a}$$

$$t = \frac{t'}{T_\circ} \tag{5b}$$

where ω is the roller speed in rad/sec, $T_{\frac{1}{2}}$ is the half period in sec, and $T_\circ$ is a characteristic time for a particle to travel one revolution along a closed steady streamline near the center of the gap between the rollers, and at a roller speed of $\omega_\circ$ when one roller is rotating. Experimentally, we determined $T_\circ$ to be $\sim$ 40 sec for a roller speed $\omega_\circ$ of 1.75 rad/sec. The value of μ corresponds to the number of revolution of a fluid element at the center of the device in half period time.

Fig. 3 shows a sequence of pictures for $\mu = 0.50$ at various time periods. The dye patterns show almost identical morphological structures as in the Newtonian case. Therefore, the transition from regular to chaotic mixing behavior with increasing value of μ should be qualitatively identical to the Newtonian results from our previous study [7]. By increasing either the roller speed or the period of blinking, the motion of a particle can go through a transition from regular to chaotic, and subsequently to *globally* chaotic behavior. In Fig. 4, the area of mixing (dye coverage) is plotted against μ for various roller speeds. This area is

measured for a total dimensionless mixing time t = 25 (equivalent to physical time of 1000 sec). The region of chaotic mixing increases rapidly as the dimensionless period μ increases from zero. When $\mu > 0.50$, the chaotic area starts to level off to an apparent saturation value that corresponds to the maximum area (very close to the side walls of the flow device) of the closed flow domain. The critical value of μ for chaotic mixing to occur is for $\mu > 0.125$. This is the same as the Newtonain result from a previous study in this laboratory [7]. Note, however, that the area of chaotic mixing shows a consistent decrease at high roller speeds ($\omega > 4.363$ rad/sec). This is clearly not due to transient or inertial effects since the area of mixing would increase for high Re and/or high S number flows. The result suggests a measurable polymer effect on the flow. One would normally expect such effects for Deborah numbers of O(1).

The Deborah number (De) in this case is defined as the ratio of the characteristic relaxation time for the polymer, τ, to a characteristic flow time, which we choose to be ω^{-1} for the time-periodic BTRM flow,

$$De = \omega \tau . \tag{6}$$

The area of mixing is replotted in Fig. 5 against De for both the Newtonian solvent and the polymer solution for various values of μ. The values of De for the solvent are calculated by multiplying the roller speed with τ for the polymer. This so-called Deborah number for the Newtonian solvent is used solely for comparison without any physical significance. The area of mixing in the polymer solution shows a very significant decrease when compared with the Newtonian data. The onset of this decrease in the area of mixing seems to occur at a critical Deborah number of $(De)_c \sim 2$. The magnitude of the decrease in mixing area increases with increasing De but decreasing μ. It is apparent that the effect of polymer on the flow is significantly larger for low $T_{\frac{1}{2}}$ cases (high frequency flows). The distinctive difference between the Newtonian and polymer solution is the disappearance of

any transient effect in the polymer solution for high frequency flows at $\mu = 0.125$. The transient effect is so prominent in the Newtonian fluid that the dyed fluid would tend to spread radially outward for $T_{\frac{1}{2}} = 1\text{sec}$ ($De = 3.6$ in Fig. 5). Thus, the area of mixing is much larger than that of the lower frequency case, $T_{\frac{1}{2}} > 1$ sec, for the same value of $\mu = 0.125$. However, the corresponding result for the polymer solution (i.e., at $\mu = 0.125$ and $De = 3.6$) shows in contrast a decrease in the area of mixing.

The reason for the decrease in mixing area in the polymer solution may be related to similar effects observed in *steady* elongational flows in the 2-roll mill where inhibition of large strain rates occurs at high Weissenberg number [2,12]. Since exponential stretching of material line on a long-time average exists in the time-periodic blinking 2-roll mill flow [7], significant deformation of the polymer is expected to occur. This would then lead to an increase in the *apparent* viscosity in the solution, and consequently would inhibit the stretching and transport of fluid elements. The increased polymer effect for high frequency flows may be because the polymer can reside in the strong flow region in the BTRM flow for many successive periods of time. In the strong flow region, significant deformation of the polymer can occur that could result in large modification to the flow. As mentioned before, since most parts of the flow domain in the BTRM flow is a *weak* flow, blinking flows with a large time period would cause the polymer to experience weak flows for most of the time and consequently leads to a smaller polymer-induced effect to the mixing and transport characteristics in the flow.

Another noteworthy point from the mixing experiments is that different results are obtained when the experiment is performed either continuously or discontinuously (i.e., stopping in between two consecutive periods). At the same value of $\mu = 0.5$ and $De = 7.2$, a 15% reduction in mixing area (compared to Newtonian case) is observed for the continuous mode of operation, but only about 8% is observed for the discontinuous case. This indicates that the polymer should not

be allowed to relax back to its equilibriuim coiled conformation at any moment of the entire experiment. The consistently deformed and aligned polymers are necessary to induce large viscoelastic effect on the mixing characteristics of the flow. viscosity. Thus, all the results shown before are obtained when the experiment is operated in the continuous mode. The above proposed mechanism for polymer effect on the flow is also supported by results for fluid transport in the Newtonian and polymer solution presented in the next subsection.

3.2 Transport of Blob of Passive Tracer

In the steady corotating two-roll mill flow, the convective transport of fluid is inhibited by the existence of the stagnation streamline (the figure-eight-shaped separatrix made up of two homoclinic orbits). By time-modulating the steady flow (i.e., implementing the BTRM flow in this case), materials can be transported across the separatrix, and thus chaotic mixing can occur over a large region of the flow. The amount of fluid transport across the separatrix depends on the characteristic frequency of the flow which is $1/T$. The mechanism of transport has been related in our previous study [7] to the so-called *lobe dynamics* due to *tangling* of the stable and unstable manifolds that originated from the central hyperbolic point. The basic ideas of transport via lobe dynamics were introduced first by Rom-Kedar *et al.* [16] in their study of mixing and transport in the oscillating vortex pair (OVP) flow. A more detailed discussion can be found in Ref. [7] of the similarity of the flow structures observed in the BTRM and the OVP flows.

In the present study, quantitative measurements are performed of the transport rate for the polymer solution in the BTRM flow. The transport of fluid from the region inside the separatrix to the region outside is measured by filling the annular region in the right separatrix with a thin layer of dye. This inner region is labelled as region B. The other inner region (the annulus region between the

left separatrix and roller #1) is labelled as region A, whereas the outer region is labelled as region C. Fig. 6 shows results for the *area* of fluid transported into the outer region C versus dimensionless mixing time t for both the Newtonian and polymer fluid, and for $\mu = 0.125$ and 0.50. The results are obtained at $\omega = 8.73$ rad /sec, or $De = 3.6$. The amount of fluid transport is greatly enhanced by increasing the characteristic blinking period μ for both solutions. From $t = 1$ to 2 ($t' = 40$ to 80 sec), the rate of transport for $\mu = 0.50$ is four times that of the case for $\mu = 0.125$ for both the polymer solution and its Newtonian solvent. However, a significant decrease in the rate of fluid transport into the outer region for the polymer solution is evident in Fig. 6, presumably reflecting a decrease in lobe size. The measurable decrease in the rate of fluid transport across the separatrix is up to 20% at $t = 2$ for both values of μ. Thus, the effect of polymer on the flow has resulted in the inhibition of transport (or stretching) of material fluid.

As discussed in the last subsection, the mechanism for the polymer-induced flow effect is believed to be similar to the effect of the polymer in the steady case where a strong flow would inhibit high strain rates due to elongated and aligned polymers. Although the time-periodic blinking flow in this study consists of mostly *weak* flow regions, the region between the rollers represents a region of converging flow that has an extensional component in the velocity gradient tensor. If the polymer is being elongated to some extent at each time that it passes through the extensional zone and is maintained in this stretched state by the shearing action at other regions, then it is possible for the polymer to create a significant effect on the flow. Nollert and Olbricht [8] have shown by using an elastic nonlinear dumbbell model for a test polymer molecule that large deformations of the polymer can occur in a time-periodic flow consisting of alternating simple shear and extensional flow. The reason is that the polymer has a long retraction time for conformational diffusion from an extended state back to the equilibrium coiled state. This means that once the polymer is being stretched in a strong flow region

for some time interval, it can be maintained in this stretched state or even extended further in weak flow regions at other times. Therefore, the inhibition effect observed is believed to be the result of extended polymer molecules that create large elongational stress over a broad region of the flow field. An analytical and numerical study of the two-roll mill flow is now being pursued in this laboratory in order to provide a better understanding of the deformation of microstructures in the BTRM flow.

4. Concluding Remarks

The effect of polymer does not change the general qualitative features of chaotic mixing in the BTRM flow. The area of chaotic mixing and the rate of fluid transport increases with increasing values of the characteristic period of oscillation μ. By increasing either the roller speed or the time period of blinking, efficient mixing and an enhanced rate of fluid transport can occur over a large region of the flow due to globally chaotic behavior. However, the area of mixing and rate of fluid transport in the polymer solution show a significant decrease from the Newtonian results. This decrease in mixing area is about 15% of the total mixing area for $\mu = 0.50$ and $t = 25$, and the decrease in fluid transport rates is about 20% for the same μ but at $t = 2$. These measurable effects are dependent on the Deborah number which is a measure of the viscoelastic effect of the polymer to the flow. The onset of polymer-induced flow effect occurs at a critical Deborah number of $(De)_c \sim 2$. The viscoelastic effect leads to the inhibition of material line stretching and fluid transport.

The result for the area of chaotic mixing in the polymer solution shows the most deviation from the Newtonian measurements for a fast blinking case of $T_{\frac{1}{2}} = 1$ sec at a Deborah number of $De = 3.6$. This is believed to be due to the sensitivity of the response of polymer to the details of the types of time-varying flow (in the Lagrangian point of view) in the BTRM. Nollert and Olbricht [8]

have demonstrated that large deformation of a polymer depends on the time of *pre-stretching* by an inital period of extensional flow followed by a steady simple shear flow. When the time of pre-stretching by extensional flow is a few times ($> 2\tau$) the characteristic relaxation time of the polymer, significant extension of the polymer occurs, and this highly stretched state can then be maintained in a weak flow at later times. The requirement of a residence time (in the strong flow region) of comparable magnitude to the characteristic relaxation time of the polymer is consistent with the high frequency flow effect observed in this study. For high frequency flow ($T_{\frac{1}{2}} = 1$ sec), the polymer that resides in the extensional region in between the rollers could have a long residence time before it is being convected to other weak flow regions.

A complementary investigation on the kinematics of the BTRM flow is essential to clarify the suggested mechanism for the polymer-induced flow effect. Work is currently being pursued on the numerical calculation of the time-periodic BTRM flow, and the dynamics (conformation change) of polymer in this flow via a simple dumbbell model. Further work is also directed at correlating the effect of high Deborah number to the mixing characteristics by using various polymer samples with a wide range of relaxation times. This would allow us a better understanding on the roles of large flow strength (shear rate) and long relaxation time of polymer to the polymer-induced flow effect.

References

[1] Gardner, K., Pike, E. R., Miles, M. J., Keller, A., Tanaka, K., *Polymer*, **23**, 1435 (1982).

[2] Dunalp, P. N., Leal, L. G., *J. Non-Newt. Fluid Mech.*, **23**, 5 (1987).

[3] Tanner, R. I., *A.I.Ch.E. Journal*, **22**, 910 (1976).

[4] Olbricht, W. L., Rallison, J. M., Leal, L. G., *J. Non-Newt. Fluid Mech.*, **10**, 291 (1982).

[5] Durst, F., Haas, R., Interlhal, W., *Rheol. Acta*, **21**, 572 (1982).

[6] James, D. F., Saringer, J. H., *J. Fluid Mech.*, **97**, 655 (1980).

[7] Ng, R. C.-Y., James, D. F., Leal, L. G., "*Chaotic Mixing and Transport in a Two-Dimensional Time-Periodic Stokes Flow – the Blinking Two-Roll Mill (BTRM): I. Newtonian FLuids,*" to appear (1989).

[8] Nollert, M. U., Olbricht, W. L., *Rheol. Acta* **24**, 3 (1985).

[9] Moser, J., *Stable and Random Motions in Dynamical Systems*, Princeton University Press (1973).

[10] Lichtenberg, A. J., Lieberman, M. A., *Regular & Stochastic Motion*, Springer Verlag, New York (1983).

[11] Aref, H., *J. Fluid Mech.*, **143**, 1 (1984).

[12] Ng, R. C.-Y., Leal, L. G., "*Concentration Effects on Birefringence and Flow Modification of Semi-Dilute Polymer Solutions in Extensional Flows,*" to appear (1989).

[13] Ferry, J. D., *Viscoelastic Properties of Polymers*, John Wiley & Sons, Inc., New York (1970).

[14] Chaiken, J., Chevray, R., Tabor, M., Tan, Q. M., *Proc. Roy. Soc. Lond. A.*, **408**, 165 (1986).

[15] Chien, W.-L., Rising, H., Ottino, J. M., *J. Fluid Mech.*, **170**, 355 (1986).

[16] Rom-Kedar, V., Leonard, A., Wiggins, S., "*An Analytical Study of Transport, Mixing and Chaos in an Unsteady Vortical Flow,*" *J. Fluid Mech.*, to appear (1989).

Figure Captions

Figure 1. Schematic for the BTRM experiment.

Figure 2. Roller speed, ω, versus time for the two rollers, with $T_{\frac{1}{2}}$ being the half period.

Figure 3. Dye patterns in the BTRM experiment for $\mu = 0.50$, $T_{\frac{1}{2}} = 12$ sec, and at various times: (a) t = 0, (b) t = 5, (c) t = 10, and (d) t = 15 (total mixing time = t $\times$40 sec).

Figure 4. Area of mixing (dye coverage) A, normalized by A_R (area of the roller), versus the characteristic period μ in the 1500 ppm PS2 solution for various roller speeds ω(rad/sec): $\omega = 1.745(\times)$; $\omega = 4.363(\triangle)$; $\omega = 8.725(\square)$; $\omega = 17.450(+)$.

Figure 5. Area of mixing (dye coverage) A, normalized by A_R (area of the roller), versus the Deborah number (De) for the Newtonian solvent (solid line), and for the 1500 ppm PS2 solution, at various characteristic periods: $\mu = 0.05(\times)$; $\mu = 0.125(\triangle)$; $\mu = 0.25(\square)$; $\mu = 0.50(+)$; $\mu = 1.00(\nabla)$.

Figure 6. Fluid transport into region C (A_C), normalized by the area of annulus of dye in region B (A_{B_o}) at t = 0, versus dimensionless time t for the Newtonian solvent (lines), and for the 1500 ppm solution (symbols) at $De = 3.6$ for two cases of μ: $\mu = 0.125$(dashed line, $\times$); $\mu = 0.50$(solid line, $\triangle$).

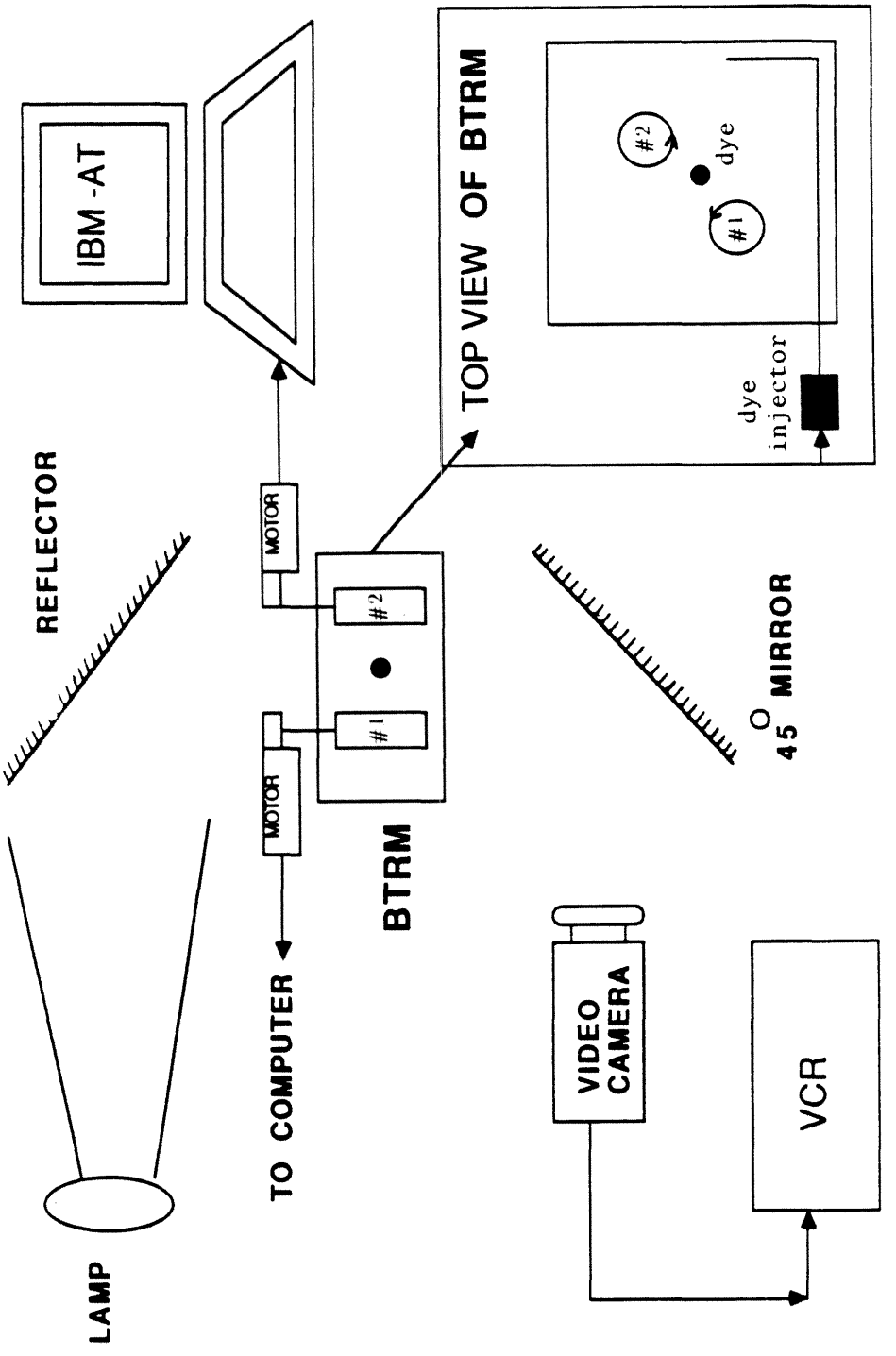
IBM-AT
REFLECTOR
MOTOR
MOTOR
#2
#1
BTRM
TO COMPUTER
LAMP
TOP VIEW OF BTRM
#2
dye
#1
dye injector
45° MIRROR
VIDEO CAMERA
VCR

Fig. 1

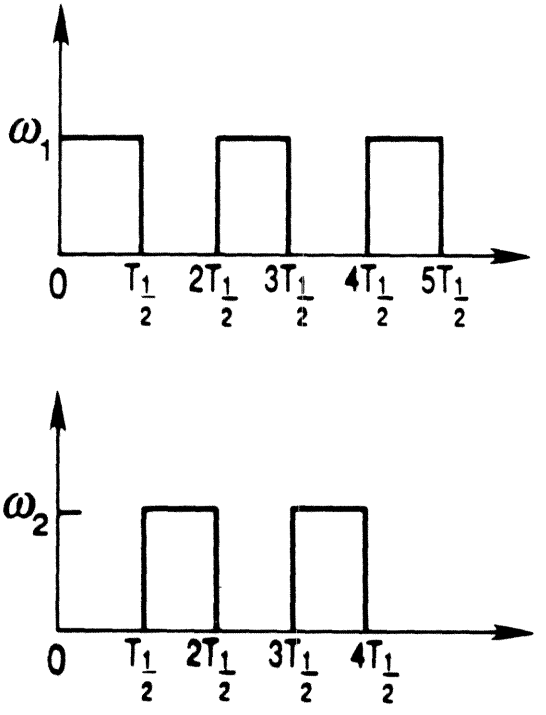

Fig. 2

(a)

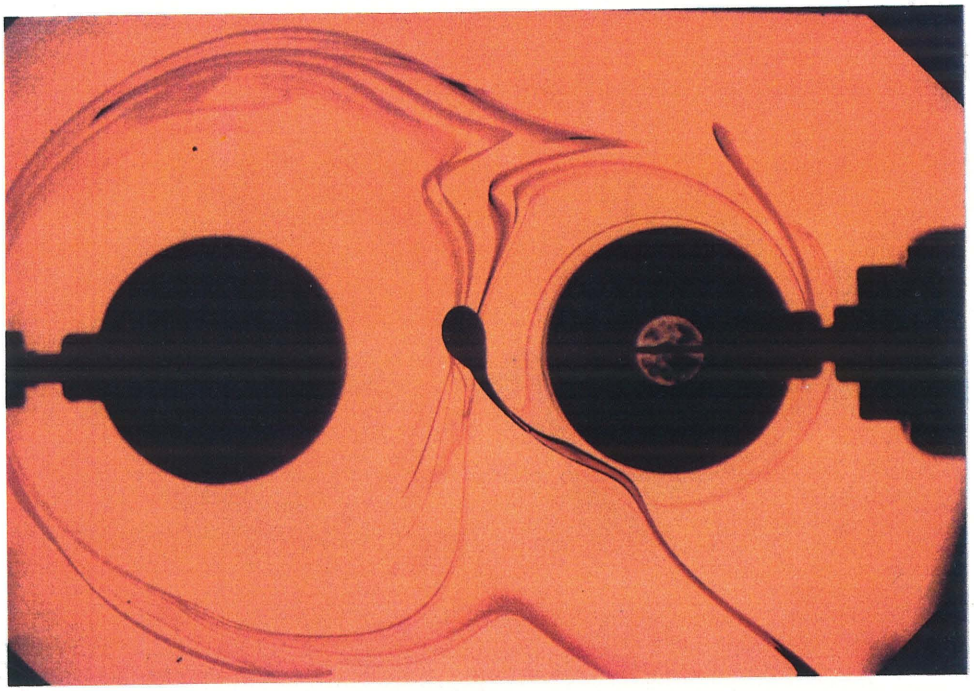

(b)

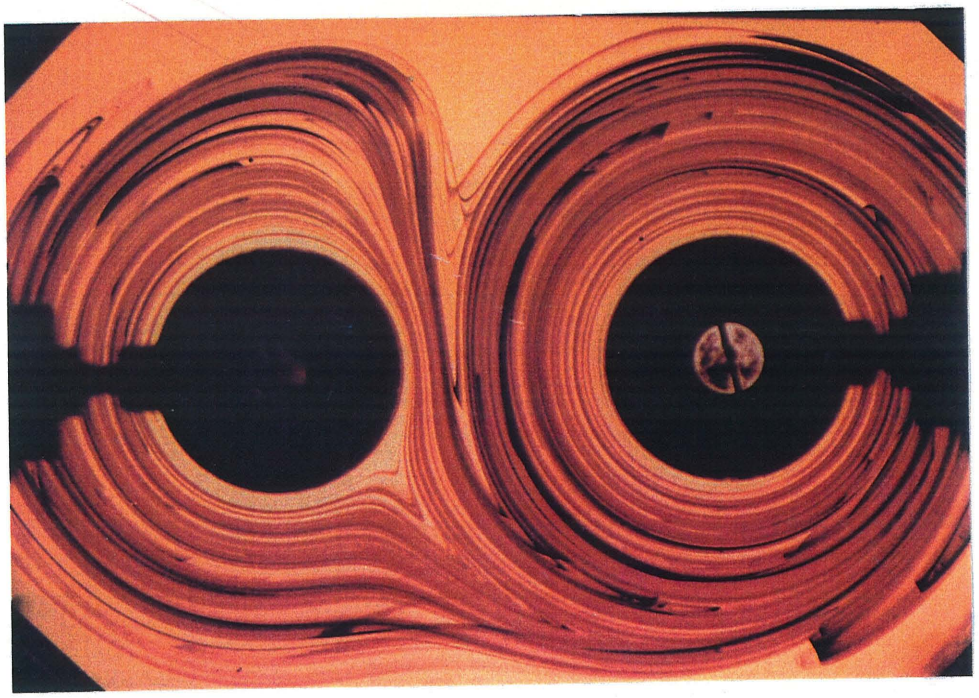

Fig. 3

(c)

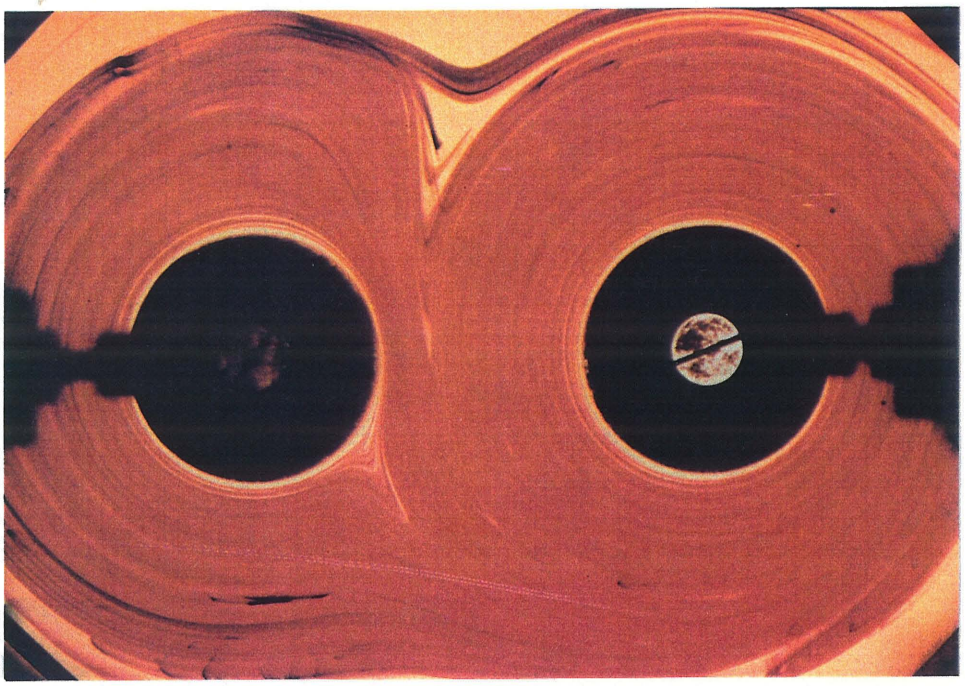

(d)

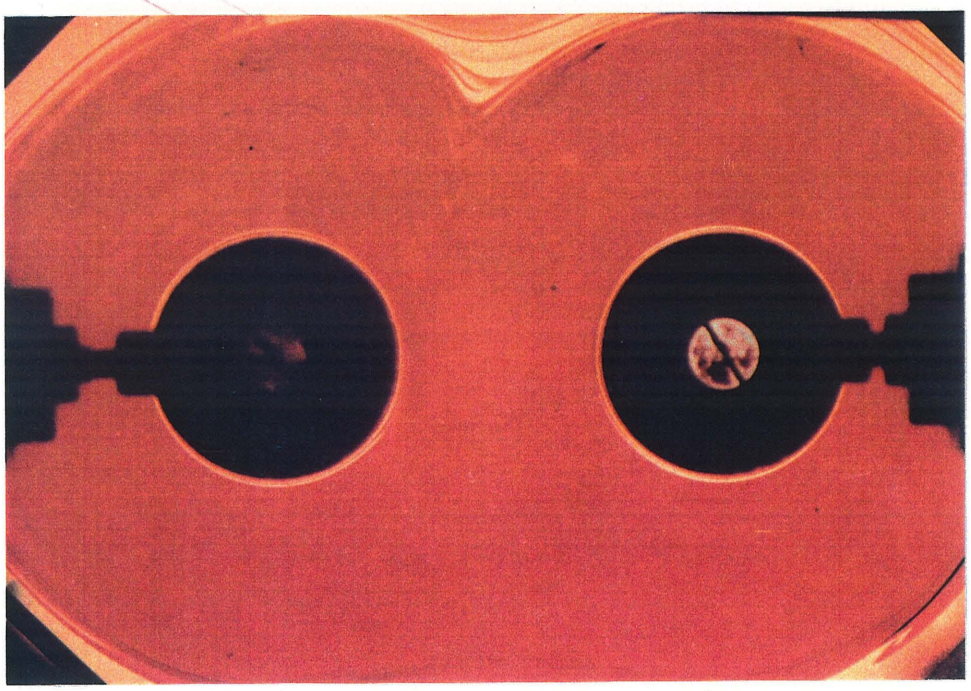

Fig. 3

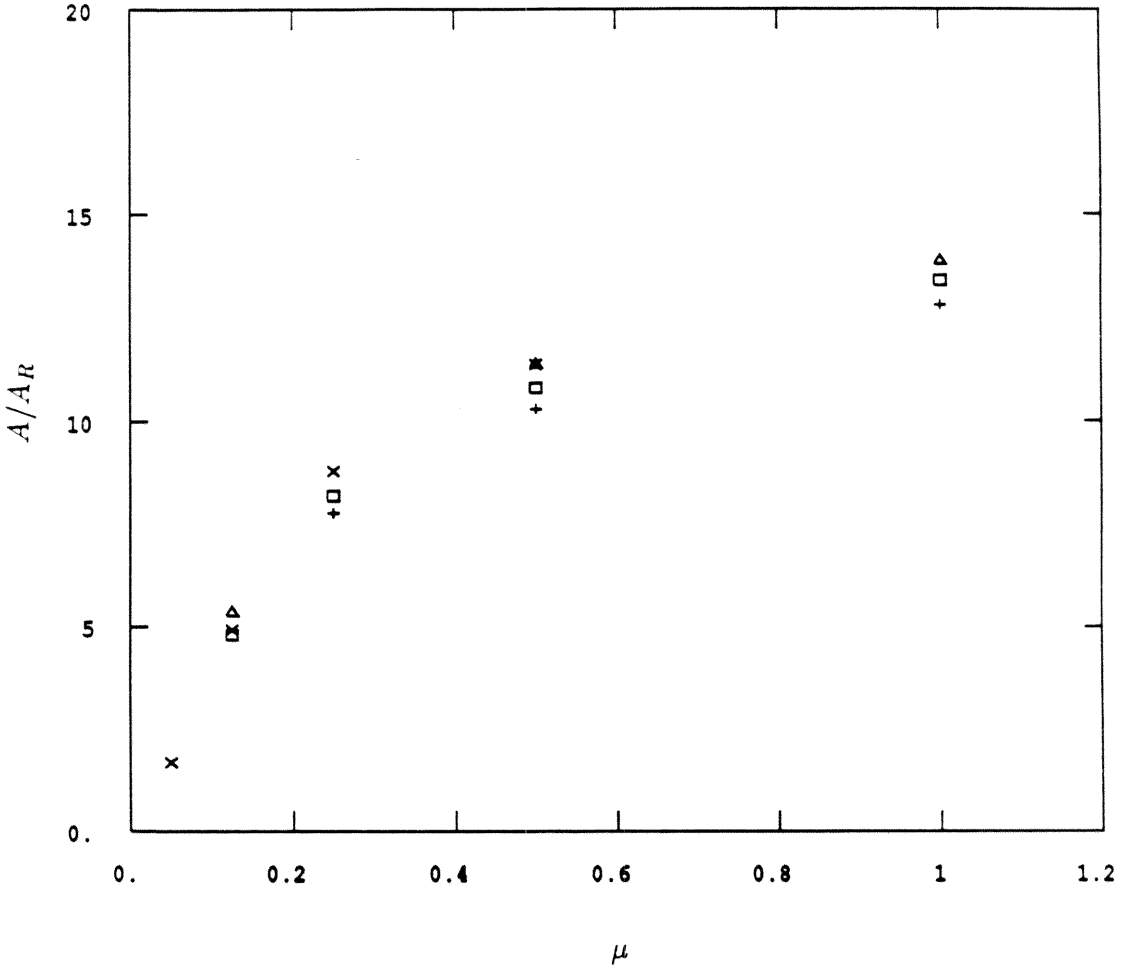

Fig. 4

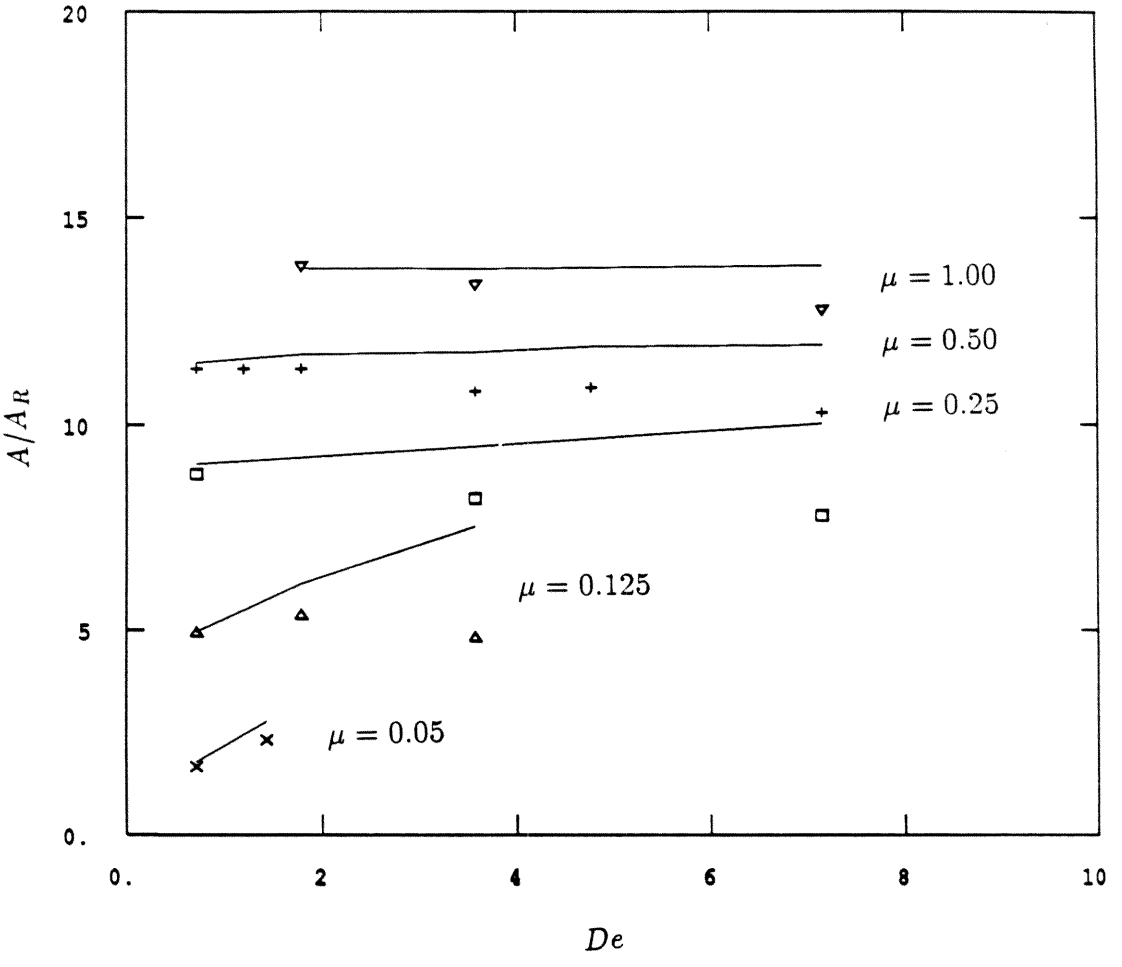

Fig. 5

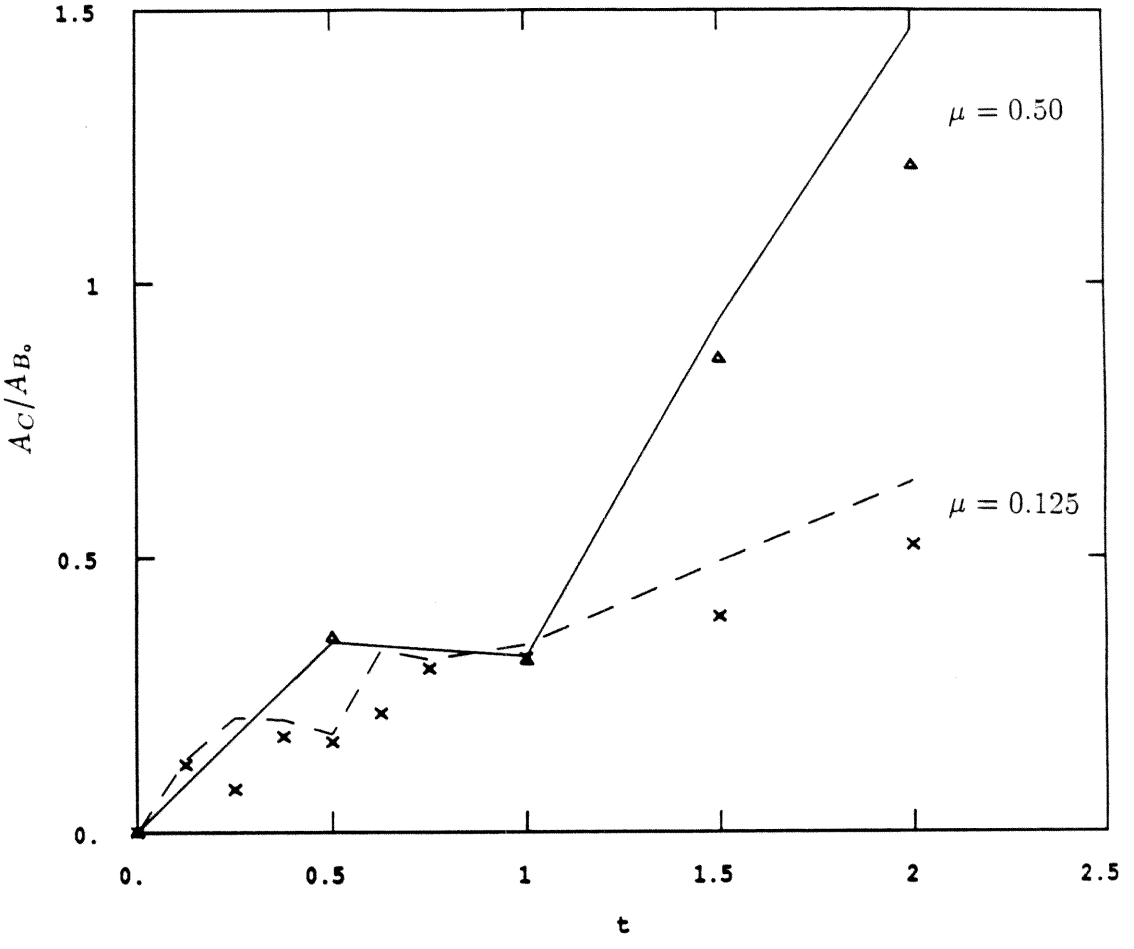

Fig. 6